Nuclear Spin Isomer Conversion of Molecular Hydrogen in Prussian Blue Analogs

大坪, 宥太

https://doi.org/10.15017/4059995

出版情報：九州大学, 2019, 博士（理学）, 課程博士
バージョン：
権利関係：

Nuclear Spin Isomer Conversion of Molecular Hydrogen in Prussian Blue Analogs

Yuta Ohtsubo

March 2020

Department of Chemistry

Graduate School of Science

Kyushu University

Contents

General Introduction **1**

Hydrogen Energy *1*

Hydrogen Storage *2*

Nuclear Spin Isomers of Molecular Hydrogen *4*

Ortho-Para Conversion and Boil-Off Problem *6*

Ortho-Para Conversion Acceleration by Solid Catalysts *8*

Ortho-Para Conversion by Porous Coordination Polymers *10*

Prussian Blue (PB) and Prussian Blue Analogs (PBAs) *13*

Purpose of This Research *16*

Reference *17*

Chapter 1 **24**

Abstract *24*

Introduction *25*

Physical Measurements *26*

Sample Preparation *27*

Results and Discussion *33*

Conclusions *79*

References *80*

Chapter 2 **85**

Abstract *85*

Introduction *86*

Physical Measurements *89*

Sample Preparation *91*

Results and Discussion *93*

Conclusions *114*

References *115*

Concluding Remarks **119**

List of Publications **120**

Acknowledgments **121**

General Introduction

Hydrogen Energy

Molecular hydrogen (H_2) is the simplest and lightest molecule consisting of two hydrogen atoms and exists as a gas at a wide temperature range because of the extremely low melting point (13.99 K) and boiling point (20.27 K) at ambient pressure (**Table 1**). The gravimetric energy density of H_2 is 33.3 kWh/kg, which is approximately 2.7 times larger than that of general types of gasoline and the highest value in all materials due to the extremely low density (0.0899 g L^{-1}) at standard temperature and pressure (STP).[1] The combustion process of H_2 to release the latent energy produces only water (H_2O), an environmentally-friendly material as the combustion product. In addition to the abovementioned industrial and environmental aspects, from the viewpoints of the renewability and richness in supply, H_2 is receiving a lot of attention as a promising energy carrier to replace conventional fossil fuels (*e.g.* petroleum and coal) which are limited in quantity and produce carbon dioxide (CO_2), a greenhouse gas during the energy production process. Therefore, the diverse research fields regarding H_2 including systems of production, storage, delivery, and energy conversion have been vigorously investigated to realize a hydrogen society.[2] Among them, the establishment of highly efficient hydrogen storage methods has been one of the most important challenges over recent decades.

Table 1. Physical and chemical properties of molecular hydrogen (H_2).

Molecular Weight	2.01588
Interatomic Distance	0.74 nm
Molecular Diameter	0.269 nm
Density	0.0899 g L^{-1} (STP)
Bond Energy	432 kJ mol^{-1}
Melting Point (*m.p.*)	13.99 K
Boiling Point (*b.p.*)	20.27 K
Triple Point	13.80 K, 7.041 kPa
Critical Point	32.94 K, 1.286 MPa
Heat of Fusion (ΔH_{fus})	0.117 kJ mol^{-1}
Heat of Vaporization (ΔH_{vap})	0.904 kJ mol^{-1}
Gravimetric Energy Density	33.3 kWh kg^{-1}

Hydrogen Storage

The United States Department of Energy (DOE) has roughly classified hydrogen storage methods into two types: material-based and physical-based methods. Each method is subdivided into additional detail based on several physical and chemical factors (*e.g.* volumetric density, gravimetric density, storage materials, storage pressure, and operating temperature; **Figure 1**).[3]

In the case of the material-based methods (*e.g.* porous materials, metal hydrides, and organic molecules), hydrogen is stored both molecularly and atomically. Porous materials (*e.g.* activated carbon[4] and zeolite[5]) feature easy uptake and release processes due to the physisorption; however, the storage amount at mild condition is relatively low both volumetrically and gravimetrically. Metal hydrides (*e.g.* $LaNi_5H_6$ and $NaAlH_4$)[6] also have been widely investigated as the storage materials and can generally store hydrogen with high volumetric density; however, the gravimetric density is considerably lower because of the metal element components. 3-Methyl-1,2-BN-cyclopentane and ammonia borane (NH_3BH_3) are the representative materials classified into chemical hydrogen methods.[7] These compounds have a high density for hydrogen both volumetrically and gravimetrically; however, because the hydrogen is atomically stored through strong chemical bonds, appropriate catalytic treatments are required to release hydrogen by breaking the chemical bonds and to restore hydrogen into the materials after the release. In terms of subjects described above, physical-based methods are practically used much more than material-based methods thanks to the relatively high volumetric density and the superior reversibility.

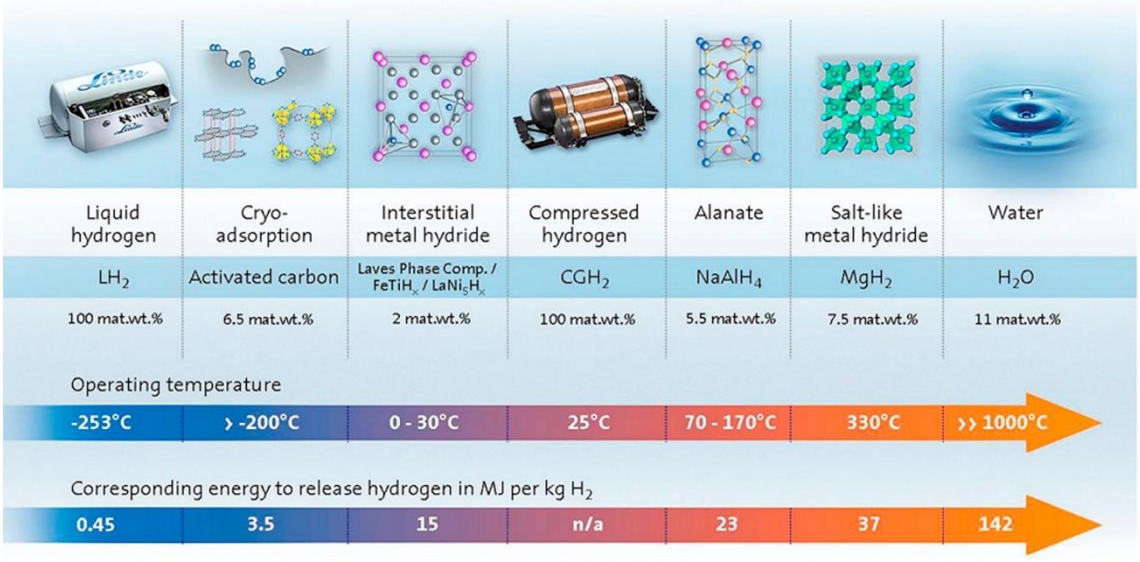

Figure 1. Classification of hydrogen storage.[3a]

The properties of basic physical-based hydrogen storage methods are tabulated (**Table 2**).[8] Although each storage method has both advantages and disadvantages in terms of the energy density and storage condition, compression and liquefaction have been widely used as storage methods thanks to the higher delivery efficiency. For example, as one of the disadvantages, compressed H_2 gas needs to be handled carefully because of the extremely strong reactivity and the high diffusion coefficient. In the case of liquid H_2 storage, which is also a superior and promising method for efficient H_2 transport, one of the most obvious problems is ascribed to the extremely low storage temperature. Liquid H_2 is stored in a cryogenic tank at 20 K and ambient pressure because of the low boiling point of 20.27 K at 1 atm (**Table 1**). Therefore, an efficient cooling process for liquefaction has been required; however, the most essential and latent problem in liquid H_2 storage is the wasted consumption by boil-off caused by interconversion between nuclear spin isomers of H_2 as well as the technical aspect of the storage vessel.

Table 2. Properties of basic physical-based hydrogen storage methods.[8]

	Compression	Liquefaction	Ultimate Target by DOE
Volumetric Density / kg m^{-3}	< 40	70.8	70
Gravimetric Density / wt%	13	Size-dependent	7.5
Storage Pressure / bar	800	1	5–12
Operating Temperature / K	298	21	230–330

Nuclear Spin Isomers of Molecular Hydrogen

Nuclear spin isomers exist in molecules containing two or more same atomic nuclei of which nuclear spin angular momentum is not zero (*e.g*. molecular hydrogen (H_2), molecular deuterium (D_2), and methane (CH_4)) in equivalent positions of the molecule. For example, because atomic hydrogen (^1H) is a fermion with a nuclear spin angular momentum of 1/2, H_2 comprises of two different nuclear spin isomers: ortho-hydrogen (o-H_2) with a parallel nuclear spin pair (I = 1) and para-hydrogen (p-H_2) with an antiparallel nuclear spin pair (I = 0), where I is the total nuclear spin angular momentum (**Figure 2a**).[9] The chemical properties (*e.g*. boiling point) of the two nuclear spin isomers are quite similar because their electronic structures are the same; however, the physical properties (*e.g*. specific heat capacity and thermal conductivity) are slightly different to a certain extent owing to the different internal energy originating from the rotational levels.[9b,c] The rotational energy (E_{rot}) of the nuclear spin isomers is quantized by rotational quantum number (J) according to Pauli exclusion principle and expressed by an equation of $E_{rot} = BJ(J + 1)$, where B is the rotational constant and approximately 7.35 meV for H_2 in a free rotational state and J is exclusively even and odd values for p-H_2 and o-H_2, respectively (**Equation 1** and **Figure 2a**). The abundance ratio of the nuclear spin isomer ([o-H_2]/[p-H_2]) at a thermal equilibrium state is temperature-dependent based on Boltzmann distribution, where k_B and T are Boltzmann constant and temperature, respectively (**Equation 1** and **Figure 2b**).[9d] The [o-H_2]/[p-H_2] value is almost precisely 3 over room temperature (RT) because of the almost simillar statistical multiplicity in the rotational states, and this mixture is usually regarded as normal-hydrogen (n-H_2). With decreasing temperature, the p-H_2 proportion gradually increases and the [o-H_2]/[p-H_2] value reaches approximately 1 around liquid N_2 temperature (77 K). Below liquid H_2 temperature (20 K), p-H_2 accounts for approximately 99.8 % in the isomeric mixtures because almost only the lowest rotational level of p-H_2 with J = 0 is populated due to the sufficiently large value of B.

$$[\mathrm{o\text{-}H_2}]/[\mathrm{p\text{-}H_2}] = \frac{\sum_{J=\mathrm{odd}} 3(2J+1)\exp\left\{-\frac{E_{\mathrm{rot}}}{k_B T}\right\}}{\sum_{J=\mathrm{even}} (2J+1)\exp\left\{-\frac{E_{\mathrm{rot}}}{k_B T}\right\}} = \frac{\sum_{J=\mathrm{odd}} 3(2J+1)\exp\left\{-\frac{BJ(J+1)}{k_B T}\right\}}{\sum_{J=\mathrm{even}} (2J+1)\exp\left\{-\frac{BJ(J+1)}{k_B T}\right\}}$$

Equation 1. Nuclear spin isomer ratio of molecular hydrogen.

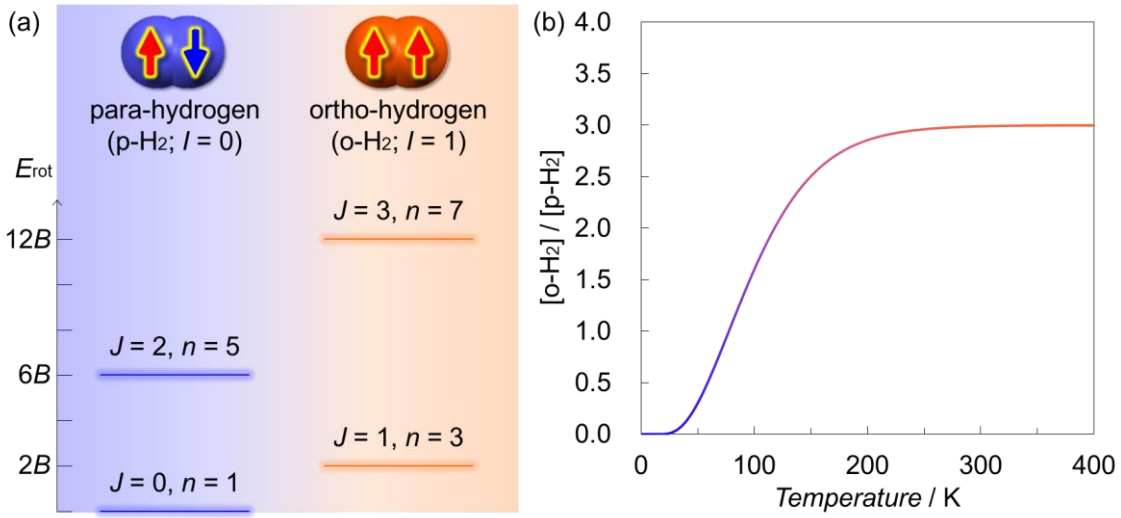

Figure 2. (a) Nuclear spin isomers for H_2 (p-H_2 and o-H_2) and their rotational energy diagram, where I, E_{rot}, B, J, and n denote total nuclear spin angular momentum, rotational energy, rotational constant, rotational quantum number, and degeneracy number, respectively. (b) Temperature-dependent nuclear spin isomer ratio ([o-H_2]/[p-H_2]) for H_2 in the free rotational state.

Ortho-Para Conversion and Boil-Off Problem

The nuclear spin conversion for H_2 corresponding to a transition from o-H_2 to p-H_2 ($J = 0 \leftarrow 1$), referred to as ortho-para (o-p) conversion, is theoretically a spin forbidden process according to a nuclear spin selection rule. Therefore, the o-p conversion expressed as a second-order reaction is extremely slow. In an isolated state (*e.g.* gas phase), the o-p conversion proceeds with a conversion time of the order of 10^{20} s because of the almost negligible intermolecular interaction.[10a] The conversion rate for liquid H_2 is ~1.14% h^{-1}.[10b] In the solid phase, the rate was calculated to be 1.94% h^{-1},[10c] which was in good agreement with the experimental results of ~1.9% h^{-1}.[10d,e] Because of the extremely slow conversion rates, the [o-H_2]/[p-H_2] value in n-H_2 remains constant for a while even after liquefaction by an immediate cooling process; however, the o-p conversion slightly and gradually proceeds in liquefied H_2 through interactions with the inner wall of the storage vessel and intermolecular collisions between H_2 (**Figure 3**). Because the gradual interconversion generates a conversion heat of ~1400 J mol^{-1} per n-H_2 (~1050 J mol^{-1} per o-H_2), which is sufficiently higher than the heat of vaporization of ~900 J mol^{-1} (**Table 1**), the immediately liquefied H_2 is easily evaporated again, which is referred to as a "boil-off" problem (**Figure 3**).[11a] If n-H_2 at RT is liquefied without any catalytic treatment, the estimated weight loss by the boil-off is ~50% after 1 week and 63.8% of the initial weight is evaporated at the end with a rate of ~18% day^{-1}.[11b] According to the requirement from the DOE, the content of p-H_2 should be usually 95% or more for the liquid storage.[8b,11c] In order to solve the boil-off problem in advance, o-H_2 should be converted to p-H_2 as smoothly and completely as possible by solid catalyst before liquefaction (**Figure 3**). In industrial applications, catalytic treatment is used to accelerate the o-p conversion until an equilibrium state is reached at each temperature. The continuous conversion with the temperature lowering is the most theoretically efficient process because the more the conversion process becomes stepwise, the lower the energy loss becomes.[11c]

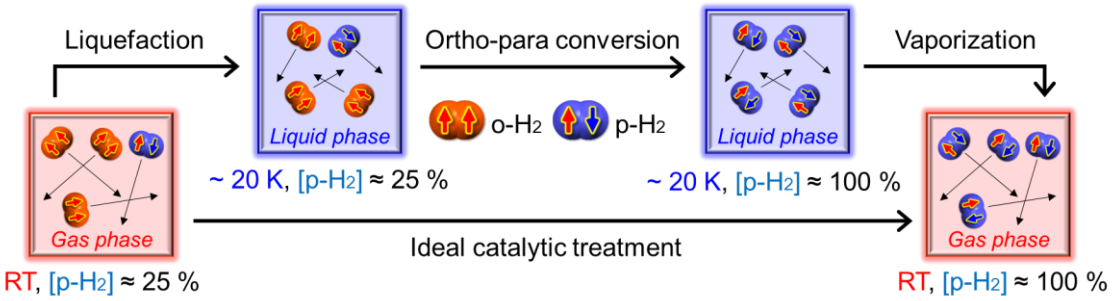

Figure 3. Schematic processes of liquefaction, ortho-para (o-p) conversion, vaporization and ideal catalytic treatment for H_2, and the o-p ratio at each point.

Ortho-Para Conversion Acceleration by Solid Catalysts

The conversion rate rapidly increases with pressure, increasing to 58% h^{-1} at 12.8 GPa[12a] and ~260% h^{-1} at 58 GPa;[12b] however, high pressurization is impractical due to difficulties with handling and the potential explosion hazard. In order to accelerate o-p conversion through a catalytic process, a two-step method is practically used in industries, where H_2 at RT is cooled down to first liquid N_2 temperature (77 K) and subsequently to liquid H_2 temperature (20 K). As the conversion catalyst, metal oxides or hydroxides (*e.g.* FeO(OH) and Cr_2O_3)[13] and diamagnetic metals (*e.g.* Cu and Ag)[14] have been vigorously investigated and industrially used. The conversion time from the p-H_2 concentration of 25% to 90% is ~330 min for FeO(OH) at 20 K and 1 atm, which is 6.6 times faster than that of Cr_2O_3.[13d] However, there is still room to improve the conversion rate and efficiency due to low contact frequency between o-H_2 and the catalyst because only the surface of the solid catalysts is available for the acceleration of the o-p conversion.

Highly pure amorphous solid water (ASW) systems have also been widely investigated for utility as the o-p conversion catalysts,[15] where o-p conversion at a time of ~370 s on the surface has been observed by resonance-enhanced multi-photon ionization (REMPI) for the highly sensitive and rotational-state selective detection.[15b] In addition to the conversion acceleration by the ASW system, a mechanism of o-p conversion through excitation and relaxation processes induced by an inhomogeneous electric-field of 10^{10}–10^{11} V m^{-1} on the catalyst surface has been proposed based on experimental results and theoretical analysis (**Figure 4**).[15b] In addition, there have been several proposed mechanisms for the activation of o-p conversions by giant inhomogeneous surface electric fields of non-magnetic materials.[14g,16] However, in the case of ASW, sophisticated techniques for sample preparation and extremely low handling temperatures are required.

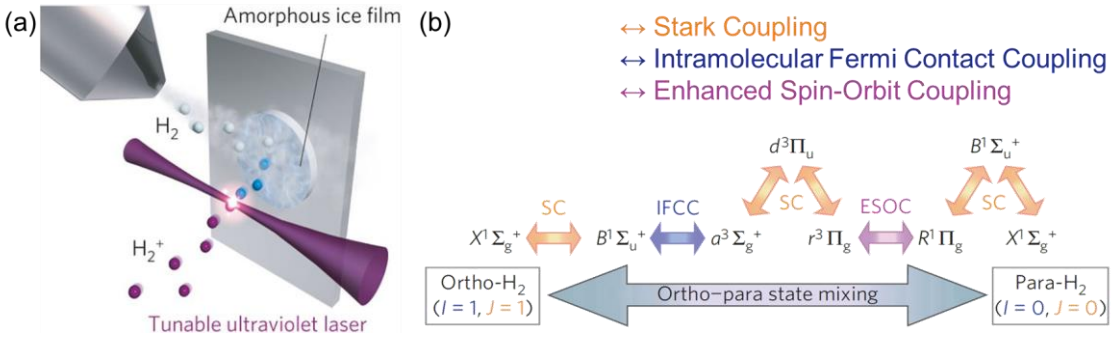

Figure 4. (a) Schematic experimental setup of resonance-enhanced multi-photon ionization (REMPI) for amorphous solid water (ASW) systems. (b) The state mixing of o-H_2 and p-H_2 under giant and inhomogeneous electric fields through stark coupling (SC: orange), intramolecular Fermi contact coupling (IFCC: blue) and enhanced spin-orbit coupling (ESOC: purple).[15b]

Ortho-Para Conversion by Porous Coordination Polymers

In terms of contact probability with substrates and efficient excitation field, porous coordination polymers (PCPs), also known as metal-organic frameworks (MOFs), are expected to be effective as next generation o-p conversion catalysts that can be easily prepared and can replace conventional catalysts because of their high specific surface area and the local electric field in the pores. PCPs are a class of porous materials synthesized by self-assembly of metal ions or clusters as versatile nodes and organic ligands as bridging linkers and exhibit a variety of physical and chemical properties based on the component properties and the periodically ordered porous structure (**Figure 5**).[17] Because molecules and ions can be adsorbed in the coordination space of PCPs through host-guest interactions (*e.g.* coordination bonds, van der Waals forces, electrostatic interactions, and π-π interactions), PCPs have been widely investigated to utilize as materials for various purposes (*e.g.* storage, separation, and catalysis; **Figure 5**). Contrary to the cases of conventional solid catalysts for o-p conversion, the improvement in o-p conversion efficiency of PCPs is expected because the coordination space, which limits the mobility of adsorbed H_2 and enhances the effective surface area as well as the subsequent contact probability between the confined H_2 and the framework.

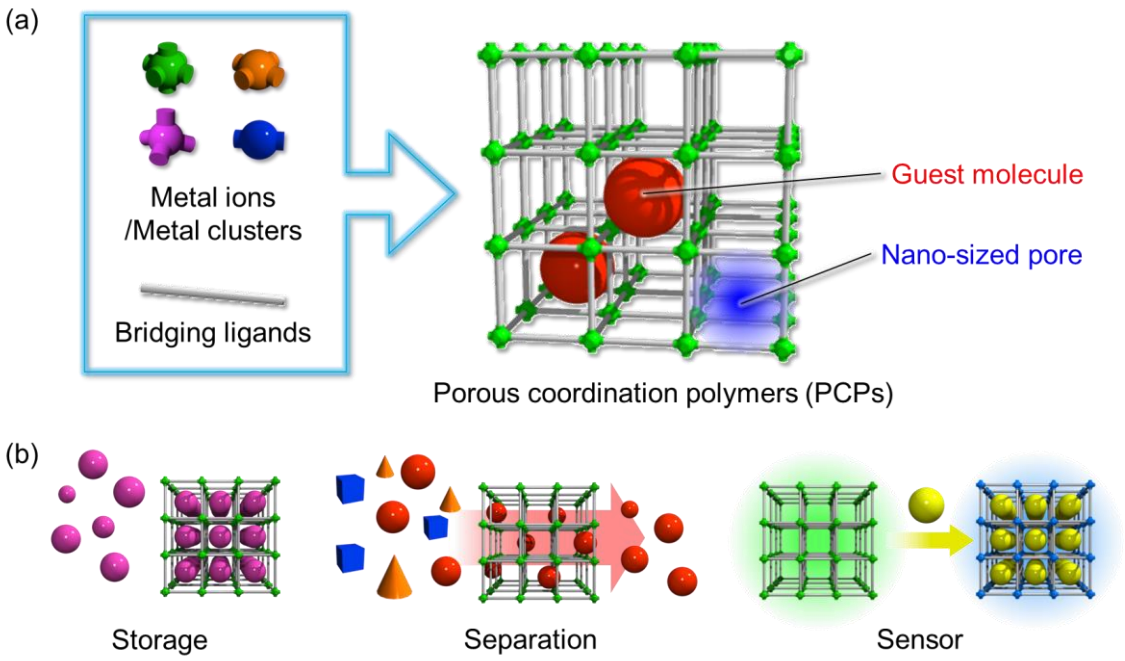

Figure 5. (a) Schematic structure of porous coordination polymer (PCP) consisting of metal ions or clusters with bridging ligands. (b) Examples of the diverse utility of PCPs.

The fundamental properties and quantum dynamics of H_2 adsorbed in $\{Zn^{II}_4O(bdc)_3\}$ (**MOF-5**; bdc^{2-} = 1,4-benzenedicarboxylate) were analyzed by *in-situ* diffuse reflectance infrared Fourier transform spectroscopy (DRIFTS), where slow o-p conversion was observed with a conversion rate of approximately 25 % h^{-1} at 30 K, although the o-p ratio $[o\text{-}H_2]/[p\text{-}H_2]$ remains close to 3 for several hours in the adsorbent.[18a] In other PCPs, $\{M^{II}_2(dobdc)\}$ (**MOF-74(M)**; M = Mg, Co, Ni, and Zn; $dobdc^{4-}$ = 2,5-dioxidobenzene-1,4-dicarboxylate), o-p conversions were spectroscopically confirmed as well.[18b] An extremely fast o-p conversion was observed in **MOF-74(Zn)** with a conversion time of ~10 min at 40 K by *in-situ* DRIFTS, whereas the o-p conversion observed in **MOF-5** occurred over a few hours (**Figure 6**).[18c] However, no further analysis and discussion concerning the details (*e.g.* mechanism and driving force) were given unfortunately in both cases of **MOF-5** and **MOF-74(M)**.

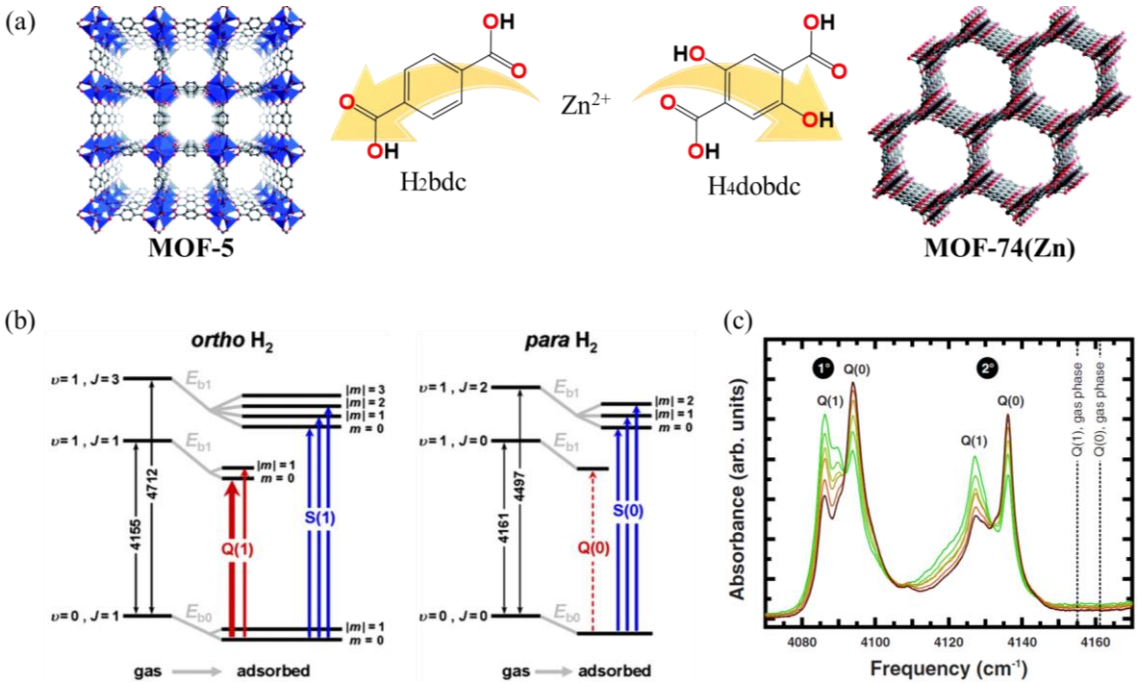

Figure 6. (a) Schematic structure and components of **MOF-5** and **MOF-74(Zn)**. (b) Energy level diagram showing the rotational-vibrational transitions for H_2, where v is the vibrational quantum number. (c) *In-situ* diffuse reflectance infrared Fourier transform spectra (DRIFTS) of **MOF-74(Zn)** with different times of 55, 95, 135, 175, 280, 600, and 2700 s (from light green to brown) after loading 1.8 H_2 per Zn at 40 K.[18b]

In order to investigate the mechanism of o-p conversion in PCPs, an experimental demonstration was performed for the first time using a Hofmann-type PCP, $\{Fe^{II}(pz)[Pd^{II}(CN)_4]\}$ (**FePd-pz**; pz = pyrazine) as a material for o-p conversion.[19] At a gas pressure of 80 kPa, **FePd-pz** adsorbed H_2 with the amount of 2.7 and 3.5 molecule pore^{-1} at 65 and 35 K, respectively (**Figure 7a**). Using a combination of *in-situ* powder X-ray diffraction (PXRD) measurement under an H_2 atmosphere and a maximum entropy method (MEM), the adsorption sites of H_2 were determined to be the pore center (site-I) and several sites scattered between adjacent pyrazine ligands (site-II) at 65 K, and a diagonally-extended site including the site-I region (site-III) at 35 K (**Figure 7b**). Site-III has a large local electric field of 7.62×10^{10} V m^{-1} at the diagonal ends, while site-I has almost no electric field, meaning that H_2 confined in **FePd-pz** at 35 K receives a large electric field gradient through site-exchange inside site-III. During the cooling process, *in-situ* Raman spectroscopy under an H_2 atmosphere revealed o-p conversion within 600 s, indicating that the large electric field gradient applied during the site-exchange of the confined H_2 is effective for the swift o-p conversion (**Figure 7c**). Although the acceleration and the experimental elucidation of the mechanism of o-p conversion were successfully achieved, the observed conversion temperature was still around the boiling point of H_2 (20.27 K), which is not suitable for practical catalytic acceleration.

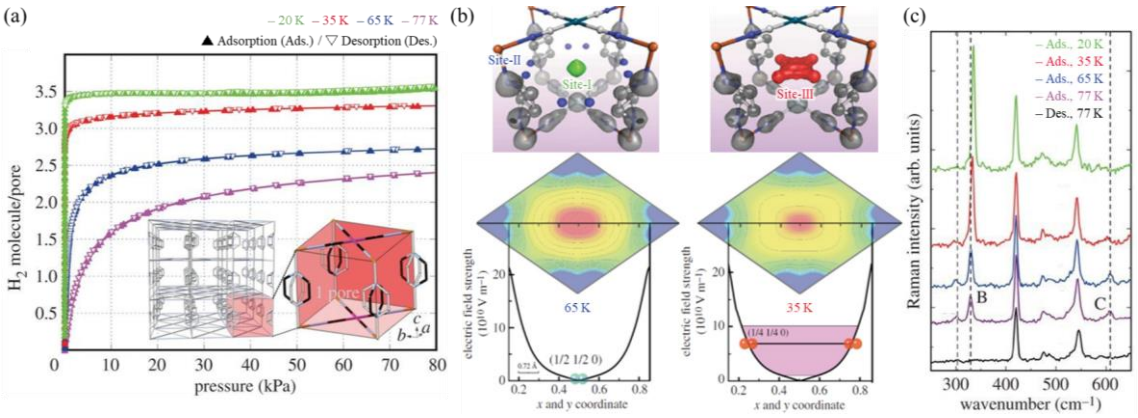

Figure 7. (a) Schematic crystal structure and temperature-dependent H_2 isotherm of $\{Fe(pz)[Pd(CN)_4]\}$ (**FePd-pz**; pz = pyrazine). (b) MEM charge densities as equidensity contour surfaces in H_2 adsorption and one-dimensional absolute electric fields in the desorbed state along the [110] direction on the (001) plane at 35 and 65 K. (c) *In-situ* temperature-dependent Raman spectra under an H_2 atmosphere.[19]

Prussian Blue (PB) and Prussian Blue Analogs (PBAs)

In order to improve o-p conversion temperature, we focused on Prussian Blue analogs (PBAs) as the next potential catalysts because of the H_2 adsorption ability, ease of synthesis, diverse components, and local anisotropy derived from the defective structure. Prussian blue (PB), which is a dark blue metal complex with a chemical formula of $\{Fe^{III}_4[Fe^{II}(CN)_6]_3\}$, has been used as a blue pigment over 300 years ago and widely studied in various functional materials for several decades.[20] Because PB is a mixed-valence complex, a combination of Fe^{2+} and $[Fe^{III}(CN)_6]^{3-}$ instead of that of Fe^{3+} and $[Fe^{II}(CN)_6]^{4-}$ during synthetic process provides the same compound. The structure of PB was determined to be a 3-D cyano-bridged structure including water molecules (**Figure 8a**).[21] Remarkably, PB is an aperiodic system because one-fourth of the $[Fe^{II}(CN)_6]^{4-}$ units result defects from the ideal framework structure because of the charge balance, and 1.5 H_2O molecules on average are coordinated to the unsaturated octahedral Fe^{3+} site. Alternatively, PBAs have a similar framework structure with a general chemical formula of $\{A_xMa_y[Mb(CN)_6]_z\}$, where A are monovalent cations (*e.g.* alkali cations and quaternary ammonium ions), and Ma and Mb are divalent or trivalent metal ions in an octahedral geometry (**Figure 8**). When A^+ ions are included into the framework or Ma and Mb ions have the same valence, the ideal frameworks can be the non-defective framework structure with the formula of $\{A^IMa^{II}[Mb^{III}(CN)_6]\}$ and $\{Ma^{III}[Mb^{III}(CN)_6]\}$, respectively (**Figure 8b and Figure 8c**). On the other hand, when Ma ions are divalent and Mb ions are trivalent, one-third of defects in $[M^{III}(CN)_6]^{3-}$ moieties are formed in the framework structure of $\{Ma_3[Mb(CN)_6]_2\}$ (**Figure 8a**). The degree of freedom in the material design of PBAs is high thanks to a variety of metal ions.

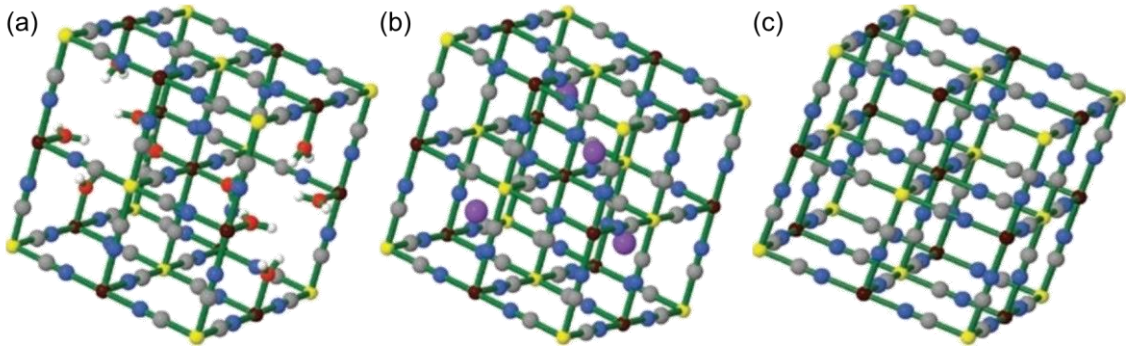

Figure 8. Schematic crystal structure of Prussian Blue (PB) and Prussian Blue Analogs (PBAs). (a) $\{Fe^{III}_4[Fe^{II}(CN)_6]_3\}$ or $\{Ma^{II}_3[Mb^{III}(CN)_6]_2\}$. (b) $\{AMa^{II}[Mb^{III}(CN)_6]\}$. (c) $\{Ma^{III}[Mb^{III}(CN)_6]\}$. All lattice water molecules are omitted for clarity. Color codes; H: white, C: gray, N: blue, O: red, A: purple, Fe^{III} for PB and Ma for PBAs: brown, Fe^{II} for PB and Mb for PBAs: yellow.[20b]

From the viewpoint of their porous structure, PBAs have been investigated as adsorbents for several kinds of small molecules and ions (*e.g.* CO_2,[22] ammonia (NH_3)[23], cesium ion (Cs^+)[24], and noble gases[25]). H_2 adsorption in PBAs was performed for the first time using $\{M^{II}_3[Co^{III}(CN)_6]_2\}$ (**M_3Co_2**; M = Mn, Fe, Co, Ni, Cu, Zn, and Cd) series.[26a,b] Moreover, H_2 adsorption in other PBAs based on $[Mb^{II}(CN)_6]^{4-}$ (M = Fe and Ru) unit[27] and nitroprusside ($[Fe^{III}(CN)_5(NO)]^{2-}$) unit[28] has widely been reported as well as hexacyanometallate ($[M^{III}(CN)_6]^{3-}$; M = Fe, Co, Rh, and Ir) series.[26]

In terms of H_2 adsorption sites in PBAs, the host-guest interactions between adsorbed H_2 and PBA framework were directly observed in $\{Mn^{II}_3[Co^{III}(CN)_6]_2\}$ (**Mn_3Co_2**) by a differential X-ray and neutron pair distribution function (PDF) analysis, which revealed that the adsorbed H_2 molecules are disordered at a single position of the pore center to obtain maximal van der Waals interactions.[29a] In $\{Cu^{II}_3[Co^{III}(CN)_6]_2\}$ (**Cu_3Co_2**), Rietveld structural refinement of the *in-situ* powder neutron diffraction measurement exhibited two H_2 adsorption sites, which are the pore center as the most prominent adsorption site and the coordination site of the exposed Cu^{2+} center resulting from $[Co^{III}(CN)_6]^{3-}$ vacancies (**Figure 9a**).[29b] Furthermore, *in-situ* neutron vibrational spectroscopy of **Cu_3Co_2** showed that an energy band around 14.7 meV was distributed, which is assigned to a rotational transition between the ground states of o-H_2 and p-H_2 (J = 0 ← 1), suggesting a range of local binding potentials of the adsorbed H_2 because of the various potentials based on the different geometries of the Cu^{2+} sites (**Figure 9b**). In other words, the defective framework structure of PBAs can cause the split of rotational energy levels of adsorbed H_2, possibly leading a change in [o-H_2]/[p-H_2] ratio from a theoretical ratio.

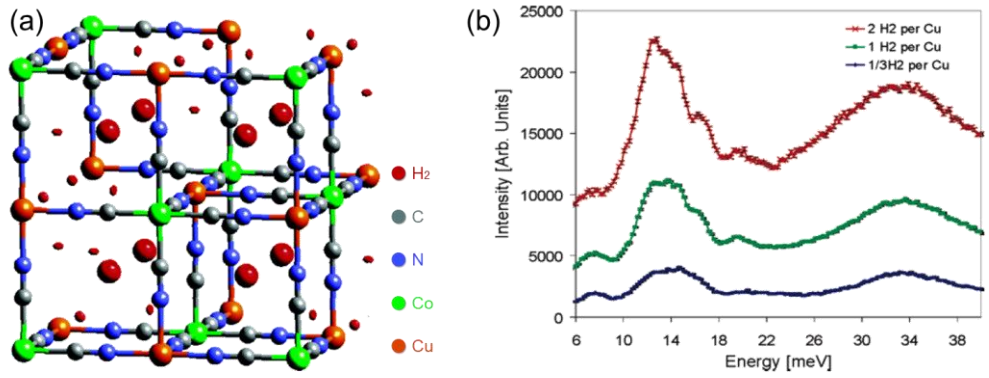

Figure 9. (a) The structure of $\{Cu^{II}_3[Co^{III}(CN)_6]_2\}$ (**Cu_3Co_2**) at an H_2 loading of 1 H_2 per Cu calculated by Rietveld refinement of high-resolution *in-situ* powder neutron diffractometry. Color codes: H_2 (red), C (gray), N (blue), Co (light green), Cu (orange). (b) *In-situ* neutron vibrational spectra of **Cu_3Co_2** with varying amounts of adsorbed H_2.[29b]

There is no report using PBAs as o-p conversion catalysts. In the case of **FePd-pz** which has regularly arranged pores, more than 2 molecules of H_2 per pore can be absorbed and the swift o-p conversion occurs by a perturbation of the electric field gradient through site-exchange in a broadened adsorption site (site-III). On the other hand, the H_2 adsorption amount in PBAs is usually less than 1 molecule per pore, which suggests that the adsorbed H_2 has high mobility even in the pore and o-p conversion through the defective sites instead of the site-exchange is expected. Moreover, the relatively high structural stability of PBAs is the reason for selection, although PCPs with a defective framework usually tend to be structurally fragile. In addition to the dynamics of H_2 molecules and the mechanical strength, from the aspect of the magnetic properties, while Fe^{II}-based Hofmann-type PCPs, $\{Fe^{II}(pz)[M^{II}(CN)_4]\}$ (M = Ni, Pd, and Pt) has a diamagnetic framework at low temperature based on the Fe^{2+} in a low spin state,[30] several PBAs can be porous magnets showing magnetic ordering at relatively higher temperature due to the short distances between the two different metal ions through the cyanide-bridge.[31] Therefore, evaluation for o-p conversion under an external magnetic field can provide beneficial knowledge regarding the effect of the magnetic field induced in the pores of the PCP on the o-p conversion of H_2. Among well-known hexacyanometallate units, because $[Mb^{III}(CN)_6]^{3-}$ (Mb = Co, Rh, and Ir) in d^6 electron state is a diamagnetic unit and $[Fe^{III}(CN)_6]^{3-}$ unit in d^5 electron state provides magnetic PBAs with low magnetic ordering temperature, we selected $[Cr^{III}(CN)_6]^{3-}$ in d^3 electron state as the component unit of PBAs for o-p conversion catalysts. $[Cr^{III}(CN)_6]^{3-}$-based PBAs usually have a higher magnetic ordering temperature than the boiling point of H_2;[31] however, their H_2 adsorption property is quite unclear because of almost no reports about this property. Hence, structural stability and adsorption ability of $[Cr^{III}(CN)_6]^{3-}$-based PBAs are worth being investigated systematically for the evaluation of o-p conversion and other practical utilities.

Purpose of This Research

In this study, we systematically synthesized PBAs using $[Cr^{III}(CN)_6]^{3-}$ as a building unit. Then, their structural stability upon desolvation, adsorption capacity, and catalytic ability for the o-p conversion of H_2 were investigated.

In Chapter 1, we have systematically synthesized defective $[Cr^{III}(CN)_6]^{3-}$-based PBAs, $\{M^{II}_3[Cr^{III}(CN)_6]_2\}$ (**M_3Cr_2**; M = VO, Cr, Mn, Fe, Co, Ni, Cu, Zn, and Cd) and non-defective $[Cr^{III}(CN)_6]^{3-}$-based PBAs, $\{In^{III}[Cr^{III}(CN)_6]\}$ (**InCr**) as a control sample, based on a typical method for synthesizing PBAs and discussed their structural stability upon application of the desolvation process of vacuuming at different temperatures, using powder X-ray diffractometry (PXRD) and Fourier transform infrared spectroscopy (FT-IR) measurements. Moreover, their N_2 and H_2 adsorption measurements have been performed at 77 K. This research is the first report about H_2 adsorption at liquid N_2 temperature (77 K) in defective $[Cr^{III}(CN)_6]^{3-}$-based PBAs with the chemical formula of $\{M^{II}_3[Cr^{III}(CN)_6]_2\}$ (**M_3Cr_2**), regardless of many reports about the H_2 adsorption in PBAs based on other hexacyanometallates, $[M^{III}(CN)_6]^{3-}$ (M = Fe, Co, Rh, and Ir).

In Chapter 2, we have aimed to improve o-p conversion temperature using defective PBAs, $\{M^{II}_3[Cr^{III}(CN)_6]_2\}$ (**M_3Cr_2**; M = Mn and Ni), which has local anisotropic pore spaces due to the structural defects and is expected to have the effect of a local electric field and magnetic field in the pores. We have confirmed the catalytic ability of **M_3Cr_2** for the o-p conversion of H_2 by *in-situ* Raman microspectroscopy under an H_2 atmosphere at cryogenic temperatures (**Figure 10**). In the same way, we have evaluated the effect of the inner magnetic field of **Mn_3Cr_2** on o-p conversion by the *in-situ* Raman microspectroscopy under an external magnetic field.

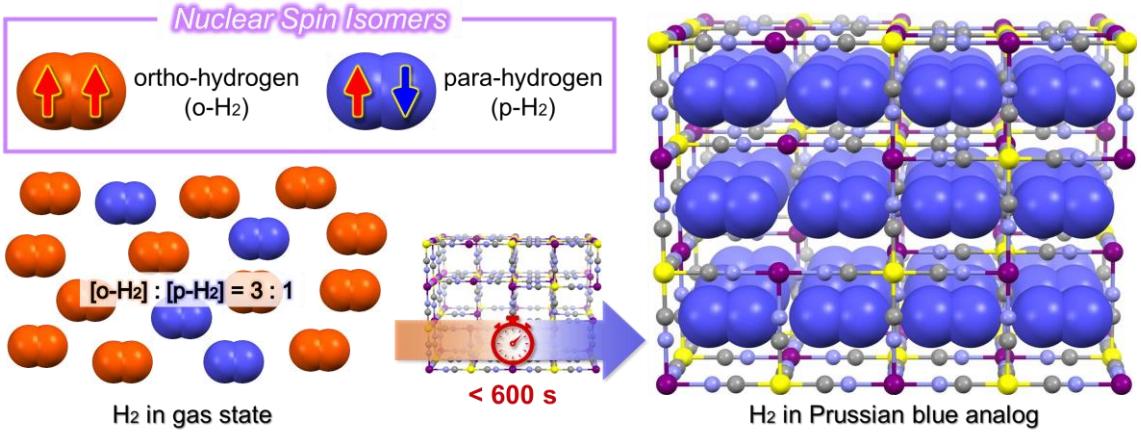

Figure 10. Schematic view of the o-p conversion of confined molecular H_2 in PBAs.

Reference

1. W. Zittel, R. Wurster, L. Bolkow, Advantages and Disadvantages of Hydrogen, *Hydrog. in the Energy Sector. Systemtechnik Gmbitt*, **1996**.
2. (a) A. Züttel, A. Remhof, A. Borgschulte, O. Friedrichs, *Philos. Trans. R. Soc. A Math. Phys. Eng. Sci.*, **2010**, *368* (1923), 3329–3342.; (b) N. Gallandat, K. Romanowicz, A. Züttel, *J. Power Energy Eng.*, **2017**, *5* (10), 34–49.
3. (a) R. von Helmolt, U. Eberle, *J. Power Sources*, **2007**, *165* (2), 833–843.; (b) A. Züttel, A. Remhof, A. Borgschulte, O. Friedrichs, *Philos. Trans. R. Soc. A Math. Phys. Eng. Sci.*, **2010**, *368* (1923), 3329–3342.
4. (a) H. Jin, Y. S. Lee, I. Hong, *Catal. Today*, **2007**, *120* (3–4), 399–406.; (b) G. Hermosilla-Lara, G. Momen, P. H. Marty, B. L. Neindre, K. Hassouni, *Int. J. Hydrog. Energy*, **2007**, *32* (10–11), 1542–1553.; (c) Y. Feng, J. Wang, Y. Liu, Q. Zheng, *Cryogenics*, **2019**, *101*, 36–42.
5. (a) F. Darkrim, A. Aoufi, P. Malbrunot, *J. Chem. Phys.*, **2000**, *112* (13), 5991–5999.; (b) H. W. Langmi, A. Walton, M. M. Al-Mamouri, S. R. Johnson, D. Book, J. D. Speight, P. P. Edwards, I. Gameson, P. A. Anderson, I. R. Harris, *J. Alloys Compd.*, **2003**, *356–357*, 710–715.; (c) N. Bouaziz, M. B. Manaa, F. Aouaini, A. B. Lamine, *Mater. Chem. Phys.*, **2019**, *225*, 111–121.
6. (a) M. A. El-Osairy, I. A. El-Osery, A. M. Metwally, M. M. Keshk, *Int. J. Hydrog. Energy*, **1992**, *17* (12), 961–964.; (b) B. Bogdanović, M. Schwickardi, *Appl. Phys. A Mater. Sci. Process*, **2001**, *72*, 221–223.; (c) M. Resana, M. D. Hamptona, J. K. Lomnessa, D. K. Slattery, *Int. J. Hydrog. Energy*, **2005**, *30* (13–14), 1417–1421.; (d) Y. Fu, M. Groll, R. Mertz, R. Kulenovic, *J. Alloys Compd.*, **2008**, *460* (1–2), 607–613.; (e) M. V. Lototskyy, V. A. Yartys, B. G. Pollet, R. C. Bowman Jr., *Int. J. Hydrog. Energy*, **2014**, *39* (11), 5818–5851.
7. (a) W. Luo, P. G. Campbell, L. N. Zakharov, S. Y. Liu, *J. Am. Chem. Soc.*, **2011**, *133* (48), 19326–19329.; (b) W. Luo, D. Neiner, A. Karkamkar, K. Parab, E. B. Garner, D. A. Dixon, D. Matson, T, Autrey, S. Y. Liu, *Dalton Trans.*, **2013**, *42* (3), 611–614.; (c) M. E. Bluhm, M. G. Bradley, R. Butterick, U. Kusari, L. G. Sneddon, **2006**, *128* (24), 7748–7749.; (d) R. J. Keaton, J. M. Blacquiere, R. T. Baker, *J. Am. Chem. Soc.*, **2007**, *129* (7), 1844–1845.; (e) B. L. Davis, D. A. Dixon, E, B. Garner, J. C. Gordon, M. H. Matus, B. Scott, F. H. Stephens, *Angew. Chem. Int. Ed.*, **2009**, *48* (37), 6812–6816.
8. (a) A. Züttel, *Mater. Today*, **2003**, *6* (9), 24–33.; (b) the United States Department of Energy (DOE), Target Explanation Document: Onboard Hydrogen Storage for Light-Duty Fuel Cell Vehicles, **2017**.; (c) J. Andersson, S. Grönkvist, *Int. J. Hydrog.*

Energy, **2019**, *44* (23), 11901–11919.

9. (a) A. Farkas, Orthohydrogen, Parahydrogen and Heavy Hydrogen, *Cambridge Univ. Press*, **1935**.; (b) R. G. Bohn, C. F. Mate, *Phys. Rev. B*, **1970**, *2* (6), 2121–2126.; (c) J. E. Huebler, R. G. Bohn, *Phys. Rev. B*, **1978**, *17* (4), 1991–1996.; (d) R. W. Harkness, W. E. Deming, *J. Am. Chem. Soc*., **1932**, *54* (7), 2850–2852.
10. (a) J. C. Raich, J. R. H. Good, *Astrophys. J*., **1964**, *139* (3), 1004–1013.; (b) R. B. Scott, F. G. Brickwedde, H. C. Urey, M. H. Wahl, *J. Chem. Phys*., **1934**, *2* (8), 454–464.; (c) K. Motizuki, T. Nagamiya, *J. Phys. Soc. Jpn*., **1956**, *11* (2), 93–104.; (d) F. Schmidt, *Phys. Rev. B*, **1974**, *10* (10), 4480–4484.; (e) I. F. Silvera, *Rev. Mod. Phys*., **1980**, *52* (2), 393–452.
11. (a) N. S. Sullivan, D. Zhou, C. M. Edwards, *Cryogenics*, **1990**, *30* (8), 734–735.; (b) A. H. Larsen, F. E. Simon, C. A. Swenson, *Rev. Sci. Instrum*., **1948**, *19* (4), 266–269.; (c) C. R. Baker, R. L. Shaner, *Int. J. Hydrog. Energy*, **1978**, *3* (3), 321–334.
12. (a) M. Pravica, I. Silvera. *Phys. Rev. Lett*., **1998**, *81* (19), 4180–4183.; (b) J. H. Eggert, E. Karmon, R. J. Hemley, H. K. Mao, A. F. Goncharov, *Proc. Natl. Acad. Sci. U.S.A*., **1999**, *96* (22), 12269–12272.
13. (a) K. F. Bonhoeffer, P. Harteck, *Z. Phys. Chem*., **1929**, *4B* (1), 113–141.; (b) L. Farkas, L. Sandler, *J. Chem. Phys*., **1940**, *8* (3), 248–251.; (c) D. H. Weitzel, O. E. Park, *Rev. Sci. Instrum*., **1956**, *27* (1), 57–58.; (d) D. H. Weitzel, W. V. Loebenstein, J. W. Draper, O. E. Park, *J. Res. Natl. Bur. Std*., **1958**, *60* (3), 221–227.; (e) K. G. Petzinger, D. J. Scalapino, *Phys. Rev. B*, **1973**, *8* (1), 266–279.; (f) Y. Ishii, *Prog. Surf. Sci*., **1986**, *21* (2), 163–208.; (g) E. Ilisca, *Prog. Surf. Sci*., **1992**, *41* (3), 217–335.; (h) S. Paris, E. Ilisca, *J. Phys. Chem. A*, **1999**, *103* (25), 4964–4968.
14. (a) P. Avouris, D. Schmeisser, J. E. Demuth, *Phys. Rev. Lett*., **1982**, *48* (3), 199–202.; (b) S. Andersson, J. Harris, *Phys. Rev. Lett*., **1982**, *48* (8), 545–548.; (c) E. Ilisca, *Phys. Rev. Lett*., **1991**, *66* (5), 667–670.; (d) K. Fukutani, K. Yoshida, M. Wilde, W. A. Diño, M. Matsumoto, T. Okano, *Phys. Rev. Lett*., **2003**, *90* (9), 096103.; (e) K. Niki, T. Kawauchi, M. Matsumoto, K. Fukutani, T. Okano, *Phys. Rev. B*, **2008**, *77* (20), 201404.; (f) K. Fukutani, T. Sugimoto, *Prog. Surf. Sci*., **2013**, *88* (4), 279–348.; (g) T. Sugimoto, K. Fukutani, *Phys. Rev. Lett*., **2014**, *112* (14), 146101.
15. (a) N. Watanabe, Y. Kimura, A. Kouchi, T. Chigai, T. Hama, V. Pirronello, *Astrophys. J. Lett*., **2010**, *714* (2), L233–L237.; (b) T. Sugimoto, K. Fukutani, *Nat. Phys*., **2011**, *7*, 307–310.; (c) M. Chehrouri, J.-H. Fillion, H. Chaabouni, H. Mokrane, E. Congiu, F. Dulieu, E. Matar, X. Michaut, J. L. Lemaire, *Phys. Chem. Chem. Phys*., **2011**, *13* (6), 2172–2178.; (d) T. Hama, K. Kuwahata, N. Watanabe,

A. Kouchi, Y. Kimura, T. Chigai, V. Pirronello, *Astrophys*. *J*., **2012**, *757* (2), 185.; (e) H. Ueta, N. Watanabe, T. Hama, A. Kouchi, *Phys*. *Rev*. *Lett*., **2016**, *116* (25), 253201.

16. (a) E. Ilisca, *Eur*. *Phys*. *Lett*., **2013**, *104* (1), 18001.; (b) E. Ilisca, F. Ghiglieno, *Eur*. *Phys*. *J*. *B*, **2014**, *87*, 235.
17. (a) M. Eddaoudi, J. Kim, N. Rosi, D. Vodak, J. Wachter, M. O'Keeffe, O. M. Yaghi, *Science*, **2002**, *295* (5554), 469–472.; (b) S. Kitagawa, R. Kitaura, S. Noro, *Angew*. *Chem*., *Int*. *Ed*., **2004**, *43* (18), 2334–2375.; (c) J. L. C. Rowsell, O. M. Yaghi, *Micropor*. *Mesopor*. *Mater*., **2004**, *73* (1–2), 3–14.; (d) G. Férey, *Chem*. *Soc*. *Rev*., **2008**, *37*, 191.; (e) G. Férey, C. Serre, *Chem*. *Soc*. *Rev*., **2009**, *38* (5), 1380–1399.
18. (a) S. A. FitzGerald, K. Allen, P. Landerman, J. Hopkins, J. Matters, R. Myers, J. L. C. Rowsell, *Phys*. *Rev*. *B*, **2008**, *77* (22), 224301.; (b) N. Nijem, J.-F. Veyan, L. Kong, H. Wu, Y. Zhao, J. Li, D. C. Langreth, Y. J. Chabal, *J*. *Am*. *Chem*. *Soc*., **2010**, *132* (42), 14834–14848.; (c) S. A. FitzGerald, J. Hopkins, B. Burkholder, M. Friedman, J. L. C. Rowsell, *Phys*. *Rev*. *B*, **2010**, *81* (10), 104305.
19. T. Kosone, A. Hori, E. Nishibori, Y. Kubota, A. Mishima, M. Ohba, H. Tanaka, K. Kato, J. Kim, J. A. Real, S. Kitagawa, M. Takata, *R*. *Soc*. *open sci*., **2015**, *2* (7), 150006.
20. (a) L. Samain, F. Grandjean, G. J. Long, P. Martinetto, P. Bordet, D. Strivay, *J*. *Phys*. *Chem*. *C*, **2013**, *117* (19), 9693–9712.; (b) M. Ware, *J*. *Chem*. *Educ*., **2008**, *85* (5), 612–621.
21. (a) H. J. Buser, D. Schwarzenbach, W. Petter, A. Ludi, *Inorg*. *Chem*., **1977**, *16* (11), 2704–2710.; (b) F. Herren, P. Fischer, A. Ludi, W. Haelg, *Inorg*. *Chem*., **1980**, *19* (4), 956–959.
22. (a) R. K. Motkuri, P. K. Thallapally, B. P. McGrail, S. B. Ghorishi, *CrystEngComm*, **2010**, (12), 4003–4006.; (b) P. K. Thallapally, R. K. Motkuri, C. A. Fernandez, B. P. McGrail, G. S. Behrooz, *Inorg*. *Chem*., **2010**, *49* (11), 4909–4915.; (c) F. Karadas, H. El-Faki, E. Deniz, C. T. Yavuz, S. Aparicio, M. Atilhan, *Micropor*. *Mesopor*. *Mater*., **2012**, *162*, 91–97.; (d) S. H. Ogilvie, S. G. Duyker, P. D. Southon, V. K. Peterson, C. J. Kepert, *Chem*. *Commun*., **2013**, *49* (82), 9404–9406.
23. (a) A. Takahashi, H. Tanaka, D. Parajuli, T. Nakamura, K. Minami, Y. Sugiyama, Y. Hakuta, S. Ohkoshi, T. Kawamoto, *J*. *Am*. *Chem*. *Soc*., **2016**, *138* (20), 6376–6379.; (b) D. Parajuli, H. Noguchi, A. Takahashi, H. Tanaka, T. Kawamoto, *Ind*. *Eng*. *Chem*. *Res*., **2016**, *55* (23), 6708–6715.; (c) S. Manakasettharn, A. Takahashi, T. Kawamoto, K. Noda, Y. Sugiyama, T. Nakamura, *Anal*. *Chem*., **2018**, *90* (7), 4856–4862.; (d) Z. Wang, X. Yuan, S. Cong, Z. Chen, Q. Li, F. Geng, Z. Zhao, *ACS*

Appl. *Mater*. *Interfaces*, **2018**, *10* (17), 15065–15072.; (e) Y. Jiang, A. Takahashi, T. Kawamoto, M. Asai, N. Zhang, Z. Lei, Z. Zhang, K. Kojima, K. Imoto, K. Nakagawa, S. Ohkoshi, T. Nakamura, *Chem*. *Commun*., **2018**, *54* (84), 11961–11964.; (f) Y. Jiang, A. Takahashi, T. Kawamoto, M. Asai, N. Zhang, Z. Lei, Z. Zhang, K. Kojima, T. Nakamura, *Inorg*. *Chim*. *Acta*, **2020**, *501*, 119273.

24. (a) H. Parab, M. Sudersanan, *Water Res*., **2010**, *44* (3), 854860.; (b) M. Ishizaki, S. Akiba, A. Ohtani, Y. Hoshi, K. Ono, M. Matsuba, T. Togashi, K. Kananizuka, M. Sakamoto, A. Takahashi, T. Kawamoto, H. Tanaka, M. Watanabe, M. Arisaka, T. Nankawa, M. Kurihara, *Dalton Trans*., **2013**, *42* (45), 16049–16055.; (c) R. Chen, H. Tanaka, T. Kawamoto, M. Asai, C. Fukushima, M. Kurihara, M. Ishizaki, M. Watanabe, M. Arisaka, T. Nankawa, *ACS Appl*. *Mater*. *Interfaces*, **2013**, *5* (24), 12984–12990.; (d) T. Tatsuma, Y. Kuroiwa, K. Ishii, K. Kudo, A. Sakoda, *Chem*. *Lett*., **2014**, *43* (8), 1281–1283.; (e) X. Liu, G.-R. Chen, D.-J. Lee, T. Kawamoto, H. Tanaka, M.-L. Chen, Y.-K. Luo, *Bioresour*. *Technol*., **2014**, *160*, 142–149.; (f) J. Liu, X. Li, A. I. Rykov, Q. Fan, W. Xu, W. Cong, C. Jin, H. Tang, K. Zhu, A. S. Ganeshraja, R. Ge, X. Wang, J. Wang, *J. Mater*. *Chem*. *A*, **2017**, *5* (7), 3284–3292.; (g) T. Koshiyama, M. Tanaka, M. Honjo, Y. Fukunaga, T. Okamura, M. Ohba, *Langmuir*, **2018**, *34* (4), 1666–1672.; (h) A. Takahashi, H. Tanaka, K. Minami, K. Noda, M. Ishizaki, M. Kurihara, H. Ogawa, T. Kawamoto, *RSC Adv*., **2018**, *8*, 34808–34816.

25. M. Kämper, D.-C. M. Wagner, A. Weiss, *Angew*. *Chem*. *Int*. *Ed*., **1979**, *18* (6), 486–487.

26. (a) S. S. Kaye, J. R. Long, *J. Am*. *Chem*. *Soc*., **2005**, *127* (18), 6506–6507.; (b) K. W. Chapman, P. D. Southon, C. L. Weeks, C. J. Kepert, *Chem*. *Commun*., **2005**, (26), 3322–3324.; (c) S. Natesakhawat, J. T. Culp, C. Matranga, B. Bockrath, *J. Phys*. *Chem*. *C*, **2007**, *111* (2), 1055–1060.; (d) S. S. Kaye, J. R. Long, *Catal*. *Today*, **2007**, *120* (3–4), 311–316.; (e) L. Reguera, C. P. Krap, J. Balmaseda, E. Reguera, *J. Phys*. *Chem*. *C*, **2008**, *112*, (40), 15893–15899.; (f) C. P. Krap, J. Balmaseda, L. F. del Castillo, B. Zamora, E. Reguera, *Energy Fuels*, **2010**, *24* (1), 581–589.; (g) A.-H. Yuan, C.-X. Chu, H. Zhou, P. Yuan, K.-K. Liu, L. Li, Q.-F. Zhang, X. Chen, Y.-Z. Li, *Eur*. *J. Inorg*. *Chem*., **2010**, (6), 866–871.; (h) J. Jiménez–Gallegos, J. Rodríguez–Hernández, H. Yee–Madeira, E. Reguera, *J. Phys*. *Chem*. *C*, **2010**, *114* (11), 5043–5048.; (i) C. P. Krap, J. Balmaseda, B. Zamora, E. Reguera, *Int*. *J. Hydrog*. *Energy*, **2010**, *35* (19), 10381–10386.; (j) A. A. Al-Hajjaj, B. Zamora, D. V. Bavykin, A. A. Shah, F. C. Walsh, E. Reguera, *Int*. *J. Hydrog*. *Energy*, **2012**, *37*(1), 318−326.; (k) L. Hu, P. Zhang, Q. Chen, H. Zhong, X. Hu, X. Zheng, Y.

Wang, N. Yan, *Cryst*. *Growth Des*., **2012**, *12* (5), 2257−2264.; (l) B. Zamora, A. A. Al-Hajjaj, A. A. Shah, D. V. Bavykin, E. Reguera, *Int*. *J*. *Hydrog*. *Energy*, **2013**, *38* (15), 6406–6416.; (m) P. Bhatt, S. Banerjee, S. Anwar, M. D. Mukadam, S. S. Meena, S. M. Yusuf, *ACS Appl*. *Mater*. *Interfaces*, **2014**, *6*, 17579−17588.; (n) N. Torres, H. Osiry, A. Rodríguez, L. Martínez-dlCruz, A. A. Lemus-Santana, E. Reguera, *Z*. *Anorg*. *Allg*. *Chem*., **2018**, *644* (8–9), 415–423.

27. (a) M. Avila, L. Reguera, J. Rodríguez-Hernández, J. Balmaseda, E. Reguera, *J*. *Solid State Chem*., **2008**, *181* (11), 2899–2907.; (b) N. L. López, J. Rodríquez-Hernández, L Reguera, E Reguera, *Eur*. *J*. *Inorg*. *Chem*., **2019**, (*25*), 3023–3032.
28. (a) J. T. Culp, C. Matranga, M. Smith, E. W. Bittner, B. Bockrath, *J*. *Phys*. *Chem*. *B*, **2006**, *110* (16), 8325–8328.; (b) L. Reguera, J. Balmaseda, C.P. Krap, E. Reguera, *J*. *Phys*. *Chem*. *C*, **2008**, *112* (28), 10490–10501.; (c) L. Reguera, J. Roque, J. Hernández, E. Reguera, *Int*. *J*. *Hydrog*. *Energy*, **2010**, *35* (23), 12864−12869.
29. (a) K. W. Chapman, P. J. Chupas E. R. Maxey, J. W. Richardson, *Chem*. *Commun*., **2006**, (38), 4013–4015.; (b) M. R. Hartman V. K. Peterson, Y. Liu, S. S. Kaye, J. R. Long, *Chem*. *Mater*. **2006**, *18* (14), 3221–3224.; (c) Y. Zhao, H. Xu, L. L. Daemen, K. Lokshin, K. T. Tait, W. L. Mao, J. Luo, R. P. Currier, D. D. Hickmott, *Proc*. *Natl*. *Acad*. *Sci*. *U.S.A*., **2007**, *104* (14), 5727–5731.
30. (a) V. Niel, J. M. Martinez-Agudo, M. C. Muñoz, A. B. Gaspar, J. A. Real, *Inorg*. *Chem*., **2001**, *40* (16), 3838–3839.; (b) G. Molnár, V. Niel, A. B. Gaspar, J.-A. Real, A. Zwick, A. Bousseksou, J. J. McGarvey, *J*. *Phys*. *Chem*. *B*, **2002**, *106* (38), 9701–9707.; (c) G. Molnár, V. Niel, J.-A. Real, L. Dubrovinsky, A. Bousseksou, J. J. McGarvey, *J*. *Phys*. *Chem*. *B*, **2003**, *107* (31), 3149–3155.; (d) S. Bonhommeau, G. Molnár, A. Galet, A. Zwick, J. A. Real, J. J. McGarvey, A. Bousseksou, *Angew*. *Chem*. *Int*. *Ed*., **2005**, *44* (26), 4069–4073.; (e) S. Cobo, G. Molnár, J. A. Real, A. Bousseksou, *Angew*. *Chem*. *Int*. *Ed*., **2006**, *45* (35), 5786−5789.; (f) G. Molnár, S. Cobo, J. A. Real, F. Carcenac, E. Daran, C. Vieu, A. Bousseksou, *Adv*. *Mater*., **2007**, *19* (16), 2163–2167.; (g) I. Boldog, A. B. Gaspar, V. Martínez, P. Pardo-Ibañez, V. Ksenofontov, A. Bhattacharjee, P. Gütlich, J. A. Real, *Angew*. *Chem*. *Int*. *Ed*., **2008**, *47* (34), 6433–6437.; (h) M. Ohba, K. Yoneda, G. Agustí, M. C. Muñoz, A. B. Gaspar, J. A. Real, M. Yamasaki, H. Ando, Y. Nakao, S. Sakaki, S. Kitagawa, *Angew*. *Chem*. *Int*. *Ed*., **2009**, *48* (26), 4767–4771.; (i) P. D. Southon, L. Liu, E. A. Fellows, D. J. Price, G. J. Halder, K. W. Chapman, B. Moubaraki, K. S. Murray, J.-F. Létard, C. J. Kepert, *J*. *Am*. *Chem*. *Soc*., **2009**, *131* (31), 10998–11009.; (j) G. Agustí, R. Ohtani, K. Yoneda, A. B. Gaspar, M. Ohba, J. F. Sánchez-Royo, M. C. Muñoz, S. Kitagawa, J. A. Real, *Angew*. *Chem*. *Int*. *Ed*., **2009**, *48* (47), 8944–8947.;

(k) M. Ohba, K. Yoneda, S. Kitagawa, *CrystEngComm*, **2010**, *12* (1), 159–165.; (l) H. Ando, Y. Nakao, H. Sato, M. Ohba, S. Kitagawa, S. Sakaki, *Chem. Phys. Lett.*, **2011**, *511* (4–5), 399–404.; (m) R. Ohtani, K. Yoneda, S. Furukawa, N. Horike, S. Kitagawa, A. B. Gaspar, M. C. Muñoz, J. A. Real, M. Ohba, *J. Am. Chem. Soc.*, **2011**, *133* (22), 8600–8605.; (n) F. J. M. Lara, A. B. Gaspar, D. Aravena, E. Ruiz, M. C. Muñoz, M. Ohba, R. Ohtani, S. Kitagawa, J. A. Real, *Chem. Commun.*, **2012**, *48* (39), 4686–4688.; (o) J. A. Rodríguez-Velamazán, M. A. González, J. A. Real, M. Castro, M. C. Muñoz, A. B. Gaspar, R. Ohtani, M. Ohba, K. Yoneda, Y. Hijikata, N. Yanai, M. Mizuno, H. Ando, S. Kitagawa, *J. Am. Chem. Soc.*, **2012**, *134* (11), 5083–5089.; (p) M. M. Deshmukh, M. Ohba, S. Kitagawa, S. Sakaki, *J. Am. Chem. Soc.*, **2013**, *135* (12), 4840–4849.; (q) Z. Arcís-Castillo, F. Muñoz-Lara, M. C. Muñoz, D. Aravena, A. B. Gaspar, J. F. Sánchez-Royo, E. Ruiz, M. Ohba, R. Matsuda, S. Kitagawa, J. A. Real, *Inorg. Chem.*, **2013**, *52* (21), 12777–12783.; (r) D. Aravena, Z. A. Castillo, M. C. Muñoz, A. B. Gaspar, K. Yoneda, R. Ohtani, A. Mishima, S. Kitagawa, M. Ohba, J. A. Real, E. Ruiz, *Chem. Eur. J.*, **2014**, *20* (26), 12864–12873.; (s) M. Castro, O. Roubeau, L. Piñeiro-Lopez, J. A. Real, J. A. Rodríguez-Velamazan, *J. Phys. Chem. C*, **2015**, *119* (30), 17334–17343.; (t) D. M. Sagar, F. G. Baddour, P. Konold, J. Ullom, D. A. Ruddy, J. C. Johnson, R. Jimenez, *J. Phys. Chem. Lett.*, **2016**, *7* (1), 148–153.; (u) R. Ohtani, S. Hayami, *Chem. Eur. J.*, **2016**, *23* (10), 2236–2248.; (v) C. H. Pham, F. Paesani, *J. Phys. Chem. Lett.*, **2016**, *7* (19), 4022–4026.; (w) C. H. Pham, J. Cirera, F. Paesani, *J. Am. Chem. Soc.*, **2016**, *138* (19), 6123–6126.; (x) Z.-P. Ni, J.-L. Liu, Md. N. Hoque, W. Liu, J.-Y. Li, Y.-C. Chen, M.-L. Tong, *Coord. Chem. Rev.*, **2017**, *335*, 28–43.; (y) A. Mishima, T. Koshiyama, J. A. Real, M. Ohba, *J. Mater. Chem. C*, **2017**, *5* (15), 3706–3713.; (z) M. Sawczak, R. Jendrzejewski, D. Maskowicz, Y. Garcia, A. C. Ghosh, M. Gazda, J. Czechowski, G. Śliwiński, *Eur. J. Inorg. Chem.*, **2019**, (27), 3249–3255.

31. (a) T. Mallah, S. Thiébaut, M. Verdaguer, P. Veillet, *Science*, **1993**, *262* (5139), 1554–1557.; (b) S. Ferlay, T. Mallah, R. Ouahès, P. Veillet, M. Verdaguer, *Nature*, **1995**, *378*, 701–703.; (c) O. Sato, T. Iyoda, A. Fujishima, K. Hashimoto, *Science*, **1996**, *272* (5262), 704–705.; (d) M. Verdaguer, A. Bleuzena, V. Marvaud, J. Vaissermann, M. Seuleiman, C. Desplanches, A. Scuiller, C. Train, R. Garde, G. Gelly, C. Lomenech, I. Rosenman, P. Veillet, C. Cartier, F. Villain, *Coord. Chem. Rev.*, **1999**, *190-192*, 1023–1047.; (e) S. M. Holmes, G. S. Girolami, *J. Am. Chem. Soc.*, **1999**, *121* (23), 5593–5594.; (f) Ø. Hatlevik, W. E. Buschmann, J. Zhang, J. L. Manson, J. S. Miller, *Adv. Mater.*, **1999**, *11* (11), 914–918.; (g) S. Ohkoshi, K. Aria, Y. Sato, K. Hashimoto, *Nature Mater.*, **2004**, *3*, 857–861.; (h) T. Uemura, M.

Ohba, S. Kitagawa, *Inorg*. *Chem*., **2004**, *43* (23), 7339–7345.; (i) M. Zentková1, Z. Arnold, J. Kamarád, V. Kavečanský, M. Lukáčová, S. Mat'aš1, M. Mihalik, Z. Mitróová, A. Zentko, *J. Phys*.: *Condens*. *Matter*., **2007**, *19* (26), 266217.; (j) S. S. Kaye, H. J. Choi, J. R. Long, *J. Am*. *Chem*. *Soc*., **2008**, *130* (50), 16921–16925.; (k) H. Ohmagari, R. Ohtani, M. Nakaya, M. Ohba, M. Nakamura, L. F. Lindoy, O. Sato, S. Hayami, *Dalton Trans*., **2016**, *45* (42), 16784–16788.

Chapter 1

Evaluation of Structural Stability and Hydrogen Adsorption Ability of Prussian Blue Analogs

Abstract

Prussian Blue analogs (PBAs) are a class of cyano-bridged porous coordination polymers (PCPs) with 3-D framework structure which have superior physical properties such as gas adsorption. Although a variety of studies on their excellent chemical and physical properties such as magnetism have vigorously proceeded, there are only a few reports about molecule adsorption in defective PBAs based on $[Cr^{III}(CN)_6]^{3-}$ moiety as the building units because of their relatively lower structural stability than that of PBAs consisting of other hexacyanometallate building units. Therefore, in this chapter, $[Cr(CN)_6]^{3-}$-based defective PBAs $\{M^{II}_3[Cr^{III}(CN)_6]_2 \cdot nH_2O\}$ (**$M_3Cr_2 \cdot nH_2O$**; M = VO, Cr, Mn, Fe, Co, Ni, Cu, Zn, and Cd) and a non-defective PBA $\{In^{III}[Cr^{III}(CN)_6] \cdot nH_2O\}$ (**$InCr \cdot nH_2O$**) as a reference material were used for systematic investigations on their structural stability and H_2 adsorption ability for practical usage. From the results of powder X-ray diffractometry (RXPD) and Fourier transform infrared (FT-IR) spectroscopy of the samples activated at different temperatures, the activation temperature was optimized to be 60℃. Moreover, several PBAs with unsaturated metal sites which have high stability upon application of the activation process of heating under vacuum exhibited a large Brunauer-Emmett-Teller surface area (SA_{BET}) of 415–684 $cm^3\ g^{-1}$ and a great H_2 uptake of 1.06–1.42 wt% at 77 K and 100 kPa, which are sufficiently comparable to the reported values of other PBAs.

Introduction

Prussian Blue analogs (PBAs) are a class of cyano-bridged porous coordination polymers (PCPs) having a 3-D framework structure with a general chemical formula of $\{A_xMa_y[Mb(CN)_6]_z\}$, where A is monovalent cations (*e.g.* alkali cations and quaternary ammonium ions) and Ma and Mb are divalent or trivalent metal ions. When Ma ions are divalent and Mb ions are trivalent, one-third of $[M^{III}(CN)_6]^{3-}$ moieties become vacancy in the framework structure of $\{Ma^{II}_3[Mb^{III}(CN)_6]_2\}$ because of the charge balance.[1] From the viewpoints of the porous and defective structures, adsorption properties and subsequent utilities of PBAs have been widely investigated toward several kinds of small molecules and ions (*e.g.* carbon dioxide (CO_2),[1] ammonia (NH_3)[3], cesium ion (Cs^+)[4], and noble gases[5]). H_2 adsorption property of PBAs has been reported for mainly $\{M^{II}_3[Co^{III}(CN)_6]_2\}$ (**M_3Co_2**; M = Mn, Fe, Co, Ni, Cu, Zn, and Cd) series because of the relatively higher stability of $[Co^{III}(CN)_6]^{3-}$ moiety than other $[Mb^{III}(CN)_6]^{3-}$ units.[6] In addition, the H_2 adsorption sites in **Mn_3Co_2** and **Cu_3Co_2** have been defined by *in-situ* diffraction techniques as well as adsorption behavior and amount.[7]

On the other hand, $[Cr^{III}(CN)_6]^{3-}$-based PBAs have investigated as magnetic materials because of the d electronic structure of $(t_{2g})^3$ and a short distance between Cr^{3+} and the other metal centers through the bridging ligand of CN^- ion.[8] Moreover, the reports about molecule adsorption or ion adsorption using $[Cr^{III}(CN)_6]^{3-}$-based PBAs as the absorbents are extremely rare in spite of interests on the development of unique framework property interlocked with the adsorption property.[6g,6l,8j] Regarding H_2 adsorption in $[Cr^{III}(CN)_6]^{3-}$-based PBAs, although the abilities have been evaluated for non-defective PBAs including alkali ions in the pores[6g] and core-shell type PBAs,[6l] there is no report using defective $[Cr^{III}(CN)_6]^{3-}$-based PBAs as H_2 adsorbents at liquid N_2 temperature (77K) which is the most common and convenient temperature for practical utility. Therefore, in this study, several defective PBAs $\{M^{II}_3[Cr^{III}(CN)_6]_2\cdot nH_2O\}$ (**$M_3Cr_2\cdot nH_2O$**; M = VO, Cr, Mn, Fe, Co, Ni, Cu, Zn, and Cd) and non-defective PBA $\{In^{III}[Cr^{III}(CN)_6]\cdot nH_2O\}$ (**$InCr\cdot nH_2O$**) as a reference metarial were systematically synthesized using $[Cr^{III}(CN)_6]^{3-}$ as building units, and their structural stability upon application of the activation process of heating under dynamic vacuum and H_2 adsorption ability at 77 K were evaluated.

Physical Measurements

Carbon, Hydrogen, and Nitrogen Elemental Analysis (CHN-EA)

CHN-EA of C, H, and N atoms was conducted as quickly as possible after sample loading by the staff of the Technical Support Division, Graduate School of Science, Kyushu University.

Energy Dispersive X-ray Fluorescence (EDXRF) Analysis

EDXRF analysis was conducted on a Shimadzu Rayny EDX-720 to detect elements with an atomic number greater than or equal to 12 in the ambient air at RT. The results were averaged over three runs. X-ray voltage: 50 kV, X-ray current: 30 μA.

Thermogravimetry analysis (TGA)

TGA was conducted on a PerkinElmer STA6000 as quickly as possible after sample loading under a dry N_2 atmosphere. Sample weight: ~10 mg, temperature range: 25–725℃, heating rate: 10℃ min^{-1}, N_2 gas flow rate: 19.8 ml min^{-1}.

Fourier Transform Infrared (FT-IR) Spectroscopy

FT-IR spectroscopy was conducted on a PerkinElmer FT-IR Spectrometer Spectrum Two using a universal attenuated total reflection (UATR) method in the ambient air at RT. Wavenumber range: 4000–400 cm^{-1}, resolution: 4 cm^{-1}, integrated number: 4 times.

Powder X-ray Diffractometry (RXPD)

RXPD was conducted on a Rigaku Ultima IV diffractometer using graphite-monochromated CuKα radiation and reflection-free single-crystal Si sample holder in the ambient air at RT. X-ray wavelength: 1.54184 Å, X-ray voltage: 40 kV, X-ray current: 40 μA, angle range: 5–60°, scan rate: 1° min^{-1}, data collecting step: 0.02°, integrated number: 1 time.

Adsorption and Desorption Measurements

N_2 (99.999%) and H_2 (99.999%) adsorption/desorption measurements were conducted on MicrotracBEL BELSORP-max volumetric adsorption equipment at 77 K using liquid N_2 in a Dewar bottle. The prepared samples were activated again by heating at 60 ℃ for 4 h under vacuum after loading into the measurement glass tube before the measurement. Second virial coefficients: -1.824×10^{-8} (H_2), -4.328×10^{-7} (N_2); sample weight: ~35 mg, pressure range of 0–105 kPa, outgas rate: < 0.02 Pa min^{-1}.

Sample Preparation

All the chemicals were purchased as reagent grade and used without further purification. All the prepared samples were stored in a vial with screw cap and allowed to stand at 20 ℃ in the dark right before the measurements, and characterized by carbon, hydrogen, and nitrogen elemental analysis (CHN-EA), energy dispersive X-ray fluorescence (EDXRF) analysis, thermogravimetry analysis (TGA), Fourier transform infrared (FT-IR) spectroscopy, and powder X-ray diffractometry (RXPD).

$K_3[Cr^{III}(CN)_6]$

$K_3[Cr(CN)_6]$ was synthesized according to a reported synthetic method with some modifications.[9] Mossy Zn (6.0 g, 91.8 mmol) was activated by immersing in 1 M HCl for 5 min, thoroughly washed with distilled water, and dried well in advance. Then the activated mossy Zn was added to a degassed aqueous solution (40 mL) of $CrCl_3 \cdot 6H_2O$ (20.0 g, 75.1 mmol) under an N_2 gas atmosphere at RT. After stirring over 3 h and removal of the remaining unreacted Zn by suction filtration, a solid $CH_3COONa \cdot 3H_2O$ (24.0 g, 176.4 mmol) was added to the resultant deep blue solution, which resulted in a rapid precipitate of chromium(II) acetate as a bright red powder. The precipitate was collected by suction filtration under an N_2 gas atmosphere, repeatedly washed with degassed water, and dissolved in a degassed aqueous solution (50 ml) of KCN (30.0 g, 460.7 mmol). After removal of the slight precipitate by suction filtration, an excess amount of methanol (~500 ml) was added to the dark green filtrate, which provided $K_4[Cr^{II}(CN)_6]$ as a light green precipitate. The precipitate was collected by suction filtration, repeatedly washed with methanol, and allowed to stand over 2 h for the air oxidation of the Cr^{II} ion. After completion of color change to yellow, a few repeated reprecipitation from water by the addition of an excess amount of methanol gave pure $K_3[Cr^{III}(CN)_6]$. Yellow crystalline powder. Yield: 15.5 g (47.7 mmol, 63.5% vs. $CrCl_3 \cdot 6H_2O$). FT-IR (cm^{-1}): ν(C≡N) = 2130; ν(Cr–C) = 454 (vs). EDXRF analysis (%): [K]/[Cr] = 2.85. No other elements were detected.

$(V^{IV}O)_3[Cr^{III}(CN)_6]_2 \cdot nH_2O\}$ **($(VO)_3Cr_2 \cdot nH_2O$)**

All the operations for the synthesis were conducted in the dark to avoid the decomposition of $K_3[Cr^{III}(CN)_6]$. An aqueous solution (10 mL) of $K_3[Cr^{III}(CN)_6]$ (325.4 mg, 1.0 mmol) was added dropwise to an aqueous solution (10 mL) of $V^{IV}OSO_4 \cdot xH_2O$ (x = 3–4; 397.0 mg, ~1.8 mmol) with vigorous stirring at RT, resulting in precipitation of light green solid. After completing the drop and subsequent stirring for 10 mins, the dark gray suspension was allowed to stand at 10 ℃ for 1 week. After the standing, the dark gray precipitate was collected by centrifugation, repeatedly washed with distilled water to remove the unreacted reactants and the byproduct of K_2SO_4, and dried in the air. Dark gray powder. CHN-EA (%): Found: C 17.28, H 2.96, N 19.92; Calculated for $\{(V^{IV}O)_3[Cr^{III}(CN)_6]_2 \cdot 12H_2O\}$ ($C_{12}H_{24}N_{12}O_{15}V_3Cr_2$): C 17.30, H 2.90, N 20.17. FT-IR (cm^{-1}): $\nu(H_2O)$ = 3750–2800 (m, br), 3656 (w); $\nu(C{\equiv}N)$ = 2178 (m); $\delta(H_2O)$ = 1675 (w), 1606 (m); $\nu(V{=}O)$ = 977; $\nu(Cr–C)$ = 500 (vs), 419 (s). EDXRF analysis (%): [V]/[Cr] = 1.63; [K]/[V] = 0.03; [S]/[V] = 0.03.

$\{Cr^{II}_3[Cr^{III}(CN)_6]_2 \cdot nH_2O\}$ **($Cr_3Cr_2 \cdot nH_2O$)**

All the operations for the synthesis were conducted in the dark and under an Ar atmosphere to avoid the decomposition of $K_3[Cr^{III}(CN)_6]$ and the oxidation of the Cr^{2+} ion, respectively. A deoxidized aqueous solution (10 mL) by Ar-bubbling of $K_3[Cr^{III}(CN)_6]$ (325.4 mg, 1.0 mmol) was added dropwise to a deoxidized aqueous solution (10 mL) by Ar-bubbling of $Cr^{II}Cl_2$ (221.2 mg, 1.8 mmol) with vigorous stirring at RT, resulting in precipitation of black solid. After completing the drop and subsequent stirring for 10 mins, the black suspension was allowed to stand at 10 ℃ for 1 week. After the standing, the black precipitate was collected by centrifugation, repeatedly washed with distilled water to remove the unreacted reactants and the byproduct of KCl, and dried in the air. Gray powder. CHN-EA (%): Found: C 17.26, H 3.71, N 19.78; Calculated for $\{Cr^{II}_3[Cr^{III}(CN)_6]_2 \cdot 15H_2O\}$ ($C_{12}H_{30}N_{12}O_{15}Cr_5$): C 17.11, H 3.59, N 19.95. FT-IR (cm^{-1}): $\nu(H_2O)$ = 3750–2700 (m, br), 3658 (w); $\nu(C{\equiv}N)$ = 2187 (m); $\delta(H_2O)$ = 1632 (m); $\nu(Mn–C)$ = 522 (vs), 436 (s). EDXRF analysis (%): [K]/[Cr] = 0.01; [Cl]/[Cr] = 0.02.

{$Mn^{II}_3[Cr^{III}(CN)_6]_2 \cdot nH_2O$} (**$Mn_3Cr_2 \cdot nH_2O$**)

All the operations for the synthesis were conducted in the dark and under an Ar atmosphere to avoid the decomposition of $K_3[Cr^{III}(CN)_6]$ and the oxidation of the Mn^{2+} ion, respectively. A deoxidized aqueous solution (10 mL) by Ar-bubbling of $K_3[Cr^{III}(CN)_6]$ (325.4 mg, 1.0 mmol) was added dropwise to a deoxidized aqueous solution (10 mL) by Ar-bubbling of $Mn^{II}Cl_2 \cdot 4H_2O$ (356.2 mg, 1.8 mmol) with vigorous stirring at RT, resulting in precipitation of light green solid. After completing the drop and subsequent stirring for 10 mins, the light green suspension was allowed to stand at 10 ℃ for 1 week. After the standing, the light green precipitate was collected by centrifugation, repeatedly washed with distilled water to remove the unreacted reactants and the byproduct of KCl, and dried in the air. Light green powder. CHN-EA (%): Found: C 16.47, H 3.77, N 19.18; Calculated for {$Mn^{II}_3[Cr^{III}(CN)_6]_2 \cdot 16H_2O$} ($C_{12}H_{32}N_{12}O_{16}Cr_2Mn_3$): C 16.53, H 3.70, N 16.53. FT-IR (cm^{-1}): $\nu(H_2O)$ = 3750–2800 (m, br), 3651 (w), 3600 (w); $\nu(C{\equiv}N)$ = 2158 (m); $\delta(H_2O)$ = 1607 (m); $\nu(Cr–C)$ = 472 (vs). EDXRF analysis (%): [Mn]/[Cr] = 1.38; [K]/[Cr] = 0.01; [Cl]/[Cr] = 0.00.

{$Fe^{II}_3[Cr^{III}(CN)_6]_2 \cdot nH_2O$} (**$Fe_3Cr_2 \cdot nH_2O$**)

All the operations for the synthesis were conducted in the dark and under an Ar atmosphere to avoid the decomposition of $K_3[Cr^{III}(CN)_6]$ and the oxidation of the Fe^{2+} ion, respectively. A deoxidized aqueous solution (10 mL) by Ar-bubbling of $K_3[Cr^{III}(CN)_6]$ (325.4 mg, 1.0 mmol) was added dropwise to a deoxidized aqueous solution (10 mL) by Ar-bubbling of $Fe^{II}Cl_2 \cdot 4H_2O$ (357.9 mg, 1.8 mmol) with vigorous stirring at RT, resulting in precipitation of orange solid. After completing the drop and subsequent stirring for 10 mins, the orange suspension was allowed to stand at 10 ℃ for 1 week. After the standing, the orange precipitate was collected by centrifugation, repeatedly washed with distilled water to remove the unreacted reactants and the byproduct of KCl, and dried in the air. Orange powder. CHN-EA (%): Found: C 16.51, H 3.71, N 19.22; Calculated for {$Fe^{II}_3[Cr^{III}(CN)_6]_2 \cdot 16H_2O$} ($C_{12}H_{32}N_{12}O_{16}Cr_2Fe_3$): C 16.53, H 3.70, N 19.28. FT-IR (cm^{-1}): $\nu(H_2O)$ = 3750–2800 (m, br), 3648 (w), 3600 (w); $\nu(C{\equiv}N)$ = 2162 (m), 2102 (w); $\delta(H_2O)$ = 1609 (m); $\nu(Cr–C)$ = 480 (vs). EDXRF analysis (%): [Fe]/[Cr] = 1.75; [K]/[Fe] = 0.00; [Cl]/[Fe] = 0.04.

{$Co^{II}_3[Cr^{III}(CN)_6]_2 \cdot n H_2O$} (**$Co_3Cr_2 \cdot n H_2O$**)

All the operations for the synthesis were conducted in the dark to avoid the decomposition of $K_3[Cr^{III}(CN)_6]$. An aqueous solution (10 mL) of $K_3[Cr^{III}(CN)_6]$ (325.4 mg, 1.0 mmol) was added dropwise to an aqueous solution (10 mL) of $Co^{II}Cl_2 \cdot 6H_2O$ (428.3 mg, 1.8 mmol) with vigorous stirring at RT, resulting in precipitation of reddish-orange solid. After completing the drop and subsequent stirring for 10 mins, the reddish-orange suspension was allowed to stand at 10 ℃ for 1 week. After the standing, the reddish-orange precipitate was collected by centrifugation, repeatedly washed with distilled water to remove the unreacted reactants and the byproduct of KCl, and dried in the air. Reddish-orange powder. CHN-EA (%): Found: C 16.53, H 3.63, N 19.22; Calculated for {$Co^{II}_3[Cr^{III}(CN)_6]_2 \cdot 16H_2O$} ($C_{12}H_{32}N_{12}O_{16}Cr_2Co_3$): C 16.36, H 3.66, N 19.07. FT-IR (cm^{-1}): $\nu(H_2O)$ = 3750–2800 (m, br), 3651 (w), 3600 (w); $\nu(C{\equiv}N)$ = 2170 (m); $\delta(H_2O)$ = 1610 (m); $\nu(Cr–C)$ = 486 (vs). EDXRF analysis (%): [Co]/[Cr] = 1.75; [K]/[Co] = 0.00; [Cl]/[Co] = 0.04.

{$Ni^{II}_3[Cr^{III}(CN)_6]_2 \cdot n H_2O$} (**$Ni_3Cr_2 \cdot n H_2O$**)

All the operations for the synthesis were conducted in the dark to avoid the decomposition of $K_3[Cr^{III}(CN)_6]$. An aqueous solution (10 mL) of $K_3[Cr^{III}(CN)_6]$ (325.4 mg, 1.0 mmol) was added dropwise to an aqueous solution (10 mL) of $Ni^{II}Cl_2 \cdot 6H_2O$ (427.8 mg, 1.8 mmol) with vigorous stirring at RT, resulting in precipitation of greenish-blue solid. After completing the drop and subsequent stirring for 10 mins, the greenish-blue suspension was allowed to stand at 10 ℃ for 1 week. After the standing, the greenish-blue precipitate was collected by centrifugation, repeatedly washed with distilled water to remove the unreacted reactants and the byproduct of KCl, and dried in the air. Green powder. CHN-EA (%): Found: C 15.44, H 4.10, N 17.96; Calculated for {$Ni^{II}_3[Cr^{III}(CN)_6]_2 \cdot 19H_2O$} ($C_{12}H_{38}N_{12}O_{19}Cr_2Ni_3$): C 15.42, H 4.10, N 17.98. FT-IR (cm^{-1}): $\nu(H_2O)$ = 3750–2800 (m, br), 3647 (w); $\nu(C{\equiv}N)$ = 2169 (m); $\delta(H_2O)$ = 1608 (m); $\nu(Cr–C)$ = 487 (vs). EDXRF analysis (%): [Ni]/[Cr] = 1.74; [K]/[Ni] = 0.03; [Cl]/[Ni] = 0.04.

{$Cu^{II}_3[Cr^{III}(CN)_6]_2 \cdot nH_2O$} (**$Cu_3Cr_2 \cdot nH_2O$**)

All the operations for the synthesis were conducted in the dark to avoid the decomposition of $K_3[Cr^{III}(CN)_6]$. An aqueous solution (10 mL) of $K_3[Cr^{III}(CN)_6]$ (325.4 mg, 1.0 mmol) was added dropwise to an aqueous solution (10 mL) of $Cu^{II}Cl_2 \cdot 2H_2O$ (360.9 mg, 1.8 mmol) with vigorous stirring at RT, resulting in precipitation of deep green solid. After completing the drop and subsequent stirring for 10 mins, the deep green suspension was allowed to stand at 10 ℃ for 1 week. After the standing, the deep green precipitate was collected by centrifugation, repeatedly washed with distilled water to remove the unreacted reactants and the byproduct of KCl, and dried in the air. Deep green powder. CHN-EA (%): Found: C 15.18, H 3.96, N 18.06; Calculated for {$Cu^{II}_3[Cr^{III}(CN)_6]_2 \cdot 18H_2O$} ($C_{12}H_{36}N_{12}O_{18}Cr_2Cu_3$): C 15.48, H 3.90, N 18.05. FT-IR (cm^{-1}): $\nu(H_2O)$ = 3750–2700 (m, br), 3630 (w); $\nu(C{\equiv}N)$ = 2185 (w), 2116 (vs); $\delta(H_2O)$ = 1675 (w), 1607 (s); ν(Cr–C) = 503 (vs). EDXRF analysis (%): [Cu]/[Cr] = 1.47; [K]/[Cu] = 0.03; [Cl]/[Cu] = 0.04.

{$Zn^{II}_3[Cr^{III}(CN)_6]_2 \cdot nH_2O$} (**$Zn_3Cr_2 \cdot nH_2O$**)

All the operations for the synthesis were conducted in the dark to avoid the decomposition of $K_3[Cr^{III}(CN)_6]$. An aqueous solution (10 mL) of $K_3[Cr^{III}(CN)_6]$ (325.4 mg, 1.0 mmol) was added dropwise to an aqueous solution (10 mL) of $Zn^{II}Cl_2 \cdot$(245.3 mg, 1.8 mmol) with vigorous stirring at RT, resulting in precipitation of yellowish-white solid. After completing the drop and subsequent stirring for 10 mins, the yellowish-white suspension was allowed to stand at 10 ℃ for 1 week. After the standing, the yellowish-white precipitate was collected by centrifugation, repeatedly washed with distilled water to remove the unreacted reactants and the byproduct of KCl, and dried in the air. Yellowish-white powder. CHN-EA (%): Found: C 16.60, H 3.33, N 19.20; Calculated for {$Zn^{II}_3[Cr^{III}(CN)_6]_2 \cdot 14H_2O$} ($C_{12}H_{28}N_{12}O_{14}Cr_2Zn_3$): C 16.67, H 3.26, N 19.44. FT-IR (cm^{-1}): $\nu(H_2O)$ = 3750–2800 (m, br), 3655 (w); $\nu(C{\equiv}N)$ = 2175 (m); $\delta(H_2O)$ = 1610 (m); ν(Cr–C) = 485 (vs). EDXRF analysis (%): [Zn]/[Cr] = 1.38; [K]/[Zn] = 0.00; [Cl]/[Zn] = 0.05.

{$Cd^{II}_3[Cr^{III}(CN)_6]_2 \cdot nH_2O$} (**$Cd_3Cr_2 \cdot nH_2O$**)

All the operations for the synthesis were conducted in the dark to avoid the decomposition of $K_3[Cr^{III}(CN)_6]$. An aqueous solution (10 mL) of $K_3[Cr^{III}(CN)_6]$ (325.4 mg, 1.0 mmol) was added dropwise to an aqueous solution (10 mL) of $Cd^{II}Cl_2 \cdot$(330.0 mg, 1.8 mmol) with vigorous stirring at RT, resulting in precipitation of yellowish-white solid. After completing the drop and subsequent stirring for 10 mins, the yellowish-white suspension was allowed to stand at 10 ℃ for 1 week. After the standing, the yellowish-white precipitate was collected by centrifugation, repeatedly washed with distilled water to remove the unreacted reactants and the byproduct of KCl, and dried in the air. Yellowish-white powder. EA (%): Found: C 14.12, H 2.98, N 16.27; Calculated for {$Cd^{II}_3[Cr^{III}(CN)_6]_2 \cdot 15H_2O$} ($C_{12}H_{30}N_{12}O_{15}Cr_2Cd_3$): C 14.08, H 2.95, N 16.42. FT-IR (cm^{-1}): $\nu(H_2O)$ = 3750–2800 (m, br), 3656 (w), 3600 (w); $\nu(C{\equiv}N)$ = 2165 (m); $\delta(H_2O)$ = 1609 (m); ν(Cr–C) = 471 (vs). EDXRF analysis (%): [Cd]/[Cr] = 1.62; [K]/[Cd] = 0.06; [Cl]/[Cd] = 0.00.

{$In^{III}[Cr^{III}(CN)_6] \cdot nH_2O$} (**$InCr \cdot nH_2O$**)

All the operations for the synthesis were conducted in the dark to avoid the decomposition of $K_3[Cr^{III}(CN)_6]$. An aqueous solution (10 mL) of $K_3[Cr^{III}(CN)_6]$ (325.4 mg, 1.0 mmol) was added dropwise to an aqueous solution (10 mL) of $In^{III}Cl_3 \cdot$(265.4 mg, 1.2 mmol) with vigorous stirring at RT, resulting in precipitation of yellowish-white solid. After completing the drop and subsequent stirring for 10 mins, the yellowish-white suspension was allowed to stand at 10 ℃ for 1 week. After the standing, the yellowish-white precipitate was collected by centrifugation, repeatedly washed with distilled water to remove the unreacted reactants and the byproduct of KCl, and dried in the air. Yellowish-white powder. CHN-EA (%): Found: C 20.94, H 0.68, N 24.46; Calculated for {$In^{III}[Cr^{III}(CN)_6] \cdot H_2O$} ($C_6H_2N_6OCrIn$): C 21.14, H 0.59, N 24.65. FT-IR (cm^{-1}): $\nu(C{\equiv}N)$ = 2194 (m); $\delta(H_2O)$ = 1619 (m); ν(Cr–C) = 497 (vs). EDXRF analysis (%): [In]/[Cr] = 0.90; [K]/[In] = 0.00; [Cl]/[In] = 0.02.

Results and Discussion

All the samples were systematically prepared by a typical synthetic method of PBAs where the starting materials were mixed with stirring in aqueous media. The as-synthesized samples were characterized by several methods of carbon, hydrogen, and nitrogen elemental analysis (CHN-EA), energy dispersive X-ray fluorescence (EDXRF) analysis, thermogravimetry analysis (TGA), Fourier transform infrared (FT-IR) spectroscopy, and powder X-ray diffractometry (RXPD).

Regarding CHN-EA of PBAs, the weight percentage values for C and N elements result from only CN^- ions of $[Mb(CN)_6]^{3-}$ units and the value of H element results from only interstitial H_2O molecules. The resultant values of CHN-EA for all the as-synthesized samples provided the same abundance ratio of C and N elements, and had a good agreement with the weight percentage calculated from an ideal framework formula including several hydrated H_2O molecules, $\{M^{II}_3[Cr^{III}(CN)_6]_2 \cdot nH_2O\}$ (**$M_3Cr_2 \cdot nH_2O$**; (M, *n*) = (VO, 12), (Cr, 15), (Mn, 16), (Fe, 16), (Co, 16), (Ni, 19), (Cu, 18), (Zn, 14), and (Cd, 15)) and $\{In^{III}[Cr^{III}(CN)_6] \cdot H_2O\}$ (**$InCr \cdot nH_2O$**), indicating their high purity (**Table 1-1**).

Table 1-1. The observed and ideal values of carbon, hydrogen, and nitrogen elemental analysis (CHN-EA) and calculated number of H_2O molecules (*n*) for the as-synthesized PBAs, $\{M^{II}_3[Cr^{III}(CN)_6]_2 \cdot nH_2O\}$ (**$M_3Cr_2 \cdot nH_2O$**; M = VO, Cr, Mn, Fe, Co, Ni, Cu, Zn, and Cd) and $\{In^{III}[Cr^{III}(CN)_6] \cdot nH_2O\}$ (**$InCr \cdot nH_2O$**).

	n	[C] / wt%		[H] / wt%		[N] / wt%	
		Found	Calcd.	Found	Calcd.	Found	Calcd.
$(VO)_3Cr_2 \cdot nH_2O$	12	17.28	17.30	2.96	2.90	19.92	20.17
$Cr_3Cr_2 \cdot nH_2O$	15	17.26	17.11	3.71	3.59	19.78	19.95
$Mn_3Cr_2 \cdot nH_2O$	16	16.47	16.58	3.77	3.71	19.18	19.34
$Fe_3Cr_2 \cdot nH_2O$	16	16.51	16.53	3.71	3.70	19.22	19.28
$Co_3Cr_2 \cdot nH_2O$	16	16.53	16.36	3.63	3.66	19.22	19.07
$Ni_3Cr_2 \cdot nH_2O$	19	15.44	15.42	4.10	4.10	17.96	17.98
$Cu_3Cr_2 \cdot nH_2O$	18	15.18	15.48	3.96	3.90	18.06	18.05
$Zn_3Cr_2 \cdot nH_2O$	14	16.60	16.67	3.33	3.26	19.20	19.44
$Cd_3Cr_2 \cdot nH_2O$	15	14.12	14.08	2.98	2.95	16.27	16.42
$InCr \cdot nH_2O$	1	20.94	21.14	0.68	0.59	24.46	24.65

In the EDXRF analysis, the elemental ratio of [M]/[Cr] calculated from the observed weight percentage values was close to the ideal stoichiometric ratio of 1.5 for all the **$M_3Cr_2{\cdot}nH_2O$**, except **$Cr_3Cr_2{\cdot}nH_2O$** which showed existence of Cr element with a weight percentage of ~100 %, and 1 for **$InCr{\cdot}nH_2O$**, which supported the results of CHN-EA (**Table 1-2**). A trace amount of some elements from the starting materials, S of SO_4^{2-} (M =VO) form $VOSO_4{\cdot}xH_2O$, Cl (M = Cr, Mn, Fe, Co, Ni, Cu, Zn, Cd, and In) from the chloride salts, and K from $K_3[Cr(CN)_6]$, were detected as well, which were essentially neglectable because of the values below 0.7% toward the formula weight (**Table 1-2**). For the reasons mentioned above, in all the following sections in this chapter, all the prepared PBA samples were treated as having the ideal formula of $\{M^{II}_3[Cr^{III}(CN)_6]_2{\cdot}nH_2O\}$ (**$M_3Cr_2{\cdot}nH_2O$**; M = VO, Cr, Mn, Fe, Co, Ni, Cu, Zn, and Cd) and $\{In^{III}[Cr^{III}(CN)_6]{\cdot}nH_2O\}$ (**$InCr{\cdot}nH_2O$**).

Table 1-2. The observed values of energy dispersive X-ray fluorescence (EDXRF) analysis and calculated elemental ratios for the as-synthesized PBAs, $\{M^{II}_3[Cr^{III}(CN)_6]_2{\cdot}nH_2O\}$ (**$M_3Cr_2{\cdot}nH_2O$**; M = VO, Cr, Mn, Fe, Co, Ni, Cu, Zn, and Cd) and $\{In^{III}[Cr^{III}(CN)_6]{\cdot}nH_2O\}$ (**$InCr{\cdot}nH_2O$**).

	Weight percentage / wt%				Ratio		
	[M[a]]	[Cr]	[K]	[X[b]]	[M[a]]/[Cr]	[K]/[M[a]]	[X[b]]/[M[a]]
$(VO)_3Cr_2{\cdot}nH_2O$	59.935	37.553	1.380	1.132	1.63	0.03	0.03
$Cr_3Cr_2{\cdot}nH_2O$	97.928		0.736	1.335	–	0.01	0.02
$Mn_3Cr_2{\cdot}nH_2O$	59.097	40.482	0.421	0.000	1.38	0.01	0.00
$Fe_3Cr_2{\cdot}nH_2O$	64.260	34.108	0.000	1.632	1.75	0.00	0.04
$Co_3Cr_2{\cdot}nH_2O$	65.404	32.022	0.000	1.574	1.75	0.00	0.04
$Ni_3Cr_2{\cdot}nH_2O$	64.440	32.715	1.288	1.557	1.74	0.03	0.04
$Cu_3Cr_2{\cdot}nH_2O$	62.573	34.876	1.155	1.396	1.47	0.03	0.04
$Zn_3Cr_2{\cdot}nH_2O$	62.333	35.978	0.000	1.690	1.38	0.00	0.05
$Cd_3Cr_2{\cdot}nH_2O$	76.592	21.810	1.598	0.000	1.62	0.06	0.00
$InCr{\cdot}nH_2O$	66.346	33.244	0.000	0.410	0.90	0.00	0.02

[a]The directly observed element of M was V instead of VO ions in **$(VO)_3Cr_2{\cdot}nH_2O$**. [b]X is S (M = VO) and Cl (M = Cr, Mn, Fe, Co, Ni, Cu, Zn, Cd, and In).

In the FT-IR spectra, the observed peaks are assigned referring to cases of several reported PBAs.[10] The peaks observed at a low-wavenumber of 419 and 436 cm^{-1} in **$(VO)_3Cr_2 \cdot nH_2O$** and **$Cr_3Cr_2 \cdot nH_2O$**, respectively, were possibly attributed to a vibration mode between Cr^{3+} center CN^- ion (ν(Cr–C)) (**Figure 1-1** and **Table 1-3**). For the other PBAs, the ν(Cr–C) modes seemingly appeared at a lower region below 400 cm^{-1}. A bending mode between the two metal centers through CN^- ligand (δ(Cr–C≡N)) was observed in a higher wavenumber range of 471–522 cm^{-1} compared to the same vibration mode at 454 cm^{-1} of $K_3[Cr(CN)_6]$, indicating a formation of the cyano-bridged framework (**Figure 1-1** and **Table 1-3**). A relevant bending mode of K^+-including PB, $\{KFe[Fe(CN)_6]\}$, referred to as soluble PB (δ(Fe–C≡N)) appears as a strong band at 600 cm^{-1} because this mode is greatly sensitive to interstitial alkali cations;[10] however, all the as-synthesized PBAs had no peak around the same wavenumber region, supporting the results of CHN-EA and EDXRF where almost no K element was detected.

Several modes in a wide range of 2700–3750 cm^{-1} and around 1610 cm^{-1} were attributed to motions of H_2O molecules of ν(O–H) and δ(H–O–H), respectively, indicating a presence of interstitial H_2O molecules in the framework (**Figure 1-1** and **Table 1-3**). In the modes of ν(O–H), the discernible sharp peaks in 3600–3658 cm^{-1} and the greatly broadened peak in the whole wavenumber region were derived from coordination H_2O molecules on the M^{2+} sites and dynamic H_2O molecules physisorbed and linked in a hydrogen-bond network, respectively (**Figure 1-1** and **Table 1-3**). Therefore, **$InCr \cdot nH_2O$** showed only the latter mode with a tiny intensity because of no unsaturated metal site on the In^{3+} center and 0.5 physisorbed H_2O molecules per pore with a side of Cr–C≡N–In linkage (**Figure 1-1**).

The formation of cyano-bridge was confirmed as well by a higher-wavenumber shift of the intense bands assigned to a vibration mode of CN^- ion (ν(C≡N)) in a wavenumber region of 2150–2200 cm^{-1} from the same mode at 2130 cm^{-1} of the starting material, $K_3[Cr(CN)_6]$, because σ-electron in antibonding orbital mainly contributes to the coordination to central metal ion of M^{2+} (**Figure 1-1** and **Table 1-3**). The shoulder peak around 2140 cm^{-1} in **$M_3Cr_2 \cdot nH_2O$** (M =VO, Co, and Ni) were possibly derived from free CN^- groups located on the particle surface.[11] The ν(C≡N) mode at 2102 cm^{-1} for **$Fe_3Cr_2 \cdot nH_2O$** and 2116 cm^{-1} for **$Cu_3Cr_2 \cdot nH_2O$**, which were in lower wavenumber than that of $K_3[Cr(CN)_6]$, suggested that cyanide flipping explained by the linkage isomerism has occurred in these samples, as with the reports.[10b,12]

The intense peak at 977 cm^{-1} observed in only **$(VO)_3Cr_2 \cdot nH_2O$** was assigned to a vibration mode of vanadyl ion (ν(V=O)) as with the reports,[9c,10b] which was similar to the starting material of $VOSO_4 \cdot nH_2O$ (n = 3–4) for **$(VO)_3Cr_2 \cdot nH_2O$** which showed ν(V=O) mode at 999 cm^{-1} (**Figure 1-1**).[9c,10b] The observed higher-wavenumber shift of ν(V=O) possibly resulted from the change in the coordination environment of V^{4+} center. In addition, $VOSO_4 \cdot nH_2O$ showed obvious vibration modes of SO_4^{2-}, ($\nu_1(SO_4^{2-})$ = 1018 cm^{-1}, $\nu_2(SO_4^{2-})$ = 436 and 465 cm^{-1}, $\nu_3(SO_4^{2-})$ = 1074 cm^{-1}, and $\nu_4(SO_4^{2-})$ = 588 and 619 cm^{-1}), as with the reports.[9c,10b,13] In contrast, although there are exceedingly tiny peaks at 585, 1051, and 1131 cm^{-1} observed around the abovementioned peak positions in **$(VO)_3Cr_2 \cdot nH_2O$**, the peak intensities were negligibly smaller than the other peaks, suggesting sufficient washing process to remove the unreacted reactants and the byproduct of K_2SO_4, which matched with the results of CHN-EA and EDXRF analysis (**Table 1-2**).

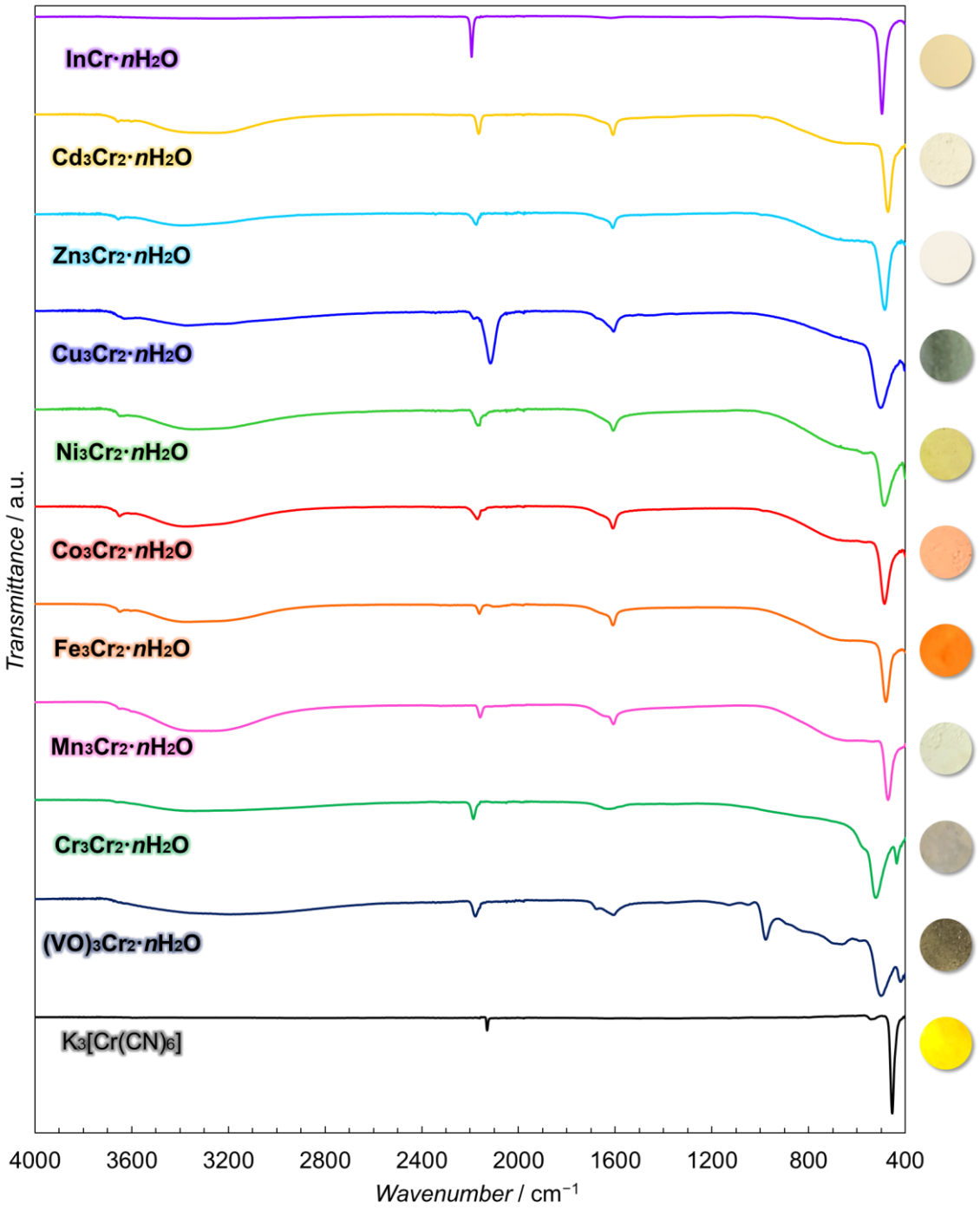

Figure 1-1. Normalized FT-IR spectra and photographs in the ambient air at RT of the starting material of $K_3[Cr^{III}(CN)_6]$ (black), the as-synthesized PBAs $\{M^{II}_3[Cr^{III}(CN)_6]_2 \cdot nH_2O\}$ (**$M_3Cr_2 \cdot nH_2O$**; M = VO (dark blue), Cr (green), Mn (pink), Fe (orange), Co (red), Ni (light green), Cu (blue), Zn (light blue), and Cd (yellow)) and $\{In^{III}[Cr^{III}(CN)_6] \cdot nH_2O\}$ (**$InCr \cdot nH_2O$**; purple). The spectra were normalized by each peak with the highest transmittance. Resolution: 4 cm^{-1}.

Table 1-3. Selected wavenumber of the observable peaks in the FT-IR spectra in the ambient air at RT of the starting material $K_3[Cr^{III}(CN)_6]$, the as-synthesized PBAs $\{M^{II}_3[Cr^{III}(CN)_6]_2 \cdot nH_2O\}$ (**$M_3Cr_2 \cdot nH_2O$**; M = VO, Cr, Mn, Fe, Co, Ni, Cu, Zn, and Cd) and $\{In^{III}[Cr^{III}(CN)_6] \cdot nH_2O\}$ (**$InCr \cdot nH_2O$**).

	ν(O–H) / cm^{-1}	ν(C≡N) / cm^{-1}	δ(H–O–H) / cm^{-1}	δ(Cr–C≡N) / cm^{-1}	ν(Cr–C) / cm^{-1}
$K_3[Cr(CN)_6]$		2130 (m)		454 (vs)	
$(VO)_3Cr_2 \cdot nH_2O$	3656 (w)	2178 (m)	1675 (w) 1606 (m)	500 (vs)	419 (s)
$Cr_3Cr_2 \cdot nH_2O$	3658 (w)	2187 (m)	1632 (m)	522 (vs)	436 (s)
$Mn_3Cr_2 \cdot nH_2O$	3651 (w) 3600 (w)	2158 (m)	1607 (m)	472 (vs)	
$Fe_3Cr_2 \cdot nH_2O$	3648 (w) 3600 (w)	2162 (m) 2102 (w)	1609 (m)	480 (vs)	
$Co_3Cr_2 \cdot nH_2O$	3651 (w) 3600 (w)	2170 (m)	1610 (m)	486 (vs)	
$Ni_3Cr_2 \cdot nH_2O$	3647 (w)	2169 (m)	1608 (m)	487 (vs)	
$Cu_3Cr_2 \cdot nH_2O$	3630 (w)	2185 (w) 2116 (vs)	1675 (w) 1607 (s)	503 (vs)	
$Zn_3Cr_2 \cdot nH_2O$	3655 (w)	2175 (m)	1610 (m)	485 (vs)	
$Cd_3Cr_2 \cdot nH_2O$	3656 (w) 3600 (w)	2165 (m)	1609 (m)	471 (vs)	
$InCr \cdot nH_2O$		2194 (m)	1619 (w)	497 (vs)	

*Mode: ν = stretching vibration, δ = bending vibration.

*Intensity: vs = very strong, s = strong, m = medium, w = weak.

The PXRD patterns of all the as-synthesized PBAs are consistent with a typical face-centered cubic (*fcc*) structural pattern of PBAs with distinct, sharp, and intense peaks, indicating a successful formation of 3-D cyano-bridged structure of PBAs (**Figure 1-2**).[1] Estimating from the peak intensity and the signal to noise (S/N) ratio, the crystallinities of **$(VO)_3Cr_2{\cdot}nH_2O$** and **$Co_3Cr_2{\cdot}nH_2O$** were slightly lower than the other PBAs (**Figure 1-2**). According to Bragg's law, the lattice spacing of (2 0 0) crystallographic plane ($d_{(200)}$) which is corresponding to length of pore side (Cr–C≡N–M) was calculated, where n, λ, and θ are a positive integer, the wavelength of X-ray (CuKα: 1.54184 Å), and glancing angle, respectively (**Equation 1-1** and **Table 1-4**).[14] The crystallographic parameter of *fcc* structure is corresponding the length of Cr–C≡N–M–N≡C–Cr which is twice as long as the pore side of $d_{(200)}$. The $2d_{(200)}$ values of the as-synthesized PBAs were in a range of 10.41–10.97 Å, which were comparable with those of the other reported PBAs. (**Table 1-4**).[1]

$$d = \frac{n\lambda}{2\sin\theta}$$

Equation 1-1. Bragg's equation.[14]

The crystallite sizes in the direction perpendicular to the (2 0 0) plane for the as-synthesized PBAs ($L_{(200)}$) were roughly calculated by Scherrer's equation using the full width half maximum (FWHM) values (β) at the (2 0 0) peak, where K (~0.939) is a dimensionless shape factor referred to as Scherrer's constant (**Equation 1-2** and **Table 1-4**).[15] The estimated values of $L_{(200)}$ were in a range of 11.0–46.6 nm. **$MCr_2{\cdot}nH_2O$** (M = VO, Cr, Co, Ni, and Cu) had a relatively smaller crystallite size than the other PBAs.

$$L = \frac{K\lambda}{\beta\cos\theta}$$

Equation 1-2. Scherrer's equation.[15]

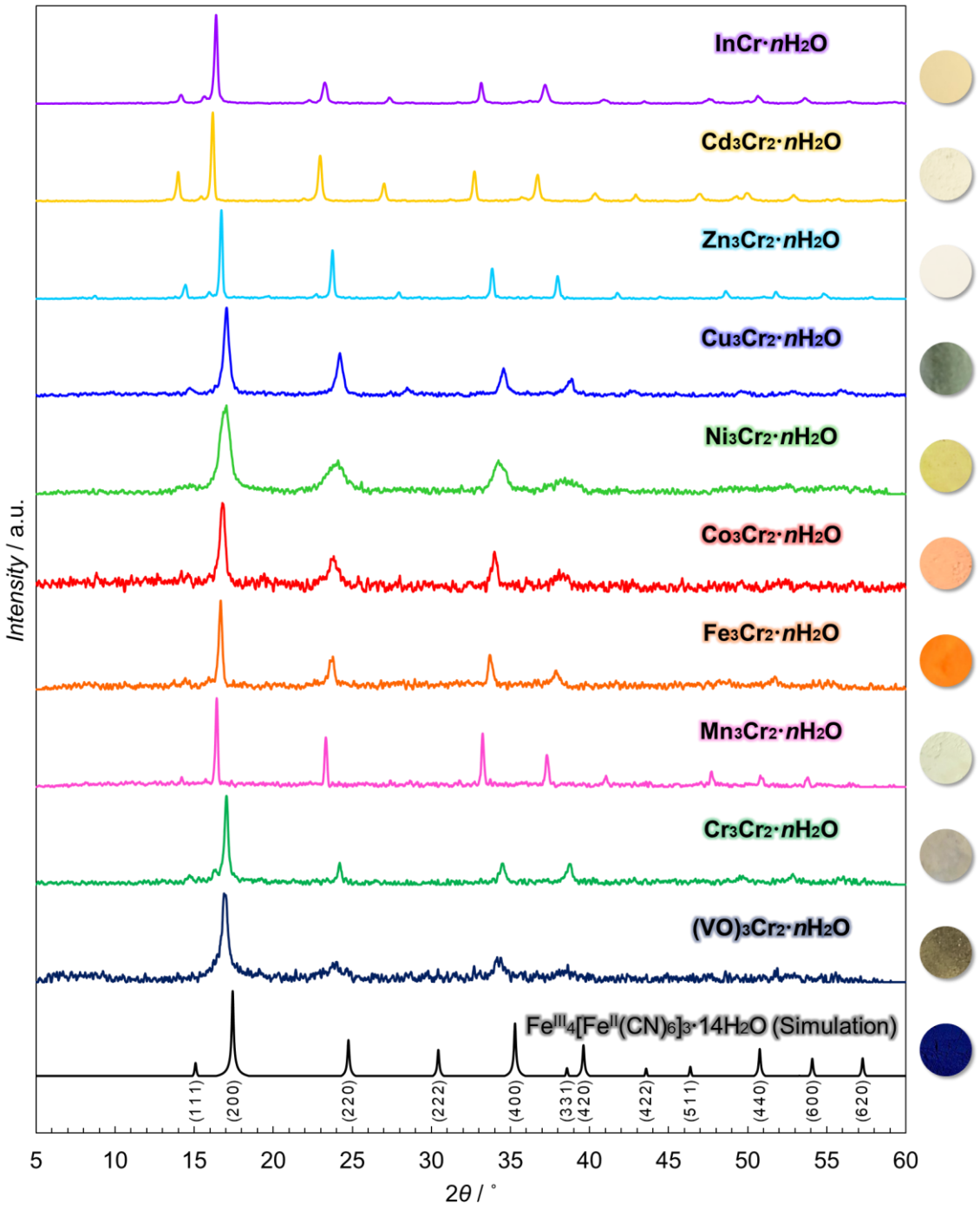

Figure 1-2. Normalized PXRD patterns and photographs in the ambient air at RT of the simulated $Fe^{III}_4[Fe^{II}(CN)_6]_4 \cdot nH_2O$ (black) with the Miller indexes,[1d] the as-synthesized PBAs $\{M^{II}_3[Cr^{III}(CN)_6]_2 \cdot nH_2O\}$ (**$M_3Cr_2 \cdot nH_2O$**; M = VO (dark blue), Cr (green), Mn (pink), Fe (orange), Co (red), Ni (light green), Cu (blue), Zn (light blue), and Cd (yellow)) and $\{In^{III}[Cr^{III}(CN)_6] \cdot nH_2O\}$ (**$InCr \cdot nH_2O$**; purple). The patterns were normalized by each peak with the strongest intensity. Scan rate: 1° min^{-1}, data collecting step: 0.02°.

Table 1-4. The observed diffraction angle ($2\theta_{(200)}$) and the full width at half maximum (FWHM) value ($\beta_{(200)}$) at a peak with a Miller index of (2 0 0) in the PXRD patterns of $\{M^{II}_3[Cr^{III}(CN)_6]_2 \cdot nH_2O\}$ (**$M_3Cr_2 \cdot nH_2O$**; M = VO, Cr, Mn, Fe, Co, Ni, Cu, Zn, and Cd) and $\{In^{III}[Cr^{III}(CN)_6] \cdot nH_2O\}$ (**$InCr \cdot nH_2O$**) in the ambient air at RT. The lattice spacing distance ($d_{(200)}$) and crystallite size in the direction perpendicular to the (2 0 0) crystallographic plane ($L_{(200)}$) were calculated from Bragg's equation and Scherrer's equation, respectively.

	$2\theta_{(200)}$ / °	$d_{(200)}$ / Å	$2d_{(200)}$ / Å	$\beta_{(200)}$ / °	$L_{(200)}$ / nm
$(VO)_3Cr_2 \cdot nH_2O$	16.93	5.23	10.47	0.48	17.5
$Cr_3Cr_2 \cdot nH_2O$	17.04	5.20	10.41	0.28	30.0
$Mn_3Cr_2 \cdot nH_2O$	16.39	5.41	10.82	0.18	46.6
$Fe_3Cr_2 \cdot nH_2O$	16.67	5.32	10.64	0.25	32.3
$Co_3Cr_2 \cdot nH_2O$	16.80	5.28	10.56	0.43	19.1
$Ni_3Cr_2 \cdot nH_2O$	16.94	5.24	10.47	0.77	11.0
$Cu_3Cr_2 \cdot nH_2O$	17.04	5.20	10.41	0.40	21.0
$Zn_3Cr_2 \cdot nH_2O$	16.72	5.30	10.60	0.18	41.9
$Cd_3Cr_2 \cdot nH_2O$	16.17	5.48	10.97	0.21	39.9
$InCr \cdot nH_2O$	16.39	5.41	10.82	0.22	38.1

In the TGA of the as-synthesized PBAs, a large weight loss started from RT until an appearance of a plateau in a temperature range of approximately 100–300℃ except **InCr** which showed a gradual weight loss over the entire measurement temperature range (**Figure 1-3**). A weight loss in such temperature range should be corresponding to the removal of interstitial H_2O molecules in PBAs. The observed values of weight loss are in good agreement with the values expected by CHN-EA except for **Cr_3Cr_2·*n*H_2O** (**Figure 1-3** and **Table 1-5**). In the case of **Cr_3Cr_2·*n*H_2O**, a weight loss of 22.0% corresponding to H_2O molecules 8.9 H_2O molecules appeared in the beginning and a gradual loss followed subsequently, indicating that approximately 6 H_2O molecules remained by heating up until ~300℃ under a dry N_2 atmosphere (**Figure 1-3** and **Table 1-5**). This result was consistent with a reported case where a residue of 6 coordination H_2O molecules existed even after heating under vacuum and harder activation cause the framework decomposition.[8j]

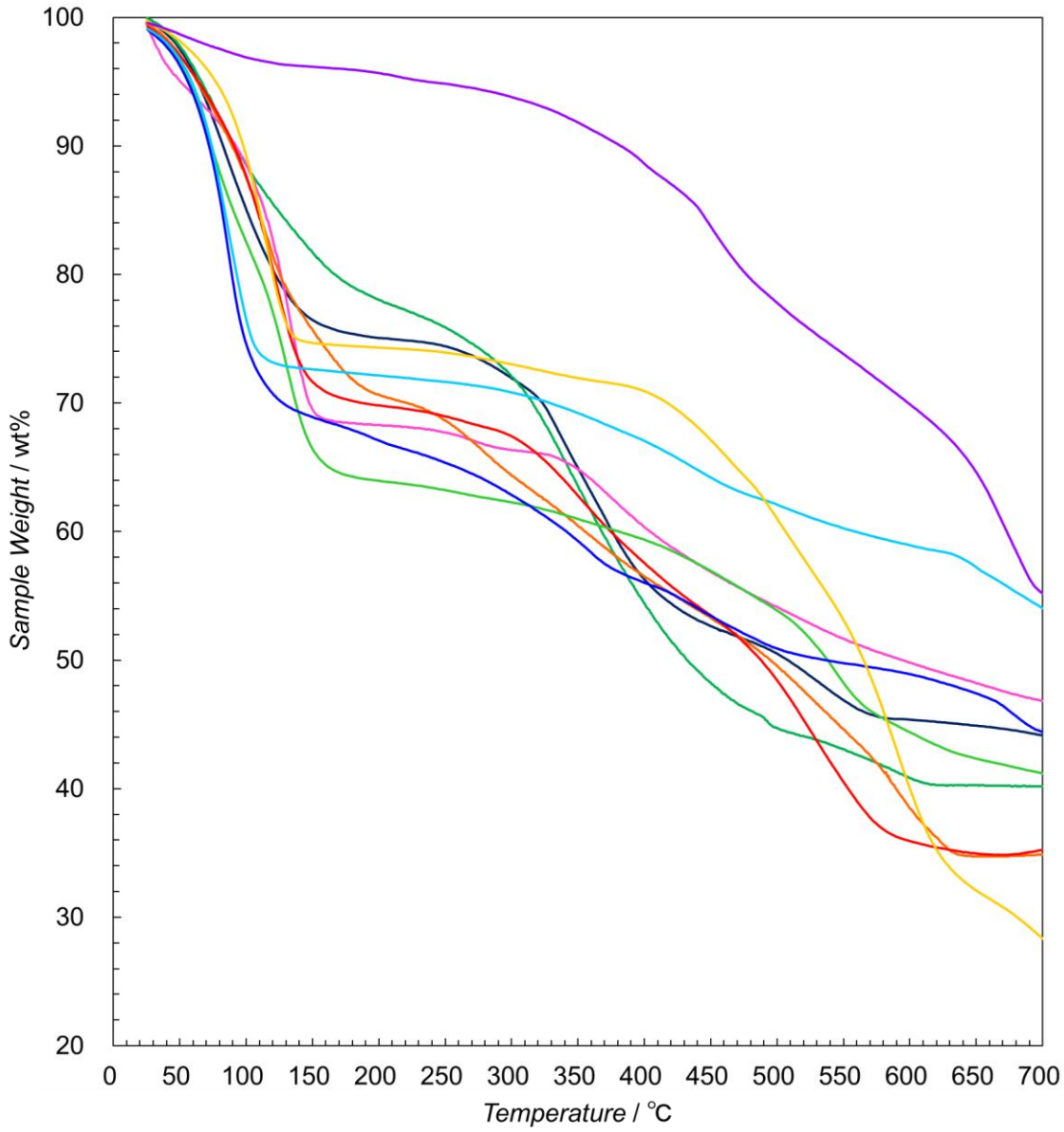

Figure 1-3. TGA curves of the as-synthesized PBAs $\{M^{II}_3[Cr^{III}(CN)_6]_2 \cdot nH_2O\}$ (**$M_3Cr_2 \cdot nH_2O$**; M = VO (dark blue), Cr (green), Mn (pink), Fe (orange), Co (red), Ni (light green), Cu (blue), Zn (light blue), and Cd (yellow)) and $\{In^{III}[Cr^{III}(CN)_6] \cdot nH_2O\}$ (**$InCr \cdot nH_2O$**; purple) under a dry N_2 atmosphere. The measurement was performed as quickly as possible after sample loading. Heating rate: 10℃ min^{-1}, N_2 gas flow rate: 19.8 ml min^{-1}.

Table 1-5. The weight percentage and the number of H_2O molecules (n) which are observed in TGA at different temperatures of 150, 200 and 250°C and expected from carbon, hydrogen, and nitrogen elemental analysis (CHN-EA) of the as-synthesized PBAs $\{M^{II}_3[Cr^{III}(CN)_6]_2 \cdot nH_2O\}$ (**$M_3Cr_2 \cdot nH_2O$**; M = VO, Cr, Mn, Fe, Co, Ni, Cu, Zn, and Cd) and $\{In^{III}[Cr^{III}(CN)_6] \cdot nH_2O\}$ (**$InCr \cdot nH_2O$**).

	wt%	n	wt%	n	wt%	n	wt%	n
	at 150°C		at 200°C		at 250°C		expected from CHN-EA	
$(VO)_3Cr_2 \cdot nH_2O$	76.5	10.5	75.1	11.4	74.4	11.8	74.1	12
$Cr_3Cr_2 \cdot nH_2O$	81.7	7.1	78.0	8.9	75.9	10.1	67.9	15
$Mn_3Cr_2 \cdot nH_2O$	69.5	14.2	68.3	15.0	67.7	15.4	66.8	16
$Fe_3Cr_2 \cdot nH_2O$	75.7	10.4	70.6	13.5	68.6	14.8	66.9	16
$Co_3Cr_2 \cdot nH_2O$	71.6	13.0	69.8	14.2	69.0	14.8	67.3	16
$Ni_3Cr_2 \cdot nH_2O$	66.4	16.6	64.0	18.5	63.2	19.1	63.4	19
$Cu_3Cr_2 \cdot nH_2O$	68.9	15.2	67.1	16.5	65.3	17.9	65.2	18
$Zn_3Cr_2 \cdot nH_2O$	72.6	12.8	72.1	13.1	71.6	13.5	70.8	14
$Cd_3Cr_2 \cdot nH_2O$	74.7	14.2	74.3	14.5	73.9	14.8	73.6	15
$InCr \cdot nH_2O$	96.2	0.7	95.7	0.8	94.8	1.0	94.7	1

In order to evaluate the structural stability of the PBAs upon application of the activation process for dehydration, all the as-synthesized PBAs were heated at different activation temperatures (T_{act}) of 20, 40, 60, 80, 100, 120, 140, and 160℃ under reduced pressure for 24 h to obtain each activated sample. **$(VO)_3Cr_2$**, **Cr_3Cr_2**, and **InCr** series showed almost no obvious color change and **Co_3Cr_2**, **Ni_3Cr_2**, **Zn_3Cr_2**, and **Cd_3Cr_2** series showed a slight color change to yellowish colors, whereas **Mn_3Cr_2** and **Fe_3Cr_2** series showed a gradual color change with a final darkening at the T_{act} of 140 and 160℃ (**Figure 1-4**). Noteworthy, the deep green color of **$Cu_3Cr_2 \cdot nH_2O$** rapidly turned into reddish-brown even after the activation at a low temperature of 20℃ (**Figure 1-4**). These observed color change conceivably derived from the removal of interstitial H_2O molecules and framework decomposition.

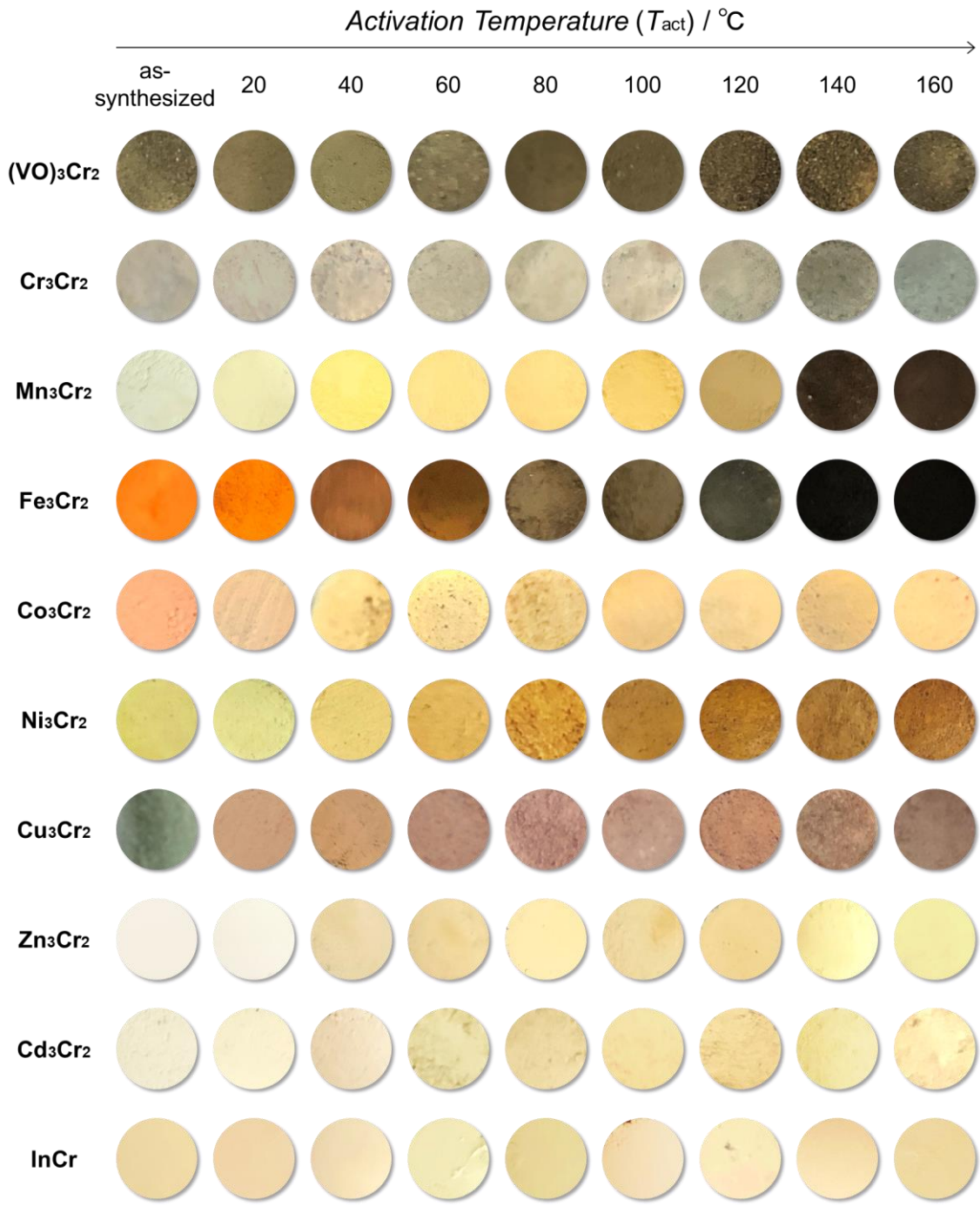

Figure 1-4. Photographs in the ambient air at RT of the as-synthesized PBAs and their activated samples heated at different activation temperatures (T_{act}) of 20, 40, 60, 80, 100, 120, 140, and 160°C under dynamic vacuum for 24 h.

In order to obtain the detailed information about the framework stability toward the activation process, PXRD measurements in the ambient air at RT were performed for all the series of PBAs activated at each temperature (**Figure 1-5**–**Figure 1-14**). Moreover, in order to discuss the stability using some parameters, relative peak intensities ($I_{T\text{act}}/I_{\text{as-syn.}}$) and relative peak FWHM values ($\beta_{\text{as-syn.}}/\beta_{T\text{act}}$) for all the samples activated at each T_{act} were calculated using the values of the as-synthesized sample ($I_{\text{as-syn.}}$ and $\beta_{\text{as-syn.}}$) as standard values, regarding the intense peak at (2 0 0) crystallographic plane (**Figure 1-15**).

On the whole, similarly to the change in sample color (**Figure 1-4**), the intensity and the FWHM values tended to decrease with T_{act} increasing in the PXRD patterns of all the activated PBA series (**Figure 1-5**–**Figure 1-14**). For example, **Co_3Cr_2**, **Ni_3Cr_2**, and **InCr** series in all the T_{act} showed only slight changes in both the relative intensity ($I_{T\text{act}}/I_{\text{as-syn.}} \geq 0.8$) and the relative FWHM value ($\beta_{\text{as-syn.}}/\beta_{T\text{act}} \geq 0.8$), indicating their greatly higher stability upon the activation until 160℃ than those of the other PBAs (**Figure 1-9**, **Figure 1-10**, **Figure 1-14**, and **Figure 1-15**). Among the three PBAs, **InCr** showed the highest stability ($I_{T\text{act}}/I_{\text{as-syn.}} \geq 0.85$; $\beta_{\text{as-syn.}}/\beta_{T\text{act}} \geq 0.9$) possibly thanks to the non-defective structure. In the patterns of **$(VO)_3Cr_2$**, **Cr_3Cr_2**, and **Zn_3Cr_2** series, although the peak intensity decreased and the FWHM values increased gradually with T_{act} increasing, the major peaks were observed with sufficiently observable intensity even at the highest T_{act} of 160℃ ($0.3 \leq I_{160℃}/I_{\text{as-syn.}} \leq 0.8$; $0.3 \leq \beta_{\text{as-syn.}}/\beta_{160℃} \leq 0.8$), suggesting relatively high stability (**Figure 1-5**, **Figure 1-6**, **Figure 1-12**, and **Figure 1-15**). The no or slight change in the sample color of these five defective PBA series (**M_3Cr_2**; M = VO, Cr, Co, Ni, and Zn) and the non-defective PBA series (**InCr**) mentioned above suggested the correlation between the color and the stability (**Figure 1-4** and **Figure 1-15**). On the other hand, the peaks in **Mn_3Cr_2**, **Fe_3Cr_2**, **Cu_3Cr_2**, and **Cd_3Cr_2** series were gradually broadened with T_{act} increasing and finally vanished at the T_{act} of 140, 80, 20 and 140℃, respectively (**Figure 1-7**, **Figure 1-8**, **Figure 1-11**, **Figure 1-13**, and **Figure 1-15**). As a matter of fact, from the viewpoints of both relative parameters, these samples conceivably showed framework decomposition over the respective T_{act} ($I_{T\text{act}}/I_{\text{as-syn.}} \leq 0.2$; $\beta_{\text{as-syn.}}/\beta_{T\text{act}} \leq 0.2$; **Figure 1-15**). In the relatively low-T_{act} region, **Mn_3Cr_2** series had stronger intensities and thinner FWHM values than **Cd_3Cr_2** series (**Figure 1-7**, **Figure 1-13**, and **Figure 1-15**). Therefore, for the above discussion, the order of structural ability depending on the metal canter (M) upon application of the heating under reduced pressure was concluded to be In > (Co, Ni) > Cr > Zn > VO > Mn > Cd > Fe > Cu.

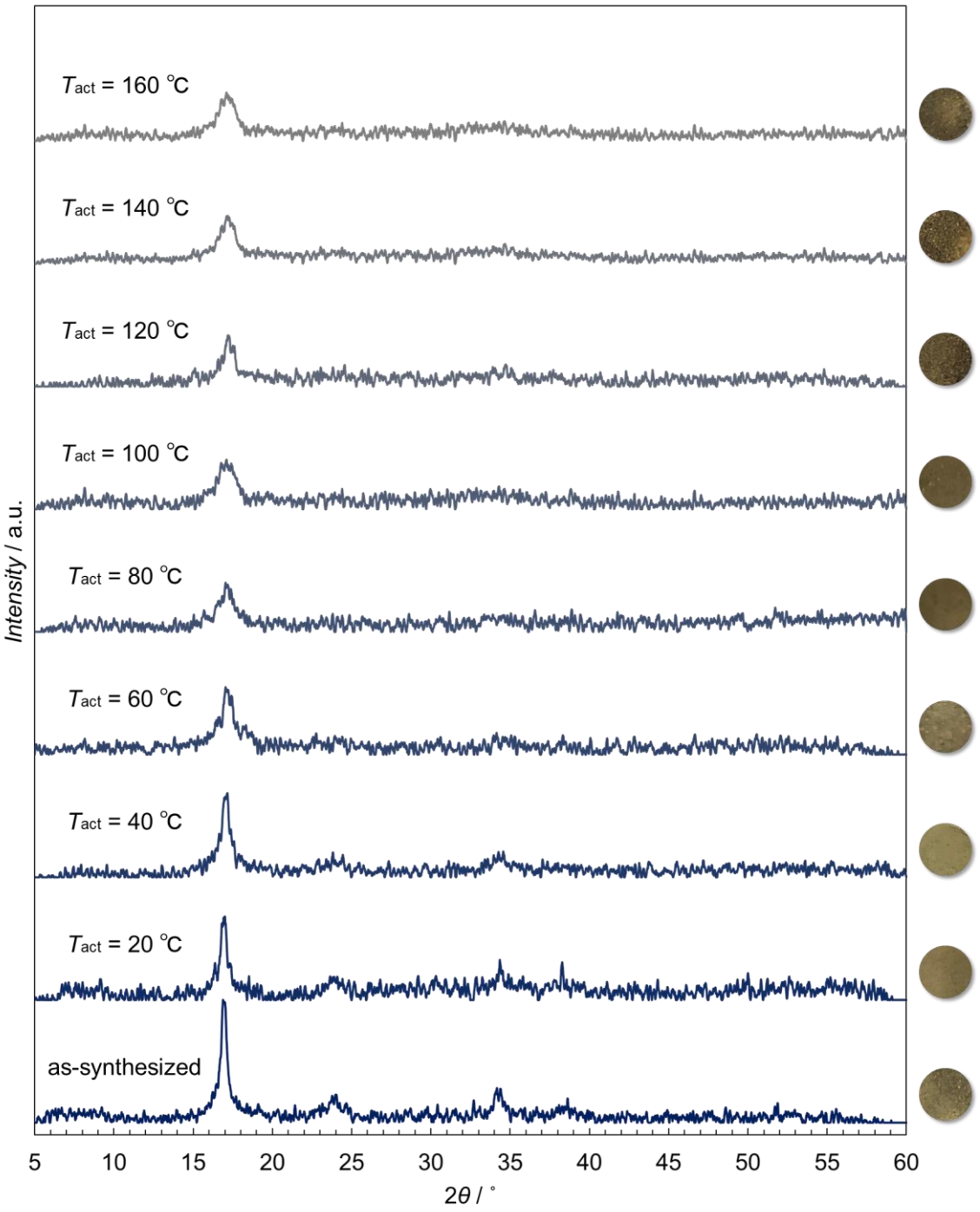

Figure 1-5. PXRD patterns in the ambient air at RT and photographs of the as-synthesized sample $\{(V^{IV}O)_3[Cr^{III}(CN)_6]_2 \cdot nH_2O\}$ (**$(VO)_3Cr_2 \cdot nH_2O$**: dark blue) and its activated samples heated at different activation temperatures (T_{act}) of 20, 40, 60, 80, 100, 120, 140, and 160℃ (colors from dark blue to gray) under reduced pressure for 24 h. The patterns were normalized by the peak with the strongest intensity of **$(VO)_3Cr_2 \cdot nH_2O$**. Scan rate: 1° min^{-1}, data collecting step: 0.02°.

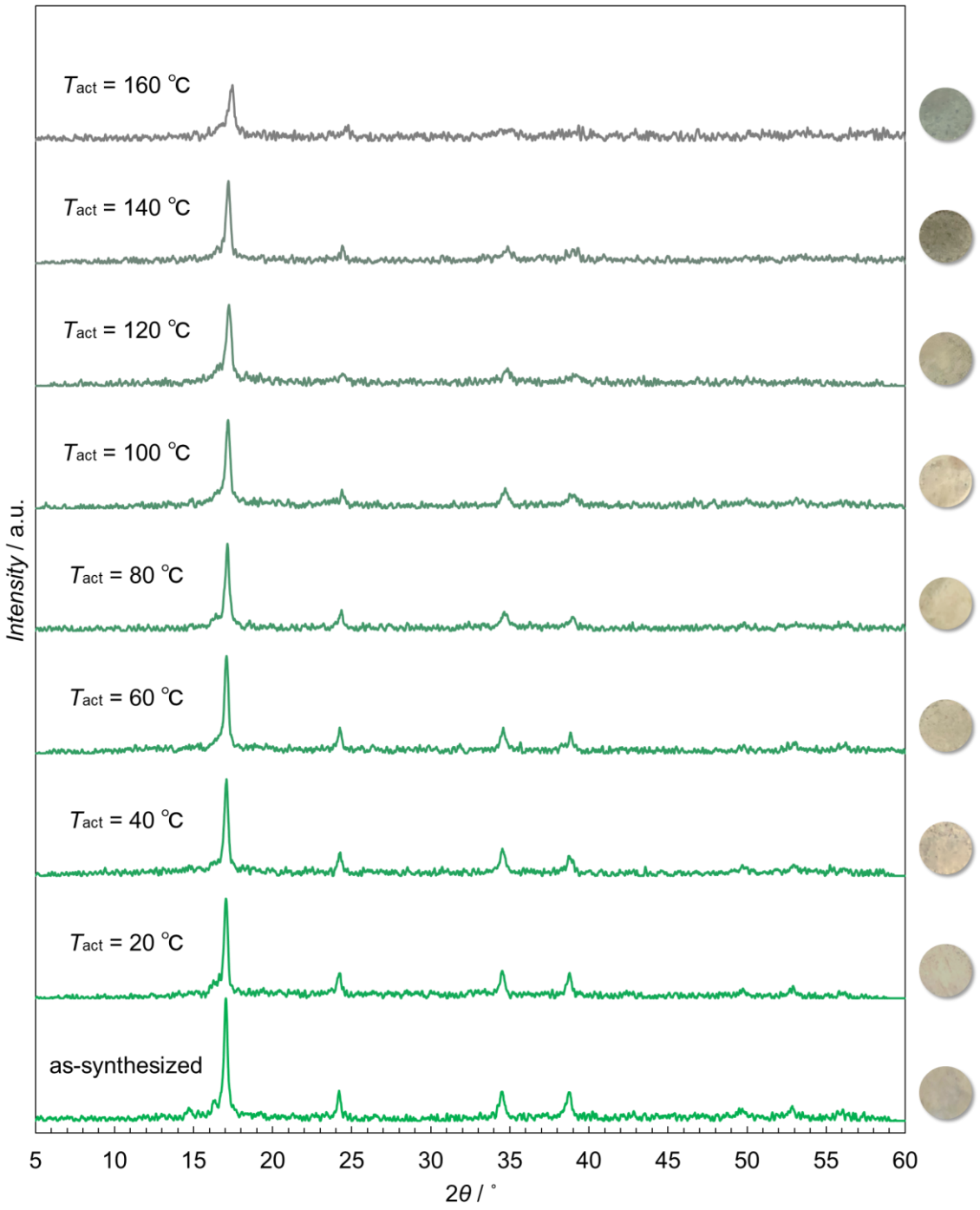

Figure 1-6. PXRD patterns in the ambient air at RT and photographs of the as-synthesized sample $\{Cr^{II}_3[Cr^{III}(CN)_6]_2 \cdot nH_2O\}$ (**$Cr_3Cr_2 \cdot nH_2O$**: green) and its activated samples heated at different activation temperatures (T_{act}) of 20, 40, 60, 80, 100, 120, 140, and 160°C (colors from green to gray) under reduced pressure for 24 h. The patterns were normalized by the peak with the strongest intensity of **$Cr_3Cr_2 \cdot nH_2O$**. Scan rate: 1° min^{-1}, data collecting step: 0.02°.

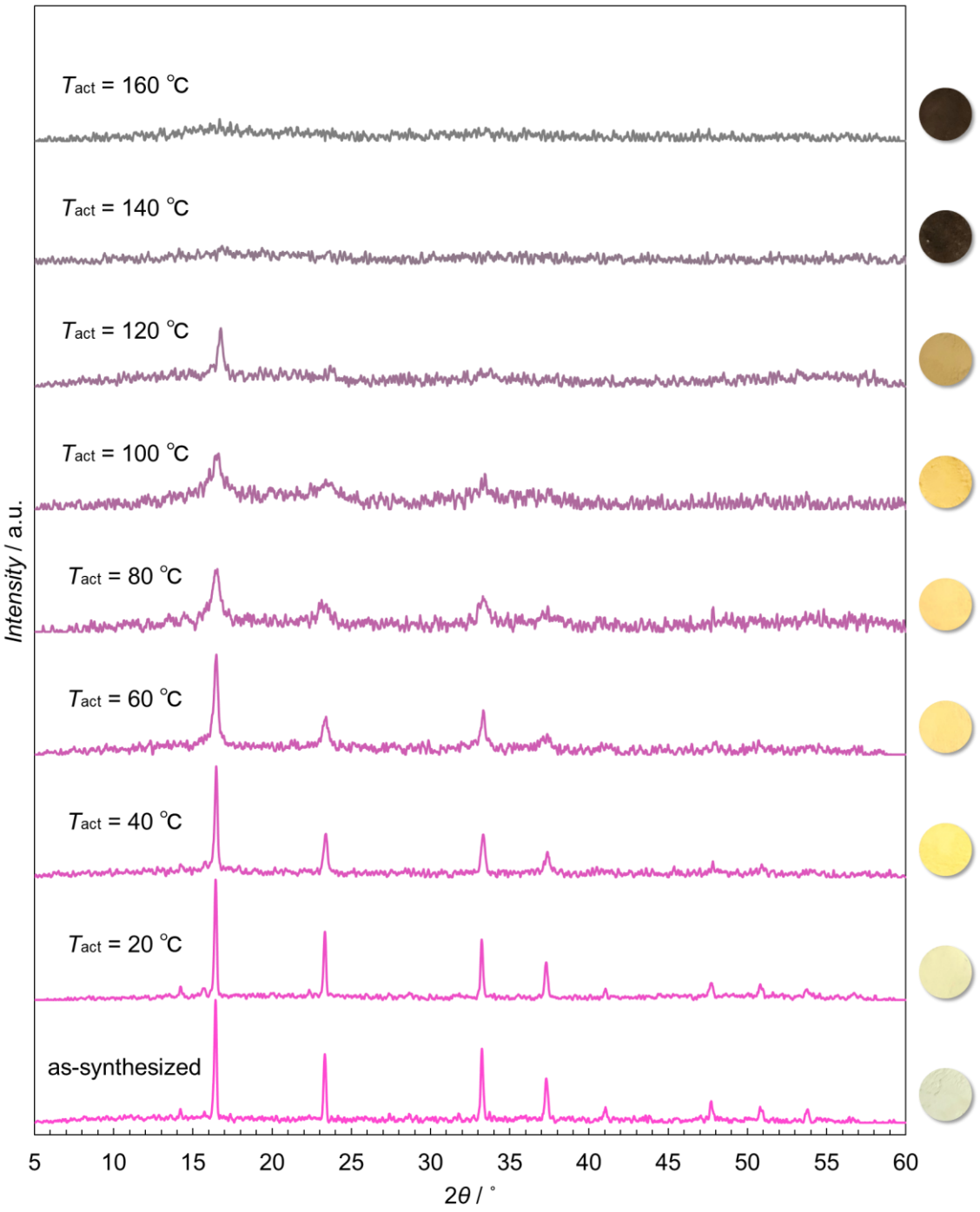

Figure 1-7. PXRD patterns in the ambient air at RT and photographs of the as-synthesized sample $\{Mn^{II}_3[Cr^{III}(CN)_6]_2 \cdot nH_2O\}$ (**$Mn_3Cr_2 \cdot nH_2O$**: pink) and its activated samples heated at different activation temperatures (T_{act}) of 20, 40, 60, 80, 100, 120, 140, and 160°C (colors from pink to gray) under reduced pressure for 24 h. The patterns were normalized by the peak with the strongest intensity of **$Mn_3Cr_2 \cdot nH_2O$**. Scan rate: 1° min^{-1}, data collecting step: 0.02°.

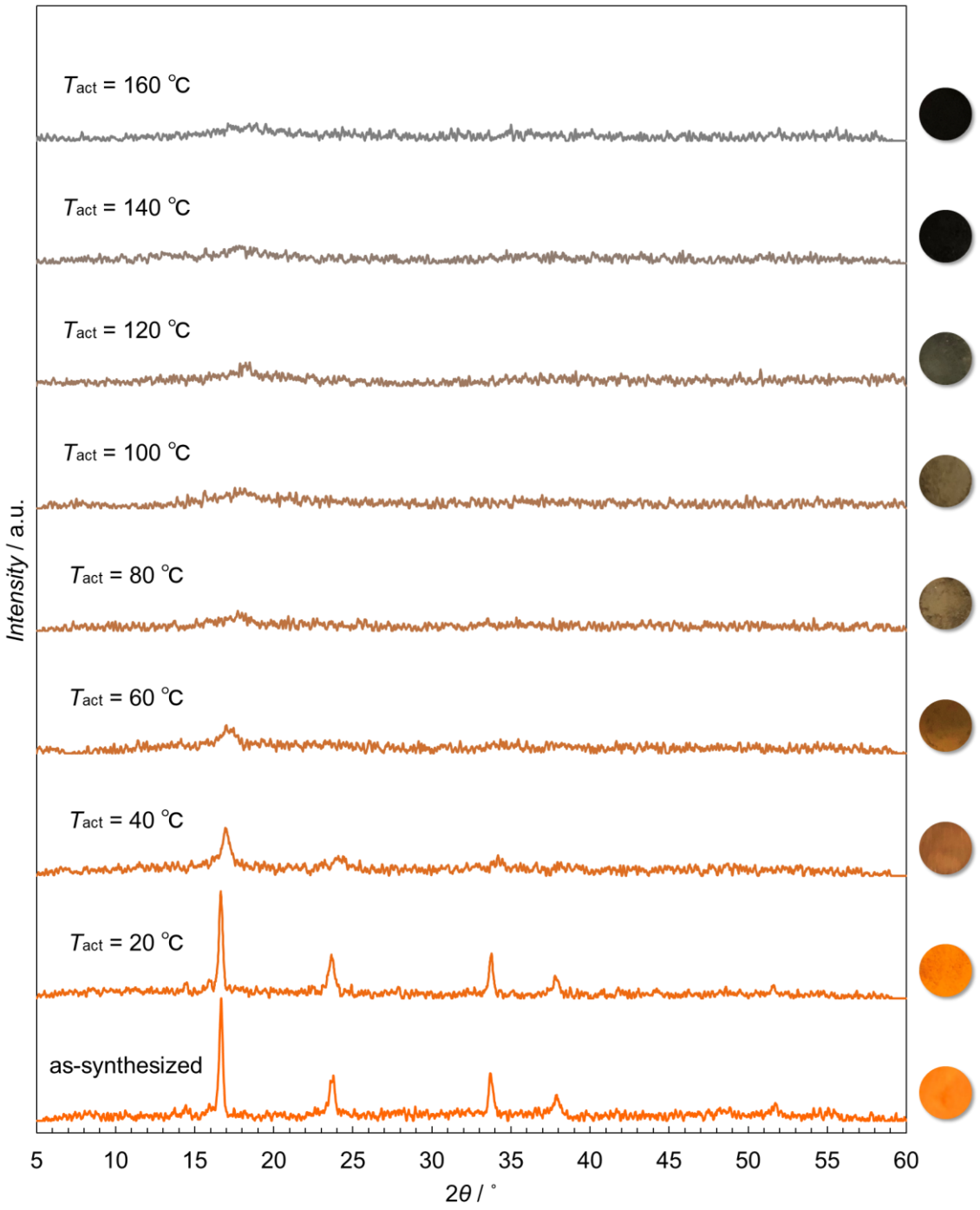

Figure 1-8. PXRD patterns in the ambient air at RT and photographs of the as-synthesized sample $\{Fe^{II}_3[Cr^{III}(CN)_6]_2 \cdot nH_2O\}$ (**$Fe_3Cr_2 \cdot nH_2O$**: orange) and its activated samples heated at different activation temperatures (T_{act}) of 20, 40, 60, 80, 100, 120, 140, and 160°C (colors from orange to gray) under reduced pressure for 24 h. The patterns were normalized by the peak with the strongest intensity of **$Fe_3Cr_2 \cdot nH_2O$**. Scan rate: 1° min^{-1}, data collecting step: 0.02°.

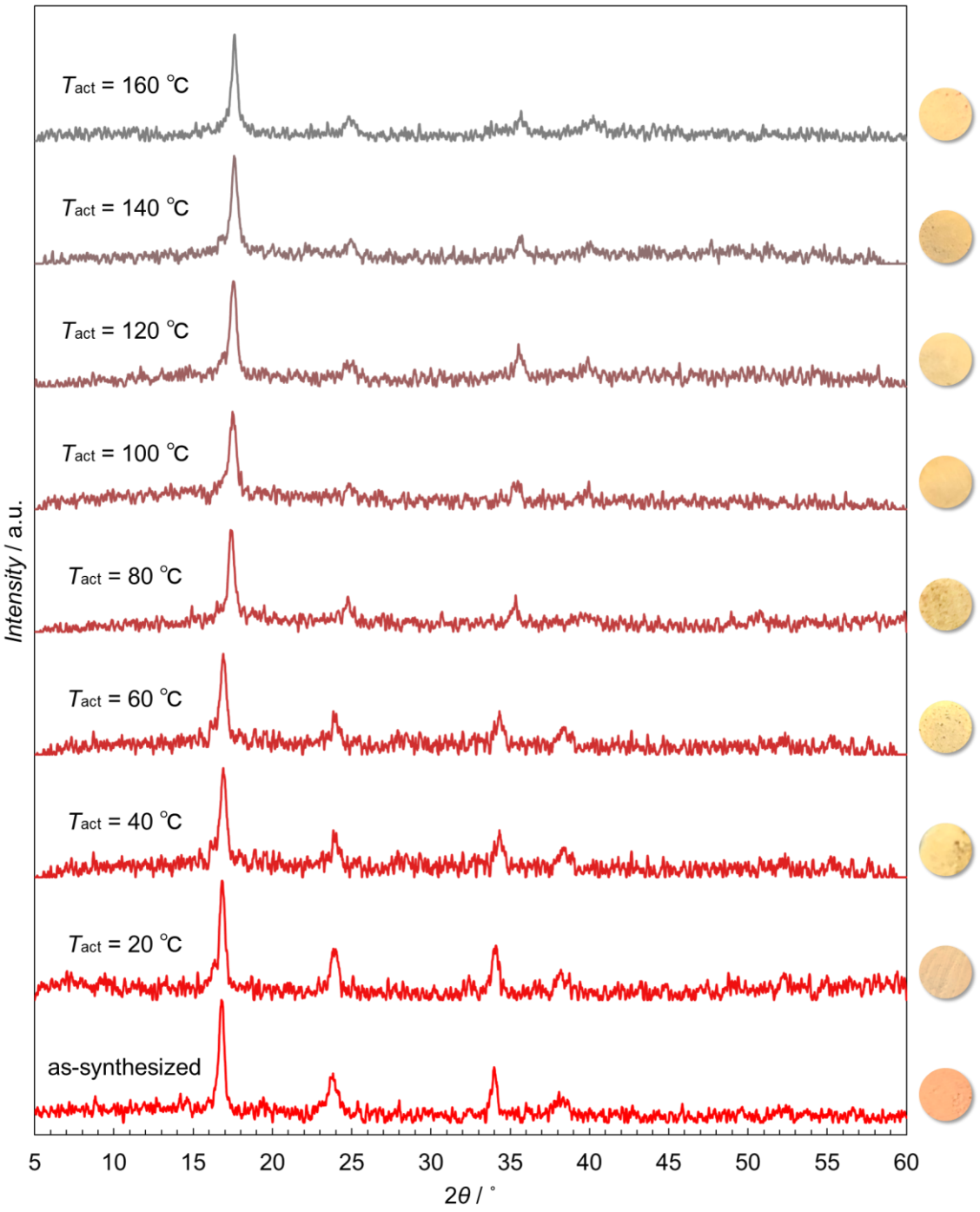

Figure 1-9. PXRD patterns in the ambient air at RT and photographs of the as-synthesized sample $\{Co^{II}_3[Cr^{III}(CN)_6]_2 \cdot nH_2O\}$ (**$Co_3Cr_2 \cdot nH_2O$**: red) and its activated samples heated at different activation temperatures (T_{act}) of 20, 40, 60, 80, 100, 120, 140, and 160℃ (colors from red to gray) under reduced pressure for 24 h. The patterns were normalized by the peak with the strongest intensity of **$Co_3Cr_2 \cdot nH_2O$**. Scan rate: 1° min^{-1}, data collecting step: 0.02°.

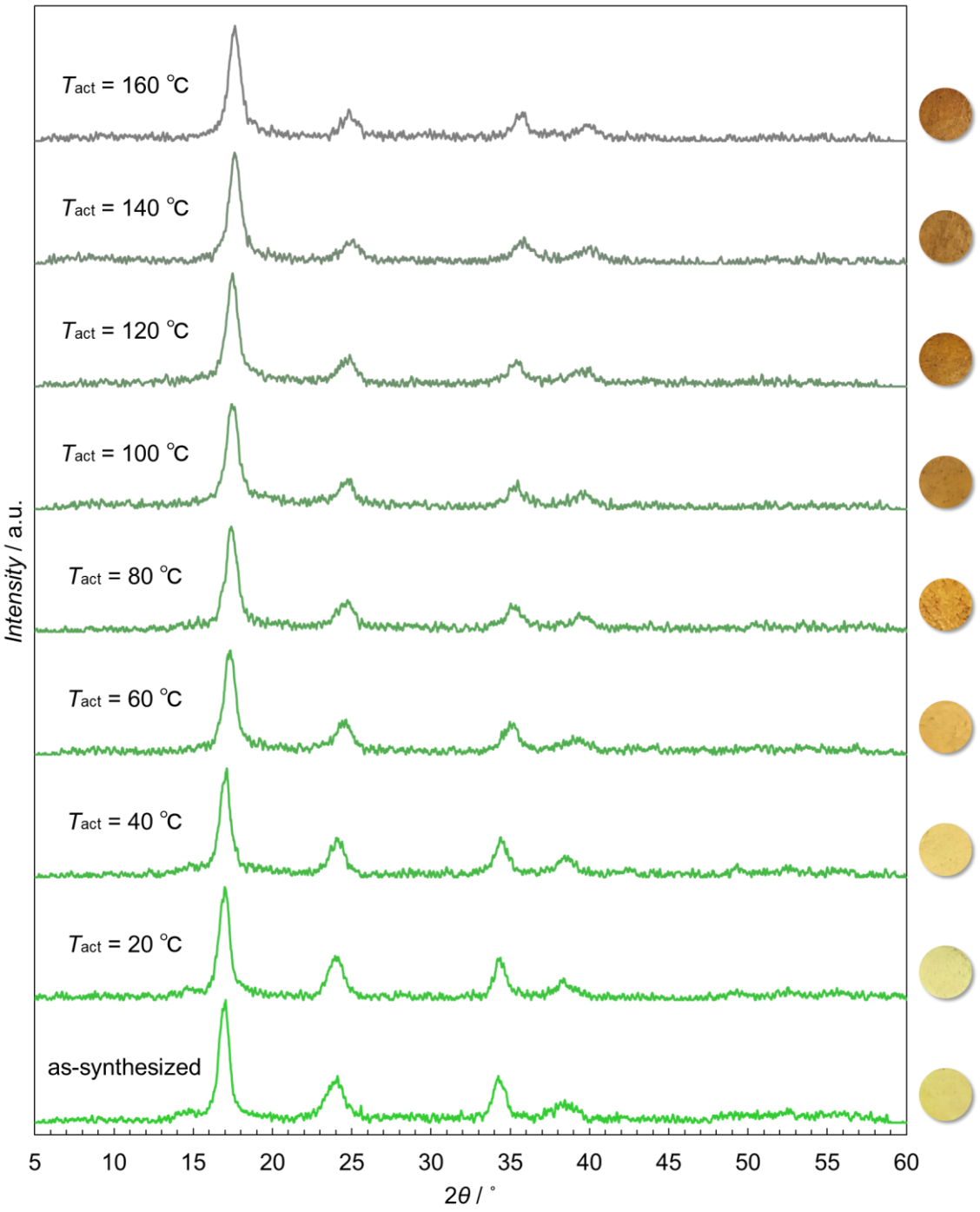

Figure 1-10. PXRD patterns in the ambient air at RT and photographs of the as-synthesized sample $\{Ni^{II}_3[Cr^{III}(CN)_6]_2 \cdot nH_2O\}$ (**$Ni_3Cr_2 \cdot nH_2O$**: light green) and its activated samples heated at different activation temperatures (T_{act}) of 20, 40, 60, 80, 100, 120, 140, and 160℃ (colors from light green to gray) under reduced pressure for 24 h. The patterns were normalized by the peak with the strongest intensity of **$Ni_3Cr_2 \cdot nH_2O$**. Scan rate: 1° min^{-1}, data collecting step: 0.02°.

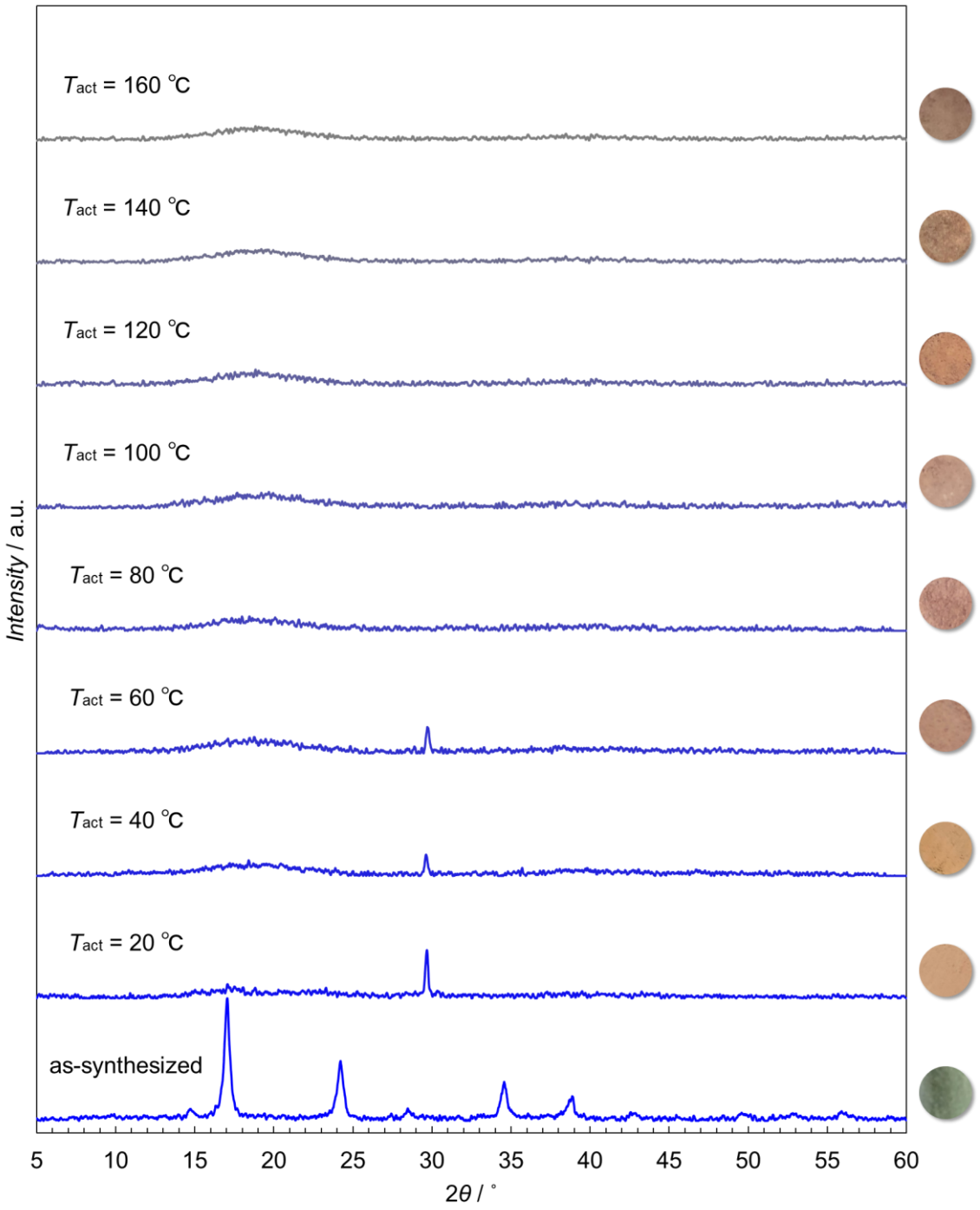

Figure 1-11. PXRD patterns in the ambient air at RT and photographs of the as-synthesized sample $\{Cu^{II}_3[Cr^{III}(CN)_6]_2 \cdot nH_2O\}$ (**$Cu_3Cr_2 \cdot nH_2O$**: blue) and its activated samples heated at different activation temperatures (T_{act}) of 20, 40, 60, 80, 100, 120, 140, and 160°C (colors from blue to gray) under reduced pressure for 24 h. The patterns were normalized by the peak with the strongest intensity of **$Cu_3Cr_2 \cdot nH_2O$**. Scan rate: 1° min^{-1}, data collecting step: 0.02°.

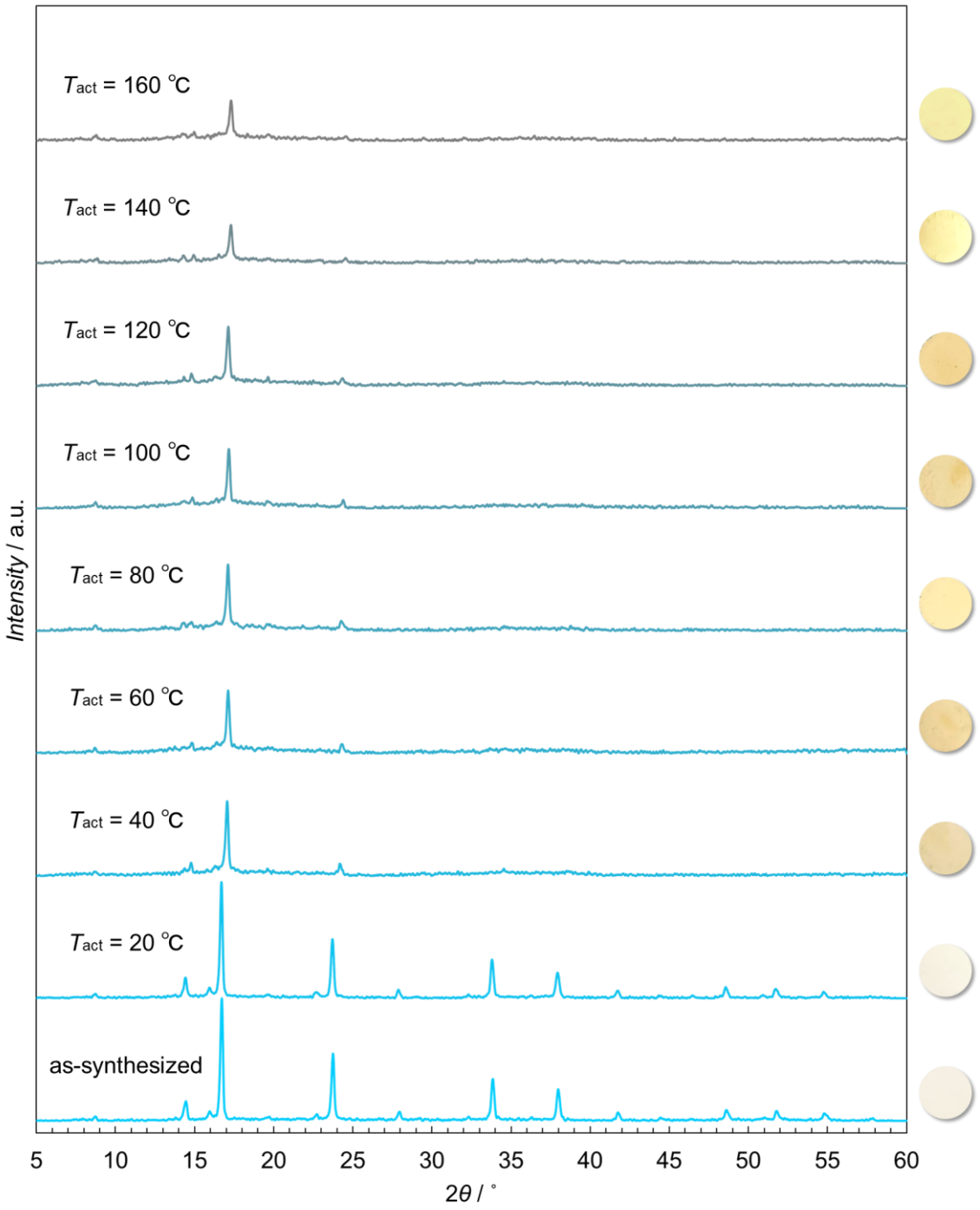

Figure 1-12. PXRD patterns in the ambient air at RT and photographs of the as-synthesized sample $\{Zn^{II}_3[Cr^{III}(CN)_6]_2 \cdot nH_2O\}$ (**$Zn_3Cr_2 \cdot nH_2O$**: light blue) and its activated samples heated at different activation temperatures (T_{act}) of 20, 40, 60, 80, 100, 120, 140, and 160°C (colors from light blue to gray) under reduced pressure for 24 h. The patterns were normalized by the peak with the strongest intensity of **$Zn_3Cr_2 \cdot nH_2O$**. Scan rate: 1° min^{-1}, data collecting step: 0.02°.

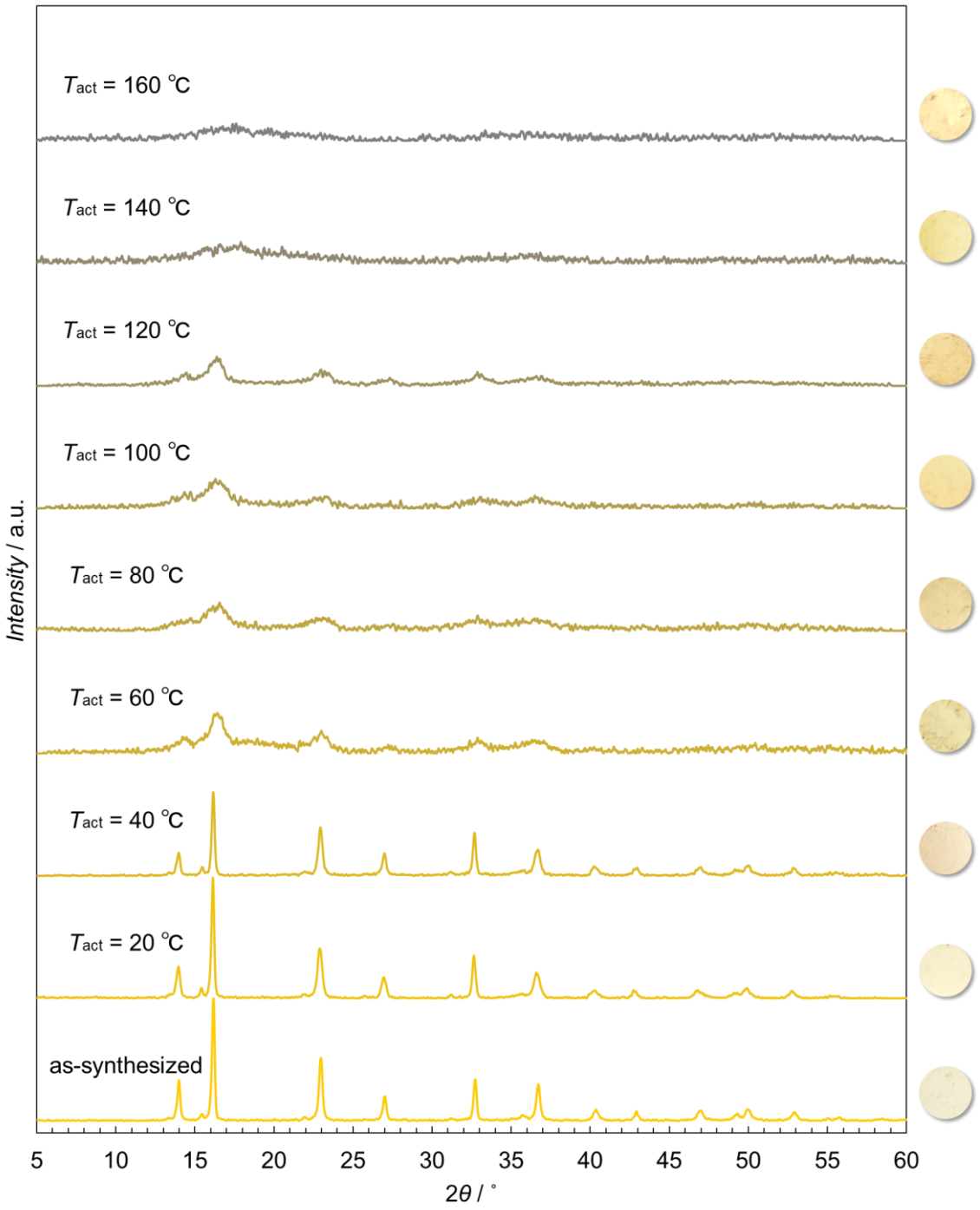

Figure 1-13. PXRD patterns in the ambient air at RT and photographs of the as-synthesized sample $\{Cd^{II}_3[Cr^{III}(CN)_6]_2 \cdot nH_2O\}$ (**$Cd_3Cr_2 \cdot nH_2O$**: yellow) and its activated samples heated at different activation temperatures (T_{act}) of 20, 40, 60, 80, 100, 120, 140, and 160°C (colors from yellow to gray) under reduced pressure for 24 h. The patterns were normalized by the peak with the strongest intensity of **$Cd_3Cr_2 \cdot nH_2O$**. Scan rate: 1° min^{-1}, data collecting step: 0.02°.

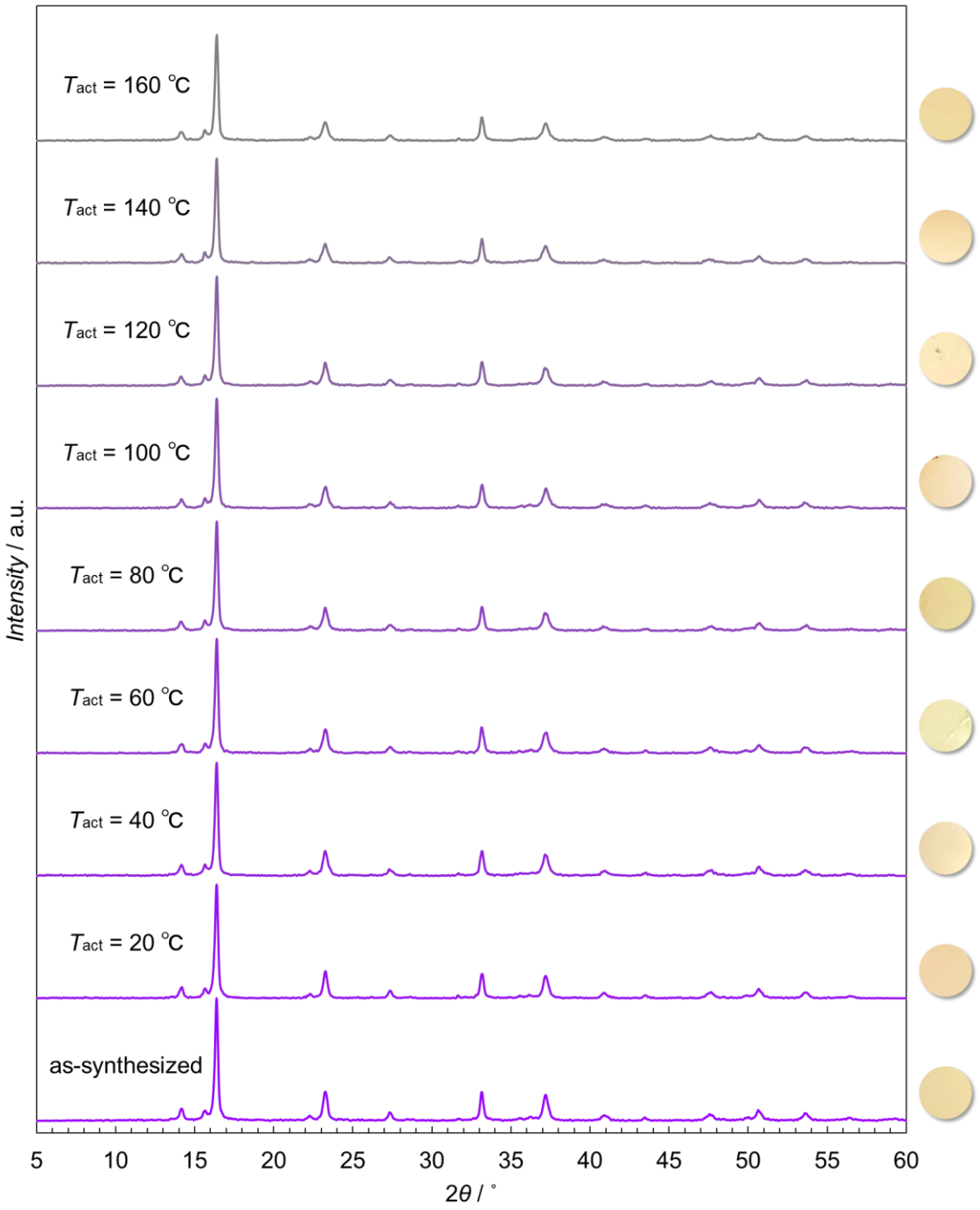

Figure 1-14. PXRD patterns in the ambient air at RT and photographs of the as-synthesized sample $\{In^{III}[Cr^{III}(CN)_6]\cdot nH_2O\}$ (**InCr·*n*H₂O**: purple) and its activated samples heated at different activation temperatures (T_{act}) of 20, 40, 60, 80, 100, 120, 140, and 160°C (colors from purple to gray) under reduced pressure for 24 h. The patterns were normalized by the peak with the strongest intensity of **InCr·*n*H₂O**. Scan rate: 1° min^{-1}, data collecting step: 0.02°.

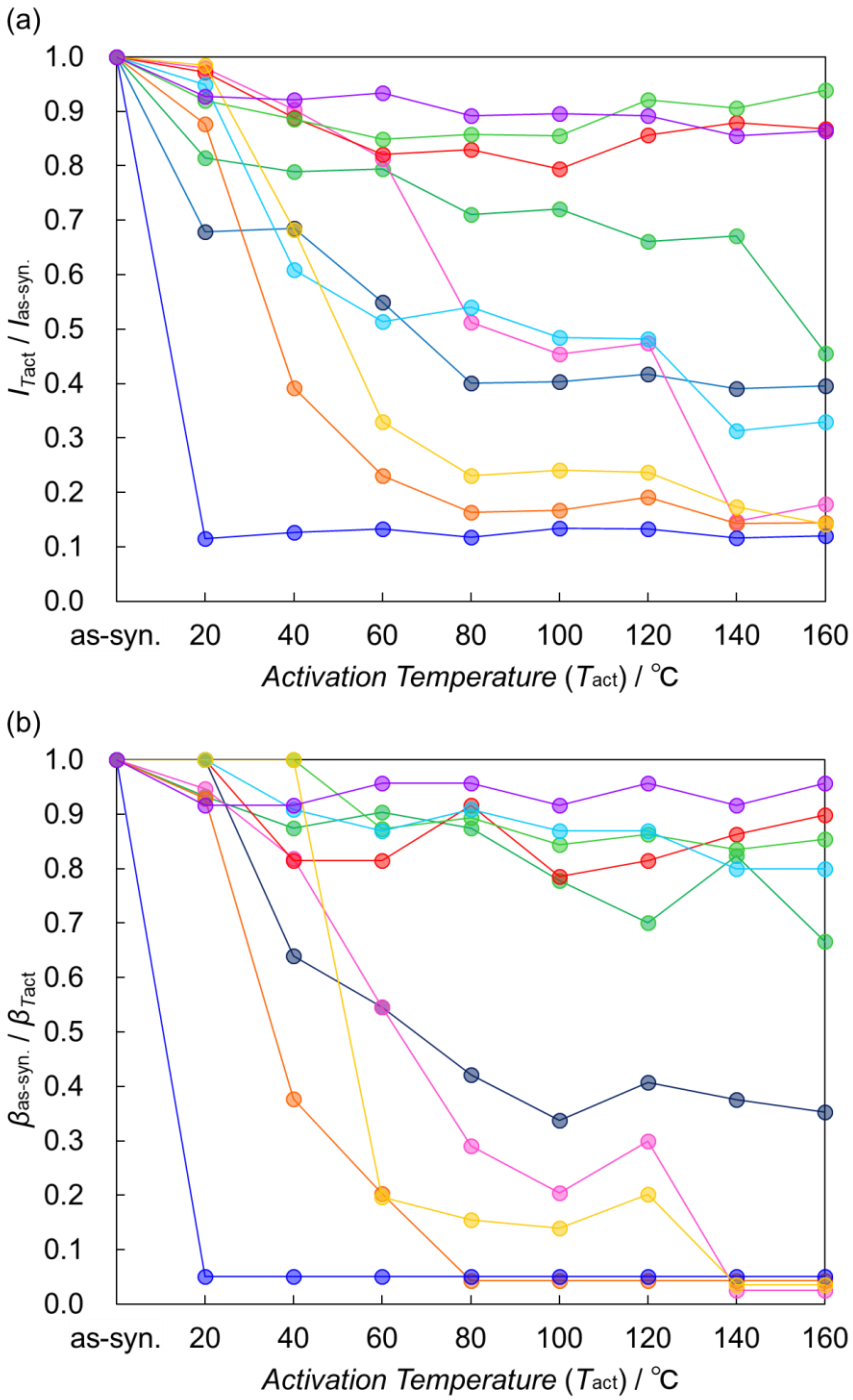

Figure 1-15. Relative values of intensity and full width at half maximum (FWHM) at (2 0 0) crystallographic plane calculated from PXRD results compared to those of the as-synthesized sample. (a) Relative peak intensity ($I_{Tact}/I_{as\text{-}syn}$). (b) Relative FWHM value ($\beta_{as\text{-}syn}/\beta_{Tact}$). Color code: $\{M^{II}{}_3[Cr^{III}(CN)_6]_2\}$ (**M$_3$Cr$_2$**; M = VO (dark blue), Cr (green), Mn (pink), Fe (orange), Co (red), Ni (light green), Cu (blue), Zn (light blue), and Cd (yellow)) series and $\{In^{III}[Cr^{III}(CN)_6]\}$ (**InCr**; purple) series.

Furthermore, as well as the PXRD measurement, FT-IR measurements in the ambient air at RT were performed for all the PBAs activated at each temperature (**Figure 1-16**–**Figure 1-25**). In the FT-IR spectra, while most of the PBA series at all the T_{act} exhibited almost no change, broadening of ν(C≡N) peaks was observed and a new peak conceivably assigned to δ(Cr–C≡N) mode gradually appeared around 575 cm^{-1} with T_{act} increasing in **Co_3Cr_2** and **Ni_3Cr_2** series, suggesting changes in the geometry of M^{2+} ion center form octahedral to another distorted preferable one such as tetrahedral and square planner, respectively (**Figure 1-19** and **Figure 1-20**). Their greatly high structural stability discussed from the PXRD measurements would support this prediction that geometry change occurred instead of framework decomposition. On the other hand, **Fe_3Cr_2** and **Cu_3Cr_2** series showed completely different behaviors from those of the abovementioned PBA series. In the case of **Fe_3Cr_2** series, the intensity of ν(C≡N) peaks at lower wavenumber than that of $K_3[Cr(CN)_6]$ increased over the T_{act} of 40℃ (**Figure 1-19**). Moreover, in a higher T_{act} range over 100℃, the peak intensity became strongly and the higher-wavenumber ν(C≡N) peak which was originally observed as a major peak in the as-synthesized sample almost vanished (**Figure 1-19**). In the case of **Cu_3Cr_2** series, similar behavior occurred over the decomposition temperatures of 20℃ and several unknown peaks newly appeared in a wavenumber range of 800–1400 cm^{-1} (**Figure 1-22**). From both results of PXRD and FT-IR measurements, **Fe_3Cr_2** and **Cu_3Cr_2** series conceivably showed cyano-bridge dissociations and a subsequent framework decomposition over 20 and 80℃, respectively.

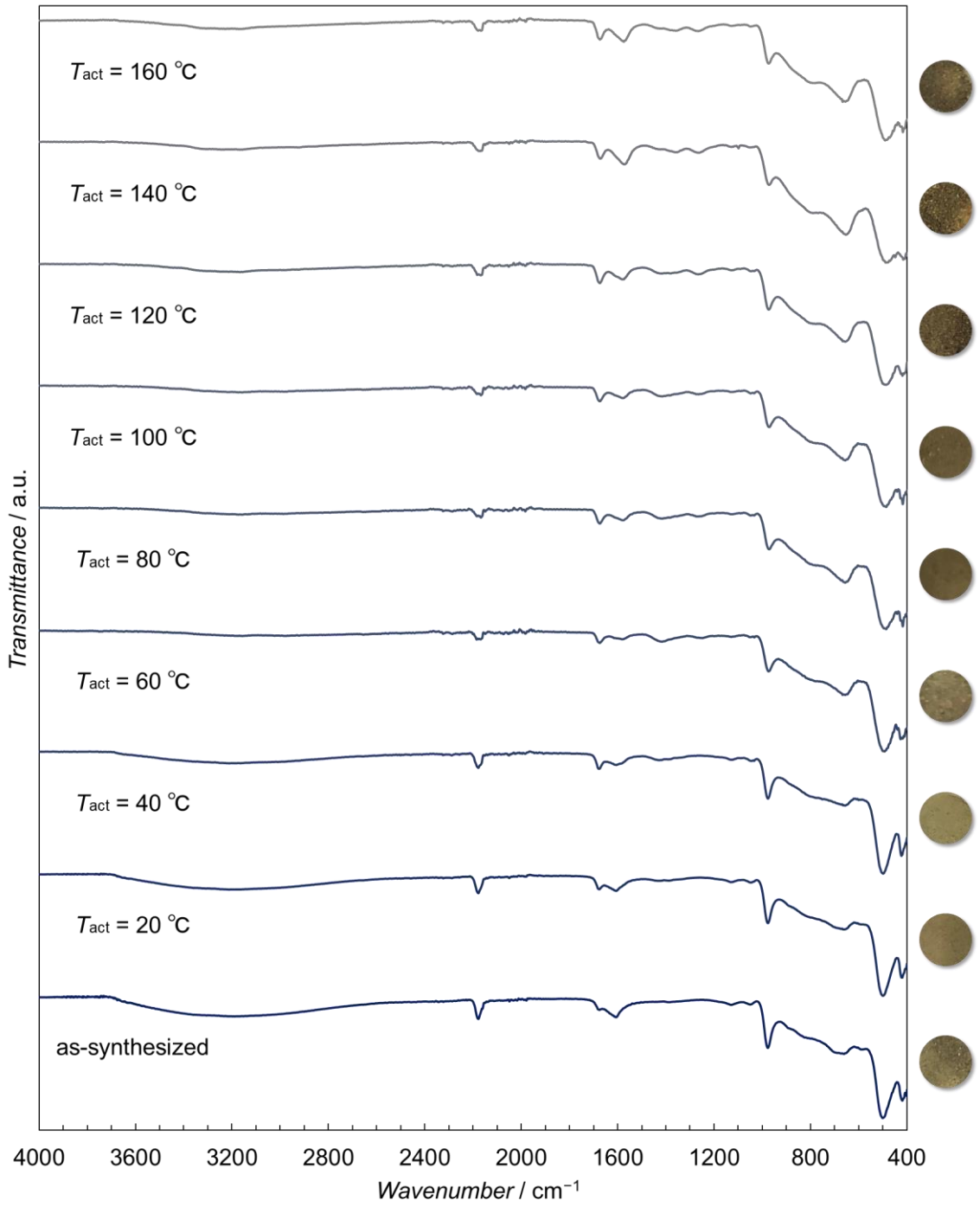

Figure 1-16. FT-IR spectra in the ambient air at RT and photographs of the as-synthesized sample $\{(V^{IV}O)_3[Cr(CN)_6]_2 \cdot nH_2O\}$ (**$(VO)_3Cr_2 \cdot nH_2O$**: dark blue) and its activated samples heated at different activation temperatures (T_{act}) of 20, 40, 60, 80, 100, 120, 140, and 160℃ (colors from dark blue to gray) under reduced pressure for 24 h. Resolution: 4 cm^{-1}.

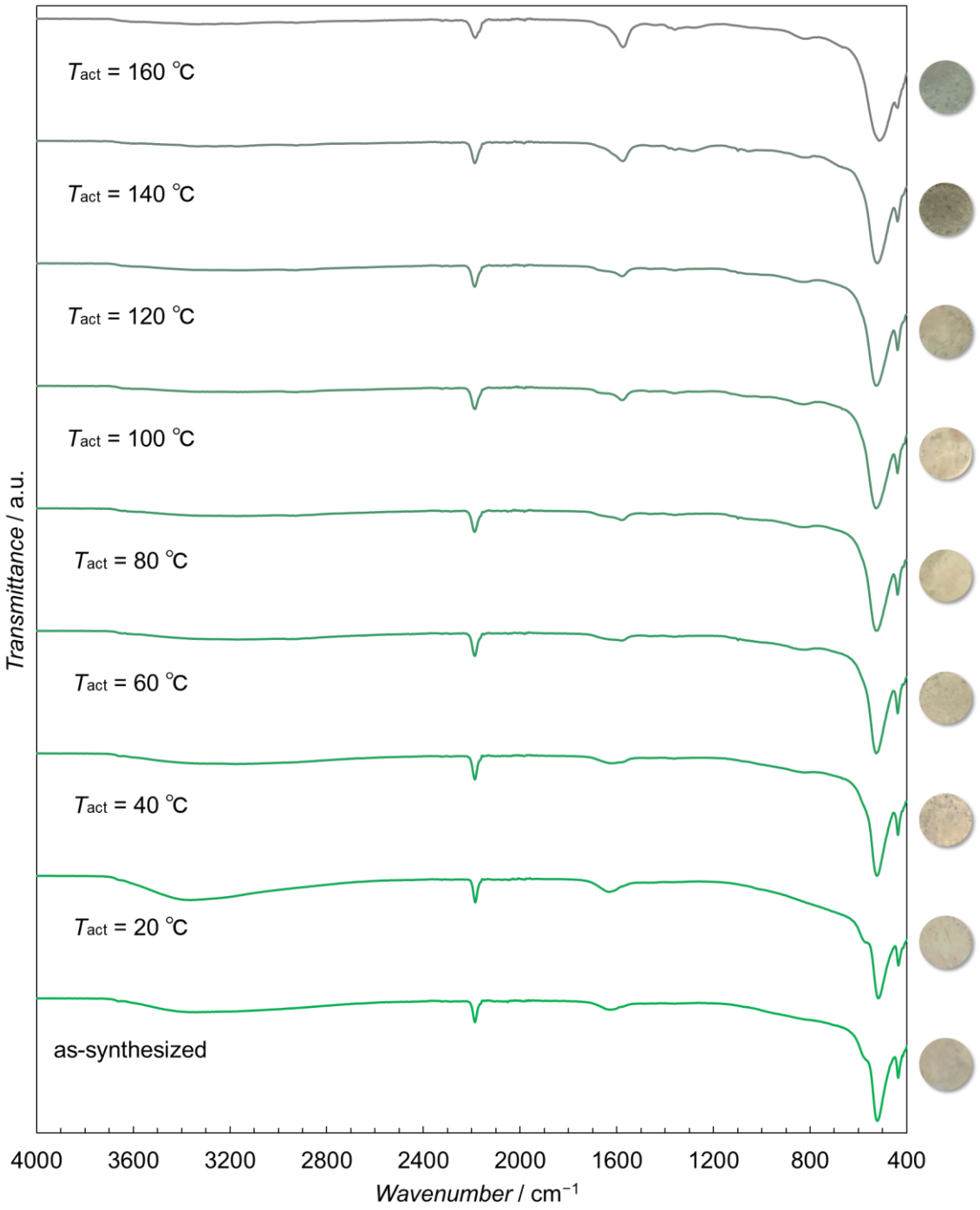

Figure 1-17. FT-IR spectra in the ambient air at RT and photographs of the as-synthesized sample $\{Cr_3[Cr(CN)_6]_2 \cdot nH_2O\}$ (**$Cr_3Cr_2 \cdot nH_2O$**: dark blue) and its activated samples heated at different activation temperatures (T_{act}) of 20, 40, 60, 80, 100, 120, 140, and 160°C (colors from green to gray) under reduced pressure for 24 h. Resolution: 4 cm^{-1}.

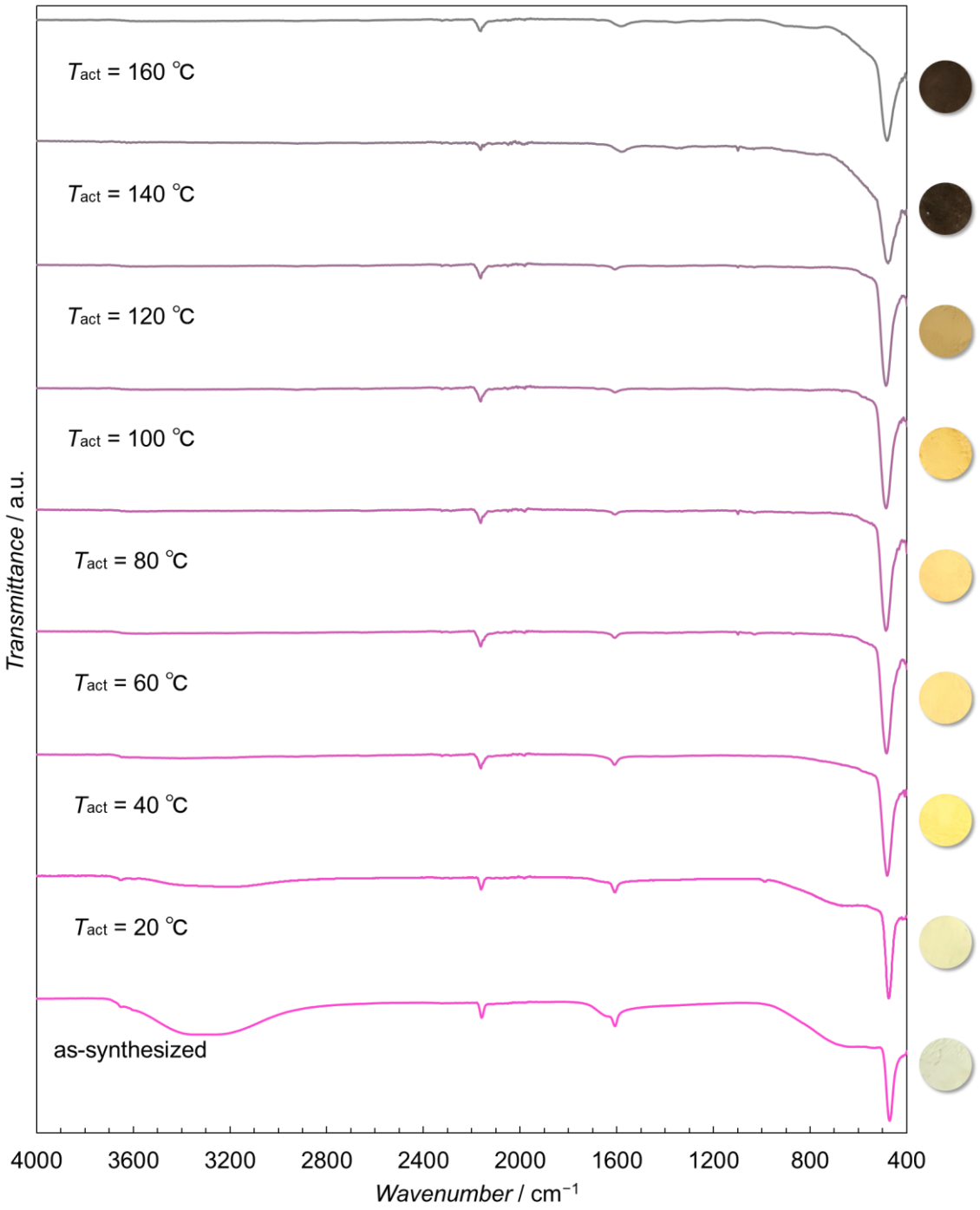

Figure 1-18. FT-IR spectra in the ambient air at RT and photographs of the as-synthesized sample $\{Mn_3[Cr(CN)_6]_2 \cdot nH_2O\}$ (**$Mn_3Cr_2 \cdot nH_2O$**: pink) and its activated samples heated at different activation temperatures (T_{act}) of 20, 40, 60, 80, 100, 120, 140, and 160℃ (colors from pink to gray) under reduced pressure for 24 h. Resolution: 4 cm^{-1}.

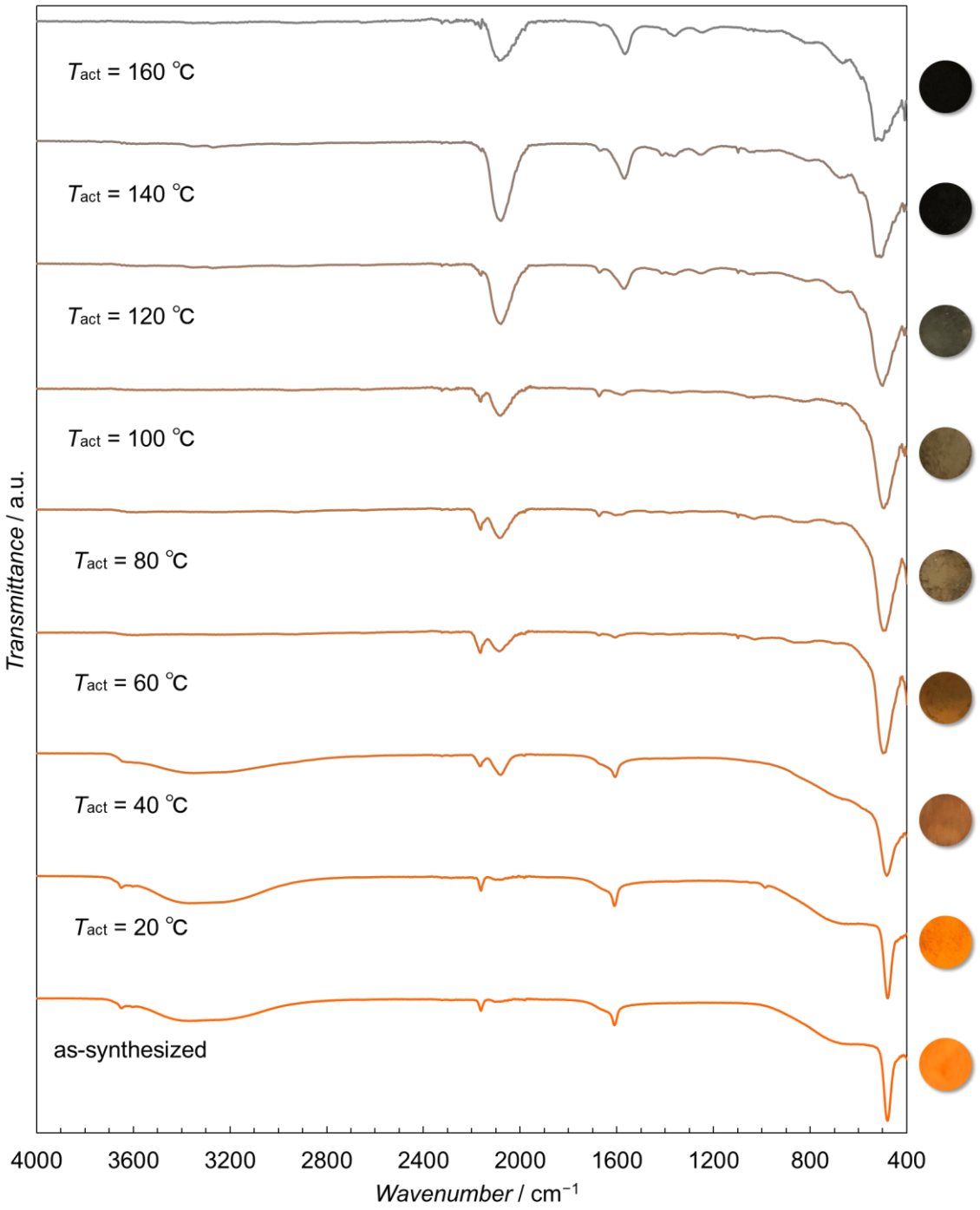

Figure 1-19. FT-IR spectra in the ambient air at RT and photographs of the as-synthesized sample $\{Fe_3[Cr(CN)_6]_2 \cdot nH_2O\}$ (**$Fe_3Cr_2 \cdot nH_2O$**: orange) and its activated samples heated at different activation temperatures (T_{act}) of 20, 40, 60, 80, 100, 120, 140, and 160℃ (colors from orange to gray) under reduced pressure for 24 h. Resolution: 4 cm^{-1}.

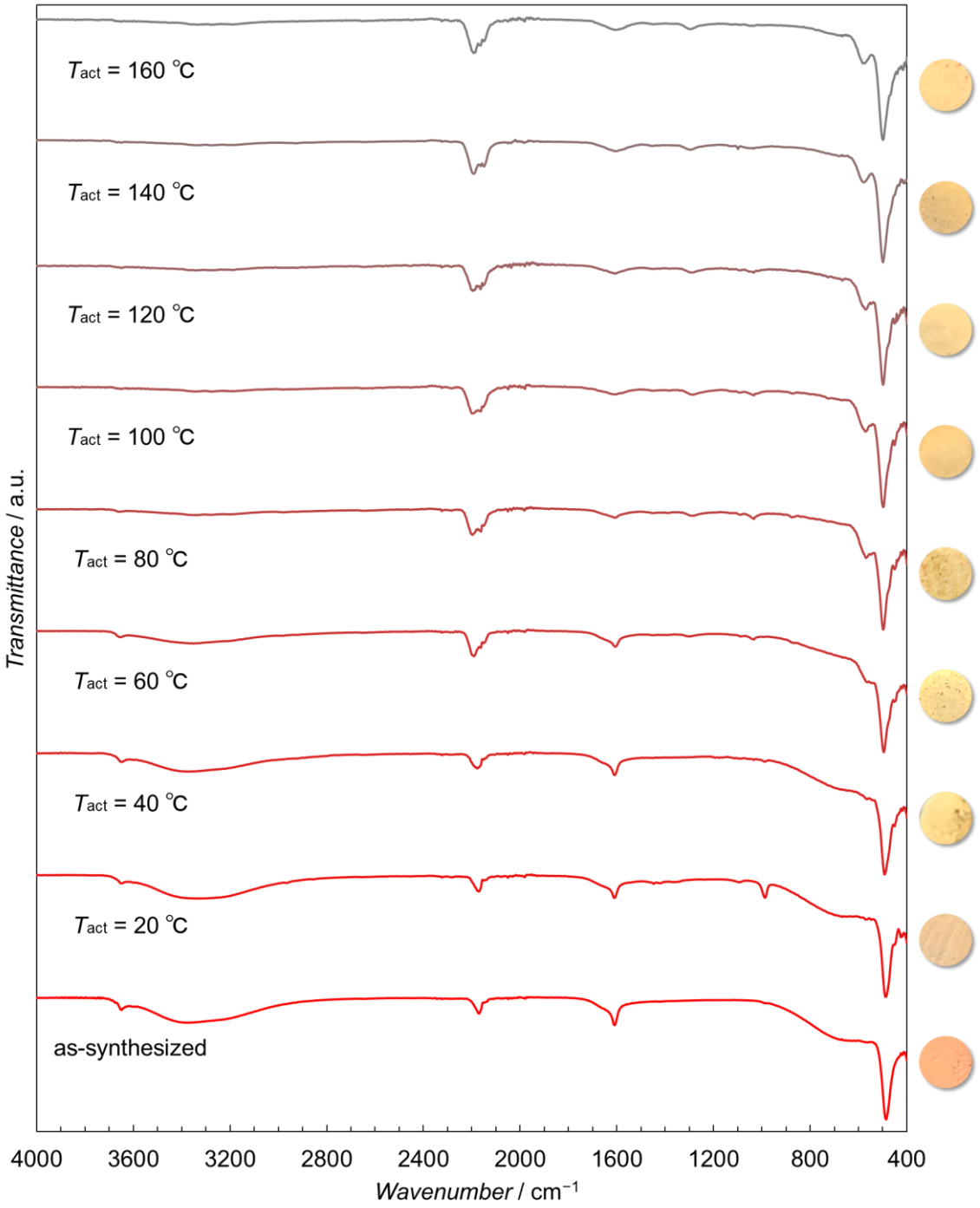

Figure 1-20. FT-IR spectra in the ambient air at RT and photographs of the as-synthesized sample $\{Co_3[Cr(CN)_6]_2 \cdot nH_2O\}$ (**$Co_3Cr_2 \cdot nH_2O$**: red) and its activated samples heated at different activation temperatures (T_{act}) of 20, 40, 60, 80, 100, 120, 140, and 160℃ (colors from red to gray) under reduced pressure for 24 h. Resolution: 4 cm^{-1}.

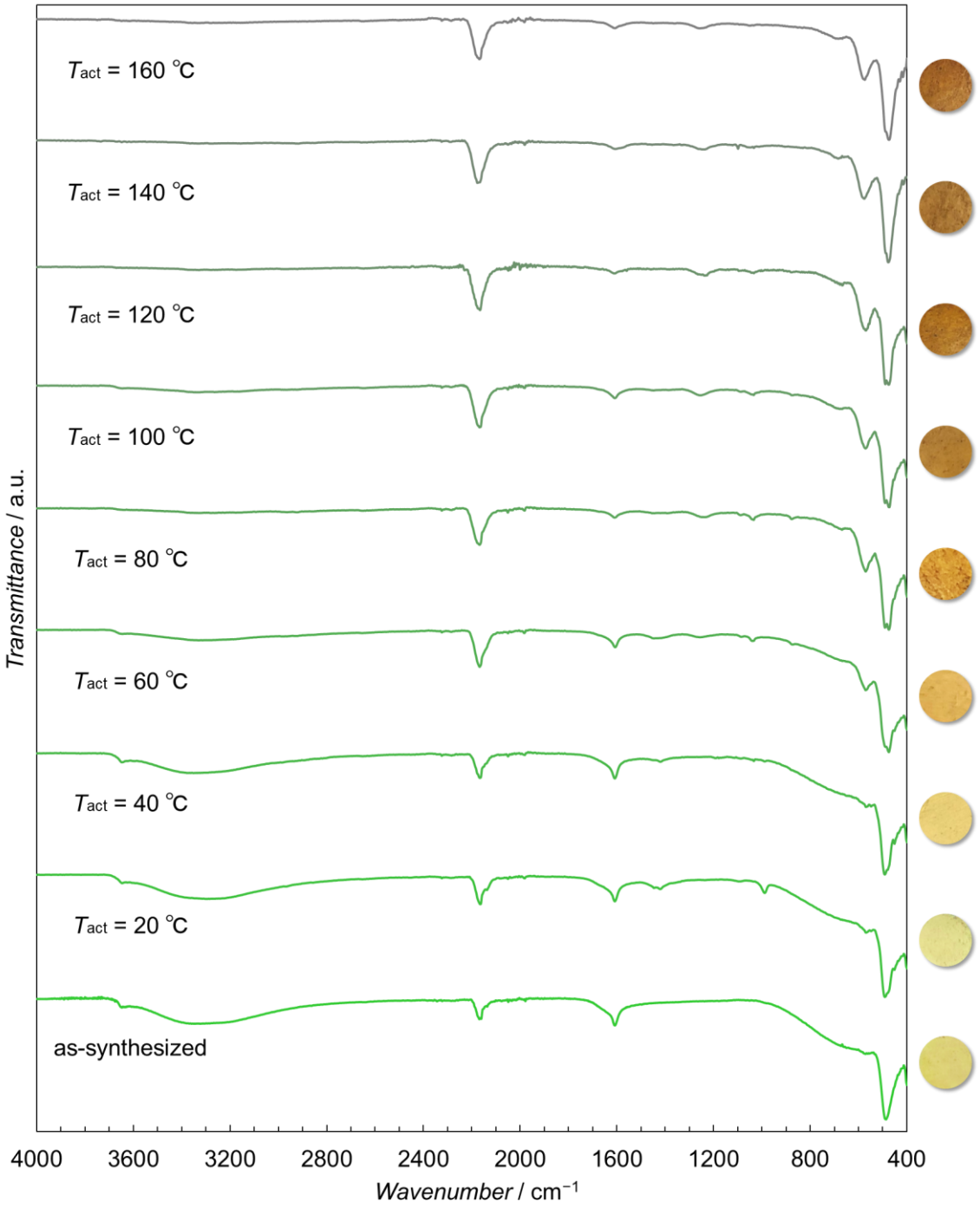

Figure 1-21. FT-IR spectra in the ambient air at RT and photographs of the as-synthesized sample $\{Ni_3[Cr(CN)_6]_2 \cdot nH_2O\}$ (**$Ni_3Cr_2 \cdot nH_2O$**: light green) and its activated samples heated at different activation temperatures (T_{act}) of 20, 40, 60, 80, 100, 120, 140, and 160°C (colors from light green to gray) under reduced pressure for 24 h. Resolution: 4 cm^{-1}.

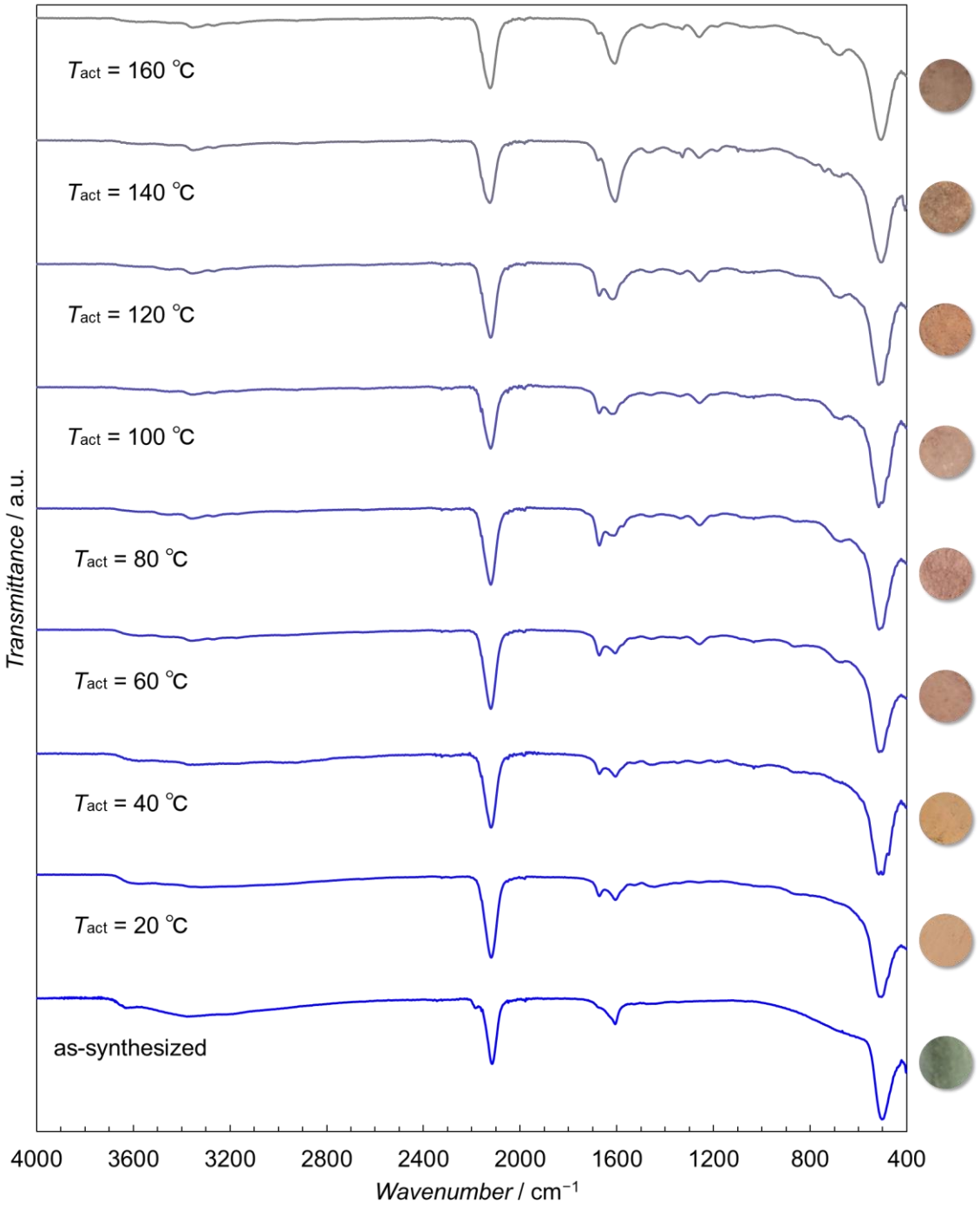

Figure 1-22. FT-IR spectra in the ambient air at RT and photographs of the as-synthesized sample $\{Cu_3[Cr(CN)_6]_2 \cdot nH_2O\}$ (**$Cu_3Cr_2 \cdot nH_2O$**: blue) and its activated samples heated at different activation temperatures (T_{act}) of 20, 40, 60, 80, 100, 120, 140, and 160℃ (colors from blue to gray) under reduced pressure for 24 h. Resolution: 4 cm^{-1}.

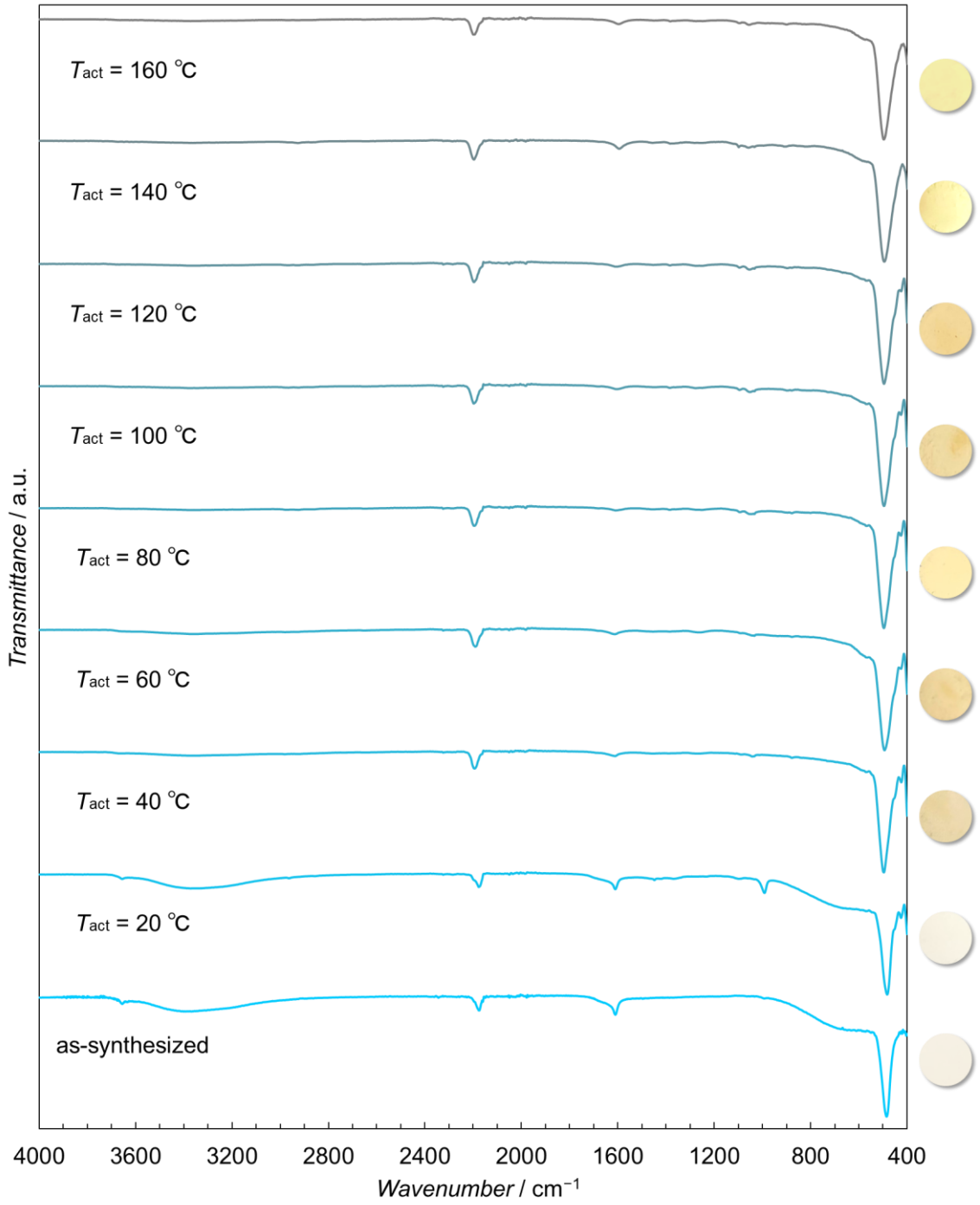

Figure 1-23. FT-IR spectra in the ambient air at RT and photographs of the as-synthesized sample $\{Zn_3[Cr(CN)_6]_2 \cdot nH_2O\}$ (**$Zn_3Cr_2 \cdot nH_2O$**: light blue) and its activated samples heated at different activation temperatures (T_{act}) of 20, 40, 60, 80, 100, 120, 140, and 160°C (colors from light blue to gray) under reduced pressure for 24 h. Resolution: 4 cm^{-1}.

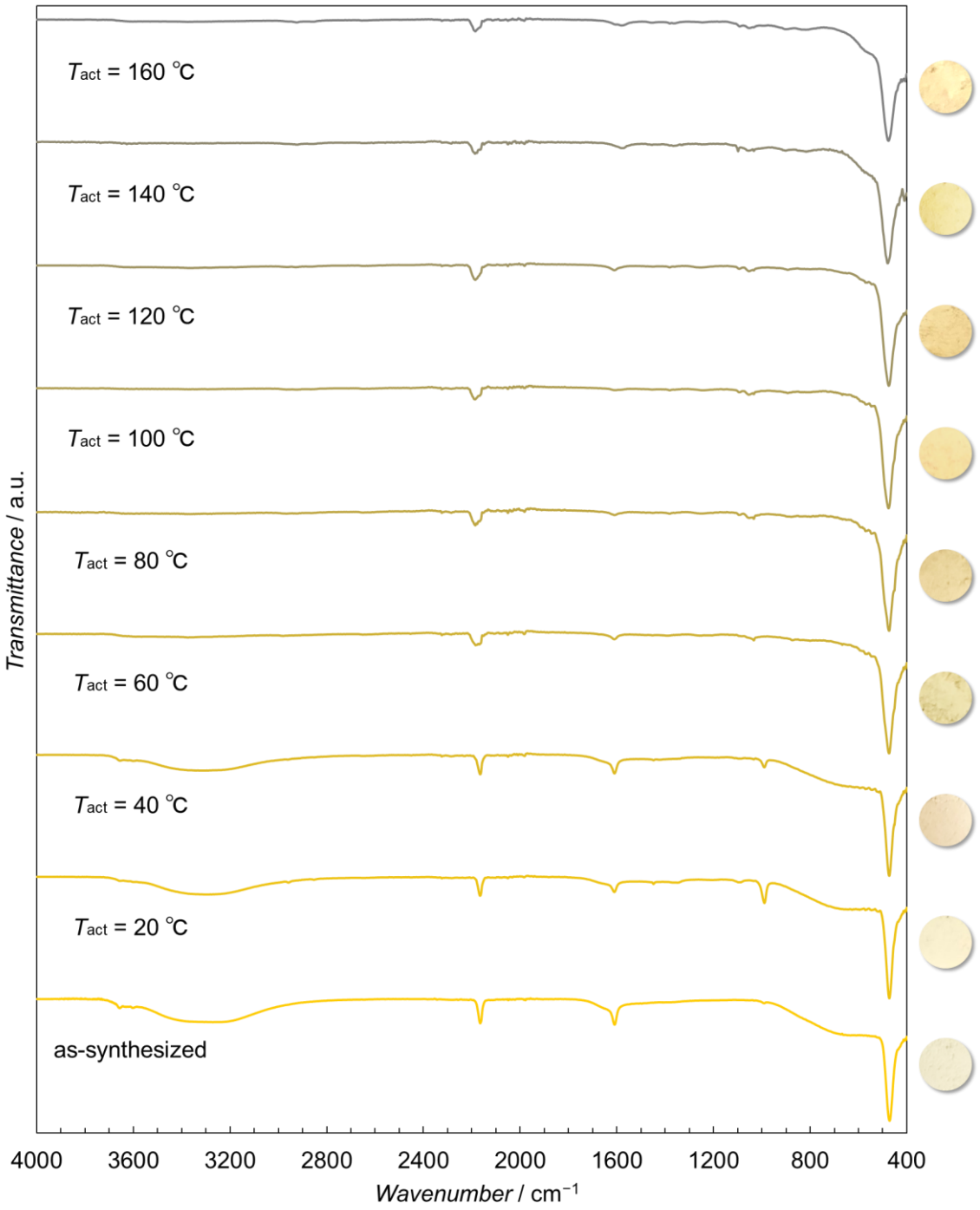

Figure 1-24. FT-IR spectra in the ambient air at RT and photographs of the as-synthesized sample $\{Cd_3[Cr(CN)_6]_2 \cdot nH_2O\}$ (**$Cd_3Cr_2 \cdot nH_2O$**: yellow) and its activated samples heated at different activation temperatures (T_{act}) of 20, 40, 60, 80, 100, 120, 140, and 160℃ (colors from yellow to gray) under reduced pressure for 24 h. Resolution: 4 cm^{-1}.

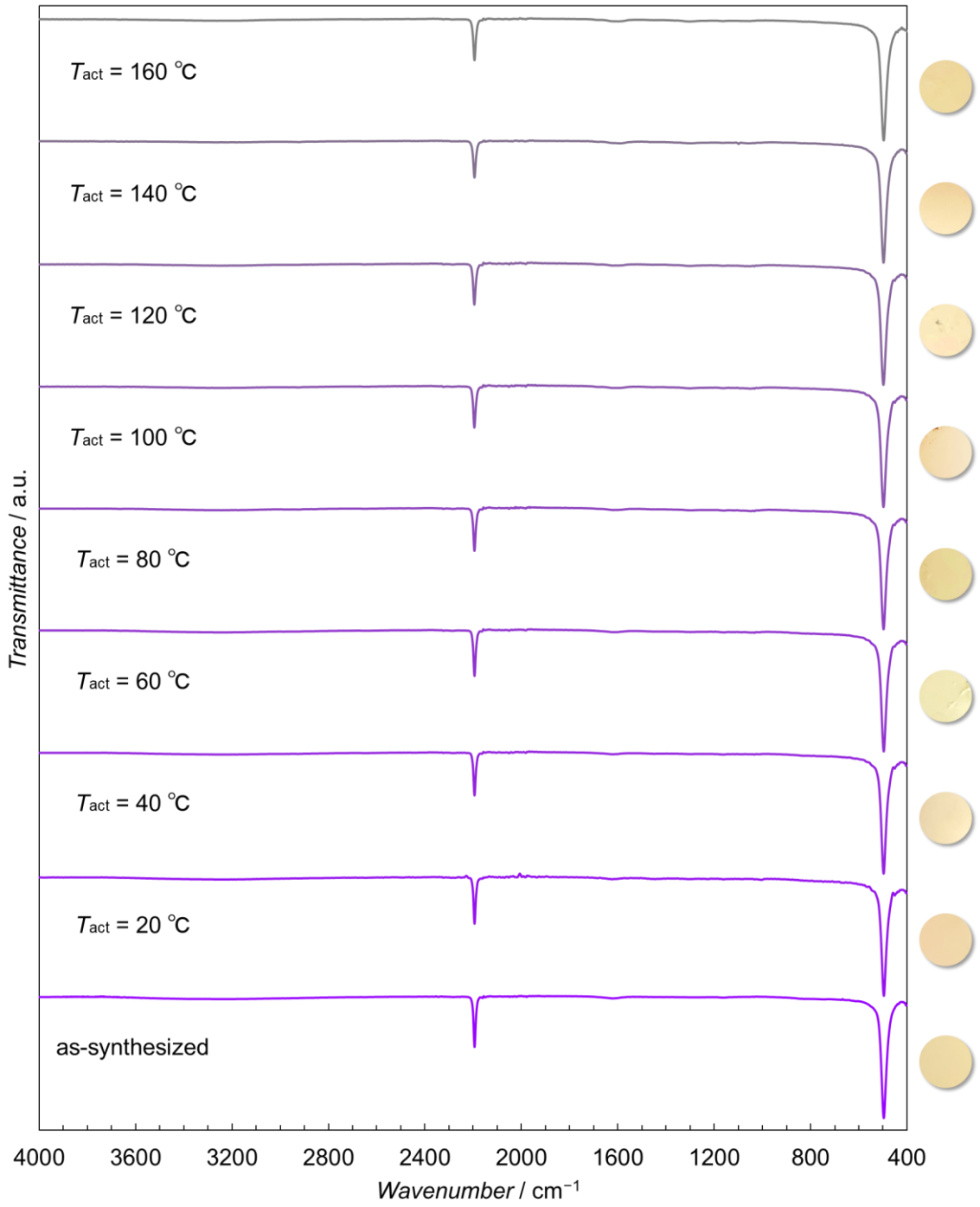

Figure 1-25. FT-IR spectra in the ambient air at RT and photographs of the as-synthesized sample {In[Cr(CN)$_6$]·nH$_2$O} (**InCr·nH$_2$O**: purple) and its activated samples heated at different activation temperatures (T_{act}) of 20, 40, 60, 80, 100, 120, 140, and 160℃ (colors from purple to gray) under reduced pressure for 24 h. Resolution: 4 cm^{-1}.

In addition to the thermal stability discussed above, the structural stability was evaluated as well using the samples which have been exposed to the air for 1 month at 20℃. Through the exposure process, **$M_3Cr_2 \cdot nH_2O$** (M = VO, Cr, Mn, Co, Ni, Zn, and Cd) and **$InCr \cdot nH_2O$** showed no change in the FT-IR spectra (**Figure 1-26**), and no remarkable decrease in the intensity and no remarkable change in the FWHM value of the PXRD peaks (**Figure 1-27**). On the other hand, the behaviors of **$Fe_3Cr_2 \cdot nH_2O$** and **$Cu_3Cr_2 \cdot nH_2O$**, which were the most and second most unstable thermally, differed from those of the other PBAs. In the case of **$Fe_3Cr_2 \cdot nH_2O$**, the transmittance of the lower-wavenumber ν(C≡N) mode at 2102 cm^{-1} was significantly enhanced after the exposure, whereas the higher-wavenumber ν(C≡N) mode at 2162 cm^{-1} showed no change in the transmittance in the FT-IR spectra (**Figure 1-26**). Regarding the PXRD measurement, **$Fe_3Cr_2 \cdot nH_2O$** maintained the pattern of typical PBAs with decrease in intensity to the same extent as some of the other PBAs; however, the peak of (2 0 0) plane was shifted from 16.67° to 16.73°, indicating a framework shrinkage from the lattice parameter from 10.64 Å to 10.60 Å (**Figure 1-27**). This shrinkage was likely derived from the linkage isomerization as mentioned before. In the case of **$Cu_3Cr_2 \cdot nH_2O$**, the transmittance of lower-wavenumber ν(C≡N) mode at 2116 cm^{-1} was slightly enhanced after the exposure, whereas the higher-wavenumber ν(C≡N) mode at 2185 cm^{-1} vanished completely in the FT-IR spectra (**Figure 1-26**). The PXRD pattern of **$Cu_3Cr_2 \cdot nH_2O$** was completely changed to an amorphous phase (**Figure 1-27**). The tendencies observed in **$Fe_3Cr_2 \cdot nH_2O$** and **$Cu_3Cr_2 \cdot nH_2O$** were quite similar to those observed in the evaluation of thermal stability. There was no relationship observed between the structural stability and the crystallite size, suggesting that the stability is strongly related to the chemical components instead of the crystallinity (**Table 1-4**).

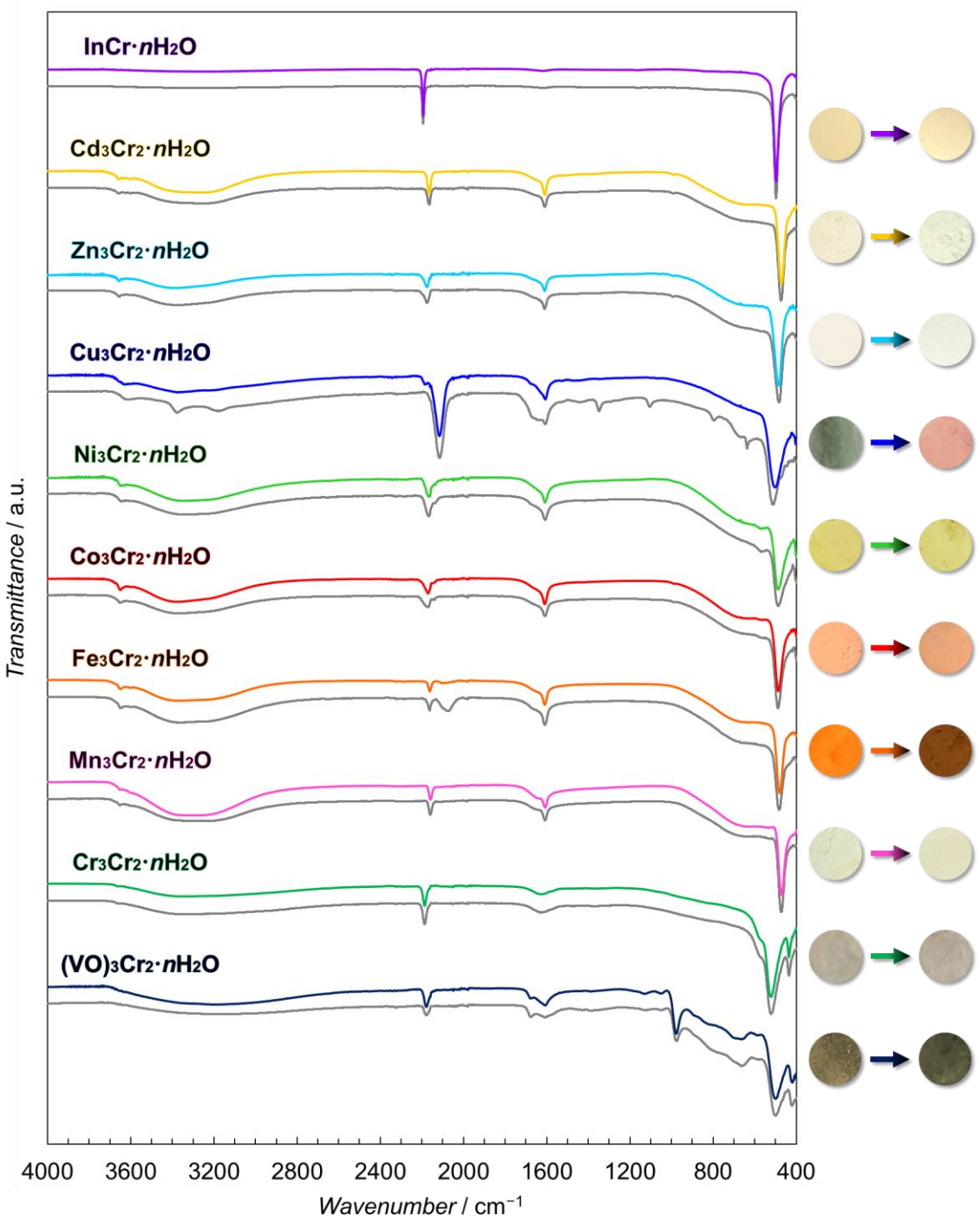

Figure 1-26. Normalized FT-IR spectra and photographs in the ambient air at RT of the as-synthesized PBAs $\{M^{II}_3[Cr^{III}(CN)_6]_2 \cdot nH_2O\}$ (**$M_3Cr_2 \cdot nH_2O$**; M = VO (dark blue), Cr (green), Mn (pink), Fe (orange), Co (red), Ni (light green), Cu (blue), Zn (light blue), and Cd (yellow)), $\{In^{III}[Cr^{III}(CN)_6] \cdot nH_2O\}$ (**$InCr \cdot nH_2O$**; purple), and those exposed to the air for 1 month (gray). The spectra were normalized by each peak with the highest transmittance. Resolution: 4 cm^{-1}.

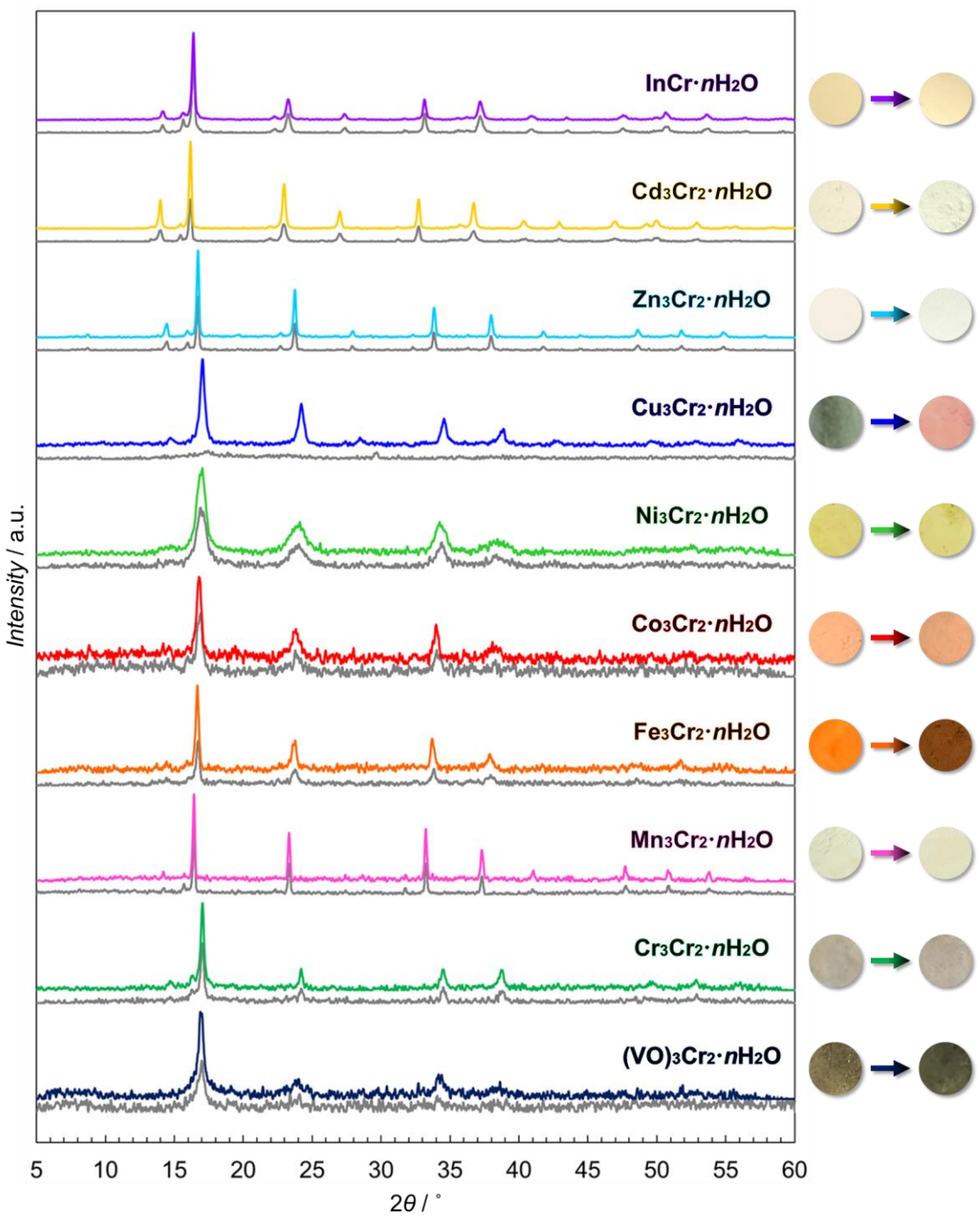

Figure 1-27. Normalized PXRD patterns and photographs in the ambient air at RT of the as-synthesized PBAs $\{M^{II}_3[Cr^{III}(CN)_6]_2 \cdot nH_2O\}$ (**$M_3Cr_2 \cdot nH_2O$**; M = VO (dark blue), Cr (green), Mn (pink), Fe (orange), Co (red), Ni (light green), Cu (blue), Zn (light blue), and Cd (yellow)), $\{In^{III}[Cr^{III}(CN)_6] \cdot nH_2O\}$ (**$InCr \cdot nH_2O$**; purple), and those exposed to the air for 1 month (gray). The patterns were normalized by each peak with the strongest intensity of the as-synthesized samples. Scan rate: 1° min^{-1}, data collecting step: 0.02°.

For the N_2 and H_2 adsorption and desorption measurements, a temperature of 60 °C was selected as the optimized T_{act} because all the PBAs except **Cu$_3$Cr$_2$** series keep the 3-D structure by the activation at this temperature. N_2 and H_2 adsorption and desorption measurements of all the activated PBAs were performed at 77 K until 105 kPa.

In the N_2 adsorption process, Brunauer-Emmett-Teller surface area (SA_{BET}) of the activated PBAs was calculated from the obtained isotherm, where the parameters of v, v_m, P_0, P, c, N_A, V, s, and a denote adsorption amount, monolayer adsorption amount, saturation pressure, measurement pressure, condensation coefficient, Avogadro's number, adsorbate volume, adsorption cross-section of the adsorbate, and adsorbent mass, respectively (**Equation 1-3**, **Figure 1-28** and **Table 1-6**).[17a] As the s value of N_2 at 77 K, 0.162 nm^2 was used. All the PBAs showed type-I or type-II behavior in the International Union of Pure and Applied Chemistry (IUPAC) classification with various adsorption amounts, indicating existence of micropores.[16] The observed type-II behavior with a dramatic increase in adsorption amount at higher pressures is likely associated with delayed capillary condensation within aggregates of nanocrystals, which is supported by the relatively small crystallite size (L) calculated from the PXRD patterns (**Table 1-4**).[17b] Among them, **Mn$_3$Cr$_2$**, **Fe$_3$Cr$_2$**, **Co$_3$Cr$_2$**, **Ni$_3$Cr$_2$**, **Zn$_3$Cr$_2$**, and **Cd$_3$Cr$_2$** series showed large SA_{BET} values in a range of 415–684 m^2 g^{-1} which is a comparable value to the reported values of **Ma$_3$Co$_2$** series (**Figure 1-28** and **Table 1-6**).[6a,b,d,e,k] **(VO)$_3$Cr$_2$**, **Cr$_3$Cr$_2$**, **Cu$_3$Cr$_2$**, and **InCr** series, however, had less and no adsorption ability (**Figure 1-28** and **Table 1-6**). None of the prepared PBAs showed a PXRD pattern which agreed with that of a two-fold interpenetrated PBA $Fe^{II}[Mn^{IV}(CN)_6]$ which has almost no void space.[18] Therefore, the observed poor adsorption ability is assumed because of slightly distorted framework structure and less number of coordination unsaturated metal sites because of the V=O bonds for **(VO)$_3$Cr$_2$**, no coordination unsaturated metal sites because of H_2O molecules coordinating to the Cr^{2+} ion centers for **Cr$_3$Cr$_2$**, exceedingly weak stability upon the activation for **Cu$_3$Cr$_2$**, and non-defective structure with extremely narrow pore window for **InCr**.

$$\frac{1}{v\{(P_0/P)-1\}} = \frac{c-1}{v_m c}\left(\frac{P}{P_0}\right) + \frac{1}{v_m c}$$

$$SA_{BET} = \frac{v_m N_A s/V}{a}$$

Equation 1-3. Equations of Brunauer-Emmett-Teller theory.[17a]

H_2 adsorption and desorption measurements were performed at 77 K until 105 kPa as well as N_2 isotherm (**Figure 1-29**). Each obtained H_2 adsorption isotherm was fitted by Langmuir-Freundlich equation as a function of adsorption amount (n_P) versus pressure (P) to obtain the expected adsorption amount at saturation (n_{max}) at 77 K using Langmuir-Freundlich constants of B and t (**Equation 1-4**, **Figure 1-29** and **Table 1-6**).[17b] The Langmuir-Freundlich equation provides more accurate predictions over a larger pressure range and at saturation than other fittings. In the cases of **Mn_3Cr_2**, **Fe_3Cr_2**, **Co_3Cr_2**, **Ni_3Cr_2**, **Zn_3Cr_2**, and **Cd_3Cr_2** which showed a relatively large SA_{BET}, the actual adsorption amounts at 100 kPa and the expected amounts were in a weight percentage range of 1.06–1.42 and 1.47–2.10 wt%, respectively (**Figure 1-29** and **Table 1-6**). This H_2 adsorption amount of $[Cr^{III}(CN)_6]^{3-}$-based PBAs are comparable to the reported values of other defective PBAs, **Ma_3Mb_2** (Mb = Fe, Co, Rh, and Ir) series (**Table 1-6**).[6] This result provides the potential of $[Cr^{III}(CN)_6]^{3-}$-based PBAs as absorbents for gas molecules and functional materials using property interlocked with the adsorption property.

$$\frac{n_P}{n_{\max}} = \frac{B * P^{(1/t)}}{1 + B * P^{(1/t)}}$$

Equation 1-4. Langmuir-Freundlich equation.[17b]

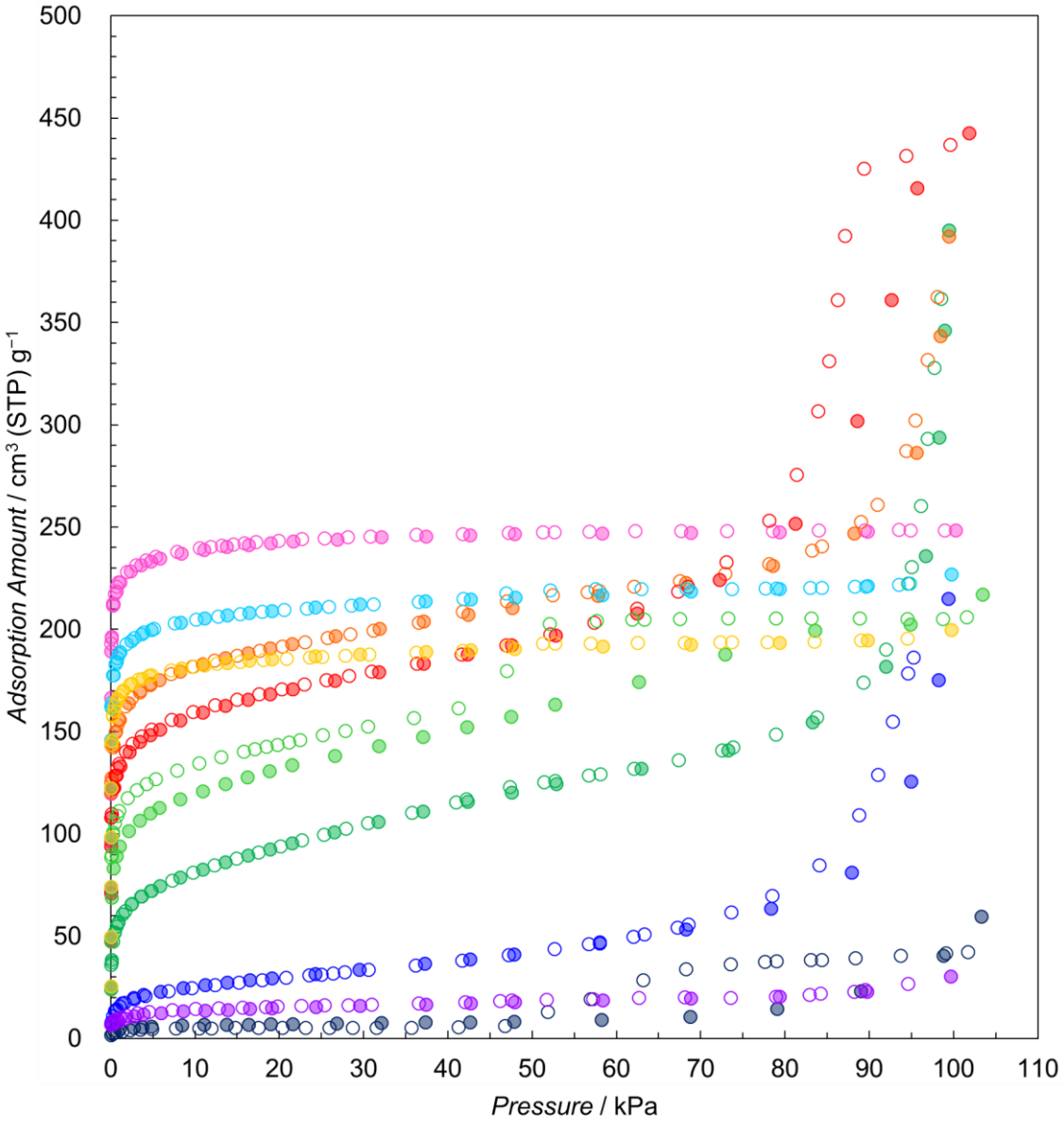

Figure 1-28. (●) Adsorption process and (○) desorption process in N_2 isotherms at 77 K of the activated PBAs $\{M^{II}_3[Cr^{III}(CN)_6]_2\}$ (**$M_3Cr_2{\cdot}nH_2O$**; M = VO (dark blue), Cr (green), Mn (pink), Fe (orange), Co (red), Ni (light green), Cu (blue), Zn (light blue), and Cd (yellow)) and $\{In^{III}[Cr^{III}(CN)_6]\}$ (**$InCr{\cdot}nH_2O$**; purple) heated at 60°C under reduced pressure for 24 h.

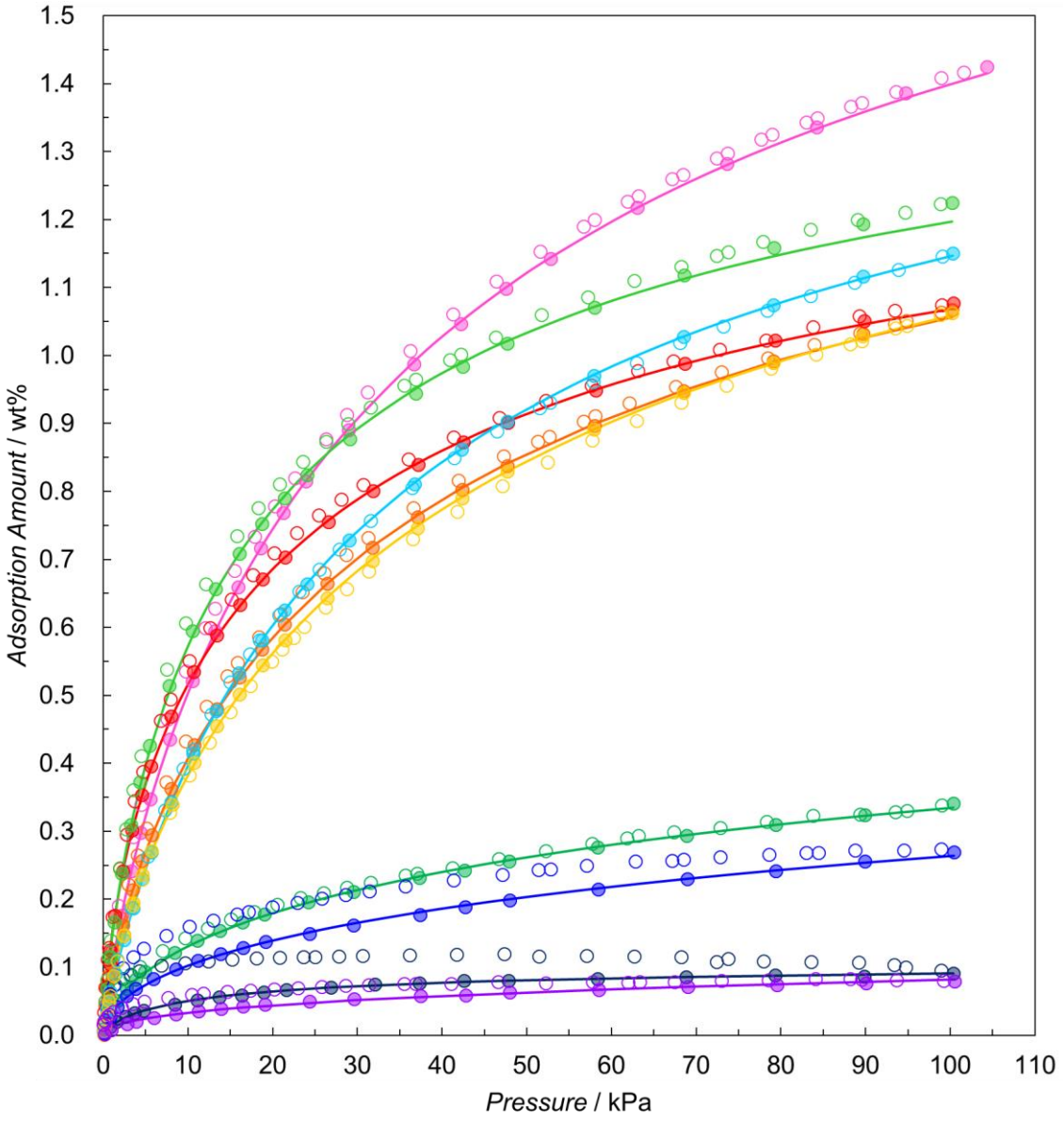

Figure 1-29. (●) Adsorption process, (○) desorption process, and (–) Langmuir-Freundlich fitting for the adsorption process in H_2 isotherms at 77 K of the activated PBAs $\{M^{II}_3[Cr^{III}(CN)_6]_2\}$ (**$M_3Cr_2\cdot nH_2O$**; M = VO (dark blue), Cr (green), Mn (pink), Fe (orange), Co (red), Ni (light green), Cu (blue), Zn (light blue), and Cd (yellow)) and $\{In^{III}[Cr^{III}(CN)_6]\}$ (**$InCr\cdot nH_2O$**; purple) heated at 60°C under reduced pressure for 24 h.

Table 1-6. Brunauer-Emmett-Teller surface area (SA_{BET}), H_2 adsorption amount at 77 K and Langmuir-Freundlich fitting parameters of the activated PBAs $\{M^{II}_3[Cr^{III}(CN)_6]_2\}$ (**$M_3Cr_2 \cdot nH_2O$**; M = VO, Cr, Mn, Fe, Co, Ni, Cu, Zn, and Cd) and $\{In^{III}[Cr^{III}(CN)_6]\}$ (**$InCr \cdot nH_2O$**) heated at 60°C under reduced pressure for 24 h.

	SA_{BET} / $m^2\ g^{-1}$	*H_2 Adsorption Amount* at 77 K / wt%		*Langmuir-Freundlich constants*	
		n_{100kPa}	n_{max}	*B*	*t*
$(VO)_3Cr_2$	19	0.09	0.11	0.15	1.35
Cr_3Cr_2	315	0.34	0.78	0.05	1.74
Mn_3Cr_2	684	1.42	2.10	0.05	1.25
Fe_3Cr_2	571	1.07	1.61	0.06	1.33
Co_3Cr_2	514	1.08	1.47	0.11	1.45
Ni_3Cr_2	415	1.22	1.54	0.10	1.30
Cu_3Cr_2	101	0.27	0.82	0.04	1.92
Zn_3Cr_2	590	1.15	1.63	0.04	1.15
Cd_3Cr_2	532	1.06	1.64	0.05	1.29
InCr	47	0.08	0.56	0.02	2.29

To the contrary, no H_2 absorption was surprisingly confirmed in dehydrated samples of other several 3-D PCPs based on $[Cr^{III}(CN)_6]^{3-}$ building units including polydentate amines as co-ligands coordinating to Ma^{2+} ions, $[Mn^{II}(en)]_3[Cr^{III}(CN)_6]_2$ (**Mn_3Cr_2-en**; en = ethylenediamine),[19a,b,d] $[Mn^{II}(glya)]_3[Cr^{III}(CN)_6]_2$ (**Mn_3Cr_2-glya**; glya = glycinamide),[19b] $[Ni(dipn)]_3[Cr^{III}(CN)_6]_2$ (**Ni_3Cr_2-dipn**; dipn = dipropylenetriamine),[19c,d] and $[Mn^{II}(NNdmenH)][Cr^{III}(CN)_6]$ (**MnCr-NNdmenH**; NNdmen = *N*,*N*-dimethylethylenediamine),[19e] indicating that the center-faced defective structure of PBAs is crucial for H_2 uptake (**Figure 1-30**).

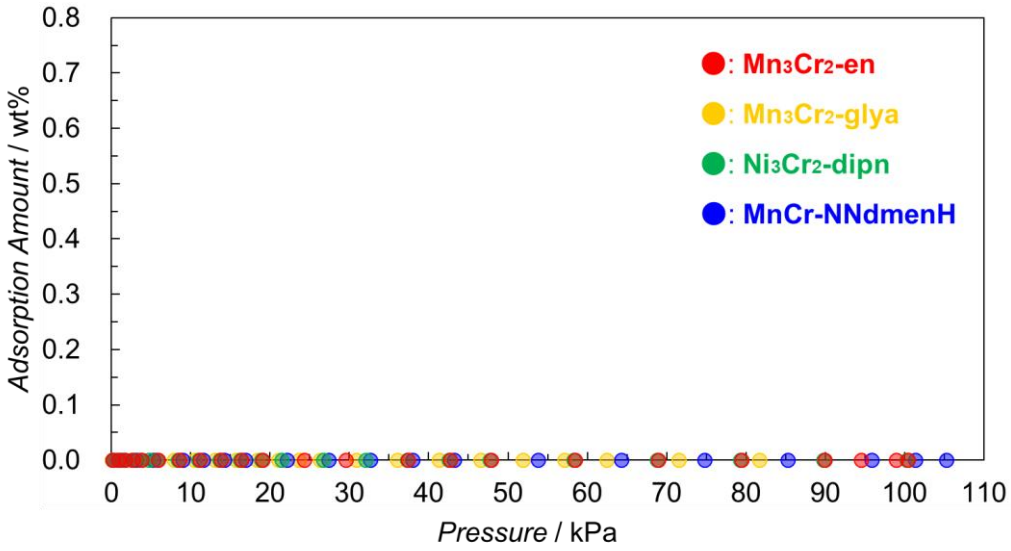

Figure 1-30. H_2 adsorption isomers at 77 K of $[Mn^{II}(en)]_3[Cr^{III}(CN)_6]_2$ (red: **Mn_3Cr_2-en**; en = ethylenediamine), $[Mn^{II}(glya)]_3[Cr^{III}(CN)_6]_2$ (yellow: **Mn_3Cr_2-glya**; glya = glycinamide), $[Ni(dipn)]_3[Cr^{III}(CN)_6]_2$ (green: **Ni_3Cr_2-dipn**; dipn = dipropylenetriamine), and $[Mn^{II}(NNdmenH)][Cr^{III}(CN)_6]$ (blue: **MnCr-NNdmenH**; NNdmen = *N*,*N*-dimethyl-ethylenediamine).

Conclusions

In summary, $[Cr^{III}(CN)_6]^{3-}$-based PBAs $\{M^{II}_3[Cr^{III}(CN)_6]_2 \cdot nH_2O\}$ (**$M_3Cr_2 \cdot nH_2O$**; M = VO, Cr, Mn, Fe, Co, Ni, Cu, Zn, and Cd) and $\{In^{III}[Cr^{III}(CN)_6] \cdot nH_2O\}$ (**$InCr \cdot nH_2O$**) were systematically synthesized and characterized by several physical analyses. The structural stability of the PBAs was evaluated by PXRD and FT-IR measurements using the samples activated at different temperatures (T_{act}) under a dynamic vacuum, where the order of stability depending on the metal canter (M) was In > (Co, Ni) > Cr > Zn > VO > Mn > Cd > Fe > Cu. After activation at the optimized T_{act} of 60℃ under reduced pressure for 24 h, **M_3Cr_2** (M = Mn, Fe, Co, Ni, Cu, Zn, and Cd) series showed a large Brunauer-Emmett-Teller surface area (SA_{BET}) of 415–684 $m^2\ g^{-1}$ and H_2 adsorption property with an adsorption amount of 1.06–1.42 wt% at 100 kPa and liquid N_2 temperature of 77 K, whereas **M_3Cr_2** (M = VO, Cr, and Cu) and **InCr** series showed less adsorption ability because of the less accessible metal sites and framework stability. These results suggested the potential of several defective $[Cr(CN)_6]^{3-}$-based PBAs as adsorbents for physical and chemical properties combined with the gas adsorption property.

References

1. (a) A. Ludi, H. U. Guedel, M. Ruegg, *Inorg. Chem.*, **1970**, *9* (10), 2224–2227.; (b) H. U. Güdel, *Acta Chem. Scand.*, **1972**, *26*, 2169–2176.; (c) H. U. Güdel, H. Stucki, A. Ludi, *Inorg. Chim. Acta*, **1973**, *7*, 121–124.; (d) H. J. Buser, D. Schwarzenbach, W. Petter, A. Ludi, *Inorg. Chem.*, **1977**, *16* (11), 2704–2710.; (e) G. W. Beall, W. O. Milligan, J. Korp, I. Bernal, *Inorg. Chem.*, **1977**, *16* (11), 2715–2718.; (f) G. W. Beall, W. O. Milligan, J. A. Petrich, B. I. Swanson, *Inorg. Chem.*, **1978**, *17* (11), 2978–2981.; (g) D. F. Mullica, W. O. Milligan, G. W. Beall, W. L. Reeves, *Acta Cryst. B*, **1978**, *34* (12), 3558–3561.; (h) D. F. Mullica, J. D. Oliver, W. O. Milligan, F. W. Hills, *Inorg. Nucl. Chem. Lett.*, **1979**, *15* (9–10), 361–365.; (i) F. Herren, P. Fischer, A. Ludi, W. Haelg, *Inorg. Chem.*, **1980**, *19* (4), 956–959.; (j) D. F. Mullica, J. T. Zielke, E. L. Sappenfield, *J. Solid State Chem.*, **1994**, *112* (1), 92–95.; (k) A. Ratuszna, S. Juszczyka, G. Małecki, *Powder Diffr.*, **1995**, *10* (4), 300–305.; (l) D. F. Mullica, P. A. B. Colot, J. A. Kautz, R. J. Smith, E. L. Sappenfield, *J. Solid State Chem.*, **1997**, *129* (1), 17–21.; (m) D. F. Mullica, F. H. Alvarez, J. A. Kautz, E. L. Sappenfield, *J. Solid State Chem.*, **1998**, *140* (1), 140–144.; (n) G. Małecki, A. Ratuszna, *Powder Diffr.*, **1999**, *14* (1), 25–30.; (o) D. F. Mullica, J. M. Farmer, J. A. Kautz, *J. Coord. Chem.*, **1999**, *48* (4), 449–457.; (p) A. Widmann, H. Kahlert, I. Petrovic-Prelevic, H. Wulff, J. V. Yakhmi, N. Bagkar, F. Scholz, *Inorg. Chem.*, **2002**, *41* (22), 5706–5715.; (q) P. Franz, C. Ambrus, A. Hauser, D. Chernyshov, M. Hostettler, J. Hauser, L. Keller, K. Krämer, H. Stoeckli-Evans, P. Pattison, H.-B. Bürgi, S. Decurtins, *J. Am. Chem. Soc.*, **2004**, *126* (50), 16472–16477.; (r) A. L. Goodwin, K. W. Chapman, C. J. Kepert, *J. Am. Chem. Soc.*, **2005**, *127* (51), 17980–17981.; (s) Z. Lü, X. Wang, Z. Liu, F. Liao, S. Gao, R. Xiong, H. Ma, D. Zhang, D. Zhu, *Inorg. Chem.*, **2006**, *45* (3), 999–1004.; (t) W. Dong, W. Zhang, Y. Ou-Yang, L.-N. Zhu, D.-Z. Liao, K. Yoshimura, Z.-H. Jiang, S.-P. Yan, P. Chen, *J. Magn. Magn. Mater.*, **2007**, *309* (1), 7–10.; (u) E. J. M. Vertelman, T. T. A. Lummen, A. Meetsma, M. W. Bouwkamp, G. Molnar, P. H. M. van Loosdrecht, P. J. van Koningsbruggen, *Chem. Mater.*, **2008**, *20* (4), 1236–1238.; (v) J.-H. Her, P. W. Stephen, C. M. Kareis, J. G. Moore, K. S. Min, J.-W. Park, G. Bali, B. S. Kennon, J. S. Miller, *Inorg. Chem.*, **2010**, *49* (4), 1524–1534.; (w) S. Adak, L. L. Daemen, M. Hartl, D. Williams, J. Summerhill, H. Nakotte, *J. Solid State Chem.*, **2011**, *184* (11), 2854–2861.; (x) C. M. Kareis, S. H. Lapidus, J.-H. Her, P. W. Stephens, J. S. Miller, *J. Am. Chem. Soc.*, **2012**, *134* (4), 2246–2254.; (y) A. I. Rykov, X. Li, J. Wang, *J. Solid State Chem.*, **2015**, *227*, 35–44.; (z) D. Wardecki, D. O. Ojwang, J. Grins, G. Svensson, *Cryst. Growth Des.*, **2017**, *17* (3), 1285–1292.

2. (a) R. K. Motkuri, P. K. Thallapally, B. P. McGrail, S. B. Ghorishi, *CrystEngComm*, **2010**, (12), 4003–4006.; (b) P. K. Thallapally, R. K. Motkuri, C. A. Fernandez, B. P. McGrail, G. S. Behrooz, *Inorg*. *Chem*., **2010**, *49* (11), 4909–4915.; (c) F. Karadas, H. El-Faki, E. Deniz, C. T. Yavuz, S. Aparicio, M. Atilhan, *Micropor*. *Mesopor*. *Mater*., **2012**, *162*, 91–97.; (d) S. H. Ogilvie, S. G. Duyker, P. D. Southon, V. K. Peterson, C. J. Kepert, *Chem*. *Commun*., **2013**, *49* (82), 9404–9406.
3. (a) A. Takahashi, H. Tanaka, D. Parajuli, T. Nakamura, K. Minami, Y. Sugiyama, Y. Hakuta, S. Ohkoshi, T. Kawamoto, *J*. *Am*. *Chem*. *Soc*., **2016**, *138* (20), 6376–6379.; (b) D. Parajuli, H. Noguchi, A. Takahashi, H. Tanaka, T. Kawamoto, *Ind*. *Eng*. *Chem*. *Res*., **2016**, *55* (23), 6708–6715.; (c) S. Manakasettharn, A. Takahashi, T. Kawamoto, K. Noda, Y. Sugiyama, T. Nakamura, *Anal*. *Chem*., **2018**, *90* (7), 4856–4862.; (d) Z. Wang, X. Yuan, S. Cong, Z. Chen, Q. Li, F. Geng, Z. Zhao, *ACS Appl*. *Mater*. *Interfaces*, **2018**, *10* (17), 15065–15072.; (e) Y. Jiang, A. Takahashi, T. Kawamoto, M. Asai, N. Zhang, Z. Lei, Z. Zhang, K. Kojima, K. Imoto, K. Nakagawa, S. Ohkoshi, T. Nakamura, *Chem*. *Commun*., **2018**, *54* (84), 11961–11964.; (f) Y. Jiang, A. Takahashi, T. Kawamoto, M. Asai, N. Zhang, Z. Lei, Z. Zhang, K. Kojima, T. Nakamura, *Inorg*. *Chim*. *Acta*, **2020**, *501*, 119273.
4. (a) H. Parab, M. Sudersanan, *Water Res*., **2010**, *44* (3), 854860.; (b) M. Ishizaki, S. Akiba, A. Ohtani, Y. Hoshi, K. Ono, M. Matsuba, T. Togashi, K. Kananizuka, M. Sakamoto, A. Takahashi, T. Kawamoto, H. Tanaka, M. Watanabe, M. Arisaka, T. Nankawa, M. Kurihara, *Dalton Trans*., **2013**, *42* (45), 16049–16055.; (c) R. Chen, H. Tanaka, T. Kawamoto, M. Asai, C. Fukushima, M. Kurihara, M. Ishizaki, M. Watanabe, M. Arisaka, T. Nankawa, *ACS Appl*. *Mater*. *Interfaces*, **2013**, *5* (24), 12984–12990.; (d) T. Tatsuma, Y. Kuroiwa, K. Ishii, K. Kudo, A. Sakoda, *Chem*. *Lett*., **2014**, *43* (8), 1281–1283.; (e) X. Liu, G.-R. Chen, D.-J. Lee, T. Kawamoto, H. Tanaka, M.-L. Chen, Y.-K. Luo, *Bioresour*. *Technol*., **2014**, *160*, 142–149.; (f) J. Liu, X. Li, A. I. Rykov, Q. Fan, W. Xu, W. Cong, C. Jin, H. Tang, K. Zhu, A. S. Ganeshraja, R. Ge, X. Wang, J. Wang, *J*. *Mater*. *Chem*. *A*, **2017**, *5* (7), 3284–3292.; (g) T. Koshiyama, M. Tanaka, M. Honjo, Y. Fukunaga, T. Okamura, M. Ohba, *Langmuir*, **2018**, *34* (4), 1666–1672.; (h) A. Takahashi, H. Tanaka, K. Minami, K. Noda, M. Ishizaki, M. Kurihara, H. Ogawa, T. Kawamoto, *RSC Adv*., **2018**, *8*, 34808–34816.
5. M. Kämper, D.-C. M. Wagner, A. Weiss, *Angew*. *Chem*. *Int*. *Ed*., **1979**, *18* (6), 486–487.
6. (a) S. S. Kaye, J. R. Long, *J*. *Am*. *Chem*. *Soc*., **2005**, *127* (18), 6506–6507.; (b) K. W. Chapman, P. D. Southon, C. L. Weeks, C. J. Kepert, *Chem*. *Commun*., **2005**,

(26), 3322–3324.; (c) S. Natesakhawat, J. T. Culp, C. Matranga, B. Bockrath, *J. Phys. Chem. C*, **2007**, *111* (2), 1055–1060.; (d) S. S. Kaye, J. R. Long, *Catal. Today*, **2007**, *120* (3–4), 311–316.; (e) L. Reguera, C. P. Krap, J. Balmaseda, E. Reguera, *J. Phys. Chem. C*, **2008**, *112*, (40), 15893–15899.; (f) C. P. Krap, J. Balmaseda, L. F. del Castillo, B. Zamora, E. Reguera, *Energy Fuels*, **2010**, *24* (1), 581–589.; (g) A.-H. Yuan, C.-X. Chu, H. Zhou, P. Yuan, K.-K. Liu, L. Li, Q.-F. Zhang, X. Chen, Y.-Z. Li, *Eur. J. Inorg. Chem.*, **2010**, (6), 866–871.; (h) J. Jiménez-Gallegos, J. Rodríguez-Hernández, H. Yee-Madeira, E. Reguera, *J. Phys. Chem. C*, **2010**, *114* (11), 5043–5048.; (i) C. P. Krap, J. Balmaseda, B. Zamora, E. Reguera, *Int. J. Hydrog. Energy*, **2010**, *35* (19), 10381–10386.; (j) A. A. Al-Hajjaj, B. Zamora, D. V. Bavykin, A. A. Shah, F. C. Walsh, E. Reguera, *Int. J. Hydrog. Energy*, **2012**, *37*(1), 318−326.; (k) L. Hu, P. Zhang, Q. Chen, H. Zhong, X. Hu, X. Zheng, Y. Wang, N. Yan, *Cryst. Growth Des.*, **2012**, *12* (5), 2257−2264.; (l) B. Zamora, A. A. Al-Hajjaj, A. A. Shah, D. V. Bavykin, E. Reguera, *Int. J. Hydrog. Energy*, **2013**, *38* (15), 6406–6416.; (m) P. Bhatt, S. Banerjee, S. Anwar, M. D. Mukadam, S. S. Meena, S. M. Yusuf, *ACS Appl. Mater. Interfaces*, **2014**, *6*, 17579−17588.; (n) N. Torres, H. Osiry, A. Rodríguez, L. Martínez-dlCruz, A. A. Lemus-Santana, E. Reguera, *Z. Anorg. Allg. Chem.*, **2018**, *644* (8–9), 415–423.; (o) N. L. López, J. Rodríquez-Hernández, L Reguera, E Reguera, *Eur. J. Inorg. Chem.*, **2019**, (*25*), 3023–3032.

7. (a) K. W. Chapman, P. J. Chupas E. R. Maxey, J. W. Richardson, *Chem. Commun.*, **2006**, (38), 4013–4015.; (b) M. R. Hartman V. K. Peterson, Y. Liu, S. S. Kaye, J. R. Long, *Chem. Mater.* **2006**, *18* (14), 3221–3224.; (c) Y. Zhao, H. Xu, L. L. Daemen, K. Lokshin, K. T. Tait, W. L. Mao, J. Luo, R. P. Currier, D. D. Hickmott, *Proc. Natl. Acad. Sci. U.S.A.*, **2007**, *104* (14), 5727–5731.

8. (a) T. Mallah, S. Thiébaut, M. Verdaguer, P. Veillet, *Science*, **1993**, *262* (5139), 1554–1557.; (b) S. Ferlay, T. Mallah, R. Ouahès, P. Veillet, M. Verdaguer, *Nature*, **1995**, *378*, 701–703.; (c) O. Sato, T. Iyoda, A. Fujishima, K. Hashimoto, *Science*, **1996**, *272* (5262), 704–705.; (d) M. Verdaguer, A. Bleuzena, V. Marvaud, J. Vaissermann, M. Seuleiman, C. Desplanches, A. Scuiller, C. Train, R. Garde, G. Gelly, C. Lomenech, I. Rosenman, P. Veillet, C. Cartier, F. Villain, *Coord. Chem. Rev.*, **1999**, *190-192*, 1023–1047.; (e) S. M. Holmes, G. S. Girolami, *J. Am. Chem. Soc.*, **1999**, *121* (23), 5593–5594.; (f) Ø. Hatlevik, W. E. Buschmann, J. Zhang, J. L. Manson, J. S. Miller, *Adv. Mater.*, **1999**, *11* (11), 914–918.; (g) S. Ohkoshi, K. Aria, Y. Sato, K. Hashimoto, *Nature Mater.*, **2004**, *3*, 857–861.; (h) T. Uemura, M. Ohba, S. Kitagawa, *Inorg. Chem.*, **2004**, *43* (23), 7339–7345.; (i) M. Zentková1, Z.

Arnold, J. Kamarád, V. Kavečanský, M. Lukáčová, S. Mat'aš1, M. Mihalik, Z. Mitróová, A. Zentko, *J. Phys.: Condens. Matter.*, **2007**, *19* (26), 266217.; (j) S. S. Kaye, H. J. Choi, J. R. Long, *J. Am. Chem. Soc.*, **2008**, *130* (50), 16921–16925.;

9. (a) J. H. Bigelow, *Inorg. Synth.*, **1946**, *2*, 203–205.; (b) J. C. Reeve, *J. Chem. Educ.*, **1985**, *62* (5), 444–445.; (c) S. Ferlay, T. Mallah, R. Ouahès, P. Veillet, M. Verdaguer, *Inorg. Chem.*, **1999**, *38* (2), 229–234.
10. (a) D. A. Dows, A. Haim, W. K. Wilmarth, *J. Inorg. Nucl. Chem.*, **1961**, *21* (1–2), 33–37.; (b) D. F. Shriver, S. A. Shriver, S. E. Anderson, *Inorg. Chem.*, **1965**, *4* (5), 725–730.; (c) R. E. Wilde, S. N. Ghosh, B. J. Marshall, *Inorg. Chem.*, **1970**, *9* (11), 2512–2516.; (d) M. Sendek, K. Csach, V. Kavečanský, M. Lukáčová, M. Maryško, Z. Mitróová, A. Zentko, *Phys. Stat. Sol. (a)*, **2003**, *196* (1), 225–228.; (e) M. Hu, S. Furukawa, R. Ohtani, H. Sukegawa, Y. Nemoto, J. Reboul, S. Kitagawa, Y. Yamauchi, *Angew. Chem. Int. Ed.*, **2012**, *51* (4), 984–988.; (f) H. Tokoro, A. Namai, M. Yoshikiyo, R. Fujiwara, K. Chiba, S Ohkoshi, *Sci. Rep.*, **2018**, *8*, 63.
11. (a) L. Catala, A. Gloter, O. Stephan, G. Rogez, T. Mallah, *Chem. Commun.*, **2006**, (9), 1018–1020.; (b) P. Bhatt, R. Bhatt, S. M. Yusuf, *AIP Conf. Proc.*, **2012**, *1447* (1), 229–230.
12. (a) E. Reguera, J. A. Bertrán, L. Nuñez, *Polyhedron*, **1994**, *13* (10), 1619–1624.; (b) H.-Z. Kou, S. Gao, J. Zhang, G.-H. Wen, G. Su, R. K. Zheng, X. X. Zhang, *J. Am. Chem. Soc.*, **2001**, *123* (47), 11809–11810.; (c) W. Kosaka, K. Nomura, K. Hashimoto, S. Ohkoshi, *J. Am. Chem. Soc.*, **2005**, *127* (24), 8590–8591.; (d) C.-M. Liu, S. Gao, H.-Z. Kou, D.-Q. Zhang, H.-L. Sun, D.-B. Zhu, *Cryst. Growth Des.*, **2006**, *6* (1), 94–98.; (e) M. Arai, M. Miyake, M Yamada, *J. Phys. Chem. C*, **2008**, *112* (6), 1953–1962.
13. (a) J. Tudo, *Rev. Chim. Miner.*, **1965**, *2*, 53−117.; (b) G. Ladwig, *Z. Anorg. Allg. Chem.*, **1969**, *364* (5–6), 225–240.; (c) Z. I. Ezhkova, B. E. Zaitsev, L. I. Konysheva, V. A. Matveevicheva, N. I. Nekhorosheva, O.-V. Y. Polotnyuk, S. P. Chaikovskii, *Kinet. Catal.*, **1972**, *13*, 1149.; (d) V. N. Krasil'nikov, M. P. Glazyrin, A. A. Ivakin, *Russ. J. Inorg. Chem.*, **1983**, *28* (8), 1197.; (e) S. Boghosian, K. M. Eriksen, R. Fehrmann, K. Nielsen, *Acta Chem. Scand.*, **1995**, *49*, 703–708.
14. (a) W. H. Bragg, W. L. Bragg, *Proc. R. Soc. Lond. A*, **1913**, *88* (605), 428–438.; (b) G. E. M. Jauncey, *Proc. Natl. Acad. Sci.* USA, **1924**, *10* (2), 57–60.; (c) W. L. Bond, *Acta Cryst.*, **1960**, *13* (10), 814–818.
15. (a) P. Scherrer, *Göttinger Nachrichten Gesell.*, **1918**, *2*, 98–100.; (b) A. L. Patterson, *Phys. Rev.*, **1939**, *56* (10), 978–982.; (c) B. Ingham, *Crystallogr. Rev.*, **2015**, *21* (4), 229–303.; (d) A. S. Vorokh, *Nanosystems: Phys. Chem. Math.*, **2018**, *9* (3), 364–

369.

16. (a) K. S. W. Sing, D. H. Everett, R. A. W. Haul, L. Moscou, R. A. Pierotti, J. Rouquérol, T. Siemieniewska, *Pure Appl*. *Chem*., **1985**, *57* (4), 603–619.; (b) M. Thommes, K. Kaneko, A. V. Neimark, J. P. Olivier, F. Rodriguez-Reinoso, J. Rouquerol, K. S. W. Sing, *Pure Appl*. *Chem*., **2015**, *87* (9–10), 1051–1069.
17. (a) S. Brunauer, P. H. Emmett, E. Teller, *J*. *Am*. *Chem*. *Soc*., **1938**, *60* (2), 309–319.; (b) F. Roquerol, J. Rouquerol, K. Sing, Adsorption by Powders and Solids: *Principles*, *Methodology and Applications*; Academic Press, London, **1999**.
18. W. E. Buschmann, J. S. Miller, *Inorg*. *Chem*. *Commun*., **1998**, *1* (5), 174–176.
19. (a) M. Ohba, N. Usuki, N. Fukita, H. Ōkawa, *Angew*. *Chem*. *Int*. *Ed*., **1999**, *38* (12), 1795–1798.; (b) N. Usuki, M. Yamada, M. Ohba, H. Ōkawa, *J*. *Solid State Chem*., **2001**, *159* (2), 328–335.; (c) W. Kaneko, M. Ohba, H. Ōkawa, S. Kitagawa, *Inorg*. *Chem*., **2006**, *45* (18), 7191–7196.; (d) M. Ohba, W. Kaneko, S. Kitagawa, T. Maeda, M. Mito, *J*. *Am*. *Chem*. *Soc*., **2008**, *130* (13), 4475–4484.; (e) W. Kaneko, M. Ohba, S. Kitagawa, *J*. *Am*. *Chem*. *Soc*., **2007**, *129* (44), 13706–13712.

Chapter 2

Swift and Efficient Nuclear Spin Conversion of Molecular Hydrogen in Prussian Blue Analogs

Abstract

Catalytic acceleration of nuclear spin conversion for molecular hydrogen (H_2), referred to as ortho-para (o-p) conversion, is strongly required for liquid H_2 storage in a long period because of two latent properties of the conversion: spin-forbidden and exothermic processes. The ortho-isomer of molecular hydrogen (o-H_2) was converted to the para-isomer (p-H_2) within 600 s by using Prussian blue analogs, $\{M^{II}_3[Cr^{III}(CN)_6]_2\}$ (**M_3Cr_2**; M = Mn and Ni), as nuclear-spin conversion catalysts. The swift conversion was confirmed by *in-situ* Raman micro-spectroscopy under an H_2 gas atmosphere (100 kPa) in a low-temperature range (20–90 K). The o-p ratio observed in **M_3Cr_2** deviated from the theoretical value based on the Boltzmann distribution of H_2 in a free rotational state to the para-rich proportion, which suggested the promotion of the o-p conversion at a higher temperature (**Figure 2-1**).

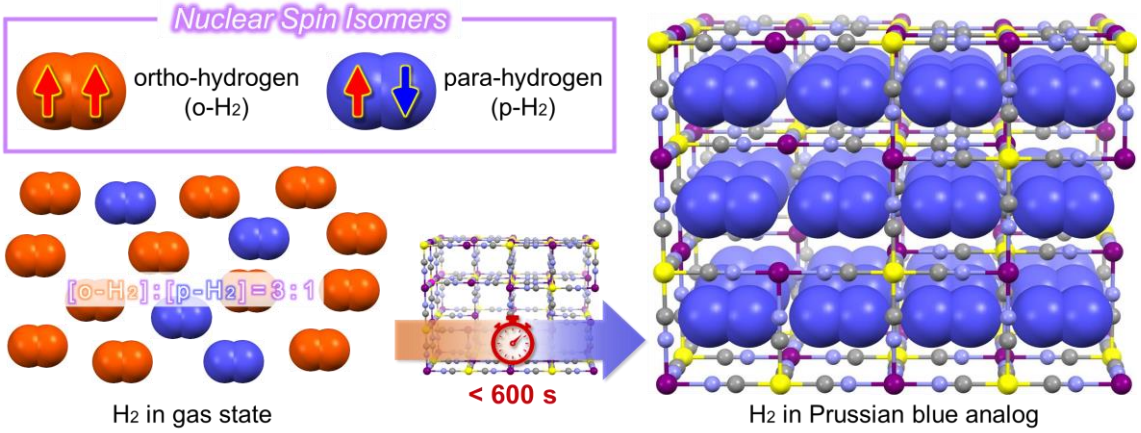

Figure 2-1. Schematic view of the swift and efficient ortho-para (o-p) conversion of molecular hydrogen (H_2) confined in PBAs.

Introduction

H_2 is a highly promising alternative energy source to conventional fossil fuels thanks to its greatly high gravimetric energy density (~141.9 MJ kg^{-1}) and an environmentally friendly combustion product of H_2O. Among conventional physical methods for H_2 storage, liquefaction is commonly used in industrial settings because it facilitates the highest volumetric energy density and transportation efficiency. Long-period storage of liquid H_2, however, is limited by not only technical problems related to the storage vessel but also a latent "boil-off problem" caused by nuclear spin interconversion between nuclear spin isomers of H_2. H_2 is comprised of two nuclear spin isomers, *i.e.* ortho-H_2 (o-H_2; $I = 1$, J = odd) and para-H_2 (p-H_2; $I = 0$, J = even), where I and J are total nuclear spin angular momentum and rotational quantum number, respectively (**Figure 2-2a**).[1] According to the Pauli exclusion principle, their rotational energy levels (E_{rot}) are quantized by the J value (**Figure 2-2a**). Moreover, the isomer ratio ([o-H_2]/[p-H_2]) is a function of temperature (T) based on the Boltzmann distribution with the rotational constant (B) of H_2 and the Boltzmann constant (k), where B/k = 84.837 K (**Equation 2-1** and **Figure 2-2b**).[1] The [o-H_2]/[p-H_2] value is almost 3 over room temperature (RT) and ~1 around liquid N_2 temperature of 77 K. At extremely low temperatures below the boiling point of H_2, almost all H_2 is p-H_2 because of the most stable rotational energy level with $J = 0$.

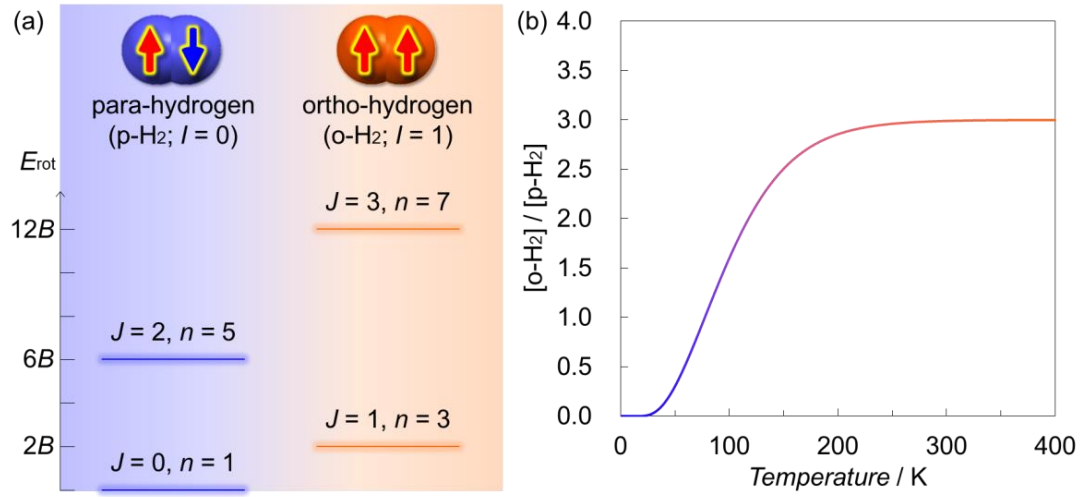

Figure 2-2. (a) Schematic image of nuclear spin isomers of H_2 (p-H_2 and o-H_2) and their rotational energy diagram of nuclear spin isomers for H_2, where I, E_{rot}, B, J, and n denote total nuclear spin angular momentum, rotational energy, rotational constant, rotational quantum number, and degeneracy number, respectively. (b) Temperature-dependent nuclear spin isomer ratio ([o-H_2]/[p-H_2]).

$$[\mathrm{o\text{-}H_2}]/[\mathrm{p\text{-}H_2}] = \frac{\sum_{J=\mathrm{odd}} 3(2J+1)\exp\left\{-\frac{E_{\mathrm{rot}}}{k_B T}\right\}}{\sum_{J=\mathrm{even}} (2J+1)\exp\left\{-\frac{E_{\mathrm{rot}}}{k_B T}\right\}} = \frac{\sum_{J=\mathrm{odd}} 3(2J+1)\exp\left\{-\frac{BJ(J+1)}{k_B T}\right\}}{\sum_{J=\mathrm{even}} (2J+1)\exp\left\{-\frac{BJ(J+1)}{k_B T}\right\}}$$

Equation 2-1. Nuclear spin isomer ratio of molecular hydrogen (H_2).

The nuclear spin conversion from o-H_2 to p-H_2, called as ortho-para (o-p) conversion, is a spin-forbidden process with conversion rates of ~10^{10} s in the gas state,[1] 1.14% h^{-1} in the liquid state,[2a] and approximately 1.9% h^{-1} in the solid-state.[2b–d] Moreover, this conversion is an exothermic reaction with heat of conversion of ~1400 J mol^{-1} for n-H_2, which is higher than the heat of vaporization of H_2 (~900 J mol^{-1}). Thus, liquid H_2, which was prepared by an immediate cooling process without any catalytic treatment still contains ~75% of o-H_2, which generates large heat through the o-p conversion.[3] This is termed as the boil-off problem. Although solid catalysts to promote o-p conversion have been actively developed to solve this problem, such as magnetic materials[4] and diamagnetic metals,[5] several challenges remain regarding the conversion rate and efficiency. These challenges arise because of the low contact probability between the catalyst surface and o-H_2. Even when amorphous solid water systems which are known to have a great catalytic ability on o-p conversion are used as the conversion catalysts, sophisticated techniques for sample preparation and extremely low handling temperatures are required.[6] Several mechanisms for the activated o-p conversions by giant inhomogeneous surface electric fields of non-magnetic materials have also been theoretically proposed.[5g,7] From the abovementioned viewpoint, porous materials with a high surface area and readily accessible space can be considered excellent o-p conversion catalysts. Hence, porous coordination polymers (**PCPs**), also known as metal-organic frameworks (**MOFs**), have the potential to be used as novel o-p conversion catalysts.[8] For example, **MOF-5** and **MOF-74** have catalyzed o-p conversion; however, the detailed mechanism of the observed conversion (*e.g.* driving force and mechanism) has not been elucidated.[9a–c] On the other hand, a high catalytic ability of a Hofmann-type PCP, $\{Fe^{II}(pz)[Pd^{II}(CN)_4]\}$ (**FePd-pz**: pz = pyrazine), for o-p conversion has been reported, which was accelerated by the perturbation of the electric field gradient through adsorption site-exchange of H_2 confined in the nano-sized pores around the boiling point of H_2 (20.27 K).[9d]

As the next step, in order to improve the conversion temperature, we focused on energy level splitting of the triply degenerated ground state of o-H_2 (J = 1) because the splitting may increase the p-H_2 proportion based on the Boltzmann distribution.[4h,5g] This phenomenon also has been reported in a Prussian blue analog (PBA), $\{Cu^{II}_3[Co^{III}(CN)_6]_2\}$, having a defective structure (**Figure 2-3**).[10] PBAs are cyanide-bridged PCPs with diverse properties, such as high H_2 adsorption ability[11] and a magnetic property[12] derived from the 3-D porous structure.[13] Therefore, in this research, we selected PBA-based porous magnets, $\{M^{II}_3[Cr^{III}(CN)_6]_2\}$ (**M_3Cr_2**; M = Mn and Ni), as new o-p conversion catalysts and verified the effect of magnetic perturbation induced in **PCPs** on o-p conversion as an additional factor to improve conversion temperature. As discussed in chapter 1, **Mn_3Cr_2** and **Ni_3Cr_2** had sufficient framework stability until 120 and 160°C, respectively, and showed the highest and the second-highest H_2 adsorption amount in weight percentage among the all prepared PBAs, which are the reason for selecting Mn^{2+} and Ni^{2+} ions as the component in addition to the magnetic property.

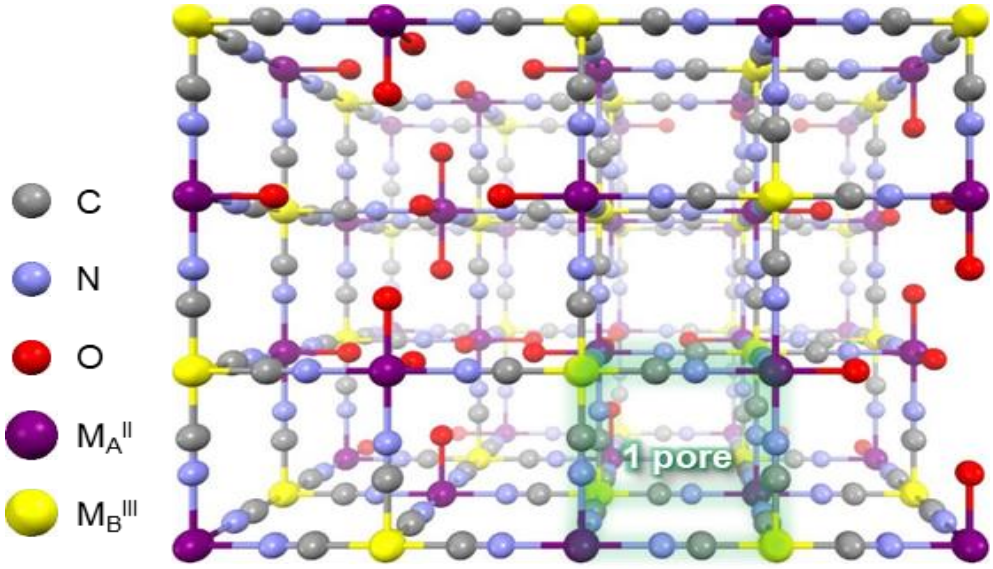

Figure 2-3. Schematic crystal structure of defective Prussian blue analogs (PBAs), $\{Ma^{II}_3[Mb^{III}(CN)_6]_2 \cdot nH_2O\}$ (**$Ma_3Mb_2 \cdot nH_2O$**). The lattice H_2O molecules and H atoms of coordinated H_2O molecules are omitted for clarity. Color codes: C (gray), N (cyan), O (red), divalent Ma (purple), trivalent Mb (yellow).

Physical Measurements

Carbon, Hydrogen, and Nitrogen Elemental Analysis (CHN-EA)

CHN-EA of C, H, and N atoms was conducted as quickly as possible after sample loading by the staff of the Technical Support Division, Graduate School of Science, Kyushu University.

Powder X-ray Diffractometry (RXPD)

RXPD was conducted on a Rigaku Ultima IV diffractometer using graphite-monochromated CuKα radiation and reflection-free single-crystal Si sample holder in the ambient air at RT. X-ray wavelength: 1.54184 Å, X-ray voltage: 40 kV, X-ray current: 40 μA, angle range: 5–60°, scan rate: 1° min^{-1}, data collecting step: 0.02°, integrated number: 1 time.

Scanning Electron Microscopy (SEM)

SEM was conducted on Micro-Calorimeter FESEM TES+ULTRA55 in The Ultramicroscopy Research Center, Kyushu University. Electron high tension (EHT) value: 10.00 keV.

Thermogravimetry analysis (TGA)

TGA was conducted on a PerkinElmer STA6000 as quickly as possible after sample loading under dry an N_2 atmosphere. Sample weight: ~10 mg, temperature range: 30–700℃, heating rate: 5℃ min^{-1}, N_2 gas flow rate: 19.8 ml min^{-1}.

Energy Dispersive X-ray Fluorescence (EDXRF) Analysis

EDXRF analysis was conducted on a Shimadzu Rayny EDX-720 to detect elements with an atomic number greater than or equal to 12 in the ambient air at RT. The results were averaged over three runs. X-ray voltage: 50 kV, X-ray current: 30 μA.

Fourier Transform Infrared (FT-IR) Spectroscopy

FT-IR spectroscopy was conducted on a JASCO FT/IR-4200 spectrometer using an attenuated total reflection (ATR) method in the ambient air at RT. Wavenumber range: 4000–650 cm^{-1}, resolution: 4 cm^{-1}, integrated number: 1024 times.

Adsorption/Desorption Measurements

N_2 (99.999%) and H_2 (99.999%) adsorption/desorption measurements were conducted on MicrotracBEL BELSORP-max volumetric adsorption equipment at 77 K using liquid N_2 in a Dewar bottle. The prepared samples were activated again by heating at 120 ℃ for 4 h under vacuum after loading into the measurement glass tube before the measurement. Second virial coefficients: -1.824×10^{-8} (H_2), -4.328×10^{-7} (N_2); sample weight: ~35 mg, pressure range of 0–105 kPa, outgas rate: < 0.02 Pa min^{-1}.

Magnetic Susceptibility Measurement

Magnetic susceptibility of the ground sample was recorded by Quantum Design MPMS-XL5R with a superconducting quantum interference device (SQUID). The sample was put into a gelatin capsule, placed in a plastic straw, fixed to the end of the sample transport rod, and activated again by heating at 330 K over 3 h in the machine before the measurement. Applied DC magnetic field: 10 Oe, minimum temperature: 2 K.

In-situ Raman Spectroscopy

Raman spectroscopy was carried on using Horiba Jobin Yvon iHR320 imaging spectrometer, Horiba Jobin Yvon Synapse CCD detector, Laser Quantum torus 532 laser, and a nickel-plated Raman sample cell (Laser beam wavelength: 532 nm, Laser beam exposure time: 30 s, Integrated number: 20 times). For *in-situ* Raman spectroscopy under an H_2 gas atmosphere, the measurement temperature was controlled by UW404 CryoMini Compressor with BELCryo-20K temperature control system using Lake Shore Model 331 Cryogenic Temperature Controller, and the H_2 gas pressure was controlled by MicrotracBEL BELSORP-max volumetric adsorption equipment. For the measurement of samples, neutral density (ND) filters with the total optical density (OD) of 1.6 were used for weakening the excitation light intensity to avoid sample decomposition. For the controlled measurement of Raman sample cell, the ND filter was not used to use an excitation laser with maximum intensity. In order to magnetize samples, a commercial neodymium magnet of 2000 Oe was embedded into the cell of the Raman sample cell.

Sample Preparation

All the chemicals were purchased as reagent grade and used without further purification. All the prepared samples were stored in a vial with screw cap and allowed to stand at RT in the dark right before the measurements and characterized by carbon, hydrogen, and nitrogen elemental analysis (CHN-EA), scanning electron microscopy (SEM), energy dispersive X-ray fluorescence (EDXRF) analysis, thermogravimetry analysis (TGA), Fourier transform infrared (FT-IR) spectroscopy, and powder X-ray diffractometry (RXPD).

$K_3[Cr^{III}(CN)_6]$

$K_3[Cr(CN)_6]$ was synthesized according to a reported synthetic method with some modifications.[12i,14] Mossy Zn (6.0 g, 91.8 mmol) was activated by immersing in 1 M HCl for 5 min, thoroughly washed with distilled water, and dried well in advance. Then the activated mossy Zn was added to a degassed aqueous solution (40 mL) of $CrCl_3 \cdot 6H_2O$ (20.0 g, 75.1 mmol) under an N_2 gas atmosphere at RT. After stirring over 3 h and removal of the remaining unreacted Zn by suction filtration, a solid $CH_3COONa \cdot 3H_2O$ (24.0 g, 176.4 mmol) was added to the resultant deep blue solution, which resulted in a rapid precipitate of chromium(II) acetate as a bright red powder. The precipitate was collected by suction filtration under an N_2 gas atmosphere, repeatedly washed with degassed water, and dissolved in a degassed aqueous solution (50 ml) of KCN (30.0 g, 460.7 mmol). After removal of the slight precipitate by suction filtration, an excess amount of methanol (~500 ml) was added to the dark green filtrate, which provided $K_4[Cr^{II}(CN)_6]$ as a light green precipitate. The precipitate was collected by suction filtration, repeatedly washed with methanol, and allowed to stand over 2 h for the air oxidation of the Cr^{II} ion. After completion of color change to yellow, a few repeated reprecipitation from water by the addition of an excess amount of methanol gave pure $K_3[Cr^{III}(CN)_6]$. Yellow crystalline powder. Yield: 15.5 g (47.7 mmol, 63.5% vs. $CrCl_3 \cdot 6H_2O$). FT-IR (cm^{-1}): ν(C≡N) = 2130; ν(Cr–C) = 454 (vs). EDXRF analysis (%): [K]/[Cr] = 2.85. No other elements were detected.

$\{Mn^{II}_3[Cr^{III}(CN)_6]_2 \cdot 14H_2O\}$ (**$Mn_3Cr_2 \cdot 14H_2O$**)

All the operations for the synthesis were conducted in the dark to avoid the decomposition of $K_3[Cr(CN)_6]$. A degassed aqueous solution (50 mL) of $K_3[Cr(CN)_6]$ (325.4 mg, 1.0 mmol) was added dropwise to a degassed aqueous solution (50 mL) of $MnCl_2 \cdot 4H_2O$ (395.8 mg, 2.0 mmol) with stirring under an N_2 gas atmosphere at RT, resulting in precipitation of light-green solid. After stirring over 2 days, the light-green precipitate was collected by centrifugation, repeatedly washed with distilled water, and dried in the air. Light-green powder. Yield: 228.3 mg (0.27 mmol, 54.8% vs. $K_3[Cr(CN)_6]$). CHN-EA (%): Found: C 17.66, H 3.26, N 20.12; Calcd. for $\{Mn_3[Cr(CN)_6]_2 \cdot 14H_2O\}$ ($C_{12}H_{28}N_{12}O_{14}Cr_2Mn_3$): C 17.30, H 3.39, N 20.17. FT-IR (cm^{-1}): ν(OH) = 3800–2900 (br), ν(C≡N) = 2162 (s), δ(H_2O) = 1611 (m). SEM-EDX analysis (%): [Mn]/[Cr] = 1.40. EDXRF analysis (%): [Mn]/[Cr] = 1.37, [K]/[Mn] < 0.05.

$\{Ni^{II}_3[Cr^{III}(CN)_6]_2 \cdot 15H_2O\}$ (**$Ni_3Cr_2 \cdot 15H_2O$**)

All the operations for the synthesis were conducted in the dark to avoid the decomposition of $K_3[Cr(CN)_6]$. An aqueous solution (50 mL) of $K_3[Cr(CN)_6]$ (325.4 mg, 1.0 mmol) was added dropwise to a aqueous solution (50 mL) of $NiCl_2 \cdot 6H_2O$ (475.4 mg, 2.0 mmol) with stirring at RT, resulting in precipitation of light-blue solid. After stirring over 2 days, the light-blue precipitate was collected by centrifugation, repeatedly washed with distilled water, and dried in the air. Green powder. Yield: 374.8 mg (0.43 mmol, 86.9% vs. $K_3[Cr(CN)_6]$). CHN-EA (%): Found: C 16.69, H 3.56, N 19.20; Calcd. for $\{Ni_3[Cr(CN)_6]_2 \cdot 15H_2O\}$ ($C_{12}H_{30}N_{12}O_{15}Cr_2Ni_3$): C 16.71, H 3.51, N 19.49. FT-IR (cm^{-1}): ν(OH) = 3800–2900 (br), ν(C≡N) = 2169 (s), δ(H_2O) = 1610 (m). SEM-EDX analysis (%): [Ni]/[Cr] = 1.57. EDXRF analysis (%): [Ni]/[Cr] = 1.78, [K]/[Ni] < 0.01.

Results and Discussion

Both **$Mn_3Cr_2 \cdot nH_2O$** and **$Ni_3Cr_2 \cdot nH_2O$** were prepared by a typical synthetic method for PBAs, which is a mixing method of respective aqueous solutions of $M^{II}Cl_2 \cdot xH_2O$ and $K_3[Cr^{III}(CN)_6]$. Energy dispersive X-ray fluorescence (EDXRF) and scanning electron microscopy with energy dispersive X-ray (SEM-EDX) analysis of **$M_3Cr_2 \cdot nH_2O$** indicated that the componential ratio ([M]/[Cr]) is consistent with the calculated value of 1.5 and the contamination of K^+ is below 0.1% in each batch (**Figure 2-4** and **Table 2-1**–**Table 2-2**). The number of total lattice and coordination H_2O molecules (n) was determined to be 14 for **Mn_3Cr_2** and 15 for **Ni_3Cr_2** by carbon, hydrogen, and nitrogen elemental analysis (CHN-EA) and thermogravimetry analysis (TGA) of **$M_3Cr_2 \cdot nH_2O$** (**Figure 2-5**). The trace amount of K^+ was ignored at this stage. In the Fourier transform infrared (FT-IR) spectra of **$M_3Cr_2 \cdot nH_2O$**, the O-H stretching mode (ν(O–H)) and H-O-H bending mode (δ(H–O–H)) in H_2O molecules were observed in 3800–2900 cm^{-1} and around 1610 cm^{-1}, respectively (**Figure 2-6**). The powder X-ray diffraction (PXRD) patterns of **$M_3Cr_2 \cdot nH_2O$** showed good crystallinity and were in good agreement with the typical diffraction pattern of PBAs (**Figure 2-7**).[12]

The dehydrated samples, **M_3Cr_2**, were prepared by heating **$M_3Cr_2 \cdot nH_2O$** at 120°C for 24 h under vacuum. In the FT-IR spectra, the broad bands of $\nu(H_2O)$ and $\delta(H_2O)$ modes disappeared and the ν(C≡N) band slightly broadened without a large wavenumber shift, indicating the removal of H_2O molecules and the retainment of the cyanide-bridged framework after the dehydration treatment, respectively (**Figure 2-6** and **Table 2-3**). The PXRD patterns exhibited essentially the same results before and after the dehydration treatment, except for a broadening and a higher angle shift in almost all the peaks, which suggested shrinkage and distortion of the lattice by a change in the coordination geometry of the M^{II} sites, with the elimination of coordinated H_2O (**Figure 2-7**).

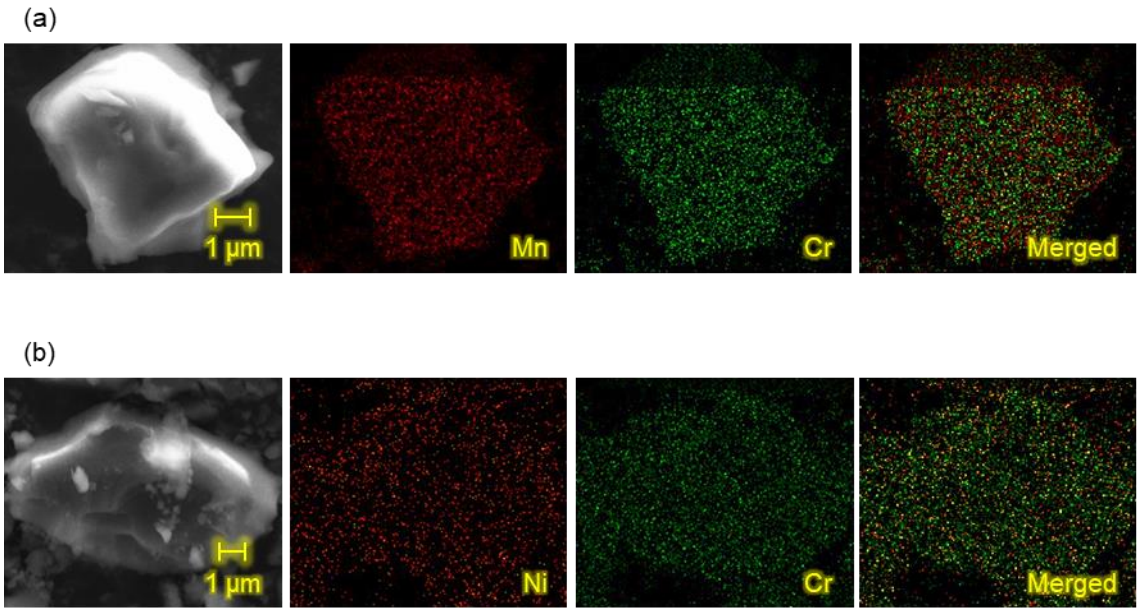

Figure 2-4. SEM images and elemental mapping of (a) **$Mn_3Cr_2 \cdot 14H_2O$** and (b) **$Ni_3Cr_2 \cdot 15H_2O$**. Color codes: Cr (green), Mn (red), and Ni (orange). Electron high tension (EHT) value: 10.00 keV.

Table 2-1. EDXRF and SEM-EDX results of **$Mn_3Cr_2 \cdot 14H_2O$**.

	[Mn] / wt%	[Cr] / wt%	[Mn] / [Cr]
SEM-EDX	59.744	40.456	1.40
EDXRF	59.142	40.858	1.37
Ideal Value	61.313	38.687	1.50

Table 2-2. EDXRF and SEM-EDX results of **$Ni_3Cr_2 \cdot 15H_2O$**.

	[Ni] / wt%	[Cr] / wt%	[Ni] / [Cr]
SEM-EDX	63.963	36.037	1.57
EDXRF	66.769	33.231	1.78
Ideal Value	62.870	37.130	1.50

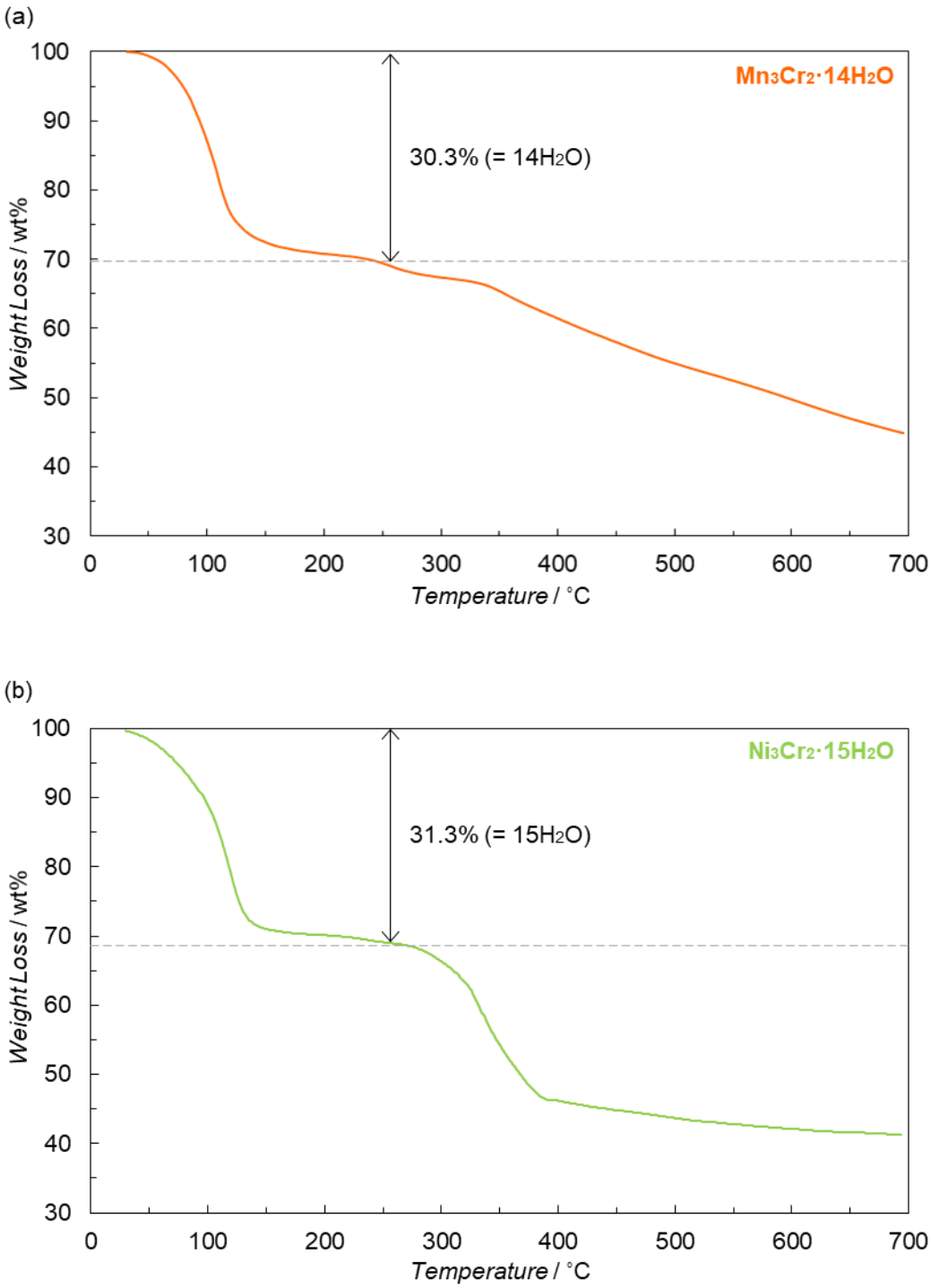

Figure 2-5. TGA curves of (a) **$Mn_3Cr_2 \cdot 14H_2O$** and (b) **$Ni_3Cr_2 \cdot 15H_2O$** under a dry N_2. The measurement was performed as quickly as possible after sample loading. Heating rate: 5°C min^{-1}, N_2 gas flow rate: 19.8 ml min^{-1}.

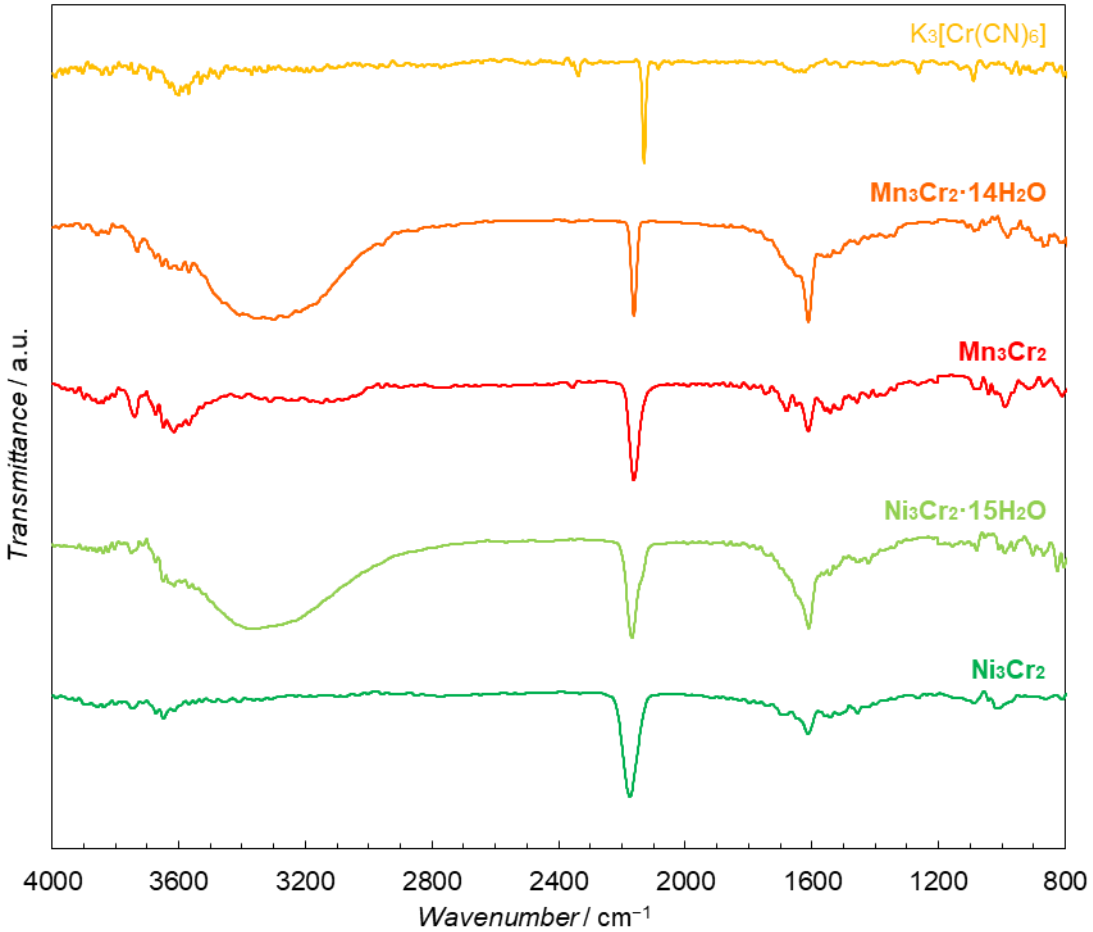

Figure 2-6. FT-IR spectra in the ambient air at RT of $K_3[Cr(CN)_6]$ (yellow), **$Mn_3Cr_2 \cdot 14H_2O$** (orange), **Mn_3Cr_2** (red), **$Ni_3Cr_2 \cdot 15H_2O$** (yellow-green), and **Ni_3Cr_2** (green). Resolution: 4 cm^{-1}, integrated number: 1024 times.

Table 2-3. The observed wavenumber of stretching vibration mode of cyanide anion (ν(C≡N)) in the FT-IR spectra in the ambient air at RT of $K_3[Cr(CN)_6]$, **$Mn_3Cr_2 \cdot 14H_2O$**, **Mn_3Cr_2**, **$Ni_3Cr_2 \cdot 15H_2O$**, and **Ni_3Cr_2**.

	ν(C≡N) / cm^{-1}
$K_3[Cr(CN)_6]$	2130
$Mn_3Cr_2 \cdot 14H_2O$	2162
Mn_3Cr_2	2162
$Ni_3Cr_2 \cdot 15H_2O$	2169
Ni_3Cr_2	2175

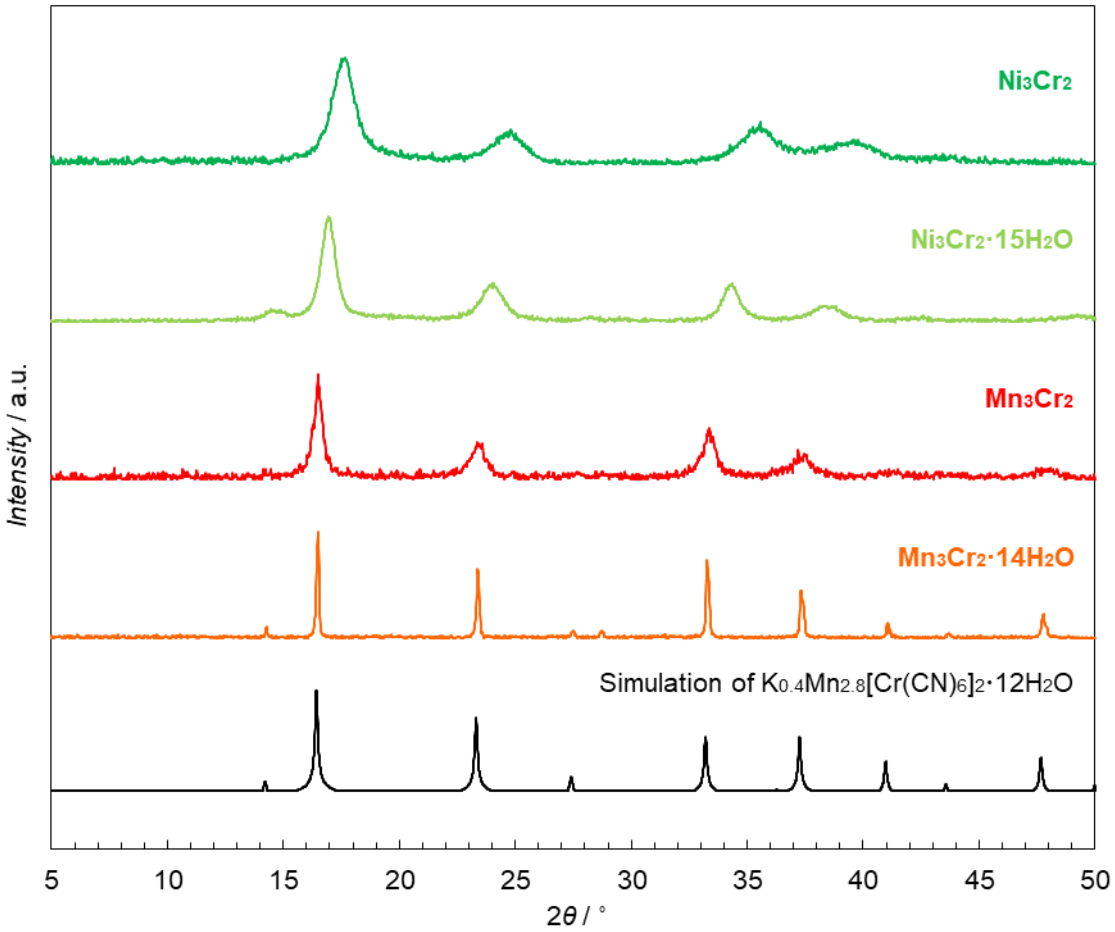

Figure 2-7. PXRD patterns in the ambient air at RT of **$Mn_3Cr_2 \cdot 14H_2O$** (orange), **Mn_3Cr_2** (red), **$Ni_3Cr_2 \cdot 15H_2O$** (yellow-green), and **Ni_3Cr_2** (green), and simulated PXRD pattern of a PBA, $K_{0.4}Mn^{II}_{2.8}[Cr^{III}(CN)_6]_2 \cdot 12H_2O$ (black).[13s] Scan rate: 1° min^{-1}, data collecting step: 0.02°, integrated number: 1 time.

The Brunauer-Emmett-Teller specific surface areas (SA_{BET}) of the dehydrated samples, **Mn_3Cr_2** and **Ni_3Cr_2**, were estimated from the results of N_2 adsorption at 77 K to be 683 and 620 $m^2\ g^{-1}$, respectively, which were in the same range of the SA_{BET} values of other reported PBAs (**Figure 2-8** and **Table 2-4**).[11] In the H_2 adsorption measurement at 77 K, both of **Mn_3Cr_2** and **Ni_3Cr_2** exhibited type-I behavior of typical microporous materials in the International Union of Pure and Applied Chemistry (IUPAC) classification,[15] with an adsorption amount of ~0.7 H_2 molecules per pore at 100 kPa (**Figure 2-3** and **Figure 2-9**).

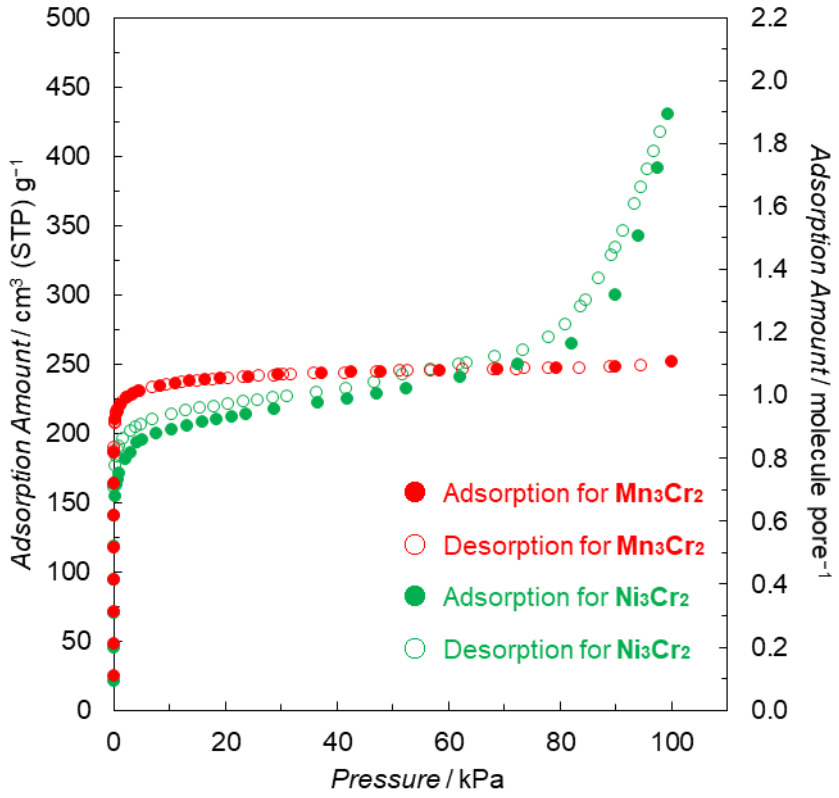

Figure 2-8. N_2 adsorption (●)/desorption (○) isotherms of **Mn_3Cr_2** (red) and **Ni_3Cr_2** (green) at 77 K.

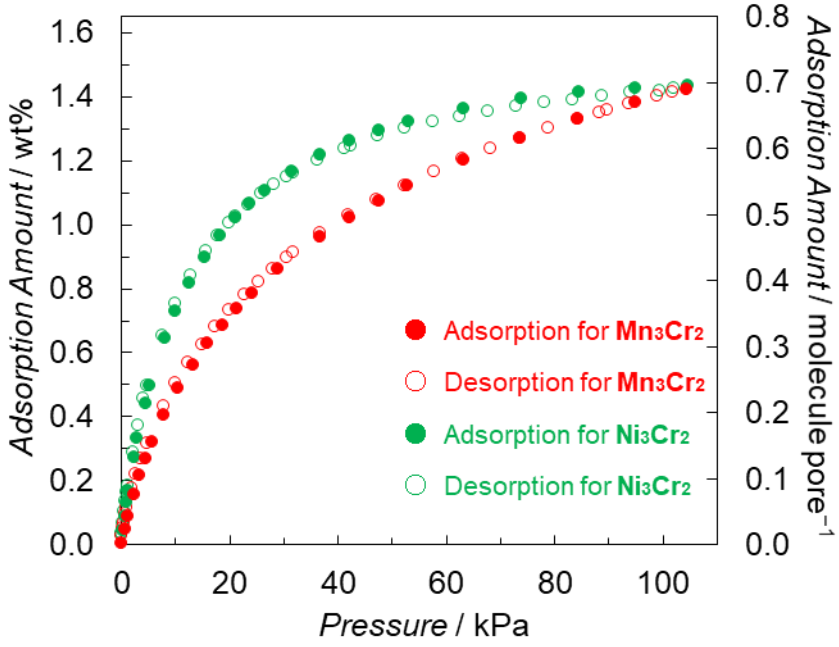

Figure 2-9. H_2 adsorption (●) and desorption (○) isotherms of **Mn_3Cr_2** (red) and **Ni_3Cr_2** (green) at 77 K.

Table 2-4. Brunauer-Emmett-Teller specific surface areas (SA_{BET}) and adsorption amount of H_2 ($n_a(H_2)$) around 100 kPa and at liquid N_2 temperature of several PBAs, $\{Ma^{II}_3[Mb^{III}(CN)_6]_2\}$ (**Ma_3Mb_2**).

PBA	SA_{BET} / $m^2\ g^{-1}$	$n_a(H_2)$ / wt%	Reference
Mn_3Cr_2	683	1.4	This work
Ni_3Cr_2	620	1.4	This work
Mn_3Co_2	870	1.5	11a
Mn_3Co_2	756	1.0	11b
Fe_3Co_2	770	1.3	11a
Fe_3Co_2	350	0.7	11b
Co_3Co_2	800	1.4	11a
Co_3Co_2	719	1.0	11b
Co_3Co_2	692	1.3	11e
Ni_3Co_2	560	1.3	11a
Ni_3Co_2	668	1.1	11b
Cu_3Co_2	730	1.7	11a
Cu_3Co_2	478	0.4	11b
Cu_3Co_2	750	1.7	11d
Zn_3Co_2	720	1.3	11a
Zn_3Co_2	697	1.1	11b
Zn_3Co_2	609	1.2	11e
Cd_3Co_2	667	1.2	11b
Cd_3Co_2	573	1.3	11k
Cd_3Co_2	376	1.0	11k

The nuclear spin state of H_2 confined in **M_3Cr_2** was confirmed by *in-situ* Raman microspectroscopy under an H_2 atmosphere at 100 kPa (**Figure 2-10**). The spectra indicated by bottom black lines were obtained under reduced pressure at 90 K, where the observed broad Raman bands around 394 cm^{-1} for **Mn_3Cr_2** and 525 cm^{-1} for **Ni_3Cr_2** were assigned to the vibration modes of the host framework (**Figure 2-10**). After the injection of H_2 gas (100 kPa), two Raman-active bands newly appeared around 355 and 588 cm^{-1} at 90 K (**Figure 2-10**). These bands were assigned to the rotational transition of $S_0(0)$ ($J = 2 \leftarrow 0$) for confined p-H_2 and $S_0(1)$ ($J = 3 \leftarrow 1$) for confined o-H_2 on comparison with the spectra of the desorption state and considering the Boltzmann distribution of H_2 (**Equation 2-1**). Moreover, Raman bands of free H_2, which correspond to the energy gap between the initial and final states of each $S_0(0)$ and $S_0(1)$ transitions, were observed at 354 and 587 cm^{-1}, respectively (**Figure 2-2a**).[16] In both types of **Mn_3Cr_2** and **Ni_3Cr_2**, the increase in total peak intensities of $S_0(0)$ and $S_0(1)$ transitions as the temperature decreased suggests an increase in the amount that is adsorbed, because the Raman bands of H_2 in a free state were not detected in the measurement condition with a relatively weak laser intensity. The peak intensity of p-H_2 gradually increased with cooling, whereas that of o-H_2 gradually decreased with cooling and almost vanished around 30 K (**Figure 2-10**). In addition to the peak intensity change, time-profiles of the intensity of both $S_0(0)$ and $S_0(1)$ transitions showed rapid saturation and constancy during the integration processing (600 s), which suggested that the system reached an equilibrium state at the initial process. This rate was based on the laser exposure time (30 s) and the cumulative number (20 times). Judging from the measurement condition and the high mobility of the adsorbed H_2, the detected o-p conversion occurred not on the surface of **Mn_3Cr_2** but inside the pore. Consequently, the o-p conversion for H_2 confined in **M_3Cr_2** was completed with a time constant of 600 s at its longest.

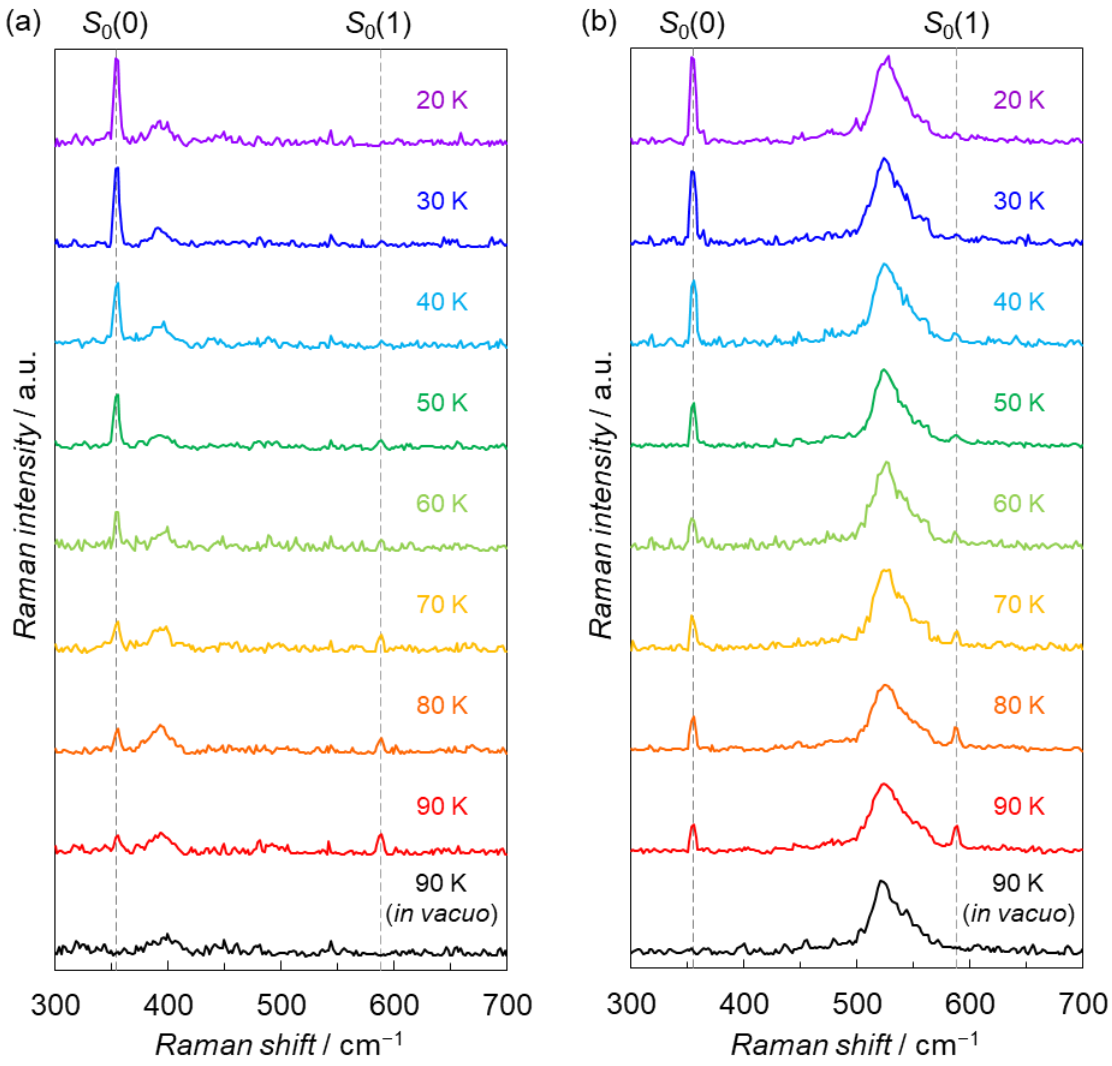

Figure 2-10. Temperature-dependent *in-situ* Raman spectra of (a) **Mn_3Cr_2** and (b) **Ni_3Cr_2** under reduced pressure (black line) and H_2 gas atmosphere at 100 kPa (colored lines) using an excitation laser with a wavelength of 532 nm. Neutral density (ND) filters with a total optical density (OD) of 1.6 were used to weaken the intensity of the excitation laser.

The [o-H_2]/[p-H_2] values observed in **M_3Cr_2** were calculated from the integrated values of the peak areas of $S_0(0)$ and $S_0(1)$ transitions obtained from the spectrum of the desorption state (**Figure 2-10**; black line) as the baseline, where $f_{T,P}(v)$ and v are the function of spectra at a certain temperature (T) and pressure (P), and the Raman shift, respectively (**Equation 2-2** and **Figure 2-11**). In the controlled experiments, where only a nickel-plated Raman sample cell without **M_3Cr_2** was used, the [o-H_2]/[p-H_2] value was constant in the temperature range from 90 to 20 K and the time range of 600 s, indicating that there is no effect of the instrument on the o-p conversion (**Figure 2-12** and **Figure 2-13**). In both cases of the observed [o-H_2]/[p-H_2] values in **M_3Cr_2**, the observed [o-H_2]/[p-H_2] values decreased with lowering temperature, and the observed values were lower than the theoretical values of free H_2 above 40 K, which indicated a successful increase in the o-p conversion temperature (**Figure 2-11**). In addition to the observed ratio, over the entire measurement temperature range, the observed full width at half maximum (FWHM) of both the $S_0(0)$ and $S_0(1)$ transitions in **M_3Cr_2** (~6 cm^{-1}) was larger than those obtained by the abovementioned controlled experiments (~3 cm^{-1}), which suggests a rotational restraint of H_2 confined in **M_3Cr_2** (**Figure 2-10** and **Figure 2-12**). Because the Boltzmann distribution relating to the [o-H_2]/[p-H_2] value depends on only the rotational constant (B) of H_2 (eq 1), the resultant deviation of the o-p ratio suggests the rotational restraint of the confined o-H_2. Such rotational restraint would be caused by the locally anisotropic potential fields derived from the structural defects of **M_3Cr_2**, which is supported by the rotational-vibrational density of states for H_2 confined in another PBA, $Cu^{II}_3[Co^{III}(CN)_6]_2$ (**Cu_3Co_2**).[10b] Because the [o-H_2]/[p-H_2] values observed for **FePd-pz** having a non-defective porous structure followed the Boltzmann distribution,[9d] the resultant deviation for **M_3Cr_2** suggested the contribution of a defective porous structure to provide a para-enriched isomer ratio. The similar results of both types of **M_3Cr_2** suggest the importance of the defective porous structure instead of the framework components for achieving effective o-p conversion and ratio.

$$[\text{o-H}_2]/[\text{p-H}_2] = \int_{581.0}^{592.1} \{f_{T,100\,\text{kPa}}(v) - f_{90\text{K},0\text{kPa}}(v)\}\mathrm{d}v \Big/ \int_{349.7}^{360.8} \{f_{T,100\,\text{kPa}}(v) - f_{90\text{K},0\text{kPa}}(v)\}\mathrm{d}v$$

Equation 2-2. An equation to calculate the observed ratio of nuclear spin isomer.

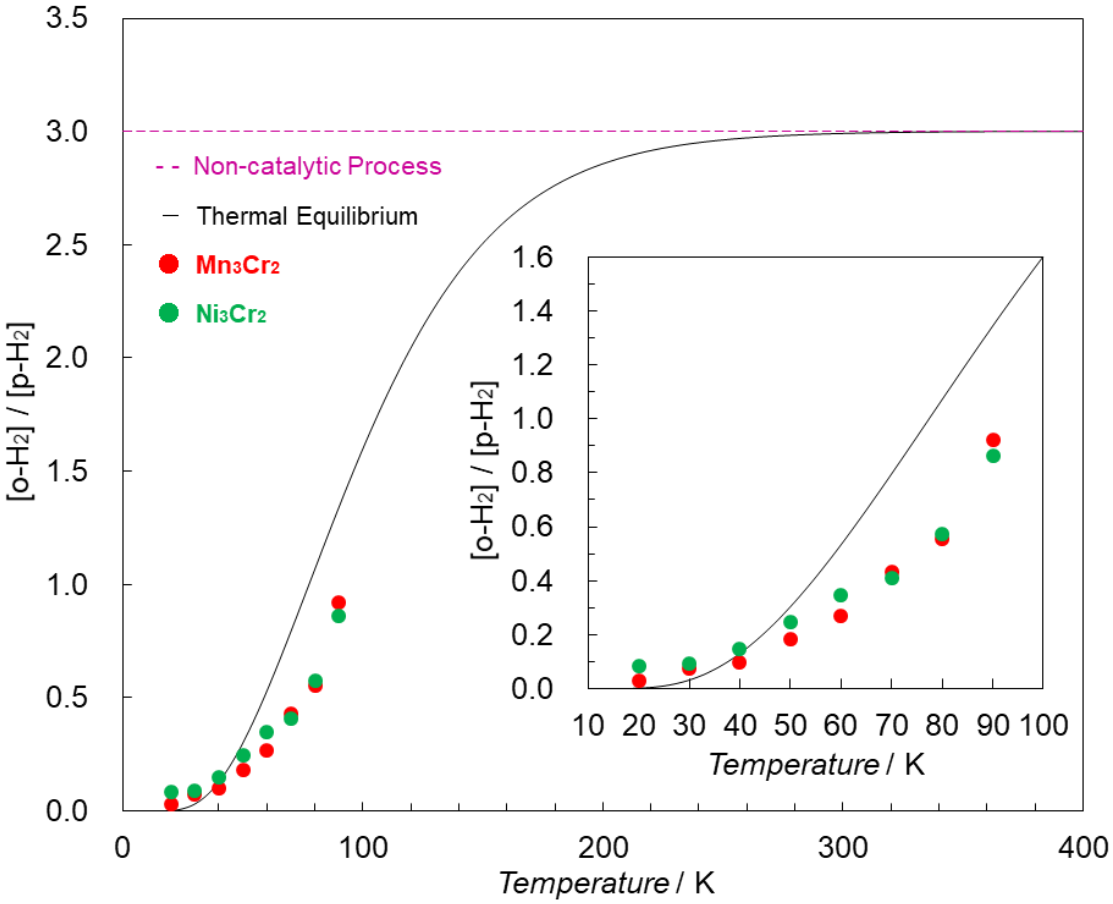

Figure 2-11. Temperature-dependent abundance ratio of the nuclear spin isomer ([o-H_2]/[p-H_2]) for H_2 confined in **Mn_3Cr_2** (red) and **Ni_3Cr_2** (green), estimated ratio obtained during cooling from room temperature without catalytic treatment (pink), and theoretical ratio in thermal equilibrium based on the Boltzmann distribution of H_2 in a free rotational state (black). The inset is an enlarged view of the low temperature region.

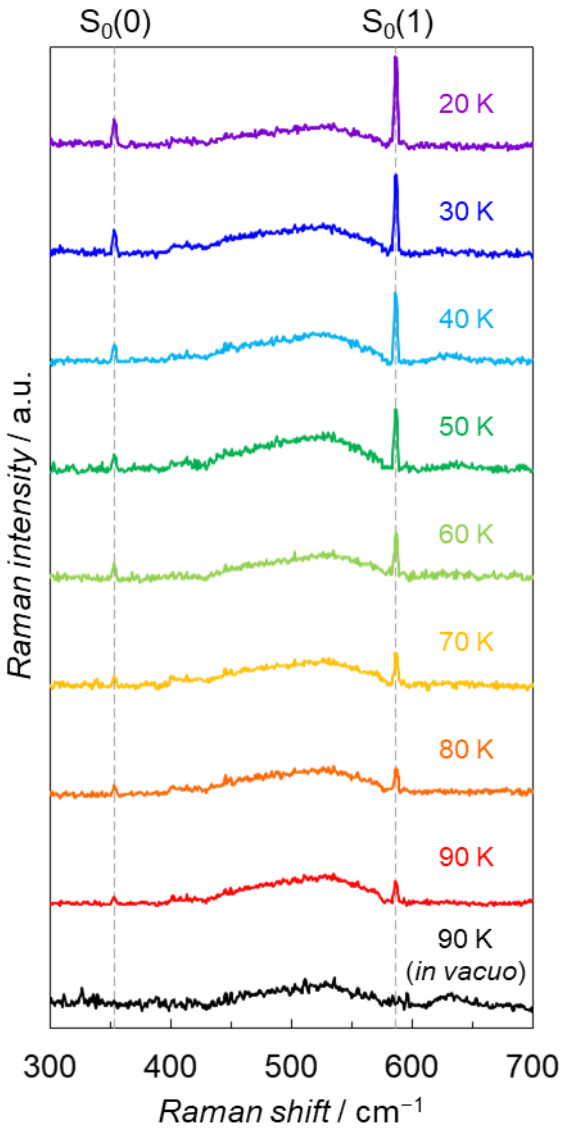

Figure 2-12. Temperature-dependent *in-situ* Raman spectra of nickel-plated Raman sample cell without **M_3Cr_2** under reduced pressure (black line) and H_2 gas atmosphere at 100 kPa (colored lines) using an excitation laser with a wavelength of 532 nm. No neutral density (ND) filter was used.

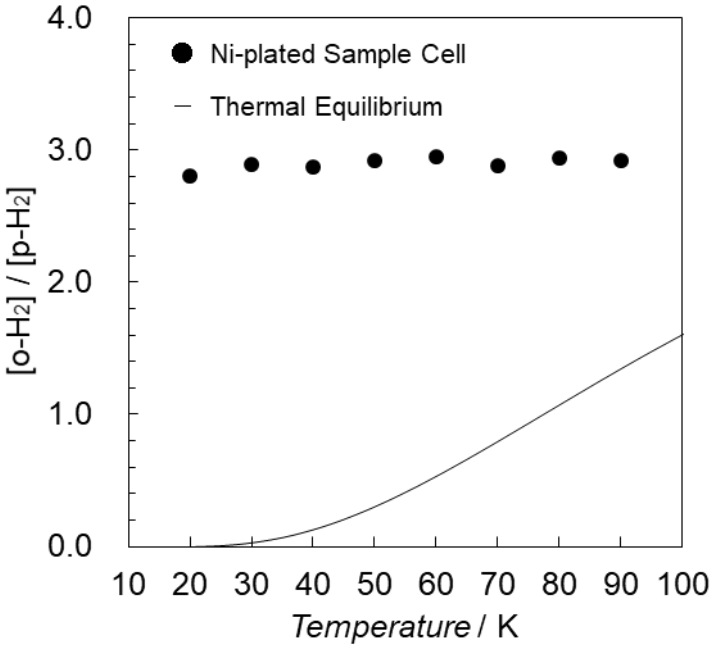

Figure 2-13. Temperature-dependent abundance ratio of the nuclear spin isomer ([o-H_2]/[p-H_2]) for H_2 observed on nickel-plated Raman sample cell (●) and theoretical ratio in thermal equilibrium based on Boltzmann distribution of H_2 in a free rotational state (–).

In order to verify the perturbation effect of the magnetic field in the pore on o-p conversion, the *in-situ* Raman spectroscopy was conducted again by using magnetized PBAs. **$Mn_3Cr_2 \cdot nH_2O$** shows ferrimagnetic behavior below a magnetic ordering temperature (T_c) of 63 K (n = 12)[12j] and 67 K (n = 15),[12e] while **$Ni_3Cr_2 \cdot nH_2O$** shows ferromagnetic behavior below T_c of 56 K (n = 9),[12i] 60 K (n = 12),[12a] and 72 K (n = 16).[12e] On the other hand, **Mn_3Cr_2** showed a ferrimagnetic ordering at 108 K (**Figure 2-14**), and **Ni_3Cr_2** showed a ferromagnetic ordering at 18 K (**Figure 2-15**). The different magnetic behavior from that of **$Ni_3Cr_2 \cdot nH_2O$** reflects a change in the magnetic interaction and a decrease in the magnetic domain size resulting from changes in the geometry and *d* electron configuration of the M^{II} sites due to dehydration.[12a,e,f,i,j,m] Because the strict orthogonality of magnetic orbitals between Ni^{2+} and Cr^{3+} is broken by the geometry changes, the ferromagnetic coupling between Ni^{2+} and Cr^{3+} is weakened. In particular, diamagnetic Ni^{2+} centers having square planar geometry are partially generated by dehydration. The diamagnetic Ni^{2+} centers break the interaction pathways and cause a fragmentation of magnetic domains. These factors resulted in a decrease in T_c and superparamagnetic-like behavior. The AC magnetic behavior of **Ni_3Cr_2** showed a slight frequency dependence, which supported the superparamagnetic-like behavior (**Figure 2-16**).

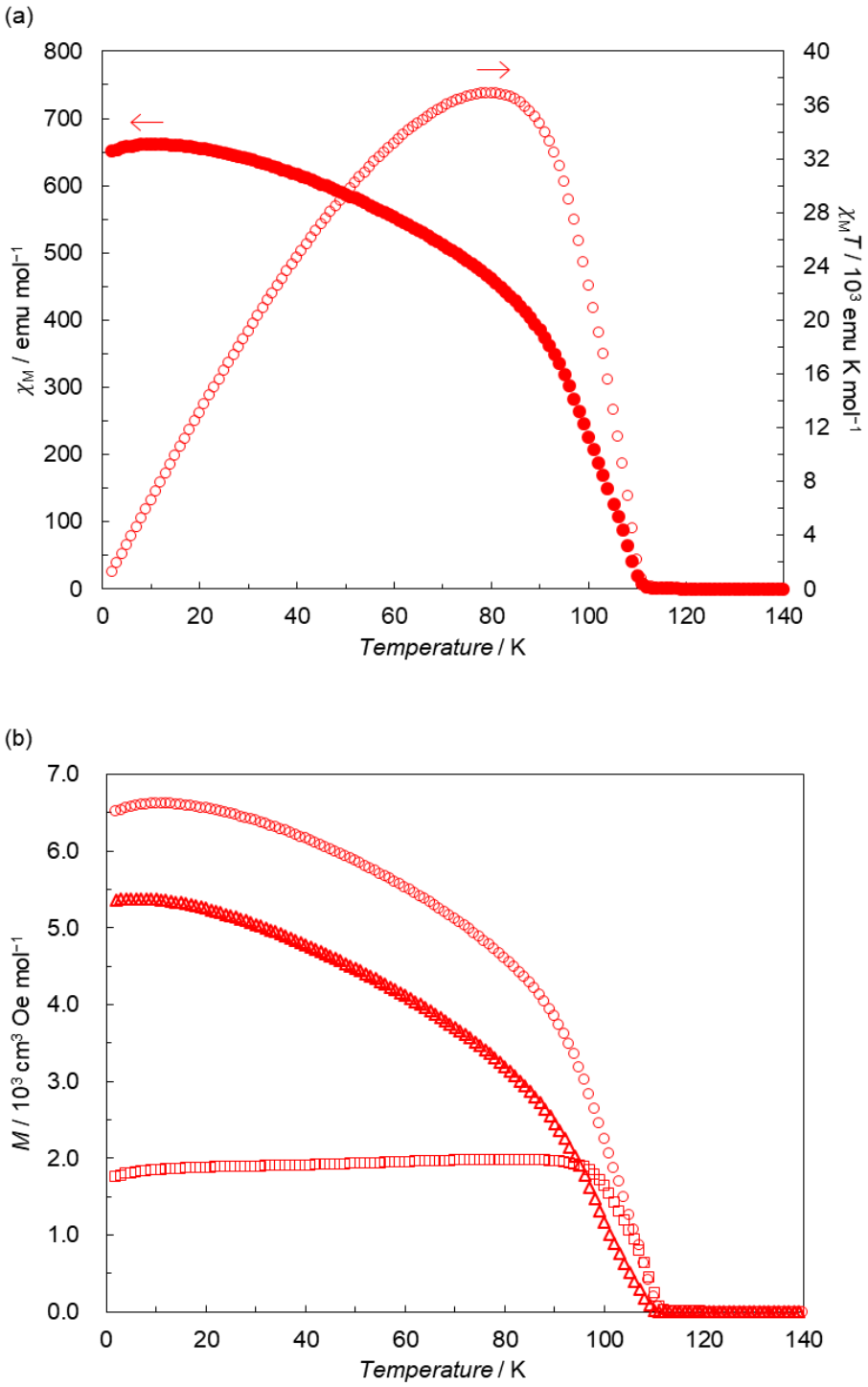

Figure 2-14. Magnetic properties of **Mn_3Cr_2** under an applied field of 10 Oe. (a) χ_M vs T plot (●) and $\chi_M T$ vs T plot (○). (b) Field-cooled magnetization (FCM; ○), remnant magnetization (RM; △), zero-field-cooled magnetization (ZFCM; □).

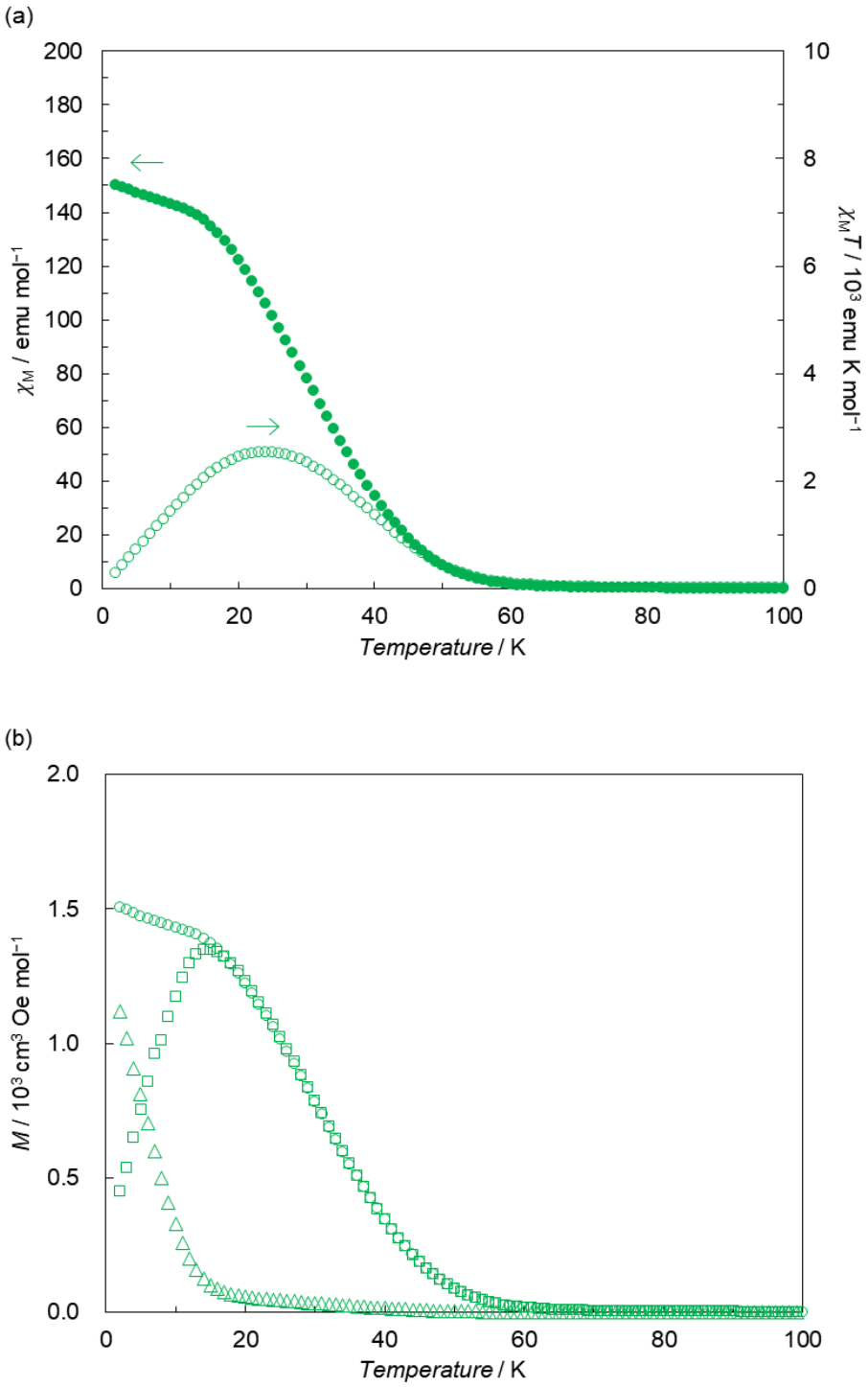

Figure 2-15. Magnetic properties of **Ni_3Cr_2** under an applied field of 10 Oe. (a) χ_M vs T plot (●) and $\chi_M T$ vs T plot (○). (b) Field-cooled magnetization (FCM; ○), remnant magnetization (RM; △), zero-field-cooled magnetization (ZFCM; □).

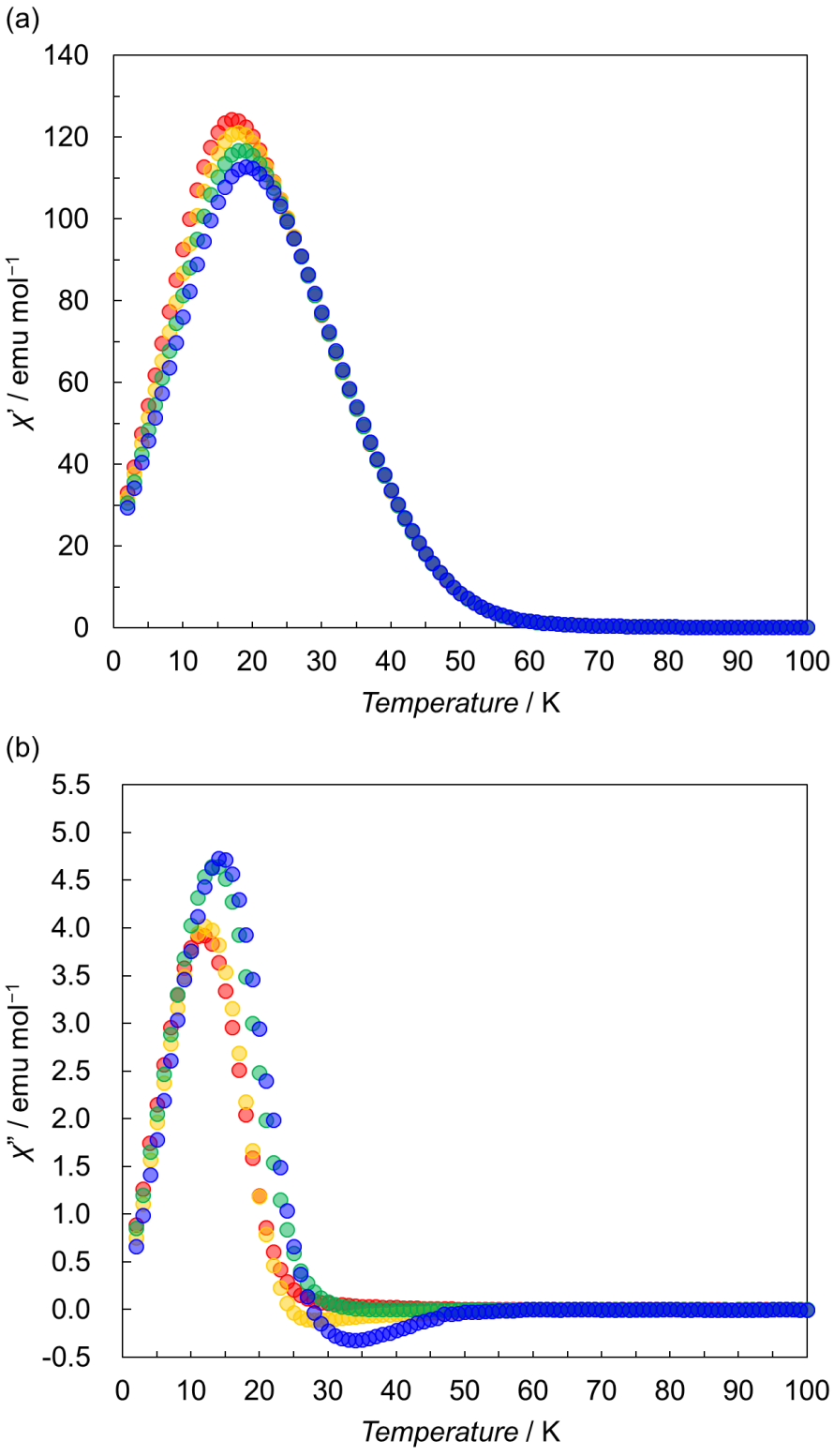

Figure 2-16. AC magnetic behavior of **Ni_3Cr_2** with frequencies of 1 (red), 10 (yellow), 100 (green), and 1000 Hz (blue). (a) χ' vs T plot. (b) χ'' vs T plot.

Because the T_c of **Ni_3Cr_2** is lower than the measurement temperature, only **Mn_3Cr_2** was used for the evaluation of the magnetic perturbation. For magnetization of **Mn_3Cr_2** during the assessment, a commercial neodymium magnet of 2000 Oe was embedded into the backside of the Raman sample cell, in which the magnetic field is sufficiently strong to magnetize **Mn_3Cr_2**. The magnetized **Mn_3Cr_2** exhibited a quick conversion within 600 s (**Figure 2-17**); however, there was no notable difference in the isomer ratio between the magnetized and the non-magnetized **Mn_3Cr_2** (**Figure 2-18**). From the viewpoint of the proposed mechanism of o-p conversion through an excitation process by external stimuli,[5g,7] the inner magnetic field and paramagnetic metal ions might play a part in the promotion of the o-p conversion. Here diamagnetic $Zn^{II}_3[Co^{III}(CN)_6]_2$ (**Zn_3Co_2**) is expected to give more significant information about effects of paramagnetic centers; however, the o-p ratio in **Zn_3Co_2**, unfortunately, could not be determined by this measurement with an excitation light wavelength of 532 nm due to extremely strong and broad fluorescent band overlapping with the Raman bands of $S_0(0)$ for p-H_2 and $S_0(1)$ for o-H_2.

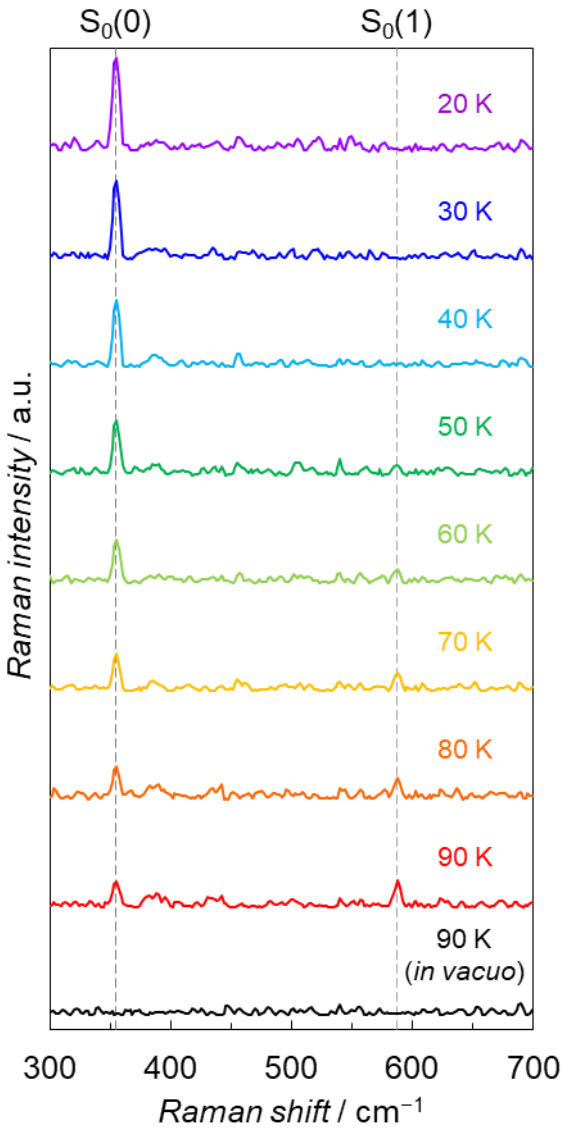

Figure 2-17. Temperature-dependent *in-situ* Raman spectra of **Mn_3Cr_2** under reduced pressure (black line) and H_2 gas atmosphere at 100 kPa (colored lines), where a neodymium magnet was embedded into the backside of Raman sample basket to magnetize the sample.

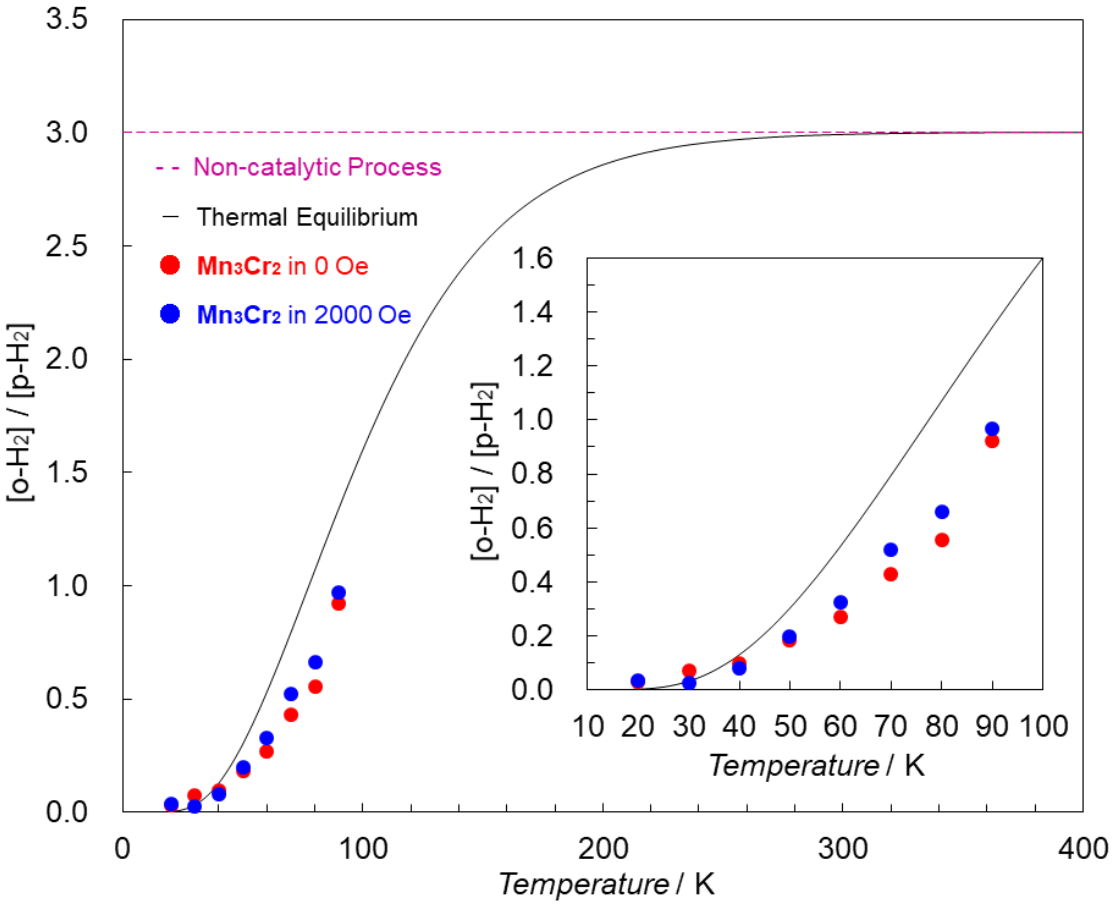

Figure 2-18. Temperature-dependent abundance ratio of the nuclear spin isomer ([o-H_2]/[p-H_2]) for H_2 confined in **Mn_3Cr_2** under external magnetic field of 0 Oe (red plots) and 2000 Oe (blue plots), estimated ratio obtained in cooling process from RT without catalytic treatment (pink), and theoretical ratio in thermal equilibrium based on the Boltzmann distribution of H_2 in the free rotational state (black line). The inset is an enlarged view of the low-temperature region.

Conclusions

In conclusion, two magnetic PBAs with a large Brunauer-Emmett-Teller surface area (SA_{BET}), $\{Mn^{II}_3[Cr^{III}(CN)_6]_2\}$ (**Mn_3Cr_2**; SA_{BET} = 683 $m^2\ g^{-1}$) and $\{Ni^{II}_3[Cr^{III}(CN)_6]_2\}$ (**Ni_3Cr_2**; SA_{BET} = 620 $m^2\ g^{-1}$), showed type-I behavior in the H_2 adsorption at 77 K and exhibited a swift ortho-para (o-p) conversion at a temperature range of 20–90 K within the time constant of 600 s, which was confirmed by *in-situ* Raman microspectroscopy under an H_2 gas atmosphere (100 kPa) and applied magnetic field (0 and 2000 Oe). Furthermore, the deviation of the o-p ratio ([o-H_2]/[p-H_2]) below the theoretical abundance ratio based on the Boltzmann distribution of H_2 in a free rotational state suggested the promotion of the o-p conversion at higher temperatures. These experimental pieces of evidence indicated the feasibility of PBAs having a defective porous framework as swift and efficient o-p conversion catalysts.

References

1. (a) A. Farkas, Orthohydrogen, Parahydrogen and Heavy Hydrogen, *Cambridge Univ. Press*, **1935**.; (b) J. W. Leachman, R. T. Jacobsen, S. G. Penoncello, E. W. Lemmon, *J. Phys. Chem.*, **2009**, *38* (3), 721–748.
2. (a) R. B. Scott, F. G. Brickwedde, H. C. Urey, M. H. Wahl, *J. Chem. Phys.*, **1934**, *2* (8), 454–464.; (b) K. Motizuki, T. Nagamiya, *J. Phys. Soc. Jpn.*, **1956**, *11* (2), 93–104.; (c) F. Schmidt, *Phys. Rev. B.*, **1974**, *10* (10), 4480–4484.; (d) I. F. Silvera, *Rev. Mod. Phys.*, **1980**, *52* (2), 393–452.
3. (a) A. H. Larsen, F. E. Simon, C. A. Swenson, *Rev. Sci. Instrum.*, **1948**, *19* (4), 266–269.; (b) G. E. Schmauch, A. H. Singleton, *Ind. Eng. Chem.*, **1964**, *56* (5), 20–31.; (c) S. A. Sherif, N. Zeytinoglu, T. N. Vezirğlu, *Int. J. Hydrog. Energy*, 1997, 22 (7), 683–688.
4. (a) K. F. Bonhoeffer, P. Harteck, *Z. Phys. Chem.*, **1929**, *4B* (1), 113–141.; (b) L. Farkas, L. Sandler, *J. Chem. Phys.*, **1940**, *8* (3), 248–251.; (c) D. H. Weitzel, O. E. Park, *Rev. Sci. Instrum.*, **1956**, *27* (1), 57–58.; (d) D. H. Weitzel, W. V. Loebenstein, J. W. Draper, O. E. Park, *J. Res. Natl. Bur. Std.*, **1958**, *60* (3), 221–227.; (e) K. G. Petzinger, D. J. Scalapino, *Phys. Rev. B*, **1973**, *8* (1), 266–279.; (f) Y. Ishii, *Prog. Surf. Sci.*, **1986**, *21* (2), 163–208.; (g) E. Ilisca, *Prog. Surf. Sci.*, **1992**, *41* (3), 217–335.; (h) S. Paris, E. Ilisca, *J. Phys. Chem. A*, **1999**, *103* (25), 4964–4968.
5. (a) P. Avouris, D. Schmeisser, J. E. Demuth, *Phys. Rev. Lett.*, **1982**, *48* (3), 199–202.; (b) S. Andersson, J. Harris, *Phys. Rev. Lett.*, **1982**, *48* (8), 545–548.; (c) E. Ilisca, *Phys. Rev. Lett.*, **1991**, *66* (5), 667–670.; (d) K. Fukutani, K. Yoshida, M. Wilde, W. A. Diño, M. Matsumoto, T. Okano, *Phys. Rev. Lett.*, **2003**, *90* (9), 096103.; (e) K. Niki, T. Kawauchi, M. Matsumoto, K. Fukutani, T. Okano, *Phys. Rev. B*, **2008**, *77* (20), 201404.; (f) K. Fukutani, T. Sugimoto, *Prog. Surf. Sci.*, **2013**, *88* (4), 279–348.; (g) T. Sugimoto, K. Fukutani, *Phys. Rev. Lett.*, **2014**, *112* (14), 146101.
6. (a) N. Watanabe, Y. Kimura, A. Kouchi, T. Chigai, T. Hama, V. Pirronello, *Astrophys. J. Lett.*, **2010**, *714* (2), L233–L237.; (b) T. Sugimoto, K. Fukutani, *Nat. Phys.*, **2011**, *7*, 307–310.; (c) M. Chehrouri, J.-H. Fillion, H. Chaabouni, H. Mokrane, E. Congiu, F. Dulieu, E. Matar, X. Michaut, J. L. Lemaire, *Phys. Chem. Chem. Phys.*, **2011**, *13* (6), 2172–2178.; (d) T. Hama, K. Kuwahata, N. Watanabe, A. Kouchi, Y. Kimura, T. Chigai, V. Pirronello, *Astrophys. J.*, **2012**, *757* (2), 185.; (e) H. Ueta, N. Watanabe, T. Hama, A. Kouchi, *Phys. Rev. Lett.*, **2016**, *116* (25), 253201.
7. (a) E. Ilisca, *Eur. Phys. Lett.*, **2013**, *104* (1), 18001.; (b) E. Ilisca, F. Ghiglieno, *Eur.*

Phys. *J*. *B*, **2014**, *87*, 235.

8. (a) M. Eddaoudi, J. Kim, N. Rosi, D. Vodak, J. Wachter, M. O'Keeffe, O. M. Yaghi, *Science*, **2002**, *295* (5554), 469–472.; (b) S. Kitagawa, R. Kitaura, S. Noro, *Angew*. *Chem*., *Int*. *Ed*., **2004**, *43* (18), 2334–2375.; (c) J. L. C. Rowsell, O. M. Yaghi, *Micropor*. *Mesopor*. *Mater*. **2004**, *73* (1–2), 3–14.; (d) G. Férey, *Chem*. *Soc*. *Rev*., **2008**, *37*, 191.; (e) G. Férey, C. Serre, *Chem*. *Soc*. *Rev*., **2009**, *38* (5), 1380–1399.
9. (a) S. A. FitzGerald, K. Allen, P. Landerman, J. Hopkins, J. Matters, R. Myers, J. L. C. Rowsell, *Phys*. *Rev*. *B* **2008**, *77* (22), 224301.; (b) N. Nijem, J.-F. Veyan, L. Kong, H. Wu, Y. Zhao, J. Li, D. C. Langreth, Y. J. Chabal, *J*. *Am*. *Chem*. *Soc*. **2010**, *132* (42), 14834–14848.; (c) S. A. FitzGerald, J. Hopkins, B. Burkholder, M. Friedman, J. L. C. Rowsell, *Phys*. *Rev*. *B* **2010**, *81* (10), 104305.; (d) T. Kosone, A. Hori, E. Nishibori, Y. Kubota, A. Mishima, M. Ohba, H. Tanaka, K. Kato, J. Kim, J. A. Real, S. Kitagawa, M. Takata, *R*. *Soc*. *open sci*. **2015**, *2* (7), 150006.
10. (a) K. W. Chapman, P. J. Chupas E. R. Maxey, J. W. Richardson, *Chem*. *Commun*., **2006**, (38), 4013–4015.; (b) M. R. Hartman V. K. Peterson, Y. Liu, S. S. Kaye, J. R. Long, *Chem*. *Mater*. **2006**, *18* (14), 3221–3224.
11. (a) S. S. Kaye, J. R. Long, *J*. *Am*. *Chem*. *Soc*., **2005**, *127* (18), 6506–6507.; (b) K. W. Chapman, P. D. Southon, C. L. Weeks, C. J. Kepert, *Chem*. *Commun*., **2005**, (26), 3322–3324.; (c) S. Natesakhawat, J. T. Culp, C. Matranga, B. Bockrath, *J*. *Phys*. *Chem*. *C*, **2007**, *111* (2), 1055–1060.; (d) S. S. Kaye, J. R. Long, *Catal*. *Today*, **2007**, *120* (3–4), 311–316.; (e) L. Reguera, C. P. Krap, J. Balmaseda, E. Reguera, *J*. *Phys*. *Chem*. *C*, **2008**, *112*, (40), 15893–15899.; (f) C. P. Krap, J. Balmaseda, L. F. del Castillo, B. Zamora, E. Reguera, *Energy Fuels*, **2010**, *24* (1), 581–589.; (g) A.-H. Yuan, C.-X. Chu, H. Zhou, P. Yuan, K.-K. Liu, L. Li, Q.-F. Zhang, X. Chen, Y.-Z. Li, *Eur*. *J*. *Inorg*. *Chem*., **2010**, (6), 866–871.; (h) J. Jiménez–Gallegos, J. Rodríguez–Hernández, H. Yee–Madeira, E. Reguera, *J*. *Phys*. *Chem*. *C*, **2010**, *114* (11), 5043–5048.; (i) C. P. Krap, J. Balmaseda, B. Zamora, E. Reguera, *Int*. *J*. *Hydrog*. *Energy*, **2010**, *35* (19), 10381–10386.; (j) A. A. Al-Hajjaj, B. Zamora, D. V. Bavykin, A. A. Shah, F. C. Walsh, E. Reguera, *Int*. *J*. *Hydrog*. *Energy*, **2012**, *37*(1), 318−326.; (k) L. Hu, P. Zhang, Q. Chen, H. Zhong, X. Hu, X. Zheng, Y. Wang, N. Yan, *Cryst*. *Growth Des*., **2012**, *12* (5), 2257−2264.; (l) B. Zamora, A. A. Al-Hajjaj, A. A. Shah, D. V. Bavykin, E. Reguera, *Int*. *J*. *Hydrog*. *Energy*, **2013**, *38* (15), 6406–6416.; (m) P. Bhatt, S. Banerjee, S. Anwar, M. D. Mukadam, S. S. Meena, S. M. Yusuf, *ACS Appl*. *Mater*. *Interfaces*, **2014**, *6*, 17579−17588.; (n) N. Torres, H. Osiry, A. Rodríguez, L. Martínez-dlCruz, A. A. Lemus-Santana, E. Reguera, *Z*. *Anorg*. *Allg*. *Chem*., **2018**, *644* (8–9), 415–423.

12. (a) V. Gadet, T. Mallah, I. Castro, M. Verdaguer, P. Veillet, *J. Am. Chem. Soc.*, **1992**, *114* (23), 9213–9214.; (b) T. Mallah, S. Thiébaut, M. Verdaguer, P. Veillet, *Science*, **1993**, *262* (5139), 1554–1557.; (c) S. Ferlay, T. Mallah, R. Ouahès, P. Veillet, M. Verdaguer, *Nature*, **1995**, *378*, 701–703.; (d) O. Sato, T. Iyoda, A. Fujishima, K. Hashimoto, *Science*, **1996**, *272* (5262), 704–705.; (e) S. Ohkoshi, T. Iyoda, A. Fujishima, K. Hashimoto, *Phys. Rev. B*, **1997**, *56* (18), 11642–11652.; (f) M. Verdaguer, A. Bleuzena, V. Marvaud, J. Vaissermann, M. Seuleiman, C. Desplanches, A. Scuiller, C. Train, R. Garde, G. Gelly, C. Lomenech, I. Rosenman, P. Veillet, C. Cartier, F. Villain, *Coord. Chem. Rev.*, **1999**, *190-192*, 1023–1047.; (g) S. M. Holmes, G. S. Girolami, *J. Am. Chem. Soc.*, **1999**, *121* (23), 5593–5594.; (h) Ø. Hatlevik, W. E. Buschmann, J. Zhang, J. L. Manson and J. S. Miller, *Adv. Mater.*, **1999**, *11* (11), 914–918.; (i) S. Ferlay, T. Mallah, R. Ouahès, P. Veillet, M. Verdaguer, *Inorg. Chem.*, **1999**, *38* (2), 229–234.; (j) N. Usuki, M. Yamada, M. Ohba, H. Ōkawa, *J. Solid State Chem.*, **2001**, *159* (2), 328–335.; (k) S. Osamu, H. Shinya, E. Yasuaki, G. Zhong-Ze, *Bull. Chem. Soc. Jpn.*, **2003**, *76* (3), 443–470.; (l) S. Ohkoshi, K. Aria, Y. Sato, K. Hashimoto, *Nature Mater.*, **2004**, *3*, 857–861.; (m) T. Uemura, M. Ohba, S. Kitagawa, *Inorg. Chem.*, **2004**, *43* (23), 7339–7345.; (n) M. Zentková1, Z. Arnold, J. Kamarád, V. Kavečanský, M. Lukáčová, S. Mat'aš1, M. Mihalik, Z. Mitróová, A. Zentko, *J. Phys.*: *Condens. Matter.*, **2007**, *19* (26), 266217.; (o) S. S. Kaye, H. J. Choi, J. R. Long, *J. Am. Chem. Soc.*, **2008**, *130* (50), 16921–16925.; (p) H. Ohmagari, R. Ohtani, M. Nakaya, M. Ohba, M. Nakamura, L. F. Lindoy, O. Sato, S. Hayami, *Dalton Trans.*, **2016**, *45* (42), 16784–16788.

13. (a) A Ludi, H. U. Guedel, M. Ruegg, *Inorg. Chem.*, **1970**, *9* (10), 2224–2227.; (b) H. U. Güdel, *Acta Chem. Scand.*, **1972**, *26*, 2169–2176.; (c) H. U. Güdel, H. Stucki, A. Ludi, *Inorg. Chim. Acta*, **1973**, *7*, 121–124.; (d) H. J. Buser, D. Schwarzenbach, W. Petter, A. Ludi, *Inorg. Chem.*, **1977**, *16* (11), 2704–2710.; (e) G. W. Beall, W. O. Milligan, J. Korp, I. Bernal, *Inorg. Chem.*, **1977**, *16* (11), 2715–2718.; (f) G. W. Beall, W. O. Milligan, J. A. Petrich, B. I. Swanson, *Inorg. Chem.*, **1978**, *17* (11), 2978–2981.; (g) D. F. Mullica, W. O. Milligan, G. W. Beall, W. L. Reeves, *Acta Cryst. B*, **1978**, *34* (12), 3558–3561.; (h) D. F. Mullica, J. D. Oliver, W. O. Milligan, F. W. Hills, *Inorg. Nucl. Chem. Lett.*, **1979**, *15* (9–10), 361–365.; (i) F. Herren, P. Fischer, A. Ludi, W. Haelg, *Inorg. Chem.*, **1980**, *19* (4), 956–959.; (j) D. F. Mullica, J. T. Zielke, E. L. Sappenfield, *J. Solid State Chem.*, **1994**, *112* (1), 92–95.; (k) A. Ratuszna, S. Juszczyka, G. Małecki, *Powder Diffr.*, **1995**, *10* (4), 300–305.; (l) D. F. Mullica, P. A. B. Colot, J. A. Kautz, R. J. Smith, E. L. Sappenfield, *J. Solid State Chem.*, **1997**, *129* (1), 17–21.; (m) D. F. Mullica, F. H. Alvarez, J. A. Kautz, E. L.

Sappenfield, *J. Solid State Chem*., **1998**, *140* (1), 140–144.; (n) G. Małecki, A. Ratuszna, *Powder Diffr*., **1999**, *14* (1), 25–30.; (o) D. F. Mullica, J. M. Farmer, J. A. Kautz, *J. Coord. Chem*., **1999**, *48* (4), 449–457.; (p) A. Widmann, H. Kahlert, I. Petrovic-Prelevic, H. Wulff, J. V. Yakhmi, N. Bagkar, F. Scholz, *Inorg. Chem*., **2002**, *41* (22), 5706–5715.; (q) P. Franz, C. Ambrus, A. Hauser, D. Chernyshov, M. Hostettler, J. Hauser, L. Keller, K. Krämer, H. Stoeckli-Evans, P. Pattison, H.-B. Bürgi, S. Decurtins, *J. Am. Chem. Soc*., **2004**, *126* (50), 16472–16477.; (r) A. L. Goodwin, K. W. Chapman, C. J. Kepert, *J. Am. Chem. Soc*., **2005**, *127* (51), 17980–17981.; (s) Z. Lü, X. Wang, Z. Liu, F. Liao, S. Gao, R. Xiong, H. Ma, D. Zhang, D. Zhu, *Inorg. Chem*., **2006**, *45* (3), 999–1004.; (t) W. Dong, W. Zhang, Y. Ou-Yang, L.-N. Zhu, D.-Z. Liao, K. Yoshimura, Z.-H. Jiang, S.-P. Yan, P. Chen, *J. Magn. Magn. Mater*., **2007**, *309* (1), 7–10.; (u) E. J. M. Vertelman, T. T. A. Lummen, A. Meetsma, M. W. Bouwkamp, G. Molnar, P. H. M. van Loosdrecht, P. J. van Koningsbruggen, *Chem. Mater*., **2008**, *20* (4), 1236–1238.; (v) J.-H. Her, P. W. Stephen, C. M. Kareis, J. G. Moore, K. S. Min, J.-W. Park, G. Bali, B. S. Kennon, J. S. Miller, *Inorg. Chem*., **2010**, *49* (4), 1524–1534.; (w) S. Adak, L. L. Daemen, M. Hartl, D. Williams, J. Summerhill, H. Nakotte, *J. Solid State Chem*., **2011**, *184* (11), 2854–2861.; (x) C. M. Kareis, S. H. Lapidus, J.-H. Her, P. W. Stephens, J. S. Miller, *J. Am. Chem. Soc*., **2012**, *134* (4), 2246–2254.; (y) A. I. Rykov, X. Li, J. Wang, *J. Solid State Chem*., **2015**, *227*, 35–44.; (z) D. Wardecki, D. O. Ojwang, J. Grins, G. Svensson, *Cryst. Growth Des*., **2017**, *17* (3), 1285–1292.

14. (a) J. H. Bigelow, *Inorg. Synth*., **1946**, *2*, 203–205.; (b) J. C. Reeve, *J. Chem. Educ*., **1985**, *62* (5), 444–445.
15. (a) K. S. W. Sing, D. H. Everett, R. A. W. Haul, L. Moscou, R. A. Pierotti, J. Rouquérol, T. Siemieniewska, *Pure Appl. Chem*., **1985**, *57* (4), 603–619.; (b) M. Thommes, K. Kaneko, A. V. Neimark, J. P. Olivier, F. Rodriguez-Reinoso, J. Rouquerol, K. S. W. Sing, *Pure Appl. Chem*., **2015**, *87* (9–10), 1051–1069.
16. (a) H. P. Gush, E. J. Allen, H. L. Welsh, W. F. J. Hare, *Can. J. Phys*., **1960**, *38* (2), 176–193.; (b) W. L. Mao, H. Mao, A. F. Goncharov, V. V. Struzhkin, Q. Guo, J. Hu, J. Shu, R. J. Hemley, M. Somayazulu, Y. Zhao, *Science*, **2002**, *297* (5590), 2247–2249.; (c) T. A. Strobel, E. D. Sloan, C. A. Koh, *J. Chem. Phys*., **2009**, *130* (1), 014506.; (d) M. J. Matthews, G. Petitpas, S. M. Aceves, *Appl. Phys. Lett*., **2011**, *99* (8), 081906. (e) L.-M. Sutherland, J. N. Knudson, M. Mocko, R. M. Renneke, *Nucl. Instrum. Methods Phys. Res. A*, **2016**, *810*, 182–185.

Concluding Remarks

In this thesis, the author systematically prepared defective $[Cr^{III}(CN)_6]^{3-}$-based Prussian Blue analogs (PBAs), $\{M^{II}_3[Cr^{III}(CN)_6]_2 \cdot nH_2O\}$ (**$M_3Cr_2 \cdot nH_2O$**), and studied on their structural stability of upon application of the activation process for dehydration, adsorption properties toward N_2 and H_2 as guest molecules at liquid N_2 temperature (77 K), and catalytic ability on nuclear spin conversion of H_2 (ortho-para (o-p) conversion). Although physical properties (*e.g.* magnetism) of defective $[Cr^{III}(CN)_6]^{3-}$-based PBAs have been widely studied, there are only a few reports regarding their adsorption property, and their H_2 adsorption property at 77 K was completely unclear. The dehydrated **M_3Cr_2** (M = Mn, Fe, Co, Ni, Zn, and Cd) which had a large specific surface area and unsaturated metal sites exhibited type-I H_2 adsorption behavior with an adsorption amount of 1.06–1.42 wt% at 100 kPa, which is a comparable value to the reported values of other PBAs. The systematic investigations on the structural stability upon application of the heating under reduced pressure and the adsorption measurements toward N_2 and H_2 at 77 K provided potential availability of several **M_3Cr_2** series as adsorption materials which have physical and/or chemical framework properties interlocked with the adsorption property. In addition to the systematic investigation on structural stability and adsorption ability, swift and efficient o-p conversion for physisorbed H_2 was achieved within 600 s at longest using **Mn_3Cr_2** and **Ni_3Cr_2** as porous catalysts, which was confirmed by *in-situ* Raman microspectroscopy under an H_2 atmosphere. This result is the first report to confirm the o-p ratio for the H_2 confined in the anisotropic pore which deviated to para-enriched proportion, providing essential and rational guidance that porous structure with framework defects is effective to improve both of o-p conversion rate and efficiency. These works highlighted the potential availability of $[Cr^{III}(CN)_6]^{3-}$-based PBAs as molecule absorbents and materials applying the adsorption properties. More systematic investigations on the adsorption property and catalytic ability for o-p conversion would provide novel and sophisticated designs for ideal catalysis of o-p conversion and other unique utilities.

List of Publications

- “Swift and Efficient Nuclear Spin Conversion of Molecular Hydrogen Confined in Prussian Blue Analogs”
  Yuta Ohtsubo, Akio Mishima, Akihiro Hori, Ryotaro Matsuda, Ryo Ohtani, Masaaki Ohba,
  Chemistry Letters, **2020**, *49* (2), 149–152. (DOI: 10.1246/cl.190829).

Acknowledgments

The study in this thesis has been carried out under the direction of Dr. Masaaki Ohba from April 2014 to March 2020 at the Department of Chemistry, Graduate School of Science, Kyushu University. The author would like to express his deepest appreciation to Dr. Masaaki Ohba (Professor; Kyushu University) for the courteous guidance and encouragement on the research. The author was able to deeply learn about porous coordination polymer chemistry and his science. The author would like to express his cordial gratitude to Dr. Akihiro Hori (Assistant professor; Nagoya University) and Dr. Akio Mishima (Former postdoctoral researcher; Nagoya University) for the cooperation on the research planning, the collaboration of the *in-situ* Raman spectroscopy under a gas atmosphere at cryogenic temperature, and the valuable discussion that improved the contents of this thesis. Moreover, the author is thankful to Dr. Hiroki Miura (Postdoctoral researcher; Dresden University of Technology), Dr. Ryo Ohtani (Associate professor; Kyushu University), Dr. Tomomi Koshiyama (Associate professor; Ritsumeikan University) and Dr. Hiroki Oshio (Professor; University of Tsukuba and Dalian University of Technology) for their fruitful comments and heartful encouragement. The author is deeply grateful to Ms. Miho Tsuji (Ph.D. candidate; Kyushu University) and Mr. Haruka Yoshino (Ph.D. candidate; Kyushu University) from Prof. Ohba group for the cooperation on the SEM measurement and the magnetometry, respectively. The author thanks to all the former and current members of Prof. Ohba group as well for the kind supports. Furthermore, the author would like to give special thanks to Dr. Seth M. Cohen (Professor; University of California, San Diego) for providing a great opportunity to work in his group and the considerate encouragement. The author was able to have a precious overseas experience. Finally, the author thanks to Advanced Graduate Course on Molecular Systems for Devices, Kyushu University, and Graduate School of Science, Kyushu University for their financial supports during his Ph.D. period, which enable the author to have great opportunity to attend many domestic and international academic conferences and oversea research experience in the University of California, San Diego.

Yuta Ohtsubo
Department of Chemistry
Graduate School of Science
Kyushu University
March 2020

Chemistry Letters

Swift and Efficient Nuclear Spin Conversion of Molecular Hydrogen Confined in Prussian Blue Analogs

Yuta Ohtsubo, Akio Mishima, Akihiro Hori, Ryotaro Matsuda,
Ryo Ohtani, and Masaaki Ohba*

Advance Publication on the web December 10, 2019
doi:10.1246/cl.190829

Chemistry Letters Vol.49, No.X (2020)

Swift and Efficient Nuclear Spin Conversion of Molecular Hydrogen Confined in Prussian Blue Analogs

Yuta Ohtsubo, Akio Mishima, Akihiro Hori, Ryotaro Matsuda, Ryo Ohtani, and Masaaki Ohba*

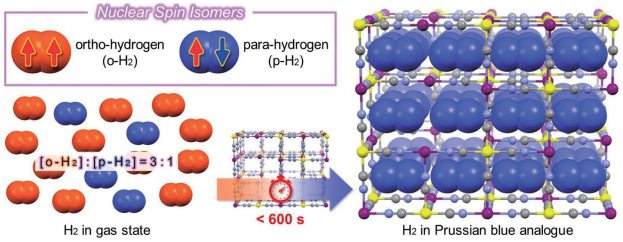

Prussian blue analogues (PBAs), $\{M^{II}_3[Cr^{III}(CN)_6]_2\}$ (**MCr**; M = Mn and Ni), effectively converted the ortho-isomer of molecular hydrogen (o-H_2) to the para-isomer (p-H_2) within 600 s as nuclear-spin conversion catalysts. In situ Raman microspectroscopy performed in an H_2 gas atmosphere (100 kPa) revealed that **MCr** accelerated the ortho-para (o-p) conversion of confined H_2 and increased the conversion temperature.

Chem. Lett. **2020**, 49 doi:10.1246/cl.190829

Received: November 11, 2019 | Accepted: December 4, 2019 | Web Released: December 10, 2019 CL-190829

Swift and Efficient Nuclear Spin Conversion of Molecular Hydrogen Confined in Prussian Blue Analogs

Yuta Ohtsubo,[1] Akio Mishima,[2] Akihiro Hori,[2] Ryotaro Matsuda,[2] Ryo Ohtani,[1] and Masaaki Ohba*[1]
[1]*Department of Chemistry, Graduate School of Science, Kyushu University, 744 Motooka, Nishi-ku, Fukuoka 819-0395, Japan*
[2]*Department of Chemistry and Biotechnology, Graduate School of Engineering, Nagoya University, Furo-cho, Chikusa-ku, Nagoya, Aichi 464-8603, Japan*

E-mail: ohba@chem.kyushu-univ.jp

The ortho-isomer of molecular hydrogen (o-H_2) was converted to the para-isomer (p-H_2) within 600 s by using Prussian blue analogs, $\{M^{II}_3[Cr^{III}(CN)_6]_2\}$ (**MCr**; M = Mn and Ni), as nuclear-spin conversion catalysts. The swift conversion was confirmed by *in-situ* Raman micro-spectroscopy under an H_2 gas atmosphere (100 kPa) in a low temperature range (20–90 K). The o-p ratio observed in **MCr** deviated from the theoretical value based on the Boltzmann distribution of H_2 in a free rotational state to the para-rich proportion, which suggested the promotion of the o-p conversion at higher temperature.

Keywords: Nuclear spin conversion | Prussian blue analogs | *In-situ* Raman microspectroscopy

H_2 is a highly promising alternative energy source to conventional fossil fuels because of its high gravimetric energy density and an environmentally friendly combustion product of H_2O. Among conventional physical methods for H_2 storage, liquefaction is commonly used in industrial settings because it facilitates the highest volumetric energy density and transportation efficiency. Long-period storage of liquid H_2, however, is limited by not only technical problems related to the storage vessel but also a latent "boil-off problem" caused by nuclear spin conversion between nuclear spin isomers. H_2 is comprised of two nuclear spin isomers, *i.e.*, ortho-H_2 (o-H_2; $I = 1, J =$ odd) and para-H_2 (p-H_2; $I = 0$, $J =$ even), where I and J are total nuclear spin angular momentum and rotational quantum number, respectively (Figure 1a).[1] Their rotational energy levels (E_{rot}) are quantized by the J value according to the Pauli exclusion principle. Moreover, the isomer ratio ([o-H_2]/[p-H_2]) is a function of temperature (T) based on the Boltzmann distribution with the rotational constant (B) of H_2 and the Boltzmann constant (k), where $B/k = 84.837$ K (eq 1, Figure 1b).[1]

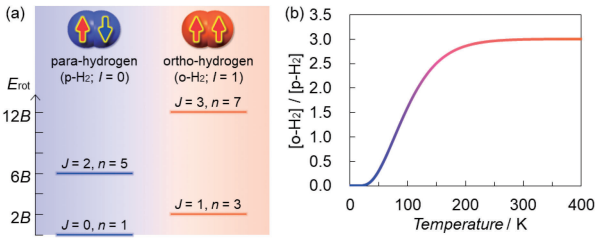

Figure 1. (a) Rotational energy diagram of nuclear spin isomers for H_2, where I, E_{rot}, B, J, and n denote total nuclear spin angular momentum, rotational energy, rotational constant, rotational quantum number, and degeneracy number, respectively. (b) Temperature-dependent nuclear spin isomer ratio ([o-H_2]/[p-H_2]).

$$[\text{o-H}_2]/[\text{p-H}_2] = \sum_{J=\text{odd}} \left[3(2J+1)\exp\left\{\frac{-BJ(J+1)}{kT}\right\}\right] \Big/ \sum_{J=\text{even}} \left[(2J+1)\exp\left\{\frac{-BJ(J+1)}{kT}\right\}\right] \quad (1)$$

The ortho-para (o-p) conversion is a spin-forbidden process with conversion rates of $\sim 10^{10}$ s in the gas state,[1] 1.14% h^{-1} in the liquid state,[2a] and approximately 1.9% h^{-1} in the solid state.[2b–2d] Moreover, this conversion is an exothermic reaction with a heat of conversion of $\sim$1.4 kJ mol^{-1} for o-H_2, which is higher than the heat of vaporization of H_2 (0.9 kJ mol^{-1}). Thus, liquid H_2, prepared by an immediate cooling process without any catalytic treatment, still contains $\sim$75% of o-H_2, which generates heat through the o-p conversion.[3] This is termed as the boil-off problem. Although solid catalysts to promote o-p conversion have been actively developed to solve this problem, such as magnetic materials[4] and diamagnetic metals,[5] several challenges remain regarding the conversion rate and efficiency. These challenges arise because of the low contact probability between the catalyst surface and o-H_2. Even when amorphous solid water systems are used as the o-p conversion catalysts, sophisticated techniques for sample preparation and extremely low handling temperature are required.[6] Several mechanisms for the activated o-p conversions by giant inhomogeneous surface electric fields of non-magnetic materials have also been proposed theoretically.[5g,7] From the abovementioned viewpoint, porous materials with a high surface area and readily accessible space can be considered excellent o-p conversion catalysts. Hence, porous coordination polymers (PCPs), also known as metal-organic frameworks (MOFs), have the potential to be used as o-p conversion catalysts.[8] MOF-5 and MOF-74 have catalyzed o-p conversion; however, the detailed mechanism of the observed conversion has not been elucidated.[9a–9c] On the other hand, we have reported a high catalytic ability of a Hofmann-type PCP, $\{Fe^{II}(\text{pyrazine})[Pd^{II}(CN)_4]\}$, for o-p conversion, which was accelerated by the perturbation of the electric field gradient through site-exchange of H_2 confined in the nano-sized pores around the boiling point of H_2 (20.27 K).[9d] In order to improve the conversion temperature, we focused on energy level splitting of the triply degenerate ground state of o-H_2 ($J = 1$) because the splitting may increase the p-H_2 proportion based on the Boltzmann distribution.[4h,5g] This phenomenon also has been reported in a Prussian blue analog (PBA) having a defective structure (Figure 2).[10c] PBAs are cyanide-bridged PCPs with diverse properties, such as high H_2 adsorption ability[10] and a magnetic property[11] derived from the 3-D porous structure.[12] Therefore, in this research, we selected PBA-based porous magnets, $\{M^{II}_3[Cr^{III}(CN)_6]_2 \cdot nH_2O\}$ (**MCr·*n*H_2O**; M = Mn and Ni), as new o-p conversion catalysts and verified the effect of magnetic perturbation induced in PCPs on o-p conversion as an additional factor to improve conversion temperature.

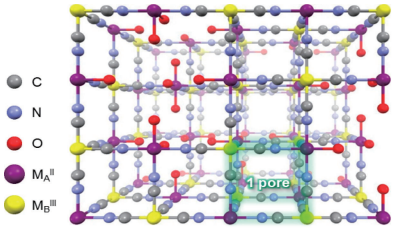

Figure 2. Schematic crystal structure of defective Prussian blue analogs (PBAs), $\{M_A^{II}{}_3[M_B^{III}(CN)_6]_2 \cdot nH_2O\}$ (**$M_AM_B \cdot nH_2O$**), where C, N, O, divalent M_A, and trivalent M_B are colored in gray, cyan, red, purple, and yellow, respectively, and lattice H_2O molecules and H atoms of coordinated H_2O molecules are omitted for clarity.

MCr·nH_2O were prepared by mixing aqueous solutions of $M^{II}Cl_2 \cdot xH_2O$ and $K_3[Cr^{III}(CN)_6]$ (see Supporting Information). Energy dispersive X-ray fluorescence (EDXRF) and scanning electron microscopy with energy dispersive X-ray (SEM-EDX) analysis of **MCr·nH_2O** indicated that the componential ratio ([M]/[Cr]) is consistent with the calculated value of 1.5 and the contamination of K^+ is below 0.1% in each batch (Figure S1 and Tables S1, S2). The number of total lattice and coordinated H_2O molecules (n) was determined to be 14 for **MnCr** and 15 for **NiCr** by elemental analysis and thermogravimetry analysis (TGA) of **MCr·nH_2O** (Figure S2). The trace amount of K^+ was ignored at this stage. In the Fourier transform infrared (FT-IR) spectra of **MCr·nH_2O**, the O-H stretching mode (ν(OH)) and H-O-H bending mode ($\delta(H_2O)$) were observed at 3800–2900 cm^{-1} and around 1610 cm^{-1}, respectively (Figure S3). The powder X-ray diffraction (PXRD) patterns of **MCr·nH_2O** were in good agreement with the typical diffraction pattern of PBAs (Figure S4).[12]

The dehydrated samples, **MCr**, were prepared by heating **MCr·nH_2O** at 120 °C for 24 h under vacuum. In the FT-IR spectra, the broad bands of ν(OH) and $\delta(H_2O)$ modes disappeared and the ν(C≡N) band slightly broadened without a large wavenumber shift, indicating the removal of H_2O molecules and the retainment of the cyanide-bridged framework after the dehydration treatment, respectively (Figure S3, Table S3). The PXRD patterns exhibited essentially the same results before and after the dehydration treatment, except for a broadening and a higher angle shift in almost all the peaks, which suggested shrinkage and distortion of the lattice by a change in the coordination geometry of the M^{II} sites, with the elimination of coordinated H_2O (Figure S4). The Brunauer-Emmett-Teller specific surface areas (SA_{BET}) of the dehydrated samples, **MnCr** and **NiCr**, were estimated from the results of N_2 adsorption at 77 K to be 683 and 620 $m^2 g^{-1}$, respectively, which were in the same range of the SA_{BET} values of other reported PBAs (Figure S5, Table S4).[10] In the H_2 adsorption measurement at 77 K, both **MnCr** and **NiCr** exhibited type-I behavior of typical microporous materials in the IUPAC classification,[13] with an adsorption amount of ~0.7 H_2 molecules per pore at 100 kPa (Figures 2, 3).

The nuclear spin state of H_2 confined in **MCr** was confirmed by *in-situ* Raman microspectroscopy under 100 kPa of H_2 atmosphere (Figure 4). The spectra indicated by bottom black lines in Figures 4(a) and 4(b) were obtained under reduced

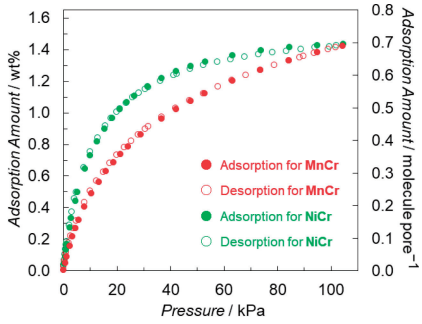

Figure 3. H_2 adsorption (●) and desorption (○) isotherms of **MnCr** (red) and **NiCr** (green) at 77 K.

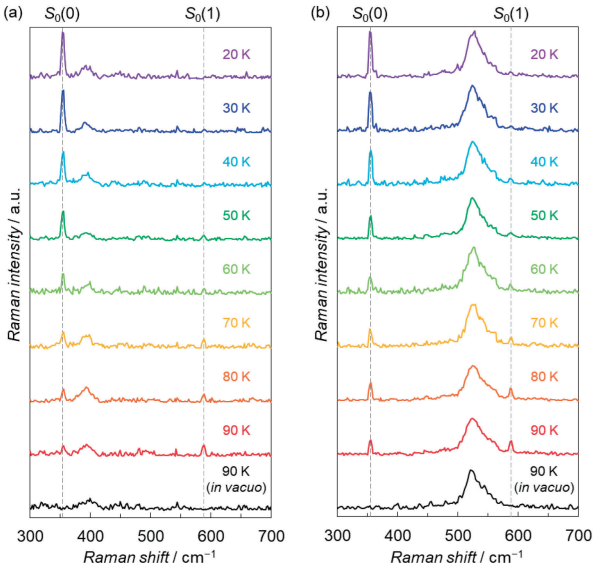

Figure 4. Temperature-dependent *in-situ* Raman spectra of (a) **MnCr** and (b) **NiCr** under reduced pressure (black line) and H_2 gas atmosphere at 100 kPa (colored lines) using an excitation laser with a wavelength of 532 nm. Neutral density (ND) filters with a total optical density (OD) of 1.6 were used to weaken the intensity of the excitation laser.

pressure at 90 K, where the observed broad Raman bands around 394 cm^{-1} for **MnCr** and 525 cm^{-1} for **NiCr** were assigned to the vibration modes of the host framework. After the injection of H_2 gas, two Raman-active bands newly appeared around 354.5 and 587.8 cm^{-1} at 90 K (Figure 4, red line). These bands were assigned to the rotational transition of $S_0(0)$ ($J = 2 \leftarrow 0$) for confined p-H_2 and $S_0(1)$ ($J = 3 \leftarrow 1$) for confined o-H_2 on comparison with the spectra of the desorption state and considering the Boltzmann distribution of H_2 (eq 1). Moreover, Raman bands of free H_2, which correspond to the energy gap between the initial and final states of each $S_0(0)$ and $S_0(1)$ transitions, were observed at 354 and 587 cm^{-1}, respectively (Figure 1a).[14] In both types of **MCr** (**MnCr** and **NiCr**), the increase of total peak intensities of $S_0(0)$ and $S_0(1)$ transitions as the temperature decreased suggests an increase in the amount that is adsorbed, because the Raman bands of free-H_2 were not detected in the measurement conditions. The peak intensity of p-H_2 gradually increased with cooling, whereas that of o-H_2 gradually decreased with cooling and almost vanished around

30 K (Figure 4). In addition, time-profiles of the intensity of both $S_0(0)$ and $S_0(1)$ transitions showed rapid saturation and constancy during the integration processing (600 s), which suggested that the system reached an equilibrium state at initial process. Consequently, the o-p conversion for H_2 confined in **MCr** was completed with a time constant of 600 s at its longest. This was based on the laser exposure time (30 s) and the cumulative number (20 times).

$$[\text{o-H}_2]/[\text{p-H}_2] = \int_{581.0}^{592.1}\{f_{T,100\,\text{kPa}}(v) - f_{90\text{K},0\,\text{kPa}}(v)\}\text{d}v \Big/ \int_{349.7}^{360.8}\{f_{T,100\,\text{kPa}}(v) - f_{90\text{K},0\,\text{kPa}}(v)\}\text{d}v \quad (2)$$

The $[\text{o-H}_2]/[\text{p-H}_2]$ values observed in **MCr** were calculated from the integrated values of the peak areas of $S_0(0)$ and $S_0(1)$ transitions obtained from the spectrum of the desorption state (Figure 4, black line) as the baseline, where $f_{T,P}(v)$ and v are the function of spectra at a certain temperature (T) and pressure (P), and the Raman shift, respectively (eq 2, Figure 5). In the controlled experiments, wherein only a nickel-plated Raman sample cell without **MCr** was used, the $[\text{o-H}_2]/[\text{p-H}_2]$ value was constant in the temperature range from 90 to 20 K and the time range of 600 s, indicating that there is no effect of the instrument on the o-p conversion (Figures S6, S7). Figure 5 shows observed $[\text{o-H}_2]/[\text{p-H}_2]$ values in **MCr**. In both cases, the observed $[\text{o-H}_2]/[\text{p-H}_2]$ values decreased with lowering temperature, and the observed values were lower than the theoretical values of free H_2 above 40 K, which indicated successful increase in the conversion temperature. In addition, over the entire measurement temperature range, the observed full width at half maximum (FWHM) of both the $S_0(0)$ and $S_0(1)$ transitions in **MCr** ($\sim$6 cm^{-1}) was larger than those obtained by the abovementioned controlled experiments ($\sim$3 cm^{-1}), which suggests a rotational restraint of H_2 confined in **MCr** (Figures 5, S6). Because the Boltzmann distribution relating to the $[\text{o-H}_2]/[\text{p-H}_2]$ value depends on only the rotational constant (B) of H_2 (eq 1), the resultant deviation of the o-p ratio suggests the rotational restraint of the confined o-H_2. Such rotational restraint would be caused by the locally anisotropic potential fields derived from the structural defects of **MCr**, which is supported by rotational-vibrational density of states for H_2 confined in a PBA, $Cu^{II}_3[Co^{III}(CN)_6]_2$.[10c] Because the $[\text{o-H}_2]/[\text{p-H}_2]$ values observed for {Fe(pyrazine)[Pd(CN)$_4$]} having a non-defective porous structure followed the Boltzmann distribution,[9d] the resultant deviation for **MCr** suggested the contribution of a defective porous structure to provide a para-enriched isomer ratio. The similar results of both types of **MCr** suggest the importance of the defective porous structure instead of the framework components for achieving effective o-p conversion and ratio.

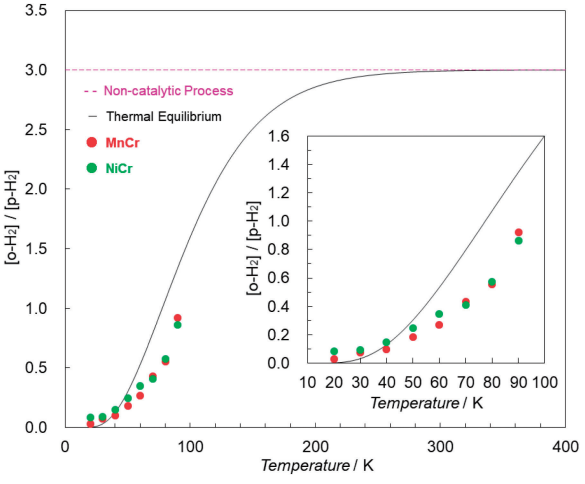

Figure 5. Temperature-dependent abundance ratio of the nuclear spin isomer ($[\text{o-H}_2]/[\text{p-H}_2]$) for H_2 confined in **MnCr** (red) and **NiCr** (green), estimated ratio obtained during cooling from room temperature without catalytic treatment (pink), and theoretical ratio in thermal equilibrium based on the Boltzmann distribution of H_2 in a free rotational state (black). The inset is an enlarged view of the low temperature region.

In order to verify the perturbation effect of the magnetic field in the pore on o-p conversion, the *in-situ* Raman spectroscopy was conducted again by using magnetized PBAs. **MnCr** showed a ferrimagnetic ordering at 108 K (Figure S8). **NiCr** showed a ferromagnetic ordering at 18 K (Figure S9). The different magnetic behavior from that of **NiCr·*n*H$_2$O** reflects a change in the magnetic interaction and a decrease in the magnetic domain size resulting from changes in the geometry and d electron configuration of the M^{II} sites due to dehydration.[11d,11j] Because the magnetic ordering temperature of **NiCr** is lower than the measurement temperature, only **MnCr** was used for the evaluation of the magnetic perturbation. For magnetization of **MnCr**, a commercial neodymium magnet of 2000 Oe was embedded into the backside of the Raman sample cell, in which the magnetic field is sufficiently strong to magnetize **MnCr**. The magnetized **MnCr** exhibited a quick conversion within 600 s (Figure S10); however, there was no notable difference in the isomer ratio between the magnetized and the non-magnetized **MnCr** (Figure S11). From the viewpoint of the proposed mechanism of o-p conversion through excitation by external stimuli,[5g,7] the inner magnetic field and paramagnetic metal ions might play a part in the promotion of the o-p conversion. Here diamagnetic $Zn^{II}_3[Co^{III}(CN)_6]_2$ (**ZnCo**) is expected to give significant information about effects of paramagnetic centers on the o-p conversion, but the o-p ratio could not be evaluated by this measurement due to a broad fluorescent band of **ZnCo** overlapping with the Raman bands of $S_0(0)$ for p-H_2 and $S_0(1)$ for o-H_2.

In conclusion, two magnetic PBAs, **MnCr** ($SA_{\text{BET}} = 683\ \text{m}^2\,\text{g}^{-1}$) and **NiCr** ($SA_{\text{BET}} = 620\ \text{m}^2\,\text{g}^{-1}$), showed type-I H_2 adsorption behavior and exhibited a swift o-p conversion within the time constant of 600 s, which was confirmed by *in-situ* Raman microspectroscopy under an H_2 gas atmosphere and applied magnetic field (0 and 2000 Oe). Furthermore, the deviation of the o-p ratio ($[\text{o-H}_2]/[\text{p-H}_2]$) below the theoretical abundance ratio based on the Boltzmann distribution of free H_2 suggested the promotion of the o-p conversion at higher temperatures. These results indicated the feasibility of PBAs having a defective porous framework as swift and efficient o-p conversion catalysts.

This work was supported by JSPS KAKENHI Grant Number of 16H06519 (Coordination Asymmetry) and 18H01997, and RIKEN Quantum Ordering project. We would like to thank Editage (www.editage.com) for English language editing.

Supporting Information is available on https://doi.org/10.1246/cl.190829.

References

1 a) A. Farkas, *Orthohydrogen, Parahydrogen and Heavy Hydrogen*, Cambridge University Press, London, **1935**. b) J. W. Leachman, R. T. Jacobsen, S. G. Penoncello, E. W. Lemmon, *J. Phys. Chem.* **2009**, *38*, 721.

2 a) R. B. Scott, F. G. Brickwedde, H. C. Urey, M. H. Wahl, *J. Chem. Phys.* **1934**, *2*, 454. b) K. Motizuki, T. Nagamiya, *J. Phys. Soc. Jpn.* **1956**, *11*, 93. c) F. Schmidt, *Phys. Rev. B* **1974**, *10*, 4480. d) I. F. Silvera, *Rev. Mod. Phys.* **1980**, *52*, 393.

3 a) A. H. Larsen, F. E. Simon, C. A. Swenson, *Rev. Sci. Instrum.* **1948**, *19*, 266. b) G. E. Schmauch, A. H. Singleton, *Ind. Eng. Chem* **1964**, *56*, 20. c) S. A. Sherif, N. Zeytinoglu, T. N. Veziroğlu, *Int. J. Hydrogen Energy* **1997**, *22*, 683.

4 a) K. F. Bonhoeffer, P. Harteck, *Z. Phys. Chem.* **1929**, *4B*, 113. b) L. Farkas, L. Sandler, *J. Chem. Phys.* **1940**, *8*, 248. c) D. H. Weitzel, O. E. Park, *Rev. Sci. Instrum.* **1956**, *27*, 57. d) D. H. Weitzel, W. V. Loebenstein, J. W. Draper, O. E. Park, *J. Res. Natl. Bur. Stand.* **1958**, *60*, 221. e) K. G. Petzinger, D. J. Scalapino, *Phys. Rev. B* **1973**, *8*, 266. f) Y. Ishii, *Prog. Surf. Sci.* **1986**, *21*, 163. g) E. Ilisca, *Prog. Surf. Sci.* **1992**, *41*, 217. h) S. Paris, E. Ilisca, *J. Phys. Chem. A* **1999**, *103*, 4964.

5 a) P. Avouris, D. Schmeisser, J. E. Demuth, *Phys. Rev. Lett.* **1982**, *48*, 199. b) S. Andersson, J. Harris, *Phys. Rev. Lett.* **1982**, *48*, 545. c) E. Ilisca, *Phys. Rev. Lett.* **1991**, *66*, 667. d) K. Fukutani, K. Yoshida, M. Wilde, W. A. Diño, M. Matsumoto, T. Okano, *Phys. Rev. Lett.* **2003**, *90*, 096103. e) K. Niki, T. Kawauchi, M. Matsumoto, K. Fukutani, T. Okano, *Phys. Rev. B* **2008**, *77*, 201404. f) K. Fukutani, T. Sugimoto, *Prog. Surf. Sci.* **2013**, *88*, 279. g) T. Sugimoto, K. Fukutani, *Phys. Rev. Lett.* **2014**, *112*, 146101.

6 a) N. Watanabe, Y. Kimura, A. Kouchi, T. Chigai, T. Hama, V. Pirronello, *Astrophys. J., Lett.* **2010**, *714*, L233. b) T. Sugimoto, K. Fukutani, *Nat. Phys.* **2011**, *7*, 307. c) M. Chehrouri, J.-H. Fillion, H. Chaabouni, H. Mokrane, E. Congiu, F. Dulieu, E. Matar, X. Michaut, J. L. Lemaire, *Phys. Chem. Chem. Phys.* **2011**, *13*, 2172. d) T. Hama, K. Kuwahata, N. Watanabe, A. Kouchi, Y. Kimura, T. Chigai, V. Pirronello, *Astrophys. J.* **2012**, *757*, 185. e) H. Ueta, N. Watanabe, T. Hama, A. Kouchi, *Phys. Rev. Lett.* **2016**, *116*, 253201.

7 a) E. Ilisca, *Eur. Phys. Lett.* **2013**, *104*, 18001. b) E. Ilisca, F. Ghiglieno, *Eur. Phys. J. B* **2014**, *87*, 235.

8 a) M. Eddaoudi, J. Kim, N. Rosi, D. Vodak, J. Wachter, M. O'Keeffe, O. M. Yaghi, *Science* **2002**, *295*, 469. b) S. Kitagawa, R. Kitaura, S. Noro, *Angew. Chem., Int. Ed.* **2004**, *43*, 2334. c) J. L. C. Rowsell, O. M. Yaghi, *Microporous Mesoporous Mater.* **2004**, *73*, 3. d) G. Férey, *Chem. Soc. Rev.* **2008**, *37*, 191. e) G. Férey, C. Serre, *Chem. Soc. Rev.* **2009**, *38*, 1380.

9 a) S. A. FitzGerald, K. Allen, P. Landerman, J. Hopkins, J. Matters, R. Myers, J. L. C. Rowsell, *Phys. Rev. B* **2008**, *77*, 224301. b) S. A. FitzGerald, J. Hopkins, B. Burkholder, M. Friedman, J. L. C. Rowsell, *Phys. Rev. B* **2010**, *81*, 104305. c) N. Nijem, J.-F. Veyan, L. Kong, H. Wu, Y. Zhao, J. Li, D. C. Langreth, Y. J. Chabal, *J. Am. Chem. Soc.* **2010**, *132*, 14834. d) T. Kosone, A. Hori, E. Nishibori, Y. Kubota, A. Mishima, M. Ohba, H. Tanaka, K. Kato, J. Kim, J. A. Real, S. Kitagawa, M. Takata, *R. Soc. Open Sci.* **2015**, *2*, 150006.

10 a) S. S. Kaye, J. R. Long, *J. Am. Chem. Soc.* **2005**, *127*, 6506. b) K. W. Chapman, P. D. Southon, C. L. Weeks, C. J. Kepert, *Chem. Commun.* **2005**, 3322. c) M. R. Hartman, V. K. Peterson, Y. Liu, S. S. Kaye, J. R. Long, *Chem. Mater.* **2006**, *18*, 3221. d) S. S. Kaye, J. R. Long, *Catal. Today* **2007**, *120*, 311. e) S. Natesakhawat, J. T. Culp, C. Matranga, B. Bockrath, *J. Phys. Chem. C* **2007**, *111*, 1055. f) L. Reguera, C. P. Krap, J. Balmaseda, E. Reguera, *J. Phys. Chem. C* **2008**, *112*, 15893. g) J. Jiménez-Gallegos, J. Rodríguez-Hernández, H. Yee-Madeira, E. Reguera, *J. Phys. Chem. C* **2010**, *114*, 5043. h) C. P. Krap, J. Balmaseda, L. F. del Castillo, B. Zamora, E. Reguera, *Energy Fuels* **2010**, *24*, 581. i) C. P. Krap, J. Balmaseda, B. Zamora, E. Reguera, *Int. J. Hydrogen Energy* **2010**, *35*, 10381. j) L. Hu, P. Zhang, Q. Chen, H. Zhong, X. Hu, X. Zheng, Y. Wang, N. Yan, *Cryst. Growth Des.* **2012**, *12*, 2257. k) P. Bhatt, S. Banerjee, S. Anwar, M. D. Mukadam, S. S. Meena, S. M. Yusuf, *ACS Appl. Mater. Interfaces* **2014**, *6*, 17579.

11 a) T. Mallah, S. Thiébaut, M. Verdaguer, P. Veillet, *Science* **1993**, *262*, 1554. b) S. Ferlay, T. Mallah, R. Ouahès, P. Veillet, M. Verdaguer, *Nature* **1995**, *378*, 701. c) O. Sato, T. Iyoda, A. Fujishima, K. Hashimoto, *Science* **1996**, *272*, 704. d) M. Verdaguer, A. Bleuzen, V. Marvaud, J. Vaissermann, M. Seuleiman, C. Desplanches, A. Scuiller, C. Train, R. Garde, G. Gelly, C. Lomenech, I. Rosenman, P. Veillet, C. Cartier, F. Villain, *Coord. Chem. Rev.* **1999**, *190–192*, 1023. e) S. M. Holmes, G. S. Girolami, *J. Am. Chem. Soc.* **1999**, *121*, 5593. f) Ø. Hatlevik, W. E. Buschmann, J. Zhang, J. L. Manson, J. S. Miller, *Adv. Mater.* **1999**, *11*, 914. g) N. Usuki, M. Yamada, M. Ohba, H. Ōkawa, *J. Solid State Chem.* **2001**, *159*, 328. h) S. Ohkoshi, K. Aria, Y. Sato, K. Hashimoto, *Nat. Mater.* **2004**, *3*, 857. i) T. Uemura, M. Ohba, S. Kitagawa, *Inorg. Chem.* **2004**, *43*, 7339. j) M. Zentková, Z. Arnold, J. Kamarád, V. Kavečanský, M. Lukáčová, S. Mat'aš, M. Mihalik, Z. Mitróová, A. Zentko, *J. Phys.: Condens. Matter* **2007**, *19*, 266217. k) S. S. Kaye, H. J. Choi, J. R. Long, *J. Am. Chem. Soc.* **2008**, *130*, 16921. l) H. Ohmagari, R. Ohtani, M. Nakaya, M. Ohba, M. Nakamura, L. F. Lindoy, O. Sato, S. Hayami, *Dalton Trans.* **2016**, *45*, 16784.

12 a) H. U. Güdel, H. Stucki, A. Ludi, *Inorg. Chim. Acta* **1973**, *7*, 121. b) Z. Lü, X. Wang, Z. Liu, F. Liao, S. Gao, R. Xiong, H. Ma, D. Zhang, D. Zhu, *Inorg. Chem.* **2006**, *45*, 999. c) W. Dong, W. Zhang, Y. Ou-Yang, L.-N. Zhu, D.-Z. Liao, K. Yoshimura, Z.-H. Jiang, S.-P. Yan, P. Cheng, *J. Magn. Magn. Mater.* **2007**, *309*, 7. d) S. Adak, L. L. Daemen, M. Hartl, D. Williams, J. Summerhill, H. Nakotte, *J. Solid State Chem.* **2011**, *184*, 2854.

13 a) K. S. W. Sing, D. H. Everett, R. A. W. Haul, L. Moscou, R. A. Pierotti, J. Rouquérol, T. Siemieniewska, *Pure Appl. Chem.* **1985**, *57*, 603. b) M. Thommes, K. Kaneko, A. V. Neimark, J. P. Olivier, F. Rodriguez-Reinoso, J. Rouquerol, K. S. W. Sing, *Pure Appl. Chem.* **2015**, *87*, 1051.

14 a) H. P. Gush, E. J. Allen, H. L. Welsh, W. F. J. Hare, *Can. J. Phys.* **1960**, *38*, 176. b) W. L. Mao, H. Mao, A. F. Goncharov, V. V. Struzhkin, Q. Guo, J. Hu, J. Shu, R. J. Hemley, M. Somayazulu, Y. Zhao, *Science* **2002**, *297*, 2247. c) T. A. Strobel, E. D. Sloan, C. A. Koh, *J. Chem. Phys.* **2009**, *130*, 014506. d) M. J. Matthews, G. Petitpas, S. M. Aceves, *Appl. Phys. Lett.* **2011**, *99*, 081906. e) L.-M. Sutherland, J. N. Knudson, M. Mocko, R. M. Renneke, *Nucl. Instrum. Methods Phys. Res. A* **2016**, *810*, 182.

Supporting Information

Chemistry Letters

Swift and Efficient Nuclear Spin Conversion of Molecular Hydrogen Confined in Prussian Blue Analogs

Yuta Ohtsubo, Akio Mishima, Akihiro Hori, Ryotaro Matsuda, Ryo Ohtani, and Masaaki Ohba*

Electronic Supporting Information for *Chemistry Letters*

Swift and Efficient Nuclear Spin Conversion of Molecular Hydrogen Confined in Prussian Blue Analogs

Yuta Ohtsubo, [1] Akio Mishima, [2] Akihiro Hori, [2] Ryotaro Matsuda,[2] Ryo Ohtani, [1] and Masaaki Ohba*[1]

[1] *Department of Chemistry, Graduate School of Science, Kyushu University, 744 Motooka, Nishi-ku, Fukuoka 819-0395, Japan*

[2] *Department of Chemistry and Biotechnology, Graduate School of Engineering, Nagoya University, Furo-cho, Chikusa-ku, Nagoya, Aichi 464-8603, Japan*

E-mail: ohba@chem.kyushu-univ.jp

Materials

All chemicals were purchased as reagent grade and used without further purification.

Synthesis of $K_3[Cr(CN)_6]$

$K_3[Cr(CN)_6]$ was synthesized according to a reported synthetic method with some modifications.[S1–S3] Mossy Zn (6.0 g, 91.8 mmol) was activated by immersing in 1 M HCl for 5 min, thoroughly washed with distilled water, and dried well in advance. Then the activated mossy Zn was added to a degassed aqueous solution (40 mL) of $CrCl_3 \cdot 6H_2O$ (20.0 g, 75.1 mmol) under a N_2 gas atmosphere at room temperature. After stirring over 3 h and removal of the remaining unreacted Zn by suction filtration, a solid $CH_3COONa \cdot 3H_2O$ (24.0 g, 176.4 mmol) was added to the resultant deep blue solution, which resulted in a rapid precipitate of chromium(II) acetate as bright red powder. The precipitate was collected by suction filtration under a N_2 gas atmosphere, repeatedly washed with degassed water, and dissolved in a degassed aqueous solution (50 ml) of KCN (30.0 g, 460.7 mmol). After removal of slight precipitate by suction filtration, an excess amount of methanol (~500 ml) was added to the dark green filtrate, which provided $K_4[Cr^{II}(CN)_6]$ as a light green precipitate. The precipitate was collected by suction filtration, repeatedly washed with methanol, and allowed to stand over 2 h for the air oxidation of the Cr^{II} ion. After completion of color change to yellow, a few repeated reprecipitation from water by an addition of an excess amount of methanol gave pure $K_3[Cr^{III}(CN)_6]$. Yellow crystalline powder. Yield: 15.5 g (47.7 mmol, 63.5% vs. $CrCl_3 \cdot 6H_2O$). FT-IR (cm^{-1}): $\nu_{C\equiv N}$ = 2130. EDXRF analysis (%): [K]/[Cr] = 2.85. No other elements were detected.

Synthesis of {$Mn_3[Cr(CN)_6]_2 \cdot 14H_2O$} ($MnCr \cdot 14H_2O$)

All the operations for the synthesis were conducted in the dark to avoid the decomposition of $K_3[Cr(CN)_6]$. A degassed aqueous solution (50 mL) of $K_3[Cr(CN)_6]$ (325.4 mg, 1.0 mmol) was added dropwise to a degassed aqueous solution (50 mL) of $MnCl_2 \cdot 4H_2O$ (395.8 mg, 2.0 mmol) with stirring under a N_2 gas atmosphere at room temperature, resulting in precipitation of light-green solid. After stirring over 2 days, the light-green precipitate was collected by centrifugation, repeatedly washed with distilled water, and dried in the air. Light-green powder. Yield: 228.3 mg (0.27 mmol, 54.8% vs. $K_3[Cr(CN)_6]$). Elemental analysis (%): Found: C 17.66, H 3.26, N 20.12; Calcd. for {$Mn_3[Cr(CN)_6]_2 \cdot 14H_2O$} ($C_{12}H_{28}N_{12}O_{14}Cr_2Mn_3$): C 17.30, H 3.39, N 20.17. FT-IR (cm^{-1}): ν(OH) = 3800–2900 (br), ν(C≡N) = 2162 (s), $\delta(H_2O)$ = 1611 (m). SEM-EDX analysis (%): [Mn]/[Cr] = 1.40. EDXRF analysis (%): [Mn]/[Cr] = 1.37, [K]/[Mn] < 0.05.

Synthesis of {$Ni_3[Cr(CN)_6]_2 \cdot 15H_2O$} ($NiCr \cdot 15H_2O$)

All the operations for the synthesis were conducted in the dark to avoid the decomposition of $K_3[Cr(CN)_6]$. An aqueous solution (50 mL) of $K_3[Cr(CN)_6]$ (325.4 mg, 1.0 mmol) was added dropwise to a aqueous solution (50 mL) of $NiCl_2 \cdot 6H_2O$ (475.4 mg, 2.0 mmol) with stirring at room temperature, resulting in precipitation of light-blue solid. After stirring over 2 days, the light-blue precipitate was collected by centrifugation, repeatedly washed with distilled water, and dried in the air. Green powder. Yield: 374.8 mg (0.43 mmol, 86.9% vs. $K_3[Cr(CN)_6]$). Elemental analysis (%): Found: C 16.69, H 3.56, N 19.20; Calcd. for {$Ni_3[Cr(CN)_6]_2 \cdot 15H_2O$} ($C_{12}H_{30}N_{12}O_{15}Cr_2Ni_3$): C 16.71, H 3.51, N 19.49. FT-IR (cm^{-1}): ν(OH) = 3800–2900 (br), ν(C≡N) = 2169 (s), $\delta(H_2O)$ = 1610 (m). SEM-EDX analysis (%): [Ni]/[Cr] = 1.57. EDXRF analysis (%): [Ni]/[Cr] = 1.78, [K]/[Ni] < 0.01.

Physical Measurement

Elemental analysis of C, H, and N atoms was conducted as quick as possible after loading sample by the staff of the Technical Support Division, Graduate School of Science, Kyushu University.

Powder X-ray diffractometry (RXPD) was conducted on a Rigaku Ultima IV diffractrometer using graphite-monochromated CuKα radiation and reflection-free single crystal Si sample holder in the air at room temperature (X-ray voltage: 40 kV, X-ray current: 40 μA, Angle range: 3–50°, Scan speed: 1° min^{-1}, Data-collecting step: 0.02°).

Scanning electron microscopy (SEM) was conducted on Micro-Calorimeter FESEM TES+ULTRA55 in The Ultramicroscopy Research Center, Kyushu University (Electron high tension (EHT) value: 10.00 keV).

Thermogravimetry analysis (TGA) was conducted on a Perkin Elmer STA6000 as quick as possible after loading sample under dry N_2 atmosphere (Temperature range: 30–700°C, Heating rate: 5°C min^{-1}, N_2 gas flow rate: 19.8 ml min^{-1}).

Energy dispersive X-ray fluorescence (EDXRF) analysis was conducted on a Shimadzu Rayny EDX-720 (X-ray voltage: 50 kV, X-ray current: 30 μA). The results were averaged over three runs.

Fourier transform infrared (FT-IR) spectroscopy was conducted on a JASCO FT/IR-4200 spectrometer using ATR method in the air at room temperature (Wavenumber range: 4000–650 cm^{-1}, Resolution: 4 cm^{-1}, Cumulative number: 1024 times).

The N_2 (99.999%) and H_2 (99.999%) adsorption/desorption measurements were conducted on MicrotracBEL BELSORP-max volumetric adsorption equipment at 77 K using liquid N_2 in a Dewar bottle (Pressure range of 0–105 kPa). The samples were activated again by heating at 120 °C for 4 h under vacuum after loading into the measurement glass tube before the measurement.

Magnetic susceptibility of the ground sample was recorded by Quantum Design MPMS-XL5R SQUID (Applied DC magnetic field: 10 Oe, Minimum temperature: 2 K). The sample was put into a gelatin capsule, placed in a plastic straw, fixed to the end of sample transport rod, and activated again by heating at 330 K over 3 h in the machine before the measurement.

Raman spectroscopy was carried on using Horiba Jobin Yvon iHR320 imaging spectrometer, Horiba Jobin Yvon Synapse CCD detector, Laser Quantum torus 532 laser, and a nickel-plated Raman sample cell (Laser beam wavelength: 532 nm, Laser beam exposure time: 30 s, Cumulative number: 20 times). For *in-situ* Raman spectroscopy under an H_2 gas atmosphere, the measurement temperature was controlled by UW404 CryoMini Compressor with BELCryo-20K temperature control system using Lake Shore Model 331 Cryogenic Temperature Controller, and the H_2 gas pressure was controlled by MicrotracBEL BELSORP-max volumetric adsorption equipment. For the measurement of samples, neutral density (ND) filters with the total optical density (OD) of 1.6 were used for weakening the excitation light intensity to avoid sample decomposition. For the controlled measurement of Raman sample cell, ND filter was not used to use an excitation laser with a maximum intensity. In order to magnetize samples, a commercial neodymium magnet of 2000 Oe was embedded into the cell of the Raman sample cell.

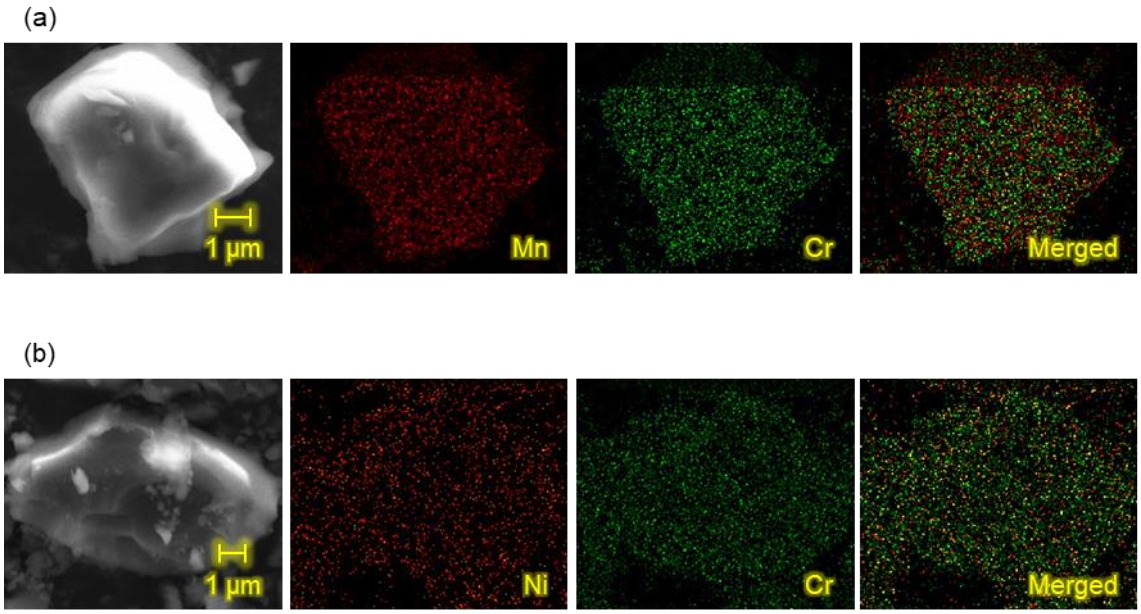

Figure S1. SEM images and elemental mapping of (a) **MnCr·14H$_2$O** and (b) **NiCr·15H$_2$O**, where Cr, Mn and Ni in the elemental mapping are colored in green, red and orange, respectively.

Table S1. EDXRF and SEM-EDX results of **MnCr·14H$_2$O**.

	[Mn] / wt%	[Cr] / wt%	[Mn] / [Cr]
SEM-EDX	59.744	40.456	1.40
EDXRF	59.142	40.858	1.37
Calculated value	61.313	38.687	1.50

Table S2. EDXRF and SEM-EDX results of **NiCr·15H$_2$O**.

	[Ni] / wt%	[Cr] / wt%	[Ni] / [Cr]
SEM-EDX	63.963	36.037	1.57
EDXRF	66.769	33.231	1.78
Calculated value	62.870	37.130	1.50

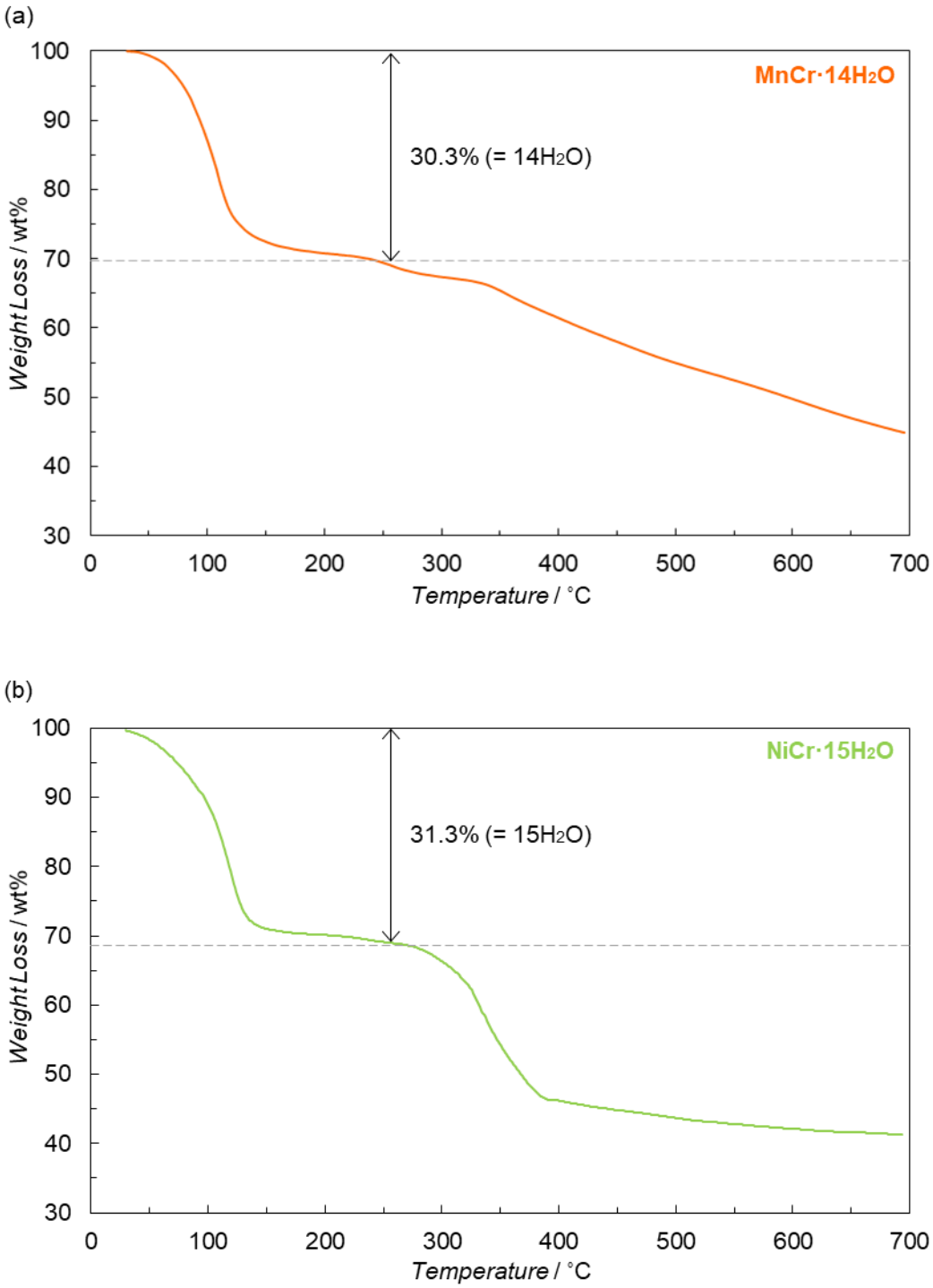

Figure S2. TGA curves of (a) **MnCr·14H$_2$O** and (b) **NiCr·15H$_2$O**.

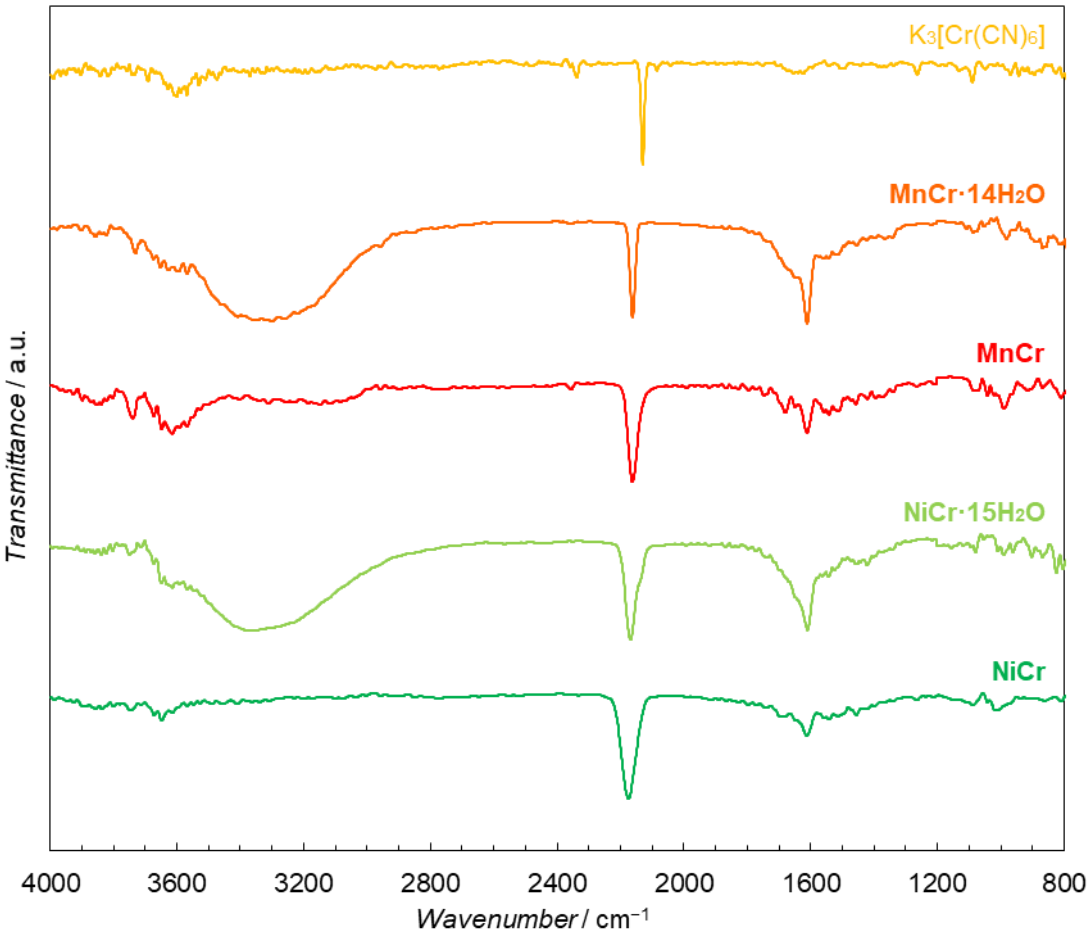

Figure S3. FT-IR spectra of $K_3[Cr(CN)_6]$ (yellow), **MnCr·14H₂O** (orange), **MnCr** (red), **NiCr·15H₂O** (yellow-green), and **NiCr** (green) in the air at room temperature.

Table S3. The observed wavenumber of stretching vibration mode of cyanide anion (ν(C≡N)) in the FT-IR spectra of $K_3[Cr(CN)_6]$, **MnCr·14H₂O**, **MnCr**, **NiCr·15H₂O**, and **NiCr** in the air at room temperature.

	ν(C≡N) / cm^{-1}
$K_3[Cr(CN)_6]$	2130
MnCr·14H₂O	2162
MnCr	2162
NiCr·15H₂O	2169
NiCr	2175

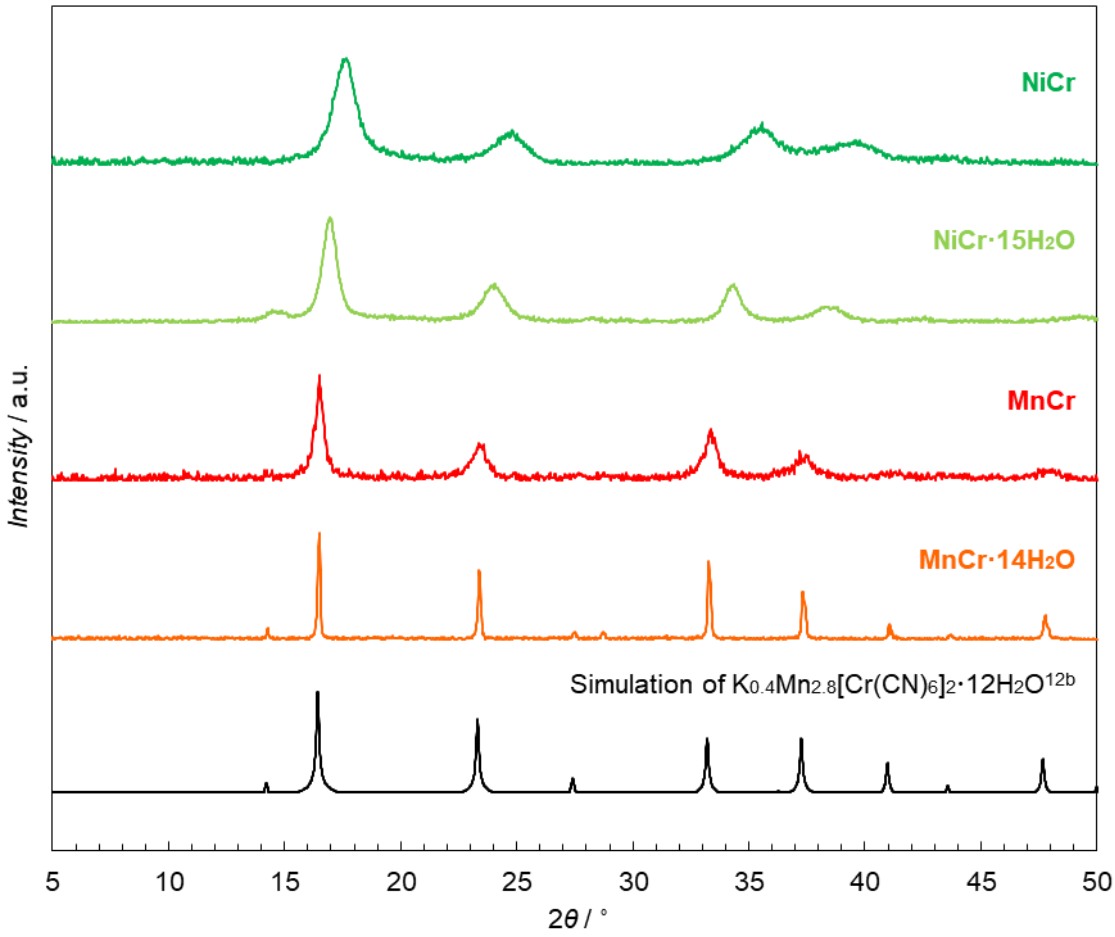

Figure S4. PXRD patterns of **MnCr·14H$_2$O** (orange), **MnCr** (red), **NiCr·15H$_2$O** (yellow-green), and **NiCr** (green) in the air at room temperature, and simulated PXRD pattern of a PBA, $K_{0.4}Mn^{II}_{2.8}[Cr^{III}(CN)_6]_2 \cdot 12H_2O$ (black).[12b]

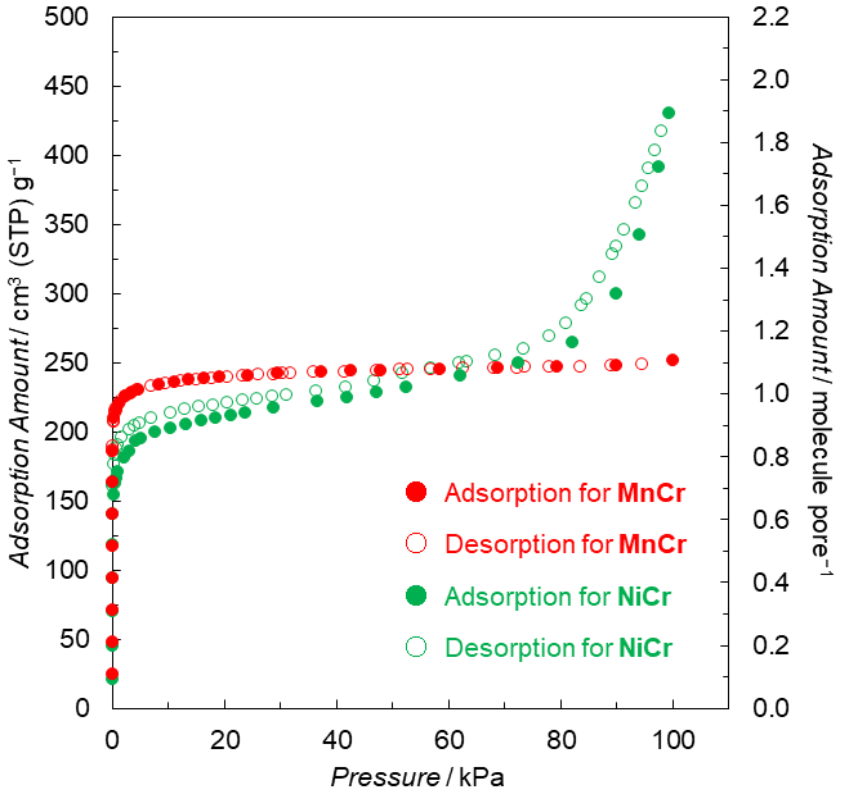

Figure S5. N_2 adsorption (●)/desorption (○) isotherms of **MnCr** (red) and **NiCr** (green) at 77 K.

Table S4. Brunauer-Emmett-Teller specific surface areas (SA_{BET}) and adsorption amount of H_2 ($n_a(H_2)$) around 100 kPa and in 75–78 K of some PBAs, $\{M_A^{II}{}_3[M_B^{III}(CN)_6]_2\}$ (**M_AM_B**).

PBA	SA_{BET} / $m^2\ g^{-1}$	$n_a(H_2)$ / wt%	Reference
MnCr	683	1.4	This work
NiCr	620	1.4	This work
MnCo	870	1.5	10a
MnCo	756	1.0	10b
FeCo	770	1.3	10a
FeCo	350	0.7	10b
CoCo	800	1.4	10a
CoCo	719	1.0	10b
CoCo	692	1.3	10e
NiCo	560	1.3	10a
NiCo	668	1.1	10b
CuCo	730	1.7	10a
CuCo	478	0.4	10b
CuCo	750	1.7	10d
ZnCo	720	1.3	10a
ZnCo	697	1.1	10b
ZnCo	609	1.2	10e
CdCo	667	1.2	10b
CdCo	573	1.3	10i
CdCo	376	1.0	10i

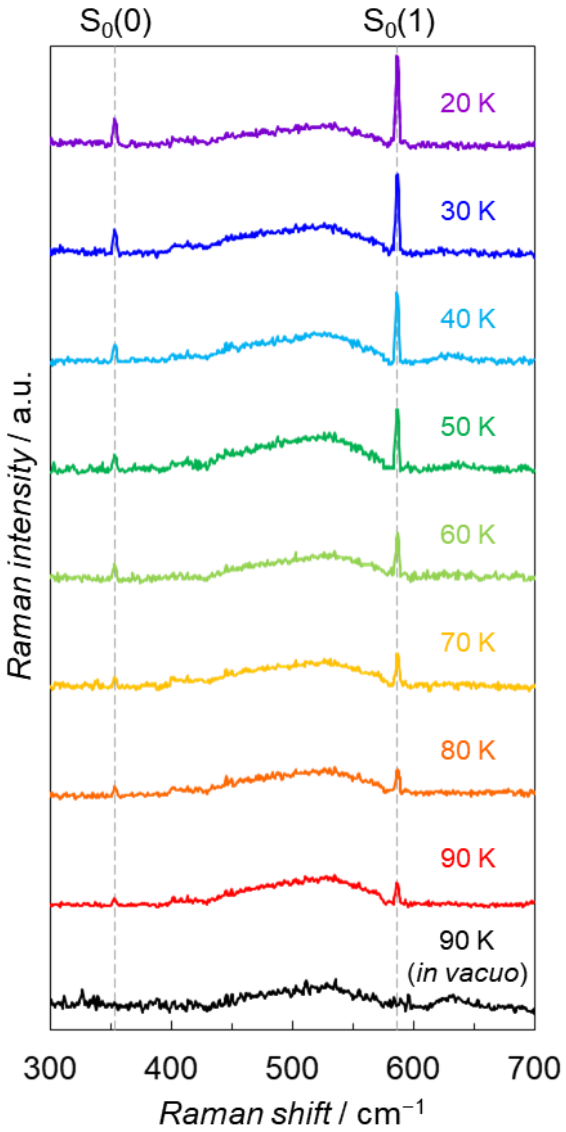

Figure S6. Temperature-dependent *in-situ* Raman spectra of nickel-plated Raman sample cell without **MCr** under reduced pressure (black line) and H_2 gas atmosphere at 100 kPa (colored lines) using an excitation laser with a wavelength of 532 nm without a neutral density (ND) filter.

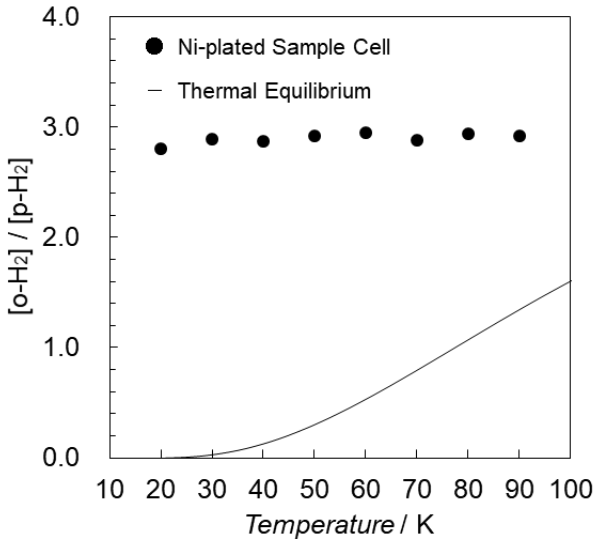

Figure S7. Temperature-dependent abundance ratio of the nuclear spin isomer ([o-H_2]/[p-H_2]) for H_2 observed on nickel-plated Raman sample cell (●) and theoretical ratio in thermal equilibrium based on Boltzmann distribution of H_2 in free rotational state (–).

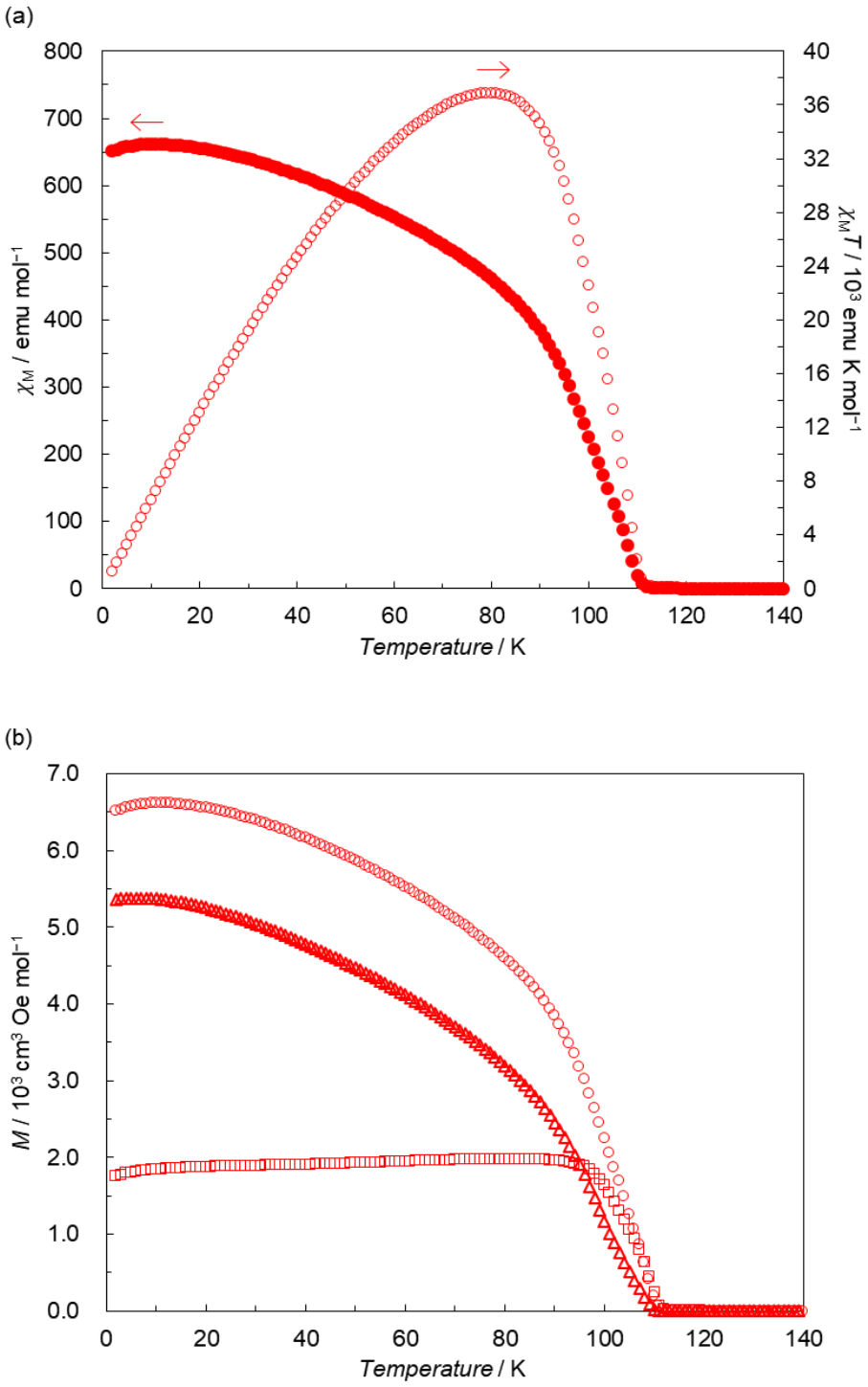

Figure S8. Magnetic properties of **MnCr** under an applied field of 10 Oe. (a) χ_M vs T plot (●) and $\chi_M T$ vs T plot (○). (b) Field-cooled magnetization (FCM; ○), remnant magnetization (RM; △), zero-field-cooled magnetization (ZFCM; □).

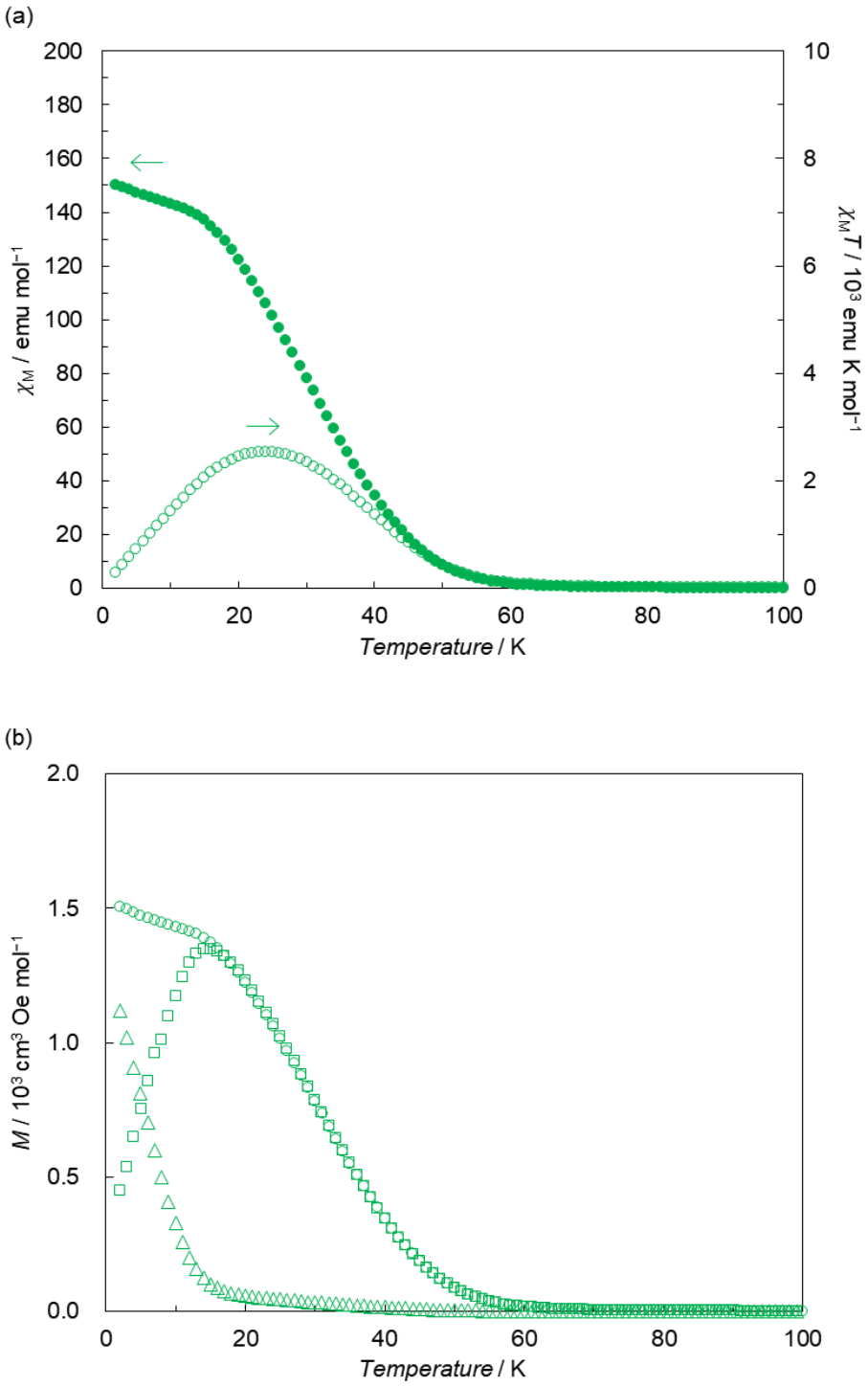

Figure S9. Magnetic properties of **NiCr** under an applied field of 10 Oe. (a) χ_M vs T plot (●) and $\chi_M T$ vs T plot (○). (b) Field-cooled magnetization (FCM; ○), remnant magnetization (RM; △), zero-field-cooled magnetization (ZFCM; □).

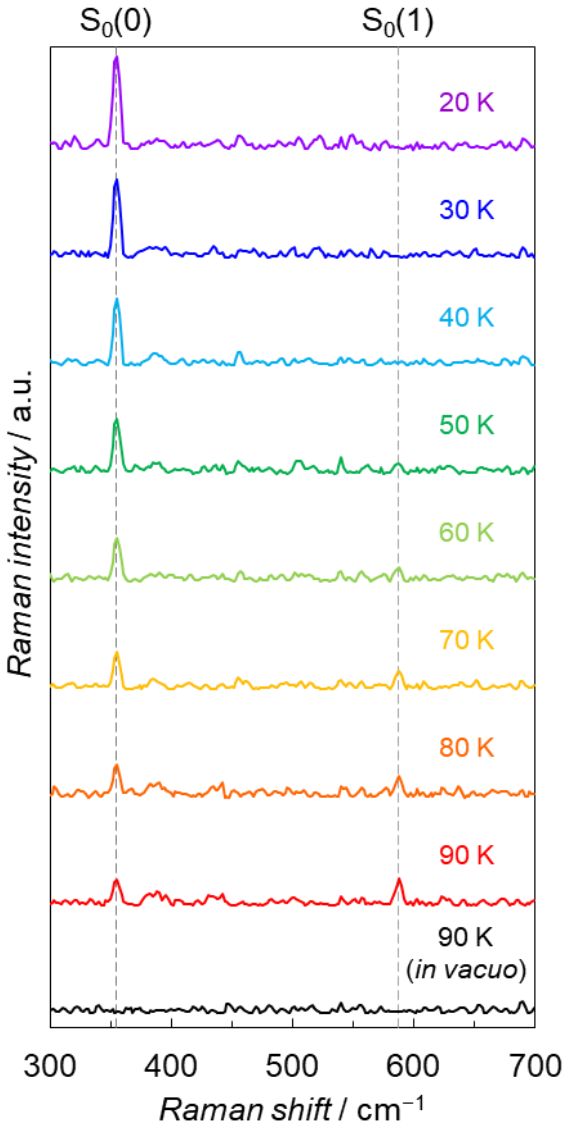

Figure S10. Temperature-dependent *in-situ* Raman spectra of **MnCr** under reduced pressure (black line) and H_2 gas atmosphere at 100 kPa (colored lines), where a neodymium magnet was embedded into the backside of Raman sample basket to magnetize the sample.

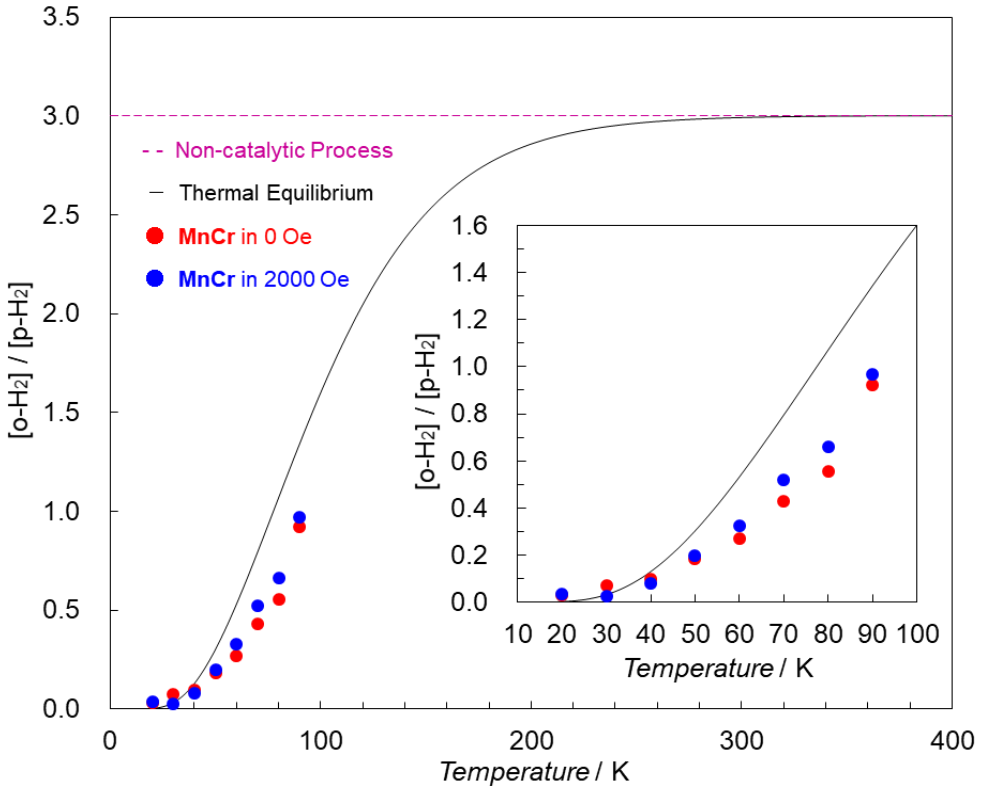

Figure S11. Temperature-dependent abundance ratio of the nuclear spin isomer ([o-H_2]/[p-H_2]) for H_2 confined in **MnCr** under external magnetic field of 0 Oe (red plots) and 2000 Oe (blue plots), estimated ratio obtained in cooling process from room temperature without catalytic treatment (pink), and theoretical ratio in thermal equilibrium based on the Boltzmann distribution of H_2 in free rotational state (black line). The inset is an enlarged view of the low temperature region.

Reference

S1 J. H. Bigelow, *Inorg*. *Synth*. **1946**, *2*, 203

S2 J. Reeve, *J. Chem. Educ*. **1985**, *62*, 444.

S3 S. Ferlay, T. Mallah, R. Ouahès, P. Veillet, M. Verdaguer, *Inorg. Chem.* **1999**, *38*, 229.